Universitat de les
Illes Balears

IFISC

DOCTORAL THESIS
2018

PHOTONIC INFORMATION PROCESSING

Julián Bueno Moragues

Universitat de les
Illes Balears

IFISC

DOCTORAL THESIS
2018

Doctoral Program of Physics

PHOTONIC INFORMATION PROCESSING

Julián Bueno Moragues

Director: Ingo Fischer
Director: Daniel Brunner
Tutor: Pere Colet

Doctor by the Universitat de les Illes Balears

Dr. Ingo Fischer, from IFISC, and Dr. Daniel Brunner, from FEMTO-ST, declare that:

that the doctoral thesis with the title *Photonic Information Processing*, presented by Julián Bueno Moragues, to obtain a doctoral degree has been completed under our supervision.

For all intents and purposes, they hereby sign this document.

Ingo Fischer
Director

Daniel Brunner
Director

Bueno

Julián Bueno Moragues
PhD student

Abstract

Abstract of the thesis

In the current thesis we experimentally study the dynamics of complex photonic systems including semiconductor laser systems with delayed feedback and spatially coupled optical systems, and employ their dynamics for information processing. Photonic delay systems offer a broad range of complex dynamics, making them excellent testbeds for the study of nonlinear dynamics. We take advantage of the complex dynamics and turn the photonic delay systems into information processing systems by applying techniques from the field of neural networks, studying their properties, and demonstrating successful performance.

First we study the dynamics of a semiconductor laser with two delayed optical feedbacks. The temporal evolution of the intensity from the laser is represented and studied in a two dimensional pseudo-space, which conveniently allows to visualize structures in the dynamics. Two dynamical regimes are being addressed in this study, Spiral Phase Defects and Defect-mediated Turbulence. Spiral Phase Defects that were predicted for this system have not been observed, and we discuss the possible reasons. Defect-mediated Turbulence is observed in a broad range of parameters. The defect-mediated dynamics is analyzed in detail by using intensity distribution and spectral analysis. The spectral analysis shows an exponential decay of the spectra for low bias currents of the semiconductor laser. For increasing bias currents, the spectra exhibit a double power law decay that merges into a single power law as the bias currents is increased. This indicates a scale-free behavior in the dynamics for high bias currents.

Next, we study the use of a semiconductor laser with a single delay optical feedback and optical injection as a delay-based reservoir computer. We study the fundamental properties of the system, specifically the properties of injection locking, consistency, and memory. We evaluate the performance of the system in a prediction task, and link the

different properties to performance. The impact of crucial experimental parameters on the properties are evaluated, and the implications discussed. Moreover, we explore further functionalities. Suitable properties and good performance are demonstrated for injection at modulation rates up to to 20 GSa/s, and also for optical injection detuned hundreds of GHz from the solitary emission of the semiconductor laser. Furthermore, we demonstrate how to create a reservoir with nodes with different sets of properties, and show that performance in a prediction task can be improved with this approach.

In the final part, we design and build a spatially extended reservoir computer with 900 coupled nonlinear nodes. The reservoir is implemented with a Spatial Light Modulator (SLM), and the nonlinearity is realized by taking advantage of the polarization modulation of the Spatial Light Modulator (SLM) together with a Polarization Beam Splitter (PBS). The coupling in the network is experimentally implemented with a Diffractive Optical Element (DOE), resulting in coupling beyond first neighbors. The input layer is implemented digitally employing the control computer. The output layer is experimentally implemented with a Digital Micro-mirror Display (DMD) and a lens, where the configuration of the Digital Micro-mirror Display (DMD) determines the values of the output weights in the reservoir computer. We evaluate the dynamics of the nodes and demonstrate suitable nonlinear dynamics in the network. Learning rules are implemented to allow the system to autonomously change the output weights based on previous performance, and to search for an optimized configuration attaining low errors in specific tasks. We demonstrate successful operation of the reservoir computer by showing that, despite some limitations, it is capable of learning reducing the error in a prediction task and finally exhibiting very low prediction errors.

Resumen de la tesis

En la presente tesis estudiamos experimentalmente la dinámica de sistemas fotónicos complejos que incluyen sistemas de láser semiconductor con retroalimentación retardada y sistemas ópticos acoplados espacialmente, y empleamos sus dinámicas para el procesamiento de la información. Los sistemas de retardo fotónico ofrecen una amplia gama de dinámicas complejas, lo que los convierte en excelentes bancos de pruebas para el estudio de dinámicas no lineales. Nosotros aprovechamos las dinámicas complejas y convertimos los sistemas fotónicos con retardo en sistemas de procesamiento de información aplicando técnicas del campo de las redes neuronales, estudiando sus propiedades, y demostrando el desempeño exitoso.

Primero, estudiamos la dinámica de un láser semiconductor con dos retroalimentaciones ópticas retardadas. La evolución temporal de la intensidad del láser es representada y estudiada en un pseudoespacio bidimensional, que convenientemente permite visualizar estructuras en la dinámica. Dos regímenes dinámicos han sido abordados en este estudio, *Spiral Phase Defects* y *Defect-mediated Turbulence*. *Spiral Phase Defects* que se predijeron para este sistema no se han observado, y discutimos las posibles razones. *Defect-mediated Turbulence* es observado en un amplio rango de parámetros. La dinámica mediada por defectos es analizada en detalle mediante el uso de la distribución de intensidad y el análisis espectral. El análisis espectral muestra un decaimiento exponencial de los espectros para bajas corrientes eléctricas del láser semiconductor. Para corrientes eléctricas más altas, los espectros muestran dos decaimientos potenciales que se fusiona en una ley de potencia única a medida que se incrementan las corrientes eléctricas. Esto indica un comportamiento sin escalas en las dinámicas para altas corrientes eléctricas.

A continuación, estudiamos el uso de un láser semiconductor con una única retroalimentación óptica retardada y una inyección óptica como un ordenador de reservorio basada en el retardo. Estudiamos las propiedades fundamentales del sistema, específicamente las propiedades de bloqueo de inyección, la consistencia, y la memoria. Evaluamos el rendimiento del sistema en una tarea de predicción y vinculamos las diferentes propiedades con el rendimiento. El impacto de parámetros experimentales cruciales en las propiedades es evaluado, y las implicaciones son analizadas. Por otra parte, exploramos otras funcionalidades. Propiedades adecuadas y buen rendimiento son demuestrados para inyección a tasas de modulación de hasta 20 GSa/s, y también para inyección óptica sintonizada a cientos de GHz de la emisión solitaria del láser semiconductor. Además, demostramos cómo crear un reservorio con nodos con diferentes conjuntos de propiedades, y mostramos que el rendimiento en una tarea de predicción se puede mejorar con esta estrategia.

En la parte final, diseñamos y construimos un ordenador de reservorio espacialmente extendido con 900 nodos no lineales acoplados. El reservorio es implementado con un Spatial Light Modulator, y la no linealidad es realizada aprovechando la modulación de polarización del Spatial Light Modulator junto con un Polarization Beam Splitter. El acoplamiento en la red es implementado experimentalmente con un DOE, lo que resulta en un acoplamiento más allá de los primeros vecinos. La capa de entrada es implementada digitalmente empleando el ordenador de control.

La capa de salida es implementada experimentalmente con un Digital Micro-mirror Display y una lente, donde la configuración del Digital Micro-mirror Display determina los valores de los pesos de salida en el ordenador de reservorio. Evaluamos la dinámica de los nodos y demostramos una dinámica no lineal adecuada en la red. Las reglas de aprendizaje son implementadas para permitir que el sistema cambie los pesos de salida de forma autónoma en función de rendimiento anterior, y para buscar una configuración optimizada que logre pocos errores en tareas específicas. Demostramos el funcionamiento exitoso del ordenador de reservorio demostrando que, a pesar de algunas limitaciones, es capaz de aprender a reducir el error en una tarea de predicción y, finalmente, exhibir errores de predicción muy bajos.

Resum de la tesis

En la present tesi estudiem experimentalment la dinàmica de sistemes fotònics complexos que inclouen sistemes de làser semiconductor amb retroalimentació retardada i sistemes òptics acoblats espacialment, i fem servir les seves dinàmiques per al processament de la informació. Els sistemes de retard fotònic ofereixen un ampli ventall de dinàmiques complexes, que els converteix en excel·lents bancs de proves per a l'estudi de dinàmiques no lineals. Nosaltres aprofitem la dinàmica complexa i convertim els sistemes fotònics amb retard en sistemes de processament d'informació aplicant tècniques del camp de les xarxes neuronals, estudiant les seves propietats, i demostrant una realització exitosa.

Primer, estudiem la dinàmica d'un làser semiconductor amb dues retroalimentacions òptiques retardades. L'evolució temporal de la intensitat del làser és representada i estudiada en un pseudoespai bidimensional, que permet visualitzar convenientment estructures en la dinàmica. Dos règims dinàmics són abordats en aquest estudi, *Spiral Phase Defects* i *Defect-mediated Turbulence*. *Spiral Phase Defects* que estaven previstos per a aquest sistema no han estat observats, i les possibles raons analitzades. *Defect-mediated Turbulence* s'observa en un ampli rang de paràmetres. La dinàmica intervinguda per defectes és analitzada en detall utilitzant la distribució d'intensitat i l'anàlisi espectral. L'anàlisi espectral mostra un decaïment exponencial en els espectres per a baixos corrents elèctrics del làser semiconductor. Per corrents electrics més alts, els espectres mostren un doble decaïment potencial que es fusiona en un sol decaïment a mesura que s'incrementa el corrent elèctric. Això indica un comportament sense escala per les dinàmiques amb gran corrents elèctrics.

A continuació, estudiem l'ús d'un làser semiconductor amb una única retroalimentació òptica amb retard i injecció òptica com a ordinador de reservori basat en retards. Estudiem les propietats fonamentals del sistema, específicament les propietats del bloqueig d'injecció, la consistència i la memòria. Avaluem el rendiment del sistema en una tasca de predicció i vinculem les diferents propietats al rendiment. L'impacte de paràmetres experimentals crucials són avaluats en les propietats, i a més se'n discuteixen les implicacions i se n'exploren altres funcionalitats. Les adequades propietats i bon rendiment són demostrats per injecció a taxes de modulació de fins 20 GSa/s, i també per injecció a freqüències òptiques centenars de GHz des de l'emissió solitària del làser semiconductor. A més, demostrem com crear un reservori amb nodes amb diferents conjunts de propietats, i demostrar que el rendiment en una tasca de predicció es pot millorar amb aquesta estratègia.

A la part final, dissenyem i construïm un ordinador de reservori espacialament estès amb 900 nodes no lineals acoblats. El reservori és implementat amb un *Spatial Light Modulator*, i la no linealitat és realitzada aprofitant la modulació de la polarització del *Spatial Light Modulator* juntament amb un *Polarization Beam Splitter*. L'acoblament a la xarxa s'implementa experimentalment amb un *Diffractive Optical Element*, resultant en un acoblament més enllà de primers veïns. La capa d'entrada és implementada digitalment emprant l'ordinador de control. La capa de sortida és implementada experimentalment amb un *Digital Micro-mirror Display* i una lent, on la configuració del *Digital Micro-mirror Display* determina els valors dels pesos de sortida a l'ordinador de reservori. Avaluam la dinàmica dels nodes i demostrem dinàmiques no lineals adequades a la xarxa. Les regles d'aprenentatge s'implementen per permetre que el sistema canviï de forma autònoma els pesos de sortida en funció de rendiment previ i busqui una configuració optimitzada que aconsegueixi errors baixos en tasques específiques. Mostrem un funcionament exitós de l'ordinador de reservori demostrant que, malgrat algunes limitacions, és capaç d'aprendre a reduir l'error en una tasca de predicció i, finalment, mostrar errors de predicció molt baixos.

Acknowledgments

I want to thank first of all my supervisors Ingo Fischer and Daniel Brunner. They have supported me since the beginning, and pushed me to do better in every aspect as a scientist. They offered me new challenges and never doubt of my skills even though I did sometimes. Also they seem to have an endless supply of patience, which I think is specially required in experimental science. I hope they still have some left for the future! For these things and more I am grateful.

I want to extend my gratitude to past and current members of the Nonlinear Photonics group. Claudio Mirasso and Miguel C. Soriano introduced me to the field and helped me to do my first steps. They kept the helpful spirit and a warm welcome throughout these years, which I wish many others to enjoy. Xavier Porte and Neus Oliver answered many questions about the lab, and never frown upon any interruption. Thomas Jüngling and Silvia Ortín offered many interesting conversations, independently of the topic and place. Apostolos Argyris has also taught us many things, and is an exemplary scientist.

During my time here I had the pleasure to share the IFISC with wonderful people. They can be found in all floors and in all rooms, and they made the time outside the lab worth to remember, being it in a party, in the S07, or around food. The list would include almost everyone in the IFISC website, including many former researchers, so it would be too long to be included here. Many thanks to the people in Femto-ST for making my stay awesome. All of them have create fonded memories that will be cheerfully kept.

People outside the IFISC also deserve recognition. I want to thanks the members in the ”Físics sense Futur” team. We went through the physics degree together, and endured the PhD in completely different topics. Our meetings always helped to heal the wounds and peace the mind. I am sure this wouldn’t have been the same without you.

Finally, I want to thank my family. Thanks to my parents for their support and understanding during these years, and also to my wife Olga for doing her best everyday for us. Without them I know this journey would not have been the same. So long, and thanks for all!

I would also like to thank the MINEICO (Ministerio de Economía, Industria y Competitividad) and to the CSIC (Consejo Superior de Investigaciones Científicas) for providing me with the economic support.

Publications and communications

Publications

- Julián Bueno, Daniel Brunner, Miguel C. Soriano, and Ingo Fischer, *Conditions for reservoir computing performance using semiconductor lasers with delayed optical feedback*, Opt. Express **25**, 2401-2412 (2017).
- Julián Bueno, Sheler Maktoobi, Luc Froehly, Ingo Fischer, Maxime Jacquot, Laurent Larger, and Daniel Brunner, *Reinforcement learning in a large-scale photonic recurrent neural network*, Optica **5**, 756-760 (2018).

Publications in preparation

- Julián Bueno, Daniel Brunner, Damià Gomila, Ingo Fischer, and Serhiy Yanchuk, *2D defects and optical turbulence in semiconductor laser dynamics with dual delayed feedback*.

Other relevant contributions

- Apostolos Argyris, Julián Bueno, and Ingo Fischer *Photonic machine learning implementation for signal recovery in optical communications*, Scientific Reports **8**, 8487 (2018).
- Julián Bueno, Daniel Brunner, and Ingo Fischer. *Consistency and memory properties of an all-optical information processing scheme*. Talk at the Conference Dynamical Systems and Brain-inspired Information Processing (Besançon, France, 2015).
- Julián Bueno, Daniel Brunner, Miguel C. Soriano, and Ingo Fischer. *Conditions for reservoir computing performance using semiconductor lasers with delayed optical feedback*. Invited talk at the Nonlinear Dynamics in Photonics for Future Information and Communication Technologies meeting (Palma de Mallorca, Spain, 2016).
- Julián Bueno, Daniel Brunner, Miguel C. Soriano, and Ingo Fischer. *Photonic Information Processing at 20GSa/s rates based on Semiconductor Lasers with Delayed Optical Feedback*. Poster presented at the European Conference on Lasers and Electro-Optics and the European Quantum Electronics Conference (Munich, Germany, 2017).

Contents

Abstract 3

Acknowledgments 8

List of publications and conference contributions 9

Page

Contents 13

1 Introduction 15
- 1.1 The semiconductor laser 16
- 1.2 Semiconductor lasers with delayed optical feedback 19
  - 1.2.1 Optical characteristics of a semiconductor laser with and without feedback 20
- 1.3 Semiconductor lasers under optical injection 24
- 1.4 Neuro-inspired information processing 26
  - 1.4.1 Reservoir computing 30
  - 1.4.2 Delay-based reservoirs 31
  - 1.4.3 Hardware implementation 34
- 1.5 Motivation and overview of this thesis 36

2 General methods 39
- 2.1 Light measurement acquisition methods 40
- 2.2 Experimental techniques for precise determination of the delay time 42
  - 2.2.1 Autocorrelation measurement of timetraces 42
  - 2.2.2 Pulse propagation technique 43

3 Dynamics of a semiconductor laser with dual delayed optical feedback 45
3.1 Introduction 46
3.2 Methodology to construct 2D spatial representations 47
3.3 Experimental scheme 49
3.4 P-I curve 51
3.5 Spiral phase defects 53
3.6 Defects-mediated turbulence 56
    3.6.1 Intensity distribution in the dynamics 60
3.7 Spectral characteristics of the dynamics 62
3.8 Summary and discussion 67

4 Time delay reservoir based on a semiconductor laser with delayed optical feedback 71
4.1 Introduction 72
4.2 Experimental setup 74
4.3 Methods for training and characterization of a delay laser reservoir 77
    4.3.1 Determination of the output weights 77
    4.3.2 Consistency 81
    4.3.3 Memory task 83
    4.3.4 Prediction tasks 85
4.4 Fundamental properties and dependence on feedback attenuation and frequency detuning 88
    4.4.1 Injection locking properties 89
    4.4.2 Consistency properties 92
    4.4.3 Memory properties 96
    4.4.4 Mackey-Glass prediction performance 99
4.5 Dependence of properties and prediction error on response laser's bias and on average injected power 101
    4.5.1 Assessing optimized bias current and injection power 104
4.6 Properties and opportunities of side-mode injection 106
4.7 Impact of noise 109
4.8 Performance at injection rates from 5GSa/s to 20GSa/s . . . 111
4.9 Emulating multiple heterogeneous reservoirs 116
    4.9.1 Memory properties 118
    4.9.2 Prediction performance 119
4.10 Discussion and summary of the results 121

5 Towards spatially extended photonic reservoir computers 127
5.1 Introduction . . . 128
5.2 Experimental setup . . . 129
5.2.1 The spatially distributed optical reservoir . . . 129
5.2.2 Implementation of the input layer . . . 141
5.2.3 Implementation of the output layer . . . 143
5.2.4 Complete schematic of the experimental setup . . . 148
5.3 Methodology to obtain optimal output weights . . . 148
5.3.1 Online reinforcement learning . . . 149
5.3.2 Stochastic weighted node selection . . . 151
5.3.3 Node filtering . . . 152
5.4 Dynamics of the reservoir . . . 153
5.4.1 Dynamics of the uncoupled network . . . 153
5.4.2 Dynamics of the coupled network . . . 157
5.5 Consistency of the dynamics . . . 161
5.6 Simulated learning . . . 165
5.6.1 Simulation versus Experiment . . . 167
5.6.2 Parameter dependencies . . . 170
5.7 Experimental results using optimized parameters . . . 172
5.8 Summary and discussion . . . 174

6 Final Summary and Outlook 179
6.1 Summary . . . 180
6.2 Outlook . . . 182

List of Figures 185

Bibliography 221

Chapter 1

Introduction

1.1 The semiconductor laser

Light is essential. In nature, light from the Sun provides the energy for plants and all subsequent life forms. Among the many light generating devices available, lasers have a special place. Lasers emit radiation thanks to the process of stimulated emission, hence the acronym Light Amplification by Stimulated Emission of Radiation (LASER). There are many kinds of lasers [1, 2]. Here we focus on the Semiconductor Laser (SL), that generates light thanks to semiconductor materials. The idea of employing a semiconductor was first reported by [3]. This was specially interesting since a semiconductor laser would offer small size and narrow linewidth emission [2]. The first laser was built in 1960 at the Hughes Research Laboratories, and the SL was first experimentally reported in 1962 by three independent research teams in General Electric [4], IBM [5], and Lincoln Laboratory [6].

Lasers have become an indispensable technology thanks to the characteristic properties of the light they generate. These properties can include beam directionality, high spectral density, monochromaticity, and coherence [7]. The light generated by lasers shows a pronounced directionality. While in other light sources, like incandescent light bulbs, light is emitted in many directions, lasers mostly emit light in one direction. This allows to easily direct light and illuminate precise areas. High beam directionality together with the high efficiency of the laser increases substantially the intensity of the emitted light when focused on a single spot. The laser design contributes to the monochromaticity of the light emitted. Lasers can emit beams with narrow spectral linewidth and high coherence properties. Coherence relates to the phase difference between different points of a wavefront over space (spatial coherence) and time (temporal coherence). The high coherence exhibited by laser beams makes them excellent light sources for applications such as for example interferometry, holography, and tomography [8, 9].

These properties brought lasers into old and new applications, and even after 25 years after its invention the laser had deeply impacted multiple fields [10]. A list of applications could be endless, but a short list can exemplify the impact of lasers in technology. Lasers are used in machining industry for cutting and drilling. The medical field uses lasers for surgical procedures involving destruction of malign tissue or stones, cauterization, or cornea reshaping. Other medical applications of lasers include imaging techniques like optical coherence tomography and optogenetics [11]. Laser are also extensively used in metrology to measure distances at very different scales, for instance. Light Detection and Ranging (LiDAR) systems use lasers to measure distances from meters to kilometers for autonomous navigation and airborne scanning, respectively. Laser interferometry can be used to detect displacements or changes of refractive index. Interferometric setups with extraordinary sensitivity have been realized to detect distance changes on the order of 10^{-18} meters to detect gravitational waves [12].

In applications regarding information technologies, SLs are highly present. Lasers have contributed to optical and holographic data storage. Optical storage reads and writes a pattern of bits from or to an optical disc. It is the technology behind CD, DVD, and Blu-ray. Holographic optical storage offers high memory density, high capacity, and fast speeds [13]. A field where SLs have a crucial role is in optical communications. Realization of continuous wave operation of the SL at room temperature together with the development of the low loss optical fiber caused a revolution in telecommunication, where information transmission through optical fiber by more than six orders of magnitude since their first commercial realization in 1975 [14]. Semiconductor Lasers are the preferred choice due to emission at suitable wavelengths for optical fiber communication. Furthermore, SL offers a variety of additionally advantages such as a small size (which volumes less than a mm^2), modulation bandwidth in the GHz range, continuous light emission, integrability in photonic circuits, high optical power, and multiple designs.

SLs do not exist as a single design only. Depending on the design and structure, a broad variety of SLs can be found. They differ in terms of maximum intensity, beam quality, wavelength tunability, light polarization, or how energy is introduced in the semiconductor material [2, 7, 15]. The basic elements of a laser are the gain medium, the resonator, and the pumping.

The gain medium is where light is amplified through a process called stimulated emission. The amplification of light transforms external energy into optical power. The semiconductor material introduces nonlinear effects, the most important one being the α factor [16]. The α factor relates changes in the carrier density with changes to the susceptibility of the semiconductor material. By defining the susceptibility as $\chi(n) = \chi_R(n) + i\chi_I(n)$ (where $\chi_R(n)$ and $\chi_I(n)$ are the real and the imaginary part, respectively), the α factor can be defined as:

$$\alpha = -\frac{d\chi_R(n)/dn}{d\chi_I(n)/dn} \tag{1.1}$$

Changes in the real part affects the optical length of the gain medium, changing the emitted frequency by the laser; and changes in the imaginary part affect the gain of the medium [15]. An $\alpha \neq 0$ implies that there exist a coupling between the phase and the amplitude of the emitted radiation and the gain medium. This coupling makes the α factor a crucial nonlinear effect that influences the dynamics of the SL under perturbations like modulation or optical injection. Furthermore, the α factor is responsible of the larger linewidth in SL compared to other kinds of lasers.

The selection of the gain medium also affects the dynamical behavior of the system. The gain medium determines the characteristic time scales of different processes inside the laser. Most semiconductor lasers fall in what is called Class B lasers. In these lasers the medium polarization decays much faster than the electric field and carrier density. Class B lasers can not exhibit chaos without external perturbations, but can exhibit damped oscillations in the intensity-population plane. Class B SLs exhibit such oscillations in the GHz range typically called Relaxation Oscillations (RO), specially when they turn on and then when emission stabilizes. The frequency of these oscillations reveals the fundamental response time of the system to the harmonic modulation of a parameter, but also to perturbations and in dynamical processes [17].

The resonator in the SL selects the emitted optical modes from the ones the gain medium generated. A resonator is an optical cavity that confines light of certain frequencies resonant with its configuration. SLs typically employ a mirror on each side of the gain medium creating a Fabry-Perot resonator, allowing only certain modes to be reflected repeatedly by the mirrors to be amplified by the gain medium. In practice, at least one component in the resonator is semitransparent to allow extraction of the light from the laser cavity. The high efficiency of the semiconductor gain medium allows to lower the reflectivity more compared with other lasers to extract even more power. Other reflecting devices can be employed instead of mirrors. In Distributed Feedback (DFB) and Distributed Bragg Reflector (DBR) lasers, grating structures with periodic changes in their index of refraction can be used to attain high reflectivity through the interference of multiple reflections. Using micro-disks or toroidal disks, the light can be confined inside the outer rim creating whispering gallery modes. In this thesis we mostly use Discrete Mode Lasers. These lasers comprise a regrowth-free ridge waveguide Fabry-Perot resonator, with etched features positioned at precise places along the ridge waveguide [18]. This allows the laser to emit with a very narrow linewidth and ensures single mode operation in a broad temperature and current range.

Last, pumping is the process to inject external energy into the laser, typically done by optical or electrical means, to excite the atoms and achieve population inversion. Optical pumping is performed by illuminating the gain medium, and can be done with either coherent or incoherent illumination. Electrical pumping is performed by providing an electrical current. Electrical pumping is used in most semiconductor due to the high electrical-to-optical efficiency of the SL and convenience.

1.2 Semiconductor lasers with delayed optical feedback

The susceptibility of the gain medium to light allows the laser to be optically pumped, but also to be susceptible to other sources of light. One of these sources can be the light emitted by the own laser that it is reflected by an external surface. This light is referred to as optical feedback. Design factors and $\alpha \neq 0$ make these devices susceptible to these contributions [15, 19]. Optical feedback can be detrimental for the laser's stable operation and even small powers can destabilize the laser, producing unwanted perturbations in the output power and broadening the spectra. These effects can be detrimental in many applications where lasers need constant optical power with narrow linewidths [20, 21].

Over time, the interest of researchers for the nonlinear characteristics of the SL and the delay dynamics increased. Thorough studies of the feedback laser systems showed that high dimensional dynamics can be obtained from a SL with optical delayed feedback. These dynamics strongly depend on several parameters such as the pump current [22], the feedback delay time [23, 24], the phase [25], the average power [22], or the polarization [26]. Far from being discarded, the feedback-induced dynamics in SLs have been employed in multiple applications ranging from random bit generation [27, 28], neuro-inspired information processing [29], range finding [30, 31], Doppler velocimetry [32], frequency stability and tunability of emission's wavelength [33], even to secure communications [34].

The SL has also been used as testbeds to study nonlinear systems in general thanks to the wide variety of nonlinear phenomena occurring under optical feedback. As oscillators they have also been used to study general concepts of nonlinear dynamics like synchronization [35–37] and network dynamics [38–40].

1.2.1 Optical characteristics of a semiconductor laser with and without feedback

In this section we illustrate the impact of optical feedback on the emission of a SL with an example. We use the laser described in Section 4.2. The light is reinjected into the laser using optical fiber components, as shown in the schematic in Figure 1.1. The loop is created by using an optical circulator, a three or four port device that routes incoming light from one port to another in a non-reciprocal way. A polarization controller and optical attenuator are included in the delay loop to control the feedback polarization and strength, respectively. The reinjected light can have different impacts depending on its properties, and even a tiny amount of the feedback can be enough to destabilize the SL [41, 42]. The polarization of the feedback light was set parallel to the polarization of the light emitted.

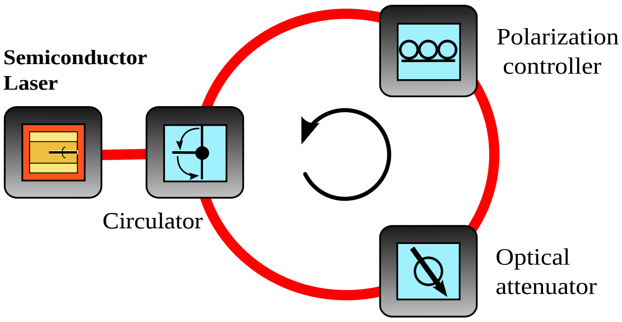

Figure 1.1: Schematic of an experimental setup in delayed feedback experiments using optical fiber components. The loop is created by connecting the third port of the circulator to the first port. The SL is connected to the second port. The black arrow represents the feedback propagation direction inside the loop, defined by the port connections' of the circulator. Additional components can be included in the loop to control for the feedback's properties.

First, we characterize the output power emitted by the laser dependence to the bias current. This dependence is typically referred to as P-I curve. In Figure 1.2(a), the P-I curve shows the average power emitted by the laser versus the bias pumping current. In black, we show the P-I curve of the SL in solitary conditions (without feedback), and in red with maximum available feedback. The curves are characterized fundamentally by the threshold current. This is the current where the laser starts to emit stimulated light. This current is slightly larger than the current at which losses equal gain inside the laser, condition referred to as transparency [1]. For higher currents the output optical power increases linearly. For solitary conditions the threshold current is 12.87 mA. To obtain the threshold current, one can perform a linear regression analysis on the power emitted above threshold, which is represented as a gray dashed line in Figure 1.2(a). The crossing of the resulting linear fit with the x-axis at zero emitted power determines the threshold current. When optical feedback is injected, the curve shifts towards lower values. This is a well-known effect originating from a reduction of the total losses due to the re-injection of the emitted light into the laser [43]. This reduces the lasing threshold current and typically increases the output power emitted by the laser close to threshold. The feedback acts as an extra cavity and it changes the balance between the laser's emission from the front to the rear facet. One can also observe that the slope of the dependencies are different. The solitary case presents a higher slope than under optical feedback, indicating a higher efficiency. The lower efficiency when including feedback is due to an effective increase of the reflectivity of the laser's facet. Different slopes in the curves introduces a cross over point where the laser emits the same power with and without optical feedback present [22, 44]. Additionally, right after threshold, the P-I curve of the feedback laser experiences a kink before following a linear trend. This kink separates the P-I curve for the linear dependence shown as a gray dashed line in Figure 1.2(a). It was already observed in [43], where kinks are referred as irregularities.

The power recorded for the P-I curves is the average power emitted in a time window much longer than the timescale of the laser's dynamics. In Figure 1.2(b) we show the amplitude evolution of the dynamics with sub-nanosecond resolution. These traces were measured AC coupled, so the DC component of the signal is unknown. These traces were obtained for $I = 13.25$ mA. In black, we show the power over time by the solitary laser, and in red the laser with maximum available feedback. The laser with optical feedback presents larger and faster fluctuations than the laser under solitary conditions. The small fluctuations in the solitary case originate from experimental noise.

To capture only the fast fluctuations on the power evolution we measure the power spectra of the dynamics as the power of the optical feedback increases, as shown in Figure 1.3. These power spectra were obtained by detecting the optical power evolution of the SL with a photodetector, and then measuring the spectra of the electrical signal with an Electrical Spectrum Analizer. In black, we show the power spectra on

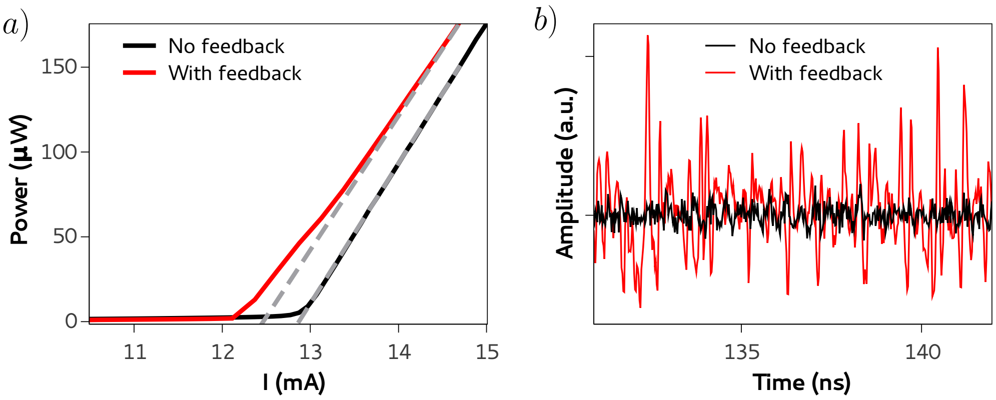

Figure 1.2: (a) P-I curve and (b) example of power time series for the SL for solitary (black) and with optical feedback (red) for $I = 13.25$ mA. Gray dashed lines indicate extrapolations from linear regression analysis of the power versus current dependence.

the laser under solitary conditions, in red for feedback attenuated by 12 dB, and green for maximum optical feedback. The power spectra of the solitary laser exhibits a pronounced peak at 2.5 GHz, corresponding to the frequency of the RO of the SL. When optical feedback is introduced, the emission spectra can substantially broaden. This indicates that the dynamic include faster and stronger oscillations as more optical feedback is added. The broad range of frequency components is a typical signature of chaotic dynamics. This relates to what we saw in the power time series, ruled by fast fluctuations of erratic amplitude.

We finish by characterizing the spectra of the electrical field with an optical spectrum. In Figure 1.4 we show the optical spectra of the cases shown in Figure 1.3 with identical color. For solitary conditions, the spectra exhibits a sharp peak indicating a main emitted frequency with 10 MHz of linewidth (limited by the instrument). On the side, one can observe two small broad peaks corresponding to the damped RO. The amplitude of between these peaks is different due to the α factor. This asymmetry can be used to determine the α factor [45]. As feedback is injected, the spectra broaden. The dominant frequency emitted and the full spectra shifts to lower frequencies as more feedback is added. These effects can be explained by the Lang-Kobayashi model, which theoretically describes the SL under optical delayed feedback [46]. When including optical feedback, the model contains solutions called External Cavity Modes, responsible for the dynamical evolution [47–49]. In the phase-

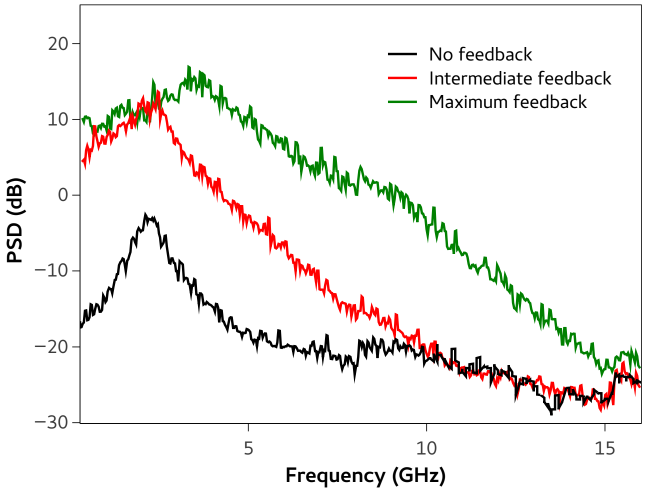

Figure 1.3: Power spectra of the SL with different feedback conditions: no feedback (blak), 12 dB attenuated feedback (red), and maximum feedback (green).

carrier density plane they are distributed in the shape of an ellipse, with an eccentricity determined by the value of α, and extending in the range $\omega = \kappa\sqrt{(\alpha^2 + 1)}$, where κ is the feedback strength [15, 17]. While solutions in the upper half of the ellipse are unstable, solutions in the lower side can be partially stable. The ellipse is tilted so the modes for negative frequency have higher gain, leading the dynamics towards those modes with high gain. Correspondingly, the emission shifts towards negative frequencies under optical feedback.

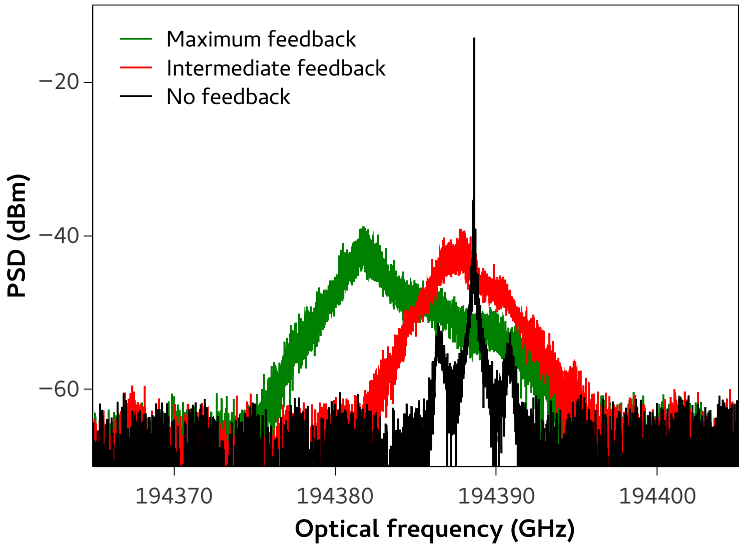

Figure 1.4: Optical spectra of the SL with different feedback conditions: no feedback (black), intermediate feedback (red), and maximum feedback (green).

1.3 Semiconductor lasers under optical injection

We have seen that the light emitted by the SL can be reinjected to stimulate complex dynamics. But light from another laser can also be injected. Optical injection is performed when the light from one laser (injection laser) is injected into another laser (response laser). This configures the lasers in a unidirectional coupling scheme. During optical injection, the injected light is meant to interact with the lasing directly, so the emission frequency of both lasers should be similar. For this reason, one can select and tune the source of the injected light so its has a frequency close to the one emitted naturally by the response laser. The idea of optical injection in lasers appeared shortly after the invention of the laser itself [50]. Optical injection in SL was triggered by the application of SL in optical communications [51]. It was demonstrated that the frequency and linewidth properties from the injection laser can be transferred to the response laser when the lasers are locked [52–54]. This is a coherent phenomenon where the response laser oscillation synchronize to the injection's. Optical injection has been used to further stabilize lasers, ensuring single mode operation of the response laser to avoid multi-mode operation and mode hopping [55], reduce noise [56, 57], reduce linewidth [58], and to suppress feedback-induced instabilities. The emission of a single laser can be injected into multiple lasers to induce in all of them emission at the same frequency. Applications that require narrow linewidth can benefit from such scheme, like spectroscopy [59], laser cooling [60, 61], and traps for atoms [62]. Furthermore, optical injection can be also used in power amplifiers or for narrow optical filter.

Optical injection can also induce nonlinear dynamics in the response laser. Under optical injection, nonlinear dynamics such as periodic oscillations, bistability, four-wave mixing, and chaos have been demonstrated [63–69]. The variety of nonlinear dynamics induced by optical injection in SLs makes these systems excellent testbeds for generation of complex dynamics. The generation of periodic oscillations can be employed for microwave generation [70]. Relaxation oscillations can be suppressed to increase modulation rates [71]. Additionally, optical injection can enhance the bandwidth of SL [72, 73]. The dynamics of SLs under optical injection have been extensively studied, theoretically [68] as well as experimentally [74]. Two parameters specially relevant for the dynamics of SL under optical injection are the injection strength and the frequency detuning. The frequency detuning is the optical frequency difference between the injection and response laser. If the frequency detuning is small and injection strong enough, the response laser is locked to injection and emits at the injection's frequency. This dependence shows a cone in parameter space where the response laser is locked. Outside this region the laser is unlocked and nonlinear dynamics can occur [15]. The cone was derived for SLs for the first time in [75], and authors showed that $\alpha \neq 0$ extended the locking region asymmetrically for negative frequencies by a factor $\sqrt{1+\alpha^2}$. Linear stability analysis showed that locked solutions are stable on the most negative frequency side of the cone, while unstable elsewhere [15, 76].

Two SLs unidirectionally coupled is the simplest configuration to study optical injection in SLs. Instead of using a free-running SL one can use a SL with optical delayed feedback, either as the injection or the response system. This modification in the injection system can create a chaotic and broadband signal that the response laser needs to lock to. Incorporating the optical feedback into the response system, as the response laser can exhibit chaotic motion and can be forced to lock to injection even under the destabilization effect of the feedback. Incorporation of feedback in one of the two nonlinear elements has proved to enhance the complexity of the dynamics as well as broaden the bandwidth [77–80] , which has been useful for several applications [27, 81–86].

Some applications require information from injection with modulated signals. The dynamical response of a SL with optical feedback under such injection has been only very recently addressed [87]. Few studies have considered the injection of a chaotic signal from a similar system [79, 88] or even from the same one [89]. Nevertheless, typical modulation schemes like amplitude modulation involve holding a value over a specific time windows. This scheme differs to injecting a chaotic or a noisy signal. Deeper understanding of the properties of SLs under delayed optical feedback and modulated optical injection is required, especially to efficiently use them for information processing. This is the fundamental motivation in Chapter 4.

1.4 Neuro-inspired information processing

In this section we move from nonlinear systems and focus on an information processing technique that benefits from complex dynamics. This technique is Reservoir Computing (RC). We make use of it in Chapter 4 and Chapter 5. Before describing in detail the intricacies of RC, we provide a brief background of the concept. RC belongs to the field of neural networks, a branch of Machine Learning. Neural networks has a biologically neuro-inspired origin. By mimicking the nervous system with an Artificial Neural Network (ANN), researchers desired to build a neuromorphic system that processes information with similar characteristics, functionalities as the brain. Fundamentally, the brain is a complex network of neurons, where every neuron is a nonlinear dynamical element connected to other neurons. The number of neurons in the brain varies among species, from 302 in simple worms as the C. elegans [90, 91] to $85 \cdot 10^9$ in humans [92]. The C. elegans shows around seven connections per neuron [91], while in the human brain the number of connections per neurons ranges from 150 to 1000 [93, 94]. Communication among neurons is performed via electrical current with a temporal distribution of spikes.

ANNs do not attempt to replicate the brain. ANNs try to mimic the most basic structure of the brain, hence its name [95]. Up to now, implementations of ANNs do not reach the amount of neurons in a human brain, and they consider neurons with much simpler response functions. First implementations of ANNs were in the early 40's [96]. The Hodgkin-Huxley model describes an excitable type of neuron, but neurons in ANN can operate with simpler nonlinear dynamics. Now there are many neuronal models more or less complex [97]. One of the most basic ANN models are the Feed-forward Neural Networks (FNNs). In FNNs, the neurons are arranged in layers and all the connections are from one layer to the next one (i.e. feed-forwarded). In Figure 1.5 we depict a FNN consisting of neurons arranged in three layers. Layers are the input layer, the hidden layer, and the output layer. Neurons are connected all to all from one layer to the next. Every connection has a connection strength called weight, which determines how much the output of a neuron affects another. Connections that run from the input to the hidden layer and from a hidden layer to the output layer are called input weights and output weights, respectively. FNNs can have multiple hidden layers and the number of neurons in each layer depends on the task at hand.

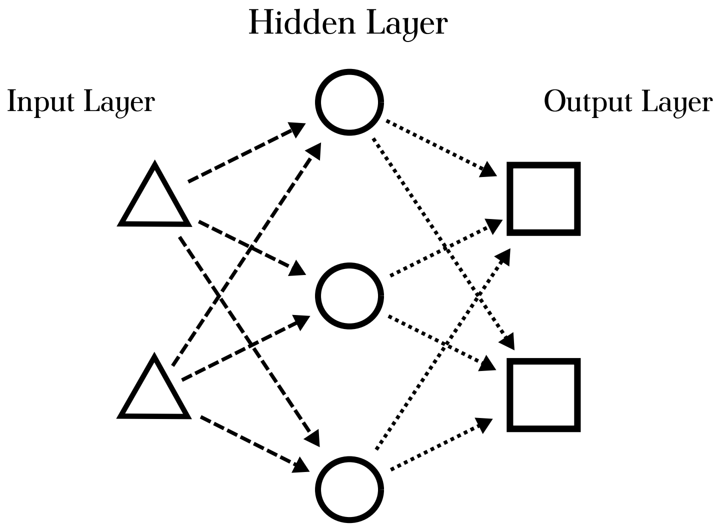

Figure 1.5: Example of an ANN. Triangles represent nodes in the input layer, circles represent nodes in the hidden layer, and squares represent nodes in the output layer. Dashed arrows represent input weights, while the dotted arrows output weights.

A fundamental neuron applies a nonlinear transformation, typically referred to as activation function, to the weighted summation of input signals from other neurons as shown in Equation (1.2).

$$x_j^{l+1} = f_{NL}\left(\sum_i \omega_{j,i}^l \cdot x_i^l \,,\, \theta\right) \tag{1.2}$$

Here f_{NL} is the activation function, x_i^l is the output of the neuron i in the layer l, $\omega_{j,i}^l$ is the weights from the neuron i in layer l to the neuron j in layer $l+1$, and θ are other internal parameters. Different activation functions can be used, but the most employed are the rectified linear unit (ReLU) and sigmoid functions (e.g. hyperbolic tangents) [98–100]. Still, simplified models of neurons dynamics like the Integrate-and-Fire can be used, which are more realistic than sigmoid functions but carry much more computational costs [101]. The input layer is the one that introduces information into the system as stimulus for the dynamical system. Information flows through the hidden layer depending on the weight arrangement and parameters. The state of the output layer encodes the output of the system to the injected information, and can be calculated from the state of the last hidden layer as in Equation (1.3).

$$y_k(n) = \sum_i \omega_{k,i}^{out} \cdot x_i^{l'}(n) \tag{1.3}$$

Here x_i^l is the output of the neuron i in the last hidden layer $l = l'$, y_k is the state of the node k in the output layer, and $\omega_{k,i}^{out}$ is the weight from the neuron i in the last hidden layer to the neuron k in the output layer.

ANNs promised important advances in sensor control and processing as well as in tasks where the brain excels such as pattern (e.g. speech and image) recognition or decision-making. The vast configuration possibilities allows these systems to implement a broad variety of different non-linear transformations of the input data according to the required task. But to make ANNs successful, it is necessary to find an optimal configuration of weights of the connections, number of layers, and number of nodes in each layer. An optimal configuration is one that minimizes the errors made by the ANN in a specific task. Finding such configuration is called learning, where the ANN is trained. Calculating the output of the network is simple but training can exhaust computational resources. As the number of weights in the system increases faster than the number of nodes, and weights are typically real numbers, the amount of configurations increases substantially. Due to the computing requirements, the first simulations of an ANN would not be conducted until 1955 at the IBM Research Laboratories [102]. The first experimental implementation was realized in 1959 with a circuit called (M)ADALINE, that was successfully implemented for adaptive removal of echoes in telephone lines [103]. (M)ADALINE included memistors, an early 3-terminal implementation of memristors made from an electroplating cell. The first successful multi-layer network was presented few years later, in 1965 [104]. Illusions in the field greatly vanished in 1969 after [105] showed that perceptrons, a type of basic neural network, could not process the XOR circuit, and that the computational resources to handle large neural networks were too high to the computers at that time. New interest re-emerged when in 1974 the back-propagation algorithm was published, which allowed the weights of FNNs to be trained efficiently [106].

While ANN with more nodes, layers, and efficient learning algorithms were developed, a new kind of neural networks with a different connectivity was invented [107]. These new ANNs, called Recurrent Neural Networks (RNNs) introduced recurrent connectivity among the neurons in the network. In RNNs there is not only connectivity among nodes in the hidden layers, but also cyclic connections and self-connections, which allowed the response of a neuron to return to the same one after passing through other neurons. An example of a RNN is shown in Figure 1.6. In FNNs, perturbations inside the network travel only forward towards the output layer. Recurrence allows for the appearance of temporal dynamics in the network. In the RNNs the information resides in the network, encoded in its dynamical state, creating an internal memory. Therefore, previous inputs could be extracted time after they were injected and could be used for subsequent computation together with more recent inputs. On the contrary, FNNs are memoryless and their present output only depend on the current input. The idea of introducing recurrence in ANNs was popularized in [108], while [109] suggested that the brain could have this kind of connectivity to account for memory. Besides the biological plausibility of recurrence in neuronal systems [95, 110], recurrence in ANNs was an important milestone since many tasks require memory. It has been shown that RNN can be Turing equivalent, i.e. capable of solving any recursive function [111]. RNN exhibits excellent performance even nowadays in combination with other techniques in tasks such as speech recognition [112], translation [113], image caption [114], and prediction [115, 116].

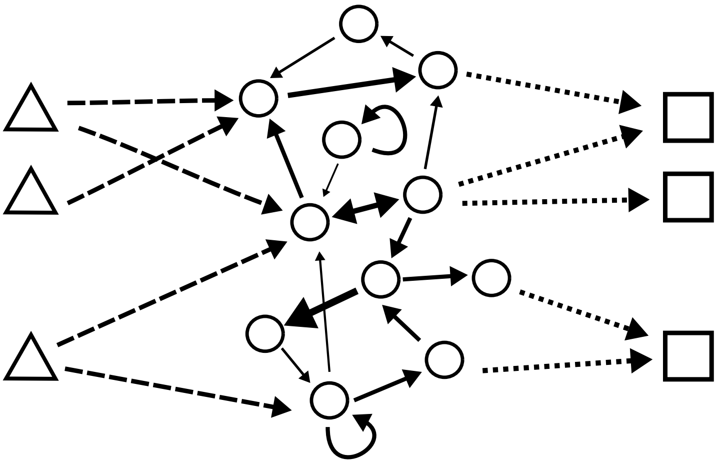

Figure 1.6: Example of a RNN. The hidden layer is a recurrent network. Connections between nodes are represented by solid arrows, with thickness representing the different connection weights.

1.4.1 Reservoir computing

While powerful, RNN are difficult to train. The training methods used for FNNs could not be applied due to the recursiveness of the network. The training algorithms available for RNNs were too slow [117, 118]. In the early 2000's, several independent works helped to solve this problem by demonstrating that successful performance in RNNs could be obtained by only training the output weights. They called this approach Echo State Network (ESN) [119], Liquid State Machine [120], and Back-Propagation Decorrelation [121]. In this framework, the hidden nodes create a recurrent network called the reservoir. Eventually, these methods were unified under the common name of Reservoir Computing (RC) [122, 123]. By reducing the number of weights that are modified, the RNN learning is much simpler and reduce its costs.

The computational power of reservoir computers arises from their capability to map the injected information onto a high dimensional space. Reservoirs are typically made of hundreds or thousands of nodes to ensure that the reservoir provides a space with enough dimensionality, since a higher dimension increases the chance of successful performance [124]. Information that is injected through the input layer has a certain dimensionality, such that inputs are not linearly separated. The reservoir creates a state space with higher dimensionality than the input space. The nonlinear mapping of the inputs in this higher dimensional space arranges them in a new way, such that they become linearly separable. In classification tasks, for example, this means that the inputs that are not separated in their original phase space can be now separated by hyperplanes in the reservoir's state space, where the output weights are their defining parameters.

To successfully operate, the reservoir computer needs to fulfill certain properties [123, 125, 126]: the separation property, approximation property, consistency, and fading memory. The separation property refers to the ability of the reservoir to provide sufficiently different responses to inputs that belong to different classes. This property allows for inputs to be more easily separable once they are mapped in the high dimensional space of the reservoir. Nevertheless, the responses of the reservoir need to be resilient to small changes in the inputs, since similar inputs of the same class need to be classified identically and not create diverging different responses in the reservoir. This corresponds to the approximation property [120]. Consistency refers to the ability of the reservoir computer to provide similar responses to the injection of similar input, hence robustness to potential noise in the input and the system itself. If the reservoir responses would not be consistent, the high dimensional projection would not be the same for identical input, and the output weights could not be efficiently optimized. And last, fading memory means that the memory in the system needs to disappear after some time. This means that the dynamical response of the reservoir to an input is affected by the recently injected inputs, but not by the once injected long time ago.

1.4.2 Delay-based reservoirs

The typical RC is a recurrent network of multiple nodes randomly connected (as in Figure 1.6). However, deterministic network topologies can be successfully used [127, 128]. A viable RNN topology is a circular network of unidirectional coupled nodes, as the Simple Cycle Reservoir in [127]. This topology is of particular interest because it can be implemented via a single nonlinear node under the influence of delayed feedback [129]. This approach is called Time Delay Reservoir (TDR) [130]. The typical TDR is illustrated in Figure 1.7. TDR makes use of the high dimensionality of delay systems to create the state space required for RC. Delay systems are specially suited for this task as the state space is infinite dimensional. This occurs since their state at time t depends on the state of the system in the time interval, defining τ as the delay time, $[t-\tau, t)$. In theory this creates an infinite dimensional system. However, in practice the dynamics of delay systems are not infinite dimensional due to finite dynamical bandwidth [131].

In TDRs, the temporal evolution of the nonlinear element determines the state of the nodes in the network. More exactly, the state of an individual node is obtained by interpreting the response of the nonlinear element over a time interval equal to θ. The network is then the collection of consecutive nodes responses during a time interval τ. Since the θ intervals of different nodes do not overlap, the number of nodes in the reservoir N is defined by $N = \tau/\theta$. The network connectivity in a TDR originates from two contributions. One of these is the feedback connectivity. Since τ is a multiple of θ, every node receives from the feedback its state in the previous τ interval. The strength of this connectivity is related to the feedback strength. Therefore, the feedback strength strongly influences the nonlinear dynamics exhibited by the reservoir and their memory. The other connectivity is from a node to the following ones in the unidirectional network [129]. The dynamical response of a node can influence the response of subsequent nodes due to the inertia in the dynamics, which can be controlled by adjusting the parameter θ (and the characteristic time scale of the dynamics if possible). If θ is smaller than the characteristic time scale of the nonlinear element, then the response of the nodes will affect multiple nodes down the network. On the other hand, if θ is larger than the response time of the characteristic node, then the connectivity among nodes is reduced and nodes behave as if they were isolated. An extremely small θ is also not desired, since such short time interval would not allow time for the nonlinear element to develop a response to the information being injected. Other configurations use a network with a duration different than the delay time to exploit different connectivities [132]. Therefore, the selection of the interval time θ is crucial. A $\theta = 0.2 \cdot T$, where T is the characteristic time of the nonlinear node dynamics', is a typical value employed in literature. Once the state of the reservoir is known, an output layer as the one described in Equation (1.3) can be used to obtain the output of the RC.

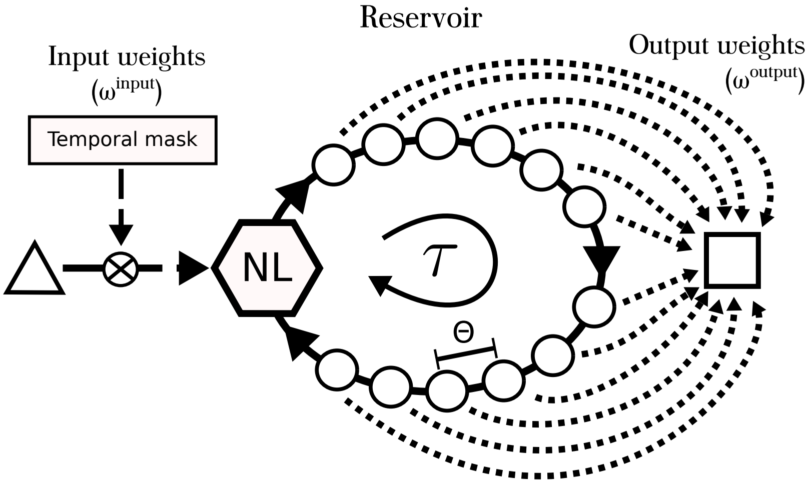

Figure 1.7: Illustration of the TDR. The reservoir is now a circular network of nodes, separated homogeneously over the delay time. This case shows the input and the output layer with just one nonlinear element.

Not only the dynamics of the reservoir are essential, how information is injected plays an important role. In a TDR the nodes are multiplexed in time, so the input layer requires a methodology illustrated in Figure 1.8. Every input of information to be processed is typically injected to all the nodes in the network by time multiplexing. This means injecting the value into the nonlinear element over a time interval τ, as shown in Figure 1.8(a). But by doing so, the response of the nonlinear element would relax to a stationary state (if operated from a stable fixed point) since the relaxation time is much shorter than the delay time. This scenario would correspond to having many nodes of the TDR with identical responses. To keep the reservoir generating different transient dynamics, every input data is multiplied with a function called the mask. This mask is a step-wise function and has a number of values equal to the number of nodes. In Figure 1.8(b) we show an example of a mask with only five values for illustrative purposes. In Figure 1.8(c) we show the resulting injected signal for the reservoir. Every mask value is associated to an individual node in the reservoir. Therefore, the mask values strongly determine the input weights in the reservoir. Not every configuration of input weights is adequate for computation. The input weights need to create responses in the reservoir with sufficient diversity. This process benefits performance of the reservoir computer since it enriches the nonlinear mapping.

If sequences of weights are repeated, nodes will exhibit similar responses and the diversity of the reservoir state decreases. Therefore, a mask with high variation of values is desired. Design of optimal input masks have attracted interest due to their clear impact on the performance of these reservoirs, and several proposals have been presented [87, 133]. Nevertheless, TDRs present an important difference. The multiplexing of the nodes in time slows the system compared to spatial networks by a factor equal to the number of nodes. Real time processing can be affected then by this feature. The ability to create an entire network of interconnected nodes, all of them with nonlinear dynamics, with just a single element attracted a lot of interest. While other systems required many individual components and the capacity to connect them (spatially distributed networks), TDRs do the job successfully with fewer components.

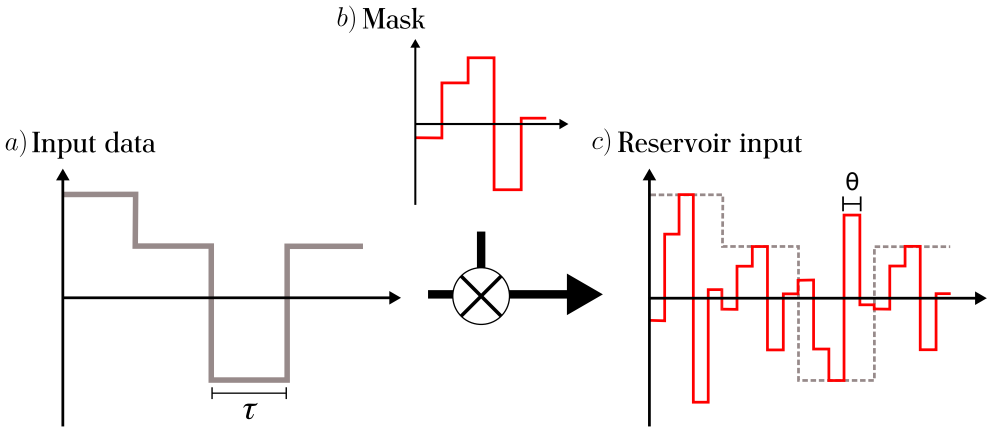

Figure 1.8: Illustration of the masking process. Each value of the data input sequence (a) to be processed is multiplied by the mask (b), resulting in the signal that is finally injected into the TDR (c).

1.4.3 Hardware implementation

Nowadays, ANNs have proved to be a state-of-the-art technique for a broad variety of applications including decision-making [134, 135], navigation [136–138], robot control [139], pattern recognition and processing [140, 141], and even drug design [142]. This was driven fundamentally by the exponential increase of computational power (that provided the power to train the networks in a tolerable time) and of raw data (necessary to train the networks with sufficient examples). In spite of their successful performance, ANNs still have a high computationally cost. In contrast, a human brain works very efficiently with little power. Therefore, there is room to explore hardware implementations of ANNs (devices with nonlinear elements connected as a network) that offer better possibilities with better efficiencies than its transistor-based computers. For this purpose, many efforts have been made to develop information processing devices that mimic neural systems. Individual neurons have been emulated with traditional circuit elements [143, 144]. Hardware implementations have explored multiple mediums and nonlinear elements, including: electronic circuits with spiking silicon neurons [145–147], spintronic oscillators [148], tensegrity robotic structures [149], and liquids [150]. Real biological neurons have even been used to harness computational power with RC [151].

But interestingly, hardware implementations of ANNs can be done with optical systems. Optical implementations of neuromorphic computers using TDRs are very desirable. Optical systems could provide benefits like high processing speed for even real time processing thanks to the fast speeds of photonic devices. Optical systems could provide the large connectivity that ANNs requires in a small space and broadcasting from one node to many others. Several approaches have been explored to connect the optical nodes and control their weights [152–155]. Implementation of the nonlinear nodes can also be done with a varierty of optical devices. Thin films optical amplifiers and optical bistability were recognized as candidates for nonlinear operation [156]. Excitable photonic devices have also been studied for its application in neuromorphic computing, including devices like microdisk lasers [157], graphene-based excitable laser [158], and saturable absorber laser [159]. Many nonlinear optical elements have proved ANN computing capabilities including Semiconductor Optical Amplifiers (SOAs) [132, 160, 161], photodetectors [152, 162, 163], ring resonators [164], SLs [29, 165], and modulators [166, 167]. Photorefracive crystals are also components that provide tunable weights and nonlinearity suitable for ANNs [168–170]. All these systems have proved capabilities for information processing with ANN techniques, with new implementations and concepts appearing for better and larger implementations, demonstrating the strong interest, possibilities, and future of the optical computing with ANNs.

1.5 Motivation and overview of this thesis

In this chapter we have introduced the SL and the complex dynamics that can arise under the influence of optical perturbations. SLs are capable of exhibiting a rich complex behavior, which is used to study these dynamics experimentally in a fundamental level. Furthermore, complex dynamics have been put to use in multiple applications, encouraging the understanding of such behaviors. For these reasons, in this thesis we aim to further study the dynamics of delayed photonic systems, use the complex dynamics of the SLs in information processing applications, and design and implement new nonlinear optical systems for application as reservoir computer. The thesis is organized as follows. In Chapter 2 we describe the methodologies used for our experimental realizations. This includes how optical power and optical spectra have been measured and what techniques we used to determine the optical delay.

In Chapter 3 we study the impact of using more than one optical delay feedback in the dynamics of a SL. Delay systems have been used to study the dynamics of systems with one spatial dimension [171, 172]. The implementation of multiple delays could be used to extend the analogy to study systems with more spatial dimension. We will use a SL under delayed optical feedback due to their well-known rich dynamics under delayed feedback, and include an additional optical delay line orders of magnitude longer than the first one. This will induce new dynamical states, and we will study its features and similarities to other nonlinear systems.

Chapter 4 studies the use of a SL under optical feedback and modulated optical injection as a TDR in an optical reservoir computer. The nonlinear dynamics present in a SL under the simultaneous influence of optical feedback and injection are centered for this information processing application. The impact of optical injection that is modulated in such systems has not been studied in detail, we will also evaluate how the modulation affects the dynamics of the system. In this chapter we will evaluate the impact of key parameters on the performance and properties of the system.

The last chapter, Chapter 5, develops an optical reservoir computer by building a large spatially extended network of nonlinear optical elements. This reservoir implements hundreds of nonlinear nodes with few components, and couple them simultaneously using passive components. We will also implement experimentally the output layer in hardware, introduce learning rules, and demonstrate successful operation with low errors in a task despite current experimental limitations.

The final chapter of the thesis will be the final conclusions of this research, and a collection of future prospects.

Chapter 2

General methods

2.1 Light measurement acquisition methods

Different characteristics of the light can be measured with different instruments. Here we describe the instruments employed to measured them in this thesis.

Average optical power

The average optical power of the light was measured using a Thorlabs power meter console with a power sensor. The sensor converts the optical power into a voltage. The console reads the voltage from the sensor and provides a power measurement taking into account the responsiveness of the sensor to the selected wavelength on the console. These devices provide optical power measurements of slow changing fields due to their bandwidth of 100 KHz, which we refer to as the average optical power. For experiments where the light's wavelength was around 1550 nm (Chapter 3 and Chapter 4) we used a PM100D console and a S154C sensor. This sensor is a InGaAs photodiode with a high responsivity in the 1550 nm, and a power range between 100 pW and 3 mW with 10 pW resolution. For experiments where the light's wavelength was around 660 nm (Chapter 5) we used a PM100A console and a S150C sensor. This sensor is a Si photodiode with adequate responsivity at 660 nm, and a power range between 100 pW and 5 mW with 10 pW resolution.

Time evolution of the optical power

Measurements of the temporal evolution of the optical power at fast timescales are crucial to observe the dynamics of an optical system. The dynamics of a SL can appear with speeds ranging from MHz to GHz, so fast detectors and acquisition systems are required. For these conditions, we used a fast photodetector to convert the optical signal into an electrical one and an oscilloscope to acquired the electrical signal. The photodetector used was a MITEQ $SCMR-100k20G-30-15-10-FA$. This photodetector works in the wavelength range from 1280 to 1580 nm, and offers a bandwidth from 100 KHz to 20 GHz. As an oscilloscope we used a Teledyne Lecroy oscilloscope, model Wavemaster 816Zi. This oscilloscope has a sampling rate of 40 GSa/s, so with a time resolution of 25 ps, and an analog bandwidth of 16 GHz. The oscilloscope's bandwidth limited the fastest dynamics that could be recorded to 16 GHz, enough to observe the fast dynamics of SL systems.

To improve the Signal-to-Noise ratio (SNR) of the recorded signals we added before the photodetector a SOA and a Optical Tunable Filter (OTF), as shown in Figure 2.1. The SOA is a polarization insensitive optical amplifier, similar to a SL but without the resonator cavity. This one is a Covega 1013XS, wavelength centered at 1550 nm. Amplification of the signal reduces the negative effects of noise in the photodetector and in the oscilloscope, enlarging the small features in the signal against the noise in the photodetector. To improve the benefits of the SOA we use it together with an OTF. The SOA emits spontaneous emission in a broad frequency spectrum that acts as noise added to the amplified signal. The OTF is a tunable bandpass filter, that once applied to the amplified signal removes the spontaneous frequency components outside the frequency range of interest. Our OTF is a Santec OTF-350, with a passband flat-top filter shape and isolation above 50 dB.

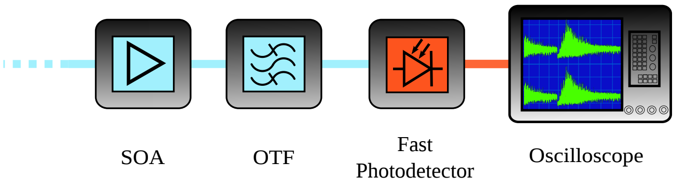

Figure 2.1: Detection section of the setup. Components used to detect the temporal evolution of optical signals and improve its SNR. Blue lines are optical fibers, orange lines are electrical cables.

Power spectra

The power spectra provides the amplitude of the different frequency components of the intensity field of the light, and we measured it with an Anritsu MS2667C. It is measured with an ESA from the electrical signal generated from the photodiode upon receiving the optical signal. This device measures the frequency spectra from 9 kHz up to 30 GHz. In practice the bandwidth is limited to 16 GHz due to the bandwidth of the electrical cables carrying the signals.

Optical spectra

To measure the optical spectra of the optical signal we employed two different Optical Spectrum Analyzer (OSA) depending on the requirements. One instrument was an Anritsu MS9710C, an OSA based on a diffraction grating which provides a wavelength resolution of 0.1 nm in the 600 to 1750 nm range. It also offers 70 dB dynamic range with 0.1 dB resolution and −90 dBm optical reception sensitivity. This high sensitivity allows to even resolve the non-emitting longitudinal modes in SLs. The second OSA is a high resolution one from Aragón Photonics, model BOSA 210. The ″B″ stands for Brillouin, as the analyzer combines the high power of a tunable laser source with the signal under test to stimulate the nonlinear Brilloun scattering on an optical fiber to create a narrow filter. This operation principle provides the BOSA with an 10 MHz resolution from 1530 to 1565 nm, capable of for example highly resolving the spectra of SL exhibiting complex dynamics.

2.2 Experimental techniques for precise determination of the delay time

Precise determination of the delay time is important in the study of delayed systems [173–176] and in the research of following chapters, since in Chapter 3 and Chapter 4 require delay times to be precise multiples of other quantities. To ensure these requirements are satisfied as close as possible we make use of the techniques described in the following.

2.2.1 Autocorrelation measurement of timetraces

The delay time can be extracted from the temporal evolution of the dynamics by evaluating its Autocorrelation Function (ACF). This method has been used previously in SL under optical delayed feedback in the context of chaos-based communications [176]. The ACF is defined in Equation (2.1).

$$ACF(t') = \frac{\langle (x(t) - \langle x(t) \rangle)\,(x(t+t') - \langle x(t) \rangle) \rangle}{\sigma_x^2} \tag{2.1}$$

where $x(t)$ is the time evolution, $\langle \rangle$ denotes time average, and $\sigma_x = \langle (x(t) - \langle x(t) \rangle) \rangle^{1/2}$. The ACF shows how similar are the values of $x(t)$ separated by $t = t'$ when averaged over all the timetrace. To extract the time delay from the intensity dynamics of a SL with delay feedback, the autocorrelation function needs to present periodic sharp peaks. The main peak would observed at $t' = 0$, while the first peak is found for t' corresponding to the delay time. The time delay of the system can be extracted from the position of the maximum of the ACF of its first peak. To do this in SL with optical feedback, the feedback strength need to be sufficiently high to create a clear signature [176, 177]. Additionally, the bias current needs to be high to reduce the so called shift of the ACF peaks [177]. This method provides a measurement of the time delay with a resolution equal to the temporal resolution used to record $x(t)$ as long as the peaks are sharp.

2.2.2 Pulse propagation technique

Another way to measure the delay time is based on sending a pulse of light inside the delay line. The setup is depicted in Figure 2.2.

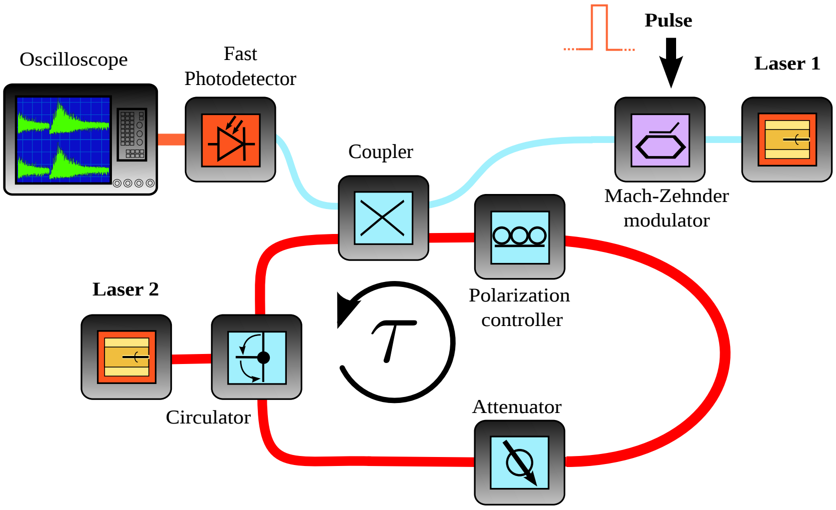

Figure 2.2: Illustration of the pulse propagation method for time delay measurement.

Laser 2 is inside the delay line, and a circulator is used to close the loop along with other components. For the method, laser 2 does not emit any optical power and is biased with a current much lower than threshold. Laser 1 and a amplitude Mach Zehnder Modulator are combined to produce the pulse of light. Laser 1 is set to emit a constant amount of power. The modulator used has a 20 GHz bandwidth and is biased to the point of lowest transmission. Then, a short pulse (of around 1 ns long) is fed to the MZM so the high value of the pulse set the transmission of the modulator to the maximum, effectively creating an optical pulse. This pulse splits in two copies at the coupler, where one copy goes to detection and the other enters the feedback cavity. The last copy travels and is reflected by the front facet of laser 2. Then the pulse travels through the rest of the feedback cavity until it reaches the optical coupler again. The pulse splits again, and a copy is sent again to detection. At this point, the oscilloscope shows a timetrace with two detected pulses. The time separation between the detected pulses corresponds to the delay time in the cavity, which can be easily extracted. The injected power needs to be high enough for the second peak to be visible, since it will experience strong losses while entering and traveling inside the feedback loop. More accurate measurements can be obtained by averaging the recorded timetraces from multiple pulse injections. This method allows to determine the delay time with a resolution equal to the temporal resolution of the oscilloscope.

Chapter 3

Dynamics of a semiconductor laser with dual delayed optical feedback

3.1 Introduction

Systems with delayed feedback are ubiquitous in nature. They are especially relevant in the context of nonlinear dynamics and control systems. Delayed feedback renders a dynamical system infinite dimensional. On top of that, delay systems may have contributions from more than one delay time, when they experience feedback from multiple contributions. For example, feedback in lasers systems can originate from reflections at different positions [31, 178, 179], close-loop control mechanisms (like PID) integrate past contributions over a time span [180], and even musical instruments exhibit their characteristic sounds from the reflections in the multiple chambers inside the instrument [181] (among other reasons). The influence of multiple delay can also be experienced also in networks of delay-coupled elements, in which different connections can experience different delay times. Neural networks [182], traffic systems [183], and gene regulatory networks [184] are examples of networks with varying coupling times. Multiple delays therefore are an important feature of real systems.

The dynamics of the Semiconductor Laser under feedback have been mostly studied using a single delay time with exceptions like [185, 186]. Likewise the single delayed feedback unfolded complex dynamics in the SL, the addition of multiple feedbacks could unravel further non-trivial scenarios. Therefore, the interest to study systems like the SL under the influence of multiple delayed feedbacks is clear, as to explore new possible dynamical regimes and to exhibit a test bed for studying the influence of multiple delayed feedbacks. In this chapter we will address the dynamics of the SL under the simultaneous effect of two optical delayed feedbacks with different time scales of the delays. The use of optical setups based on SL is especially interesting as these systems allow to realize well-controllable systems with large delays. Additionally, optical components can bring extensive customization options and flexibility to the research, as many parameters of the multiple delay system can be tuned depending on the needs. Different nonlinearities can be studied by changing the SL device employed, feedback conditions can be tuned, and delay times can range from nanoseconds up to hundreds of microseconds (and even further).

In our study we use a two delays configuration following the work in [187], in which the authors studied the dynamics of the Complex Ginzburg-Landau equation (CGLE) under two delayed feedbacks. They chose the CGLE as it is a paradigmatic system exhibiting a large variety of physical phenomena ranging from chemical reactions dynamics, nonlinear waves, superconductivity, superfluidity, liquid crystals, and even strings in field theory [188–192]. In [187] and in our configuration, the two feedbacks have very different delay times, as one delay time is two orders of magnitude larger than the other one. This distributes the delays in a hierarchical structure, where one is identified as the long delay (τ_2) and the other the short delay (τ_1). The delays were chosen on different scales, as the complexity of the resulting dynamics of a system can depend on the delay times and in the number of delays. For example, the dimension of an attractor increases linearly with delay time [193], which can unfold highly complex dynamics such as coarsening [194], square waves [195], or spatiotemporal chaos [196, 197]. In the literature on semiconductor lasers with delayed feedback, the long and the short delay regime are distinguished [198]. In their research, the authors of [187] identified two distinct kinds of spatiotemporal dynamics depending on the parameters. In particular, they found PD and DT. Additionally, they applied their research on the delay differential Lang Kobayashi equations (LKE), the model describing the SL under delayed optical feedback, and found the same kinds of dynamics. This is possible as the LKE can be reduced to the CGLE by considering oscillatory solutions of small amplitude and close to destabilization, while also expanding the equation on different time scale terms [187].

The chapter is structured as follows. First we introduce a two dimensional spatial representation of the dynamics that we will use to illustrate most of the results. After presenting the experimental setup in detail, we characterize the static properties of the system. Then we proceed by studying the dynamics of the system in the parameter regime of PD, and afterwards for DT. In the last results section, we characterize the spectra of the emission dynamics. The chapter finishes with a summary of the conducted research and a discussion.

The research of this chapter has been performed in collaboration with Prof. Serhiy Yanchuk, who was a guest professor stay in our institute..

3.2 Methodology to construct 2D spatial representations

We characterize the dynamics of the multiple feedback system from the temporal evolution of the optical intensity.

To represent these temporal evolutions we will employ a pseudo-space representations similar to the ones showed in [171]. In [171], the authors showed that purely temporal data from a single-delay system can be reorganized into a space-time domain. In that representation, the space dimension is bounded between 0 and the delay time of the system, while the time dimension is unbounded and measures the number of delay time units.

This representation allowed to visualize different dynamical regimes, and to identify features that would not be convenient using solely a purely temporal representation of the data. The use of two delays offers the possibility to represent the data in a two dimensional pseudo-space representation, as presented in [187] by extending for two delays the data representation presented in [171].

This pseudo-space representation of two delay systems is based on breaking the timeseries into intervals of length equal to the delay times and then to arrange them in a 2D representation. To do so, first we break the timeseries into N partitions of $\tau_2 + \Delta\tau_2$ length, where $\Delta\tau_2 \ll \tau_2$. Each one of these partitions has the data to become what we call a frame. The number of frames (N) then depends on the length of the time window of the recorded dynamics T, where $N = \lfloor \frac{T}{\tau_2} \rfloor$. Then, every partition is broken into smaller pieces of $\tau_1 + \Delta\tau_1$ length, where $\Delta\tau_1 \ll \tau_1$. The small offsets introduced in τ_2 and τ_1 for the 2D reconstruction allow to account for potential drifts in the laser dynamics. The number of pieces in one frame is then $m = \frac{\tau_2+\Delta\tau_2}{\tau_1+\Delta\tau_1}$. For our case is preferred that m is an integer. The m pieces then are vertically stacked one after the other to create a frame with height limited to m. The resolution of the recorded frames depends on two different aspects. The ratio $1/m$ will determine the spatial resolution in the vertical direction, while the acquisition rate of the temporal dynamics will determine the resolution in the horizontal direction.

Following the approach in [187] to introduce the offsets, our new pseudo-space coordinates are the following:

$$x = \frac{t}{\tau_1}(1 - \delta_1 \cdot \epsilon^2), \qquad y = \frac{t}{\tau_2}(1 - \delta_2 \cdot \epsilon) \tag{3.1}$$

where t is the time, $\epsilon = 1/\tau_1$, and δ_1 and δ_2 correspond to drift parameters on the dynamics in the x and y directions respectively. Parameters δ_1 and δ_2 indicate that the dynamical features drift in pseudo-space, so they are not stationary in a certain location. The specific values of δ_i can theoretically be estimated [187], but for the experimental realization they will be chosen heuristically. The resulting representation has coordinates on the horizontal direction (x-axis) and on the vertical direction (y-axis) covering $[0,1]$, and creates a 2D pseudo-space representation with temporary dependence from a purely temporal evolution with N frames. These new coordinates relate a position in the pseudo-space to a fraction relative to the delay times. The intensity emitted by the laser is then encoded in a grayscale heat map. We can construct a frame from every partition, which then we can visualize sequentially to observe how the dynamics evolves from frame to frame. This process effectively creates a video of the dynamics with N frames, where every frame corresponds to a snapshot of the dynamics in the pseudo-space.

3.3 Experimental scheme

A scheme of the setup is depicted in Figure 3.1. It consists of off-the-shelf fiber-coupled telecommunication components except for the Semiconductor Laser, which lacks the usual integrated optical isolator. The SL is a discrete mode quantum well semiconductor laser emitting at $\lambda = 1543$ nm. The linewidth enhancement factor of the laser was determined as $\alpha \sim 2$ using the Henning-Collins method [199]. The laser shows a longitudinal mode separation of 150 GHz and side mode suppression ratio of more than 40 dB. The laser temperature is kept constant at $T_{RL} = 22.00$°C. Temperature and drive current are stabilized with an accuracy of $0.01\,K$ and $0.01\,mA$, respectively.

The delayed feedback loops are realized using optical circulators, which define a propagation direction within the feedback loop and suppresses unwanted back reflections. The long and short delay lines are realized by splitting the emitted light using a 50/50 Optical Coupler (OC). Light from the two output fibers of the OC follows paths with different delay times, and is later recombined in a second 50/50 OC. From [187] we know that the delay times need to be orders of magnitude apart to allow for a 2D spatio-temporal representation. Minimization of the short delay time helps to increase the ratio $m = \tau_2/\tau_1$ ratio. To control the feedback conditions of the short delay loop, we include a polarization controller and an optical attenuator between the circulator and OC1. In the loop with delay τ_2 we include components to control its feedback conditions (a polarization controller and an optical attenuator), an optical fiber spool, and a custom-built fiber patch. The spool has a dispersion compensated optical fiber with a length of 4213 m. Such a length ensures that τ_2 will be orders of magnitude larger than τ_1. The importance of having a sufficiently long delay is detailed in [187]. The fundamental reason is to obtain a sufficiently high density of τ_1 sections in the 2D representation.

If m is chosen too small, the representation would not resolve the small dynamical features and the system would behave considerably different. The delay time ratio m should be preferably large and an integer number. To precisely match the long delay time as a multiple of the short delay time we include in the long delay line an optical fiber custom built extension patch.

The feedback polarizations from both delays were set parallel to the one of the light emitted by the SL, which is typically referred as Polarization Maintained Optical Feedback (PMOF). The feedback strengths from both feedback loops needs to be as similar and large as possible. Initially the feedback strength from the short delay was higher than for the long delay. We can attenuate the feedback strength from the long delay, but not from the short one in an independent manner. For this reason we placed a 3 dB fixed optical attenuator in the short delay, to reduce optical power right below the long delayed feedback strength. Then we used the attenuator in the long delay to finely match feedback strengths. By measuring the output power extracted from the SL and the feedback power that returns from the delay lines we determine that around 1.1% of the optical power is re-injected into the laser. These reduction by almost 20 dB from the total power originates mostly from the multiple OC (that introduces 3 dB losses), the multiple connections, and the 3 dB fixed optical attenuator.

The delay times were determined by performing autocorrelation measurements of the time traces. This procedure is explained in detail in Section 2.2.1. The short delay time in our configuration measured $\tau_1 = (73.438 \pm 0.025)$ ns, while the long delay measured $\tau_2 = (20{,}930.013 \pm 0.025)$ ns. These delay times result in a delay times ratio of $m = \tau_2/\tau_1 = 285.003$, which is close to an integer value.

The detection of the dynamics was performed in the detection arm. The detection arm used the light extracted from the laser emission by OC3. To ensure a high SNR for detection we used an optical amplifier. Additionally, we introduced an optical isolator right after OC3 to suppress any unwanted back reflections from components in the detection arm. The detection and data acquisitions were performed by a 20 GHz photodetector and a 16 GHz analog bandwidth oscilloscope acquiring at 40 GSa/s.

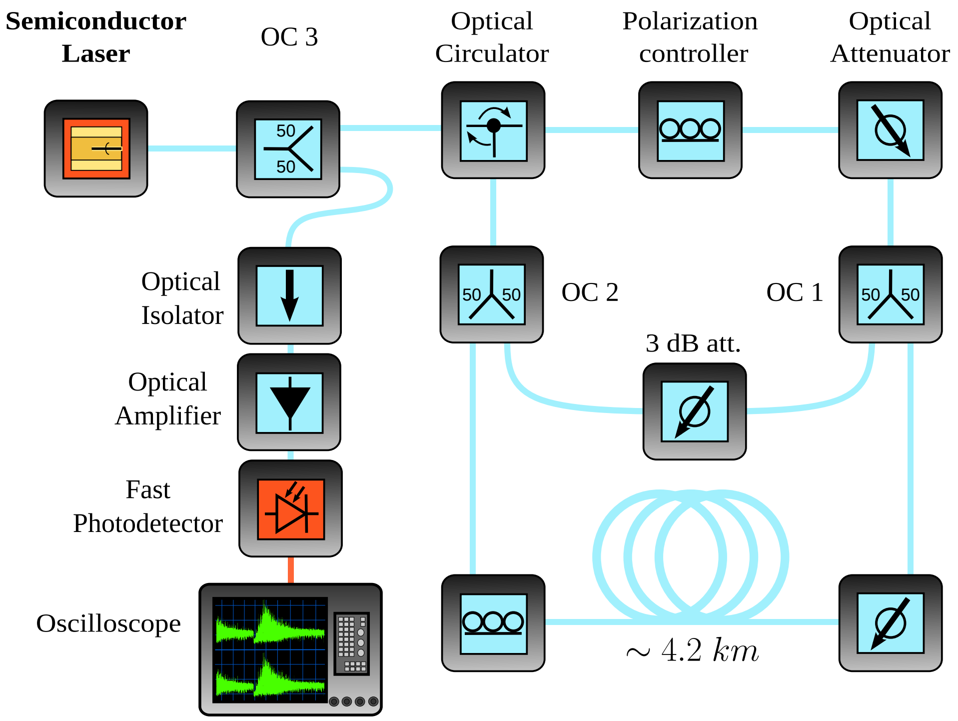

Figure 3.1: Scheme of the experimental setup with the two delay lines. Blue lines are optical fibers. The orange line is an RF electrical cable. Optical Couplers (OC) are numbered from 1 to 3.

3.4 P-I curve

Before characterizing the dynamics of the system, we characterize the output power dependence of the system to the bias current in the SL. This dependence is typically referred to as P-I curve or P-I characteristics (power versus current). It is a basic characterization of a laser system, as it shows the typical threshold behavior of the laser. The P-I curve is relevant to our case as a change in the threshold may indicate a dynamical change in the system. In particular, it is well known that including optical feedback into the system exhibits changes in the P-I curve [22]. Furthermore, the PD dynamics described in [187] appears in the region of bias current infinitesimally close to threshold under the multiple feedback. By measuring the P-I curve we obtain the values of threshold currents.

The obtained P-I curves for our system are shown in Figure 3.2. We show in black the P-I curve of the SL under solitary conditions (without feedback), in green with the short feedback loop active, and in red

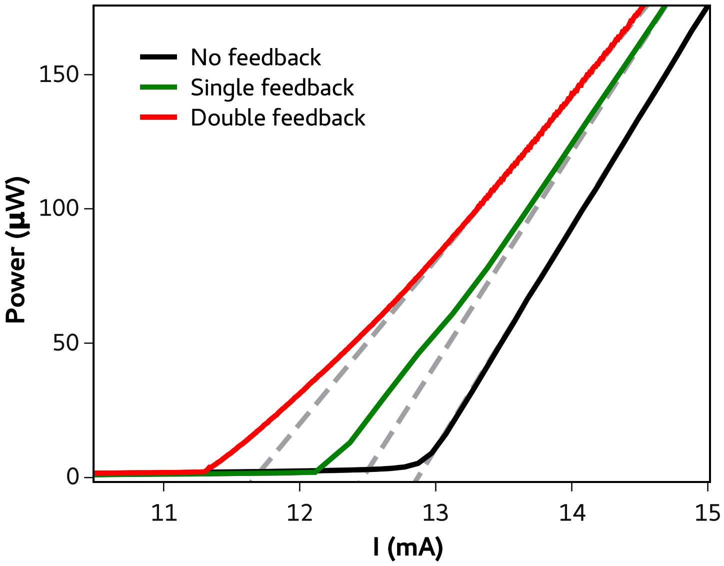

Figure 3.2: P-I curves of the SL for the three different feedback conditions: no feedback (black), single feedback (green), double feedback (red). Gray dashed lines indicate extrapolations from linear regression analysis of the power versus current dependence in the linear part at high currents.

when both feedbacks are active. We first focus on the curve for solitary conditions. We observe the threshold behavior with the laser emitting non-negligible optical power for bias currents above 13 mA. For higher currents the output optical power increases linearly. To obtain the threshold current, one can perform a linear regression analysis on the power emitted above threshold, which is represented as a gray dashed line in Figure 3.2. The crossing of the resulting linear fit with the horizontal axis determines the threshold current. Using this method we calculate the threshold current under solitary conditions as $I_{th,sol} = 12.87$ mA. The transition to the lasing state appears smooth due to the spontaneous emission in the gain medium.

Next, we analyze the impact of adding optical feedback. We discuss the case for the short delayed feedback path, but both of them provided with the same power values as feedback strengths were identical. We observe several consequences of the delayed feedback. First, the P-I curve is shifted towards lower values of bias currents, resulting in a lower threshold current under feedback conditions. This is a well-known effect [43], originating from reduced losses due to re-injection of part of the light emitted by the laser. This results in a reduction of the lasing threshold current and typically an increase of the output power emitted by the laser close to threshold. We also observe that the slopes of the P-I curves are different. The solitary case exhibits a larger slope than under optical feedback, looking like a higher quantum efficiency. The smaller slope when including feedback is due to an effective increase of the reflectivity of the laser's facet on the feedback facet's side, consequently resulting in a balance change between the laser's emission from front and rear facet. If the total power were measured from both facets, the slope of the P-I curve would be larger for the case with feedback. Additionally, in the vicinity of the solitary threshold, the P-I curve with feedback exhibits a kink which is following a linear trend. Below this kink one observes a deviation from the linear dependence shown as a gray dashed line. It was already observed already in [43], where kinks are referred as irregularities, and are attributed to the interplay between the Transverse Electric and the Transverse Magnetic modes of the SL. The presence of this kink imposes a limitation on the identification of the threshold current by the linear regression method ambivalent. Instead, one should rely on, e.g., power measurements or identifying dynamical onset via spectral analysis. By determining when the SL with one optical feedback starts to show laser emission, we obtain a threshold current of $I_{th,fb} = 12.20$ mA.

Upon activation of the second feedback loop, we measure the P-I characteristics, as depicted in the red curve. By adding these extra feedback line we are doubling the feedback rate. We find that the threshold has reduced further due to the increased total feedback. Now the threshold current was determined as $I_{th,2fb} = 11.60$ mA, indicating a total threshold reduction of 10% when both feedbacks are active. The proportional reduction of the threshold current is similar to the reduction obtained by the first feedback. Again we observe that the slope of the P-I curve is lower compared with the other cases due to the stronger feedback.

Thus, we observe that the introduction of a second delay line alters the P-I curves, by reducing the threshold current further. We determined the threshold currents of the system that will allow us to choose the range of currents in which to characterize the dynamics in the following sections.

3.5 Spiral phase defects

Once we know the threshold currents for our system, we begin where to look for the different dynamics. We firstly address Spiral Phase Defects.

PD are topological defects [200, 201] that can occur in 2D systems with complex fields, and that have been known for a long time, especially in the context of the CGLE [202, 203]. At the position of a defect, the amplitude of the complex field is $|A| = 0$, while the phase is not defined in the center and varies on a loop around the center by multiples of 2π [202]. For spatial dimensions equal or greater than two, these patterns are topologically constrained, and can only appear and disappear in pairs. By definition, the PD clearly show more clearly for the complex field amplitude. In our experiments we are unable to extract the phase for the 2D representation. Therefore, we rely on localizing pairs of points with $|A| = 0$ that appear and disappear in pairs in order to observe the PD.

According to [187], PD can appear for our experimental conditions when the bias current is close to $I_{th,2fb}$. In Figure 3.3 we show a 2D representation of the dynamics recorded for $I_r = 1.001 \cdot I_{th,2fb}$. Movies illustrating the dynamical evolution can be found as supplementary material [1]. Figure 3.3 shows that intensity experiences small fluctuations from its average value. From watching the movies one can see that most of the fluctuations change from frame to frame, indicating they are probably originating from noise. Sporadically one observe small objects with very low intensity that exist in multiple consecutive frames. Some of these objects are observable in Figure 3.3. In Figure 3.4 we zoom into one of those objects, and also how it looks $5\tau_2$ later (so 5 frames later), to analyze it in more detail. This single object with very low intensity exhibited a lifetime of 7 frames. During its observation, it was almost static and practically did not change shape. Our movies attain a maximum of 38 frames, which allows us to observe a few of these objects for each recorded timetrace at these conditions. Each one of these objects share similar characteristics as the one described here, with lifetimes ranging from 3 to 8 frames when are in the range $[0.98, 1.01] \cdot I_{th,2fb}$.

Such objects could be regarded as PD, since they share some features like they appear isolated in space and exhibit very low intensity. However, they exhibit significant differences with the theoretically expected PD, like that they appear and disappear individually, and not in pairs. The nature of PD in 2D systems is related to the creation and annihilation in pairs. Not observing that feature in our case puts in doubt that what we are observing are really PD.

Not observing PD so far in our current setup is not an indication that is not possible to observe them in other systems. Is it plausible that experimental limitations are preventing the observation of PD. The most likely reason that we did not observe phase defects is that we have spontaneous

---

[1] `https://ifisc.uib-csic.es/ondemand/julian/ddfeedback-I=11.61mA_gray.mp4`

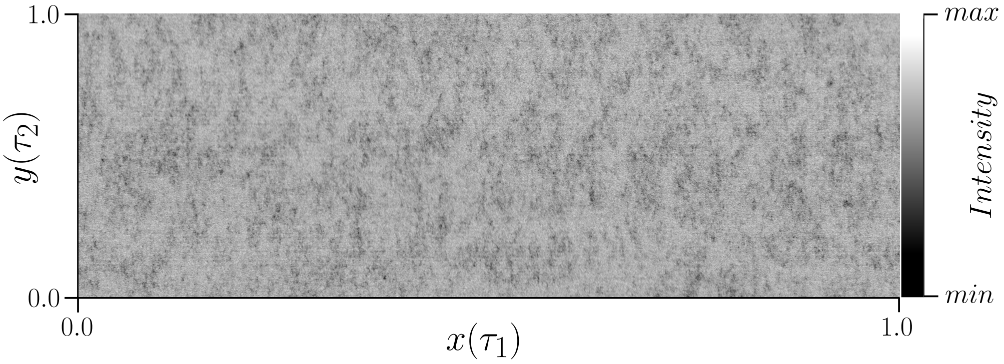

Figure 3.3: Experimental dynamics in the PD parameter range. The 2D representation illustrates the dynamics over a τ_2 interval, so an individual frame of a movie. Dynamics are characterized by an almost constant amplitude with small low intensity single objects that survive several frames. Intensity is encoded in grayscale.

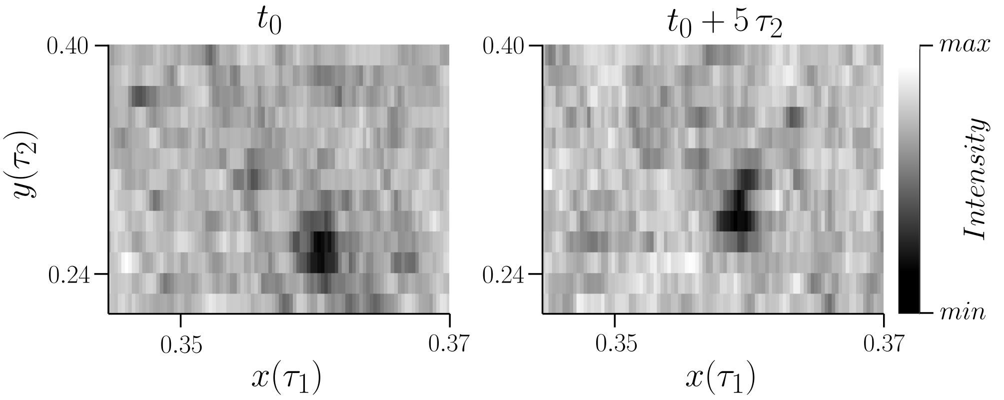

Figure 3.4: Close up on a PD candidate. Figures show how the same feature at time a) t_0 and b) $5\tau_2$ later, preserving its shape and slightly drifting.

emission very close to threshold which was not considered in the model.

3.6 Defects-mediated turbulence

We address now Defect-mediated Turbulence, the second dynamical regime described in [187]. DT is a dynamical regime characterized by spatiotemporal chaos which has been observed in reaction-diffusion systems out of equilibrium as in the CGLE in 1D [204] or in 2D [203], and even in optical 2D systems [205]. The CGLE can be applied to turbulent regimes due to oscillations near a Hopf bifurcation [204, 206, 207].Turbulence, as a terminology, is broadly used to define continuous spatiotemporal disordered structures, which exhibit chaotic fluctuations in a wide parameter range [208] ([209] for a version with figures with better contrast). Turbulent regimes have also been studied in systems with delays [171, 172]. It has been a topic of interest for a long time, reported in optical systems in [196] and recently in long-fiber lasers [210–212]. In contrast to the phase turbulence described in the previous section, DT exhibits more complex chaos originating from the interaction of an increasingly number of defects [203, 208].

DT can appear for conditions further from destabilization of a stable state, compared to PD, due to the requirement of multiple defects. In this section we aim to experimentally characterize the presence of turbulent dynamics on our SL system with multiple delays, and we do it specifically by increasing the bias current of the SL further from threshold. Increasing the bias current is expected to destabilize the system as it does for the case of a single delay. To visualize the dynamics we will use the 2D representation method pointed earlier.

First we show in Figure 3.5 a snapshot of the dynamics of the system for a bias current equal to $I_r = 11.75$ mA, a current higher compared to the phase defect regime, but below the threshold for a single feedback. Movies illustrating the dynamical evolution can be found as supplementary material [2]. From the movies we can observe that the system unfolds a spatiotemporal chaotic dynamical regime, characterized by irregular patterns with fluctuations and drops of intensity. These irregular patterns appear throughout all the pseudo-space, indicating that it is not a localized effect, were patches exhibit similar shapes and sizes without being identical. Such dynamics strongly resemble the defect mediated turbulent dynamics described in [187] and in [209]. In both works one can observe filament-looking dynamics. We observe regions in Figure 3.5 with minimum intensity that could include the phase defects generating

---

[2] `https://ifisc.uib-csic.es/ondemand/julian/ddfeedback-I=11.75mA_gray.mp4`

the dynamics in the same way as in [187, 203, 208]. In the following, we concentrate on a specific region of pseudo-space and observe how the turbulent structures evolve frame by frame. In Figure 3.6 we show a region of Figure 3.5 at time t_0 and at time $t_0 + 5 \cdot \tau_2$. By doing so, we can recognize how the dynamical evolution. It can be observed that many dynamical structures after $5 \cdot \tau_2$ are maintained with little changes. This pattern preservation indicates temporal correlation in the dynamics.

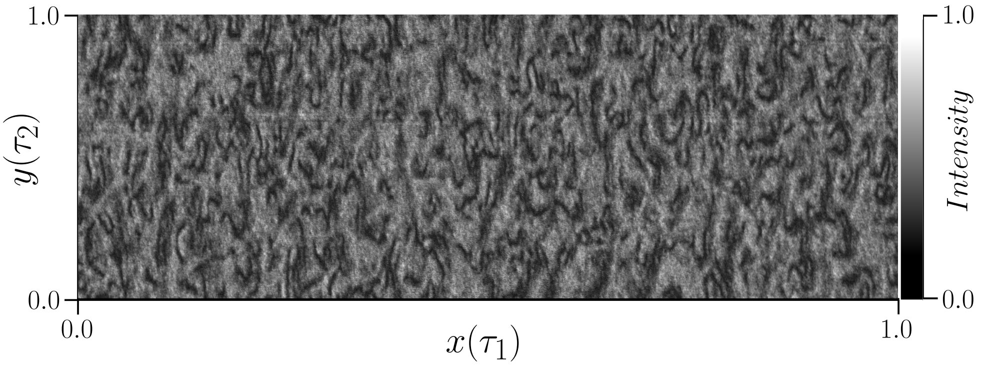

Figure 3.5: Single frame of the 2D representation of the spatiotemporal dynamics of the delay system for $I_r = 11.75$ mA. Intensity is encoded in grayscale.

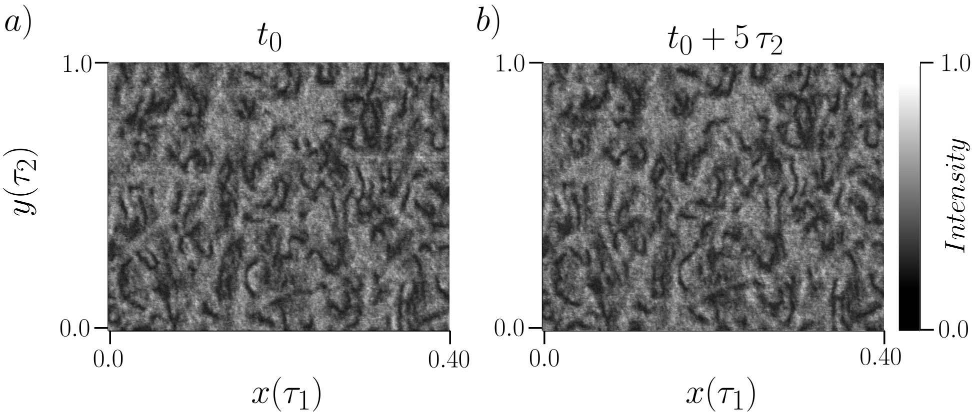

Figure 3.6: Zoom into the turbulent spatiotemporal dynamics for $I_r = 11.75$ mA. Panel a) shows the frame at t_0, while panel b) shows the frame at a later time, $t_0 + 5 \cdot \tau_2$. Intensity is encoded in grayscale.

The bias current of the SL is a crucial parameter determining the dynamics and its characteristic time scale of the system. In the following we discuss how the dynamics of the system change as we increase the bias current. In Figure 3.7 we show single frames of the 2D representation of the system's dynamics for currents in the range from 12.00 mA up to 13.00 mA. Movies illustrating the dynamical evolution can be found as supplementary material for currents 12.00 mA [3], 12.40 mA [4], and 13.00 mA [5]. We find turbulent structures as in the previous case, with the spatial features notably reducing in size. Also the characteristic temporal correlation decreases as I_r increases, indicating more rapid dynamics in the original timetraces. This is further supported by observing the movies. In [203] they report a reduction of correlation length in the same fashion as here, caused by the increase in the number of defects and the reduction of the mean distance between them. In Figure 3.8 we show how the corresponding dynamics evolved after $5 \cdot \tau_2$.

---

[3] `https://ifisc.uib-csic.es/ondemand/julian/ddfeedback-I=12.00mA_gray.mp4`

[4] `https://ifisc.uib-csic.es/ondemand/julian/ddfeedback-I=12.40mA_gray.mp4`

[5] `https://ifisc.uib-csic.es/ondemand/julian/ddfeedback-I=13.00mA_gray.mp4`

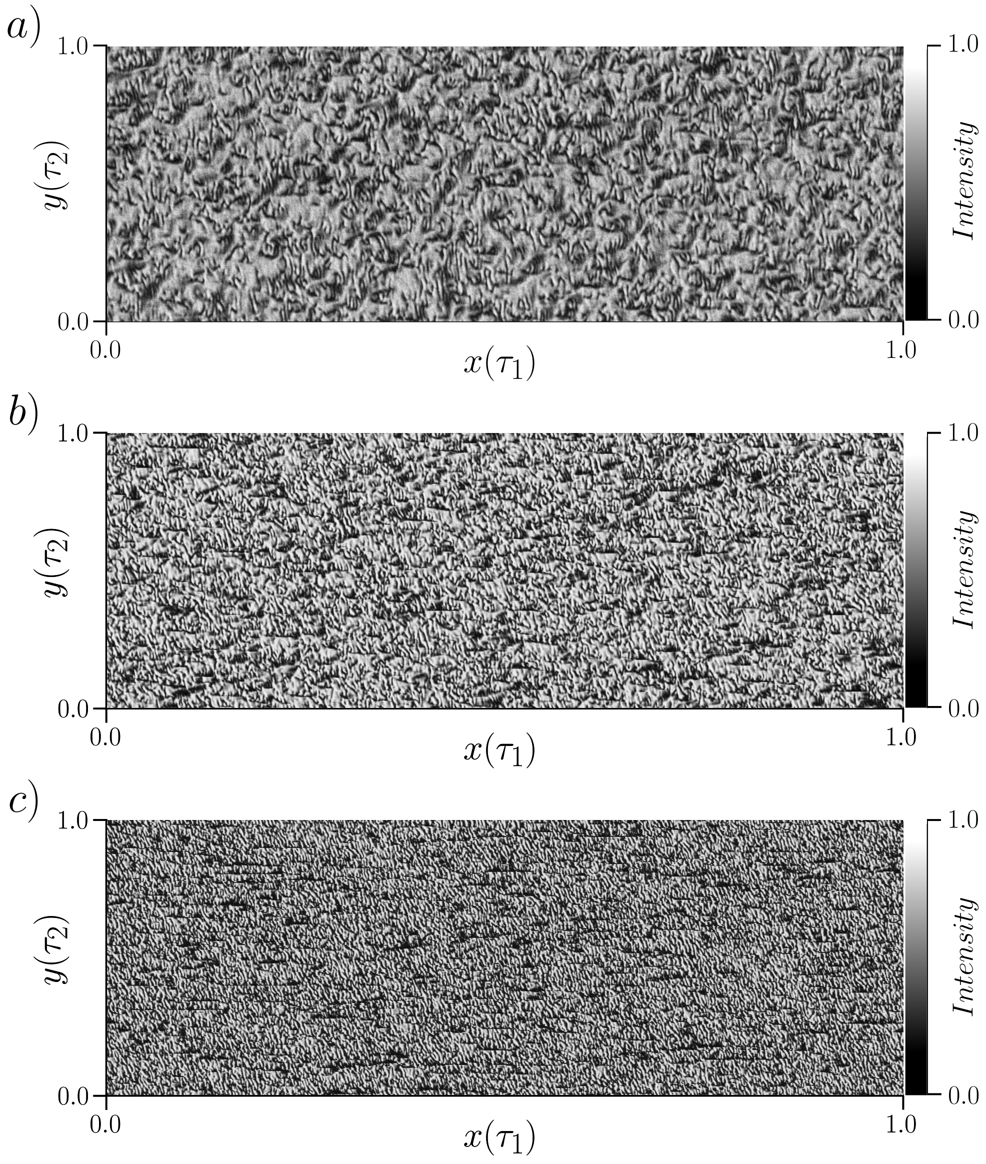

Figure 3.7: Single frames of the 2D representations of the turbulent spatiotemporal dynamics of the delay system for (a) $I_r = 12.00$, (b) 12.40 and (c) 13.00 mA. The structures exhibit a reduction of the dimension of the features. Intensity is encoded in grayscale.

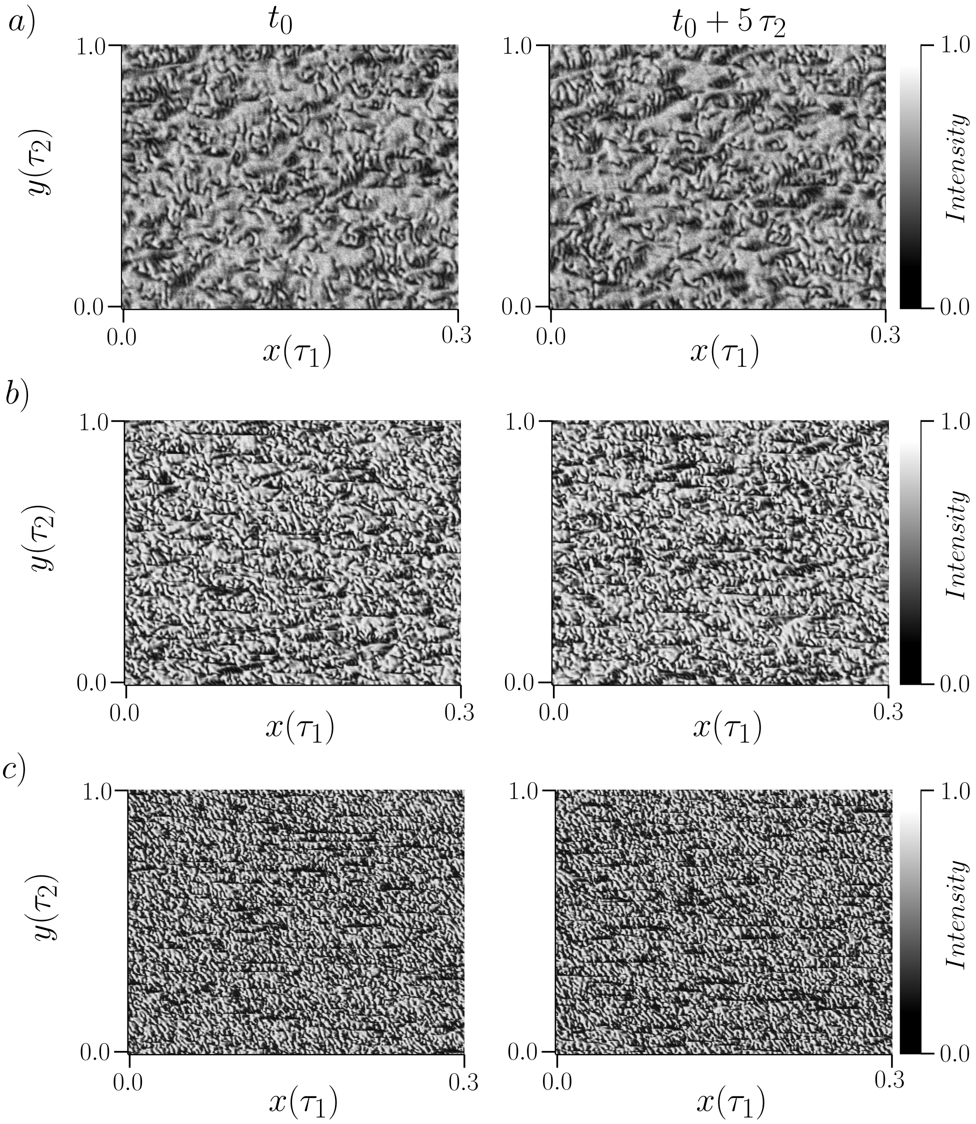

Figure 3.8: Zoom into to the turbulent spatiotemporal dynamics for $I_r = 11.75$ mA. Panel a) shows the frame at t_0, while panel b) shows the frame at a later time, $t_0 + 5 \cdot \tau_2$. Intensity is encoded in grayscale.

3.6.1 Intensity distribution in the dynamics

Further analysis of the dynamics can be performed by evaluating the intensity distribution of the dynamics. Authors of [187] observed a power-law distribution of the amplitude z in the dynamics as $P(|z|) \sim |z|^1$

for $|z| \to 0$. They observed this distribution for the turbulent regimes of the CGLE and for the LKE. The power-law scaling originates from the presence of multiple defects, which influence the amplitude distribution. Characterizing the intensity distribution of our dynamics could also provide us further insights.

In Figure 3.9 we show the intensity distribution function for the case of $I_r = 11.75$ mA. The distribution function is normalized such that the area under the curve is unity. I_{norm} are the intensity values are normalized between $[0,1]$, corresponding to the minimum and the maximum intensity values recorded for every case. The resolution of the measured intensity limits the span of the distribution to 1024 levels in our case. In the distribution function, we can clearly observe two different power laws. The first one at the initial tail corresponds to how the system's intensity rises from minimum values. One can obtain the characteristic exponent of the power law by using a linear fit in the desired section of the data in logarithmic scale. We find an exponent of 5.5, indicating a rapid increase of intensity towards intermediate values. Then, towards higher intensities, the distribution flattens. We observe a second range with power law scaling. A linear fit yields an exponent of 0.9. This slope value is similar to the slope equal to 0.5 found in [187] for the intensity. Beyond this point, probability of dynamics in large amplitude range quickly reduce.

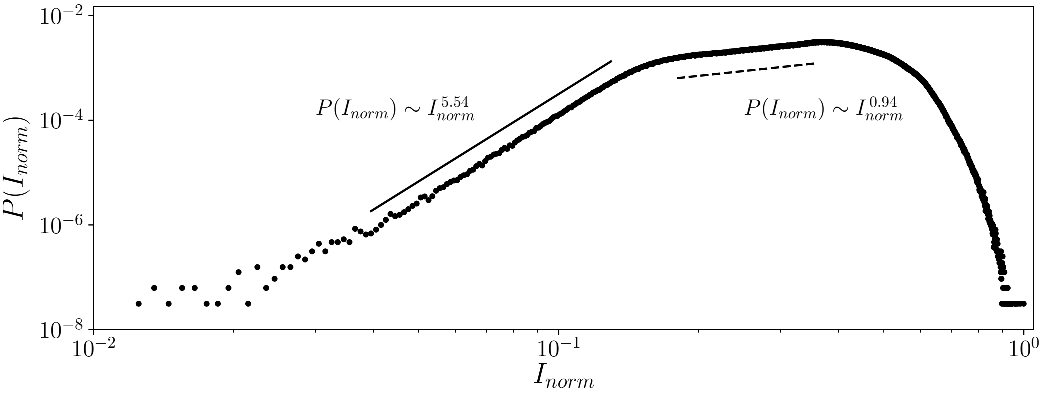

Figure 3.9: Histogram of the intensity values for $I_r = 11.75$ mA. Intensity values are normalized from minimum to maximum. Lines are reference curves for the indicated power laws.

The distribution of intensity values changes when the bias current is increased. In Figure 3.10 we show the histograms for the cases of $I_r = 11.75$ (included for easy comparison), 12.00, 12.40, and 13.00 mA, which corresponds to the examples in Figure 3.8. Distributions start ascending fast for all cases. For intensity values above 0.1, the distributions significantly change as bias current is increased. The distribution for bias currents 12.00 mA exhibit a power law with a slope of 0.4 for intensity values above 0.1 until 0.8, a smaller slope compared to the case of $I_r = 11.75$ mA and closer to the value found in [187]. Further increasing the bias current leads to distributions losing their power law behavior, and instead forming two local maxima.

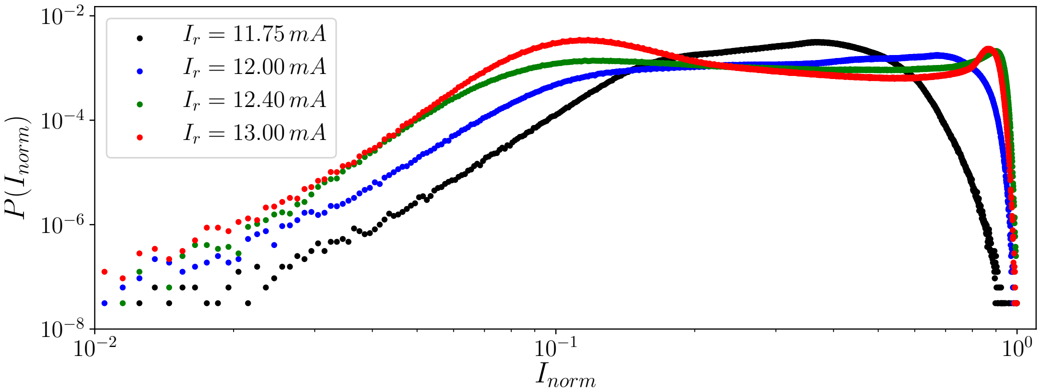

Figure 3.10: Histogram of the intensity values for different bias currents. Intensity values are normalized from minimum to maximum.

3.7 Spectral characteristics of the dynamics

Further analysis of the dynamics can be obtained performing a spectral analysis of our experimental data. By calculating the Fourier transform of the temporal dynamics one can gain further insights into the strength of different oscillatory modes in a variety of systems [196, 202, 213]. This is especially relevant in our case, as it is well known that the CGLE, as well as many delay equations with single delay, exhibit an amplitude distribution following an exponential decay as frequency increases [214, 215]. Observing different spectra in our dynamics would point towards the difference between our system and many others.

The spectral analysis of the dynamics was performed as follows. We computed the spectrum for every set of parameters by averaging the spectrum of consecutive time windows of length equal to the short delay τ_1. The spectra of the individual time windows was calculated via the fast Fourier transformation function. By using windows of τ_1 length we suppress the distinctive oscillations in the spectra from the two delay times and focus on the high frequency components that constitute the dynamics. Averaging over all the obtained spectra reduces the contribution of inherent noise in the data. It is relevant to notice that for the present realization we do not compute the full 2D spectra of the dynamics. The spectra computed here is the one in the x-axis direction, corresponding to the horizontal direction in the snapshots show in Section 3.6. A full analysis would eventually include the spectra in the y-direction, as both directions can provide different energy spectra, and therefore different information, due to the different time scales the system exhibits in perpendicular directions. We restricted our analysis on the horizontal direction since only $m = 285$ data points are available in the vertical direction, which provides a spectrum with insufficient resolution to extract sufficient relevant information. This restriction could be avoided in future experiments by increasing the aspect ratio m of the frames to further study the system's dynamics. And would also need an upgraded detection system with a larger memory depth.

In Figure 3.11 we show the energy spectra of the dynamics in the horizontal direction in a semilogarithmic plot for currents spanning from 11.50 mA to 13.00 mA. The sampling rate of the oscilloscope of 40 GSamples/s, determines the fastest frequency component we can extract, 20 GHz. In practice, the bandwidth of the components and instruments ultimately determines the fastest oscillations that we can actually confidently resolve. In our case that is 16 GHz, limited by the analog bandwidth of the oscilloscope, which is why above this limit the frequency components in Figure 3.11 quickly drops in power. For $I_r \leq I_{th,2fb} = 11.60$, the spectra is essentially flat due to the non-existing dynamics occurring in this range. For $I_{th,2fb} \leq I_r \leq 11.90$, the spectra show an exponential decay in the range of low frequencies. This is visible as a linear decrease of the spectral components in this semilogarithmic representation, and we place dashed lines to guide the eye in some cases as examples. These are also the strongest components in the individual spectra, so they govern the developed pattern. This exponential decay occurs roughly until $2.5 \cdot 10^9$, which corresponds to a time scale of 0.4 ns. The corresponding range indicates that the exponential decay characterizes the dynamics from scales of τ_1 down to half a nanosecond. This is indeed the scale of the dynamics depicted in Figure 3.5, indicating that the observed dynamics are indeed connected to the exponential decaying part of the spectra. As I_r increases, the spectra deviate more and more from the exponential decay. We can observe very sharp peaks at 5, 10, and 15 GHz, caused by the acquisition sampling rate of the oscilloscope.

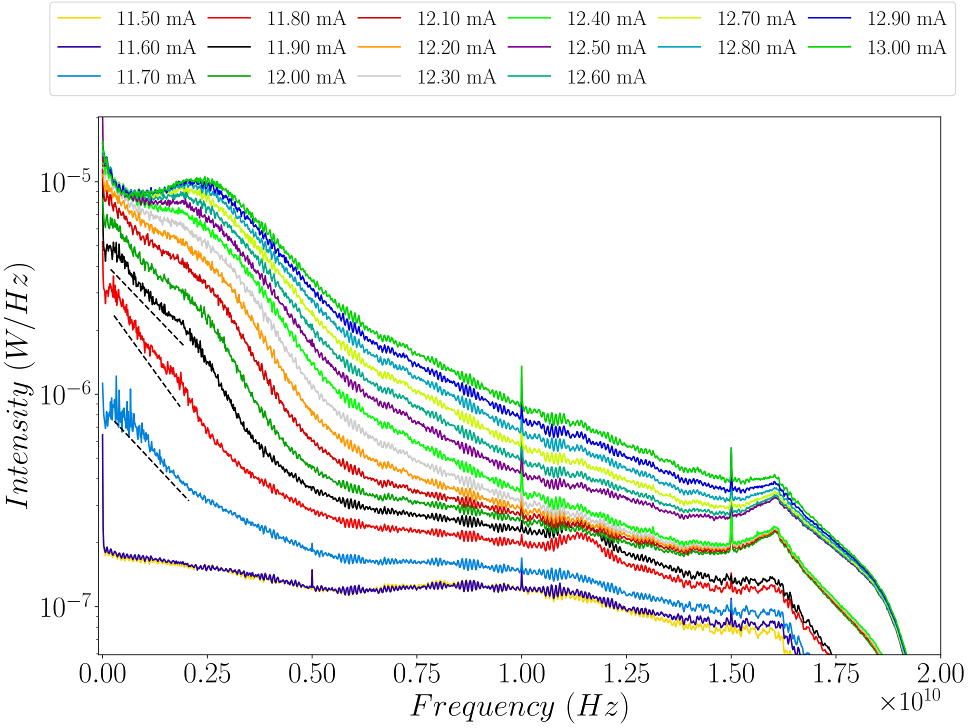

Figure 3.11: Spectra of the dynamics in semilogarithmic axis for different bias currents. Dashed lines guide the eye in the exponentially decaying region of the spectra.

In Figure 3.12 we represent the spectra in a double logarithmic representation. For higher currents, the spectra readily show a power-law scaling. The figure shows the frequencies above 1 GHz. For currents higher than the region for which exponential decay was found, the spectra start showing a double power law decay represented by the linear decay with two slopes for different spectral components. These two power law decays occur in different frequency ranges; one below 5.5 GHz, and the other between the 5.5 GHz and extending up to 15 GHz. We refer to these regions as the band 1 and the band 2, respectively. The power law decay in the band 1 is exemplified for the case of $I_r = 12.20$ mA in Figure 3.12 by a dashed line, guiding the eye along the linear regimes. We observe that the power law in the band 1 extends from the roll off of the spectra to the connection with the power law for the band 2. The roll off of the spectra appears to be connected to the characteristic relaxation oscillation frequency of the SL dynamics, as it appears consistently in the range of few GHz. For frequencies below the roll off the spectra is almost flat. The power law in the band 2 is exemplified for the case of $I_r = 11.80$ mA in Figure 3.12 by a dotted line, guiding the eye along the linear regime. This power law exhibits an inclination that gets steeper as bias current increases, and its range of validity also extends with increasing currents. In this band 2 one can observe a hump around 11 GHz, which appears for currents in the range of $(11.70, 12.00)$ mA. It is not completely clear what is the origin for this hump, but it might be related to the mode with the highest growth rate [216]. For $I_r \geqslant 12.00$ mA the hump disappears, which are the currents at which features in the 2D spatiotemporal representation become smaller and faster, as depicted in Figure 3.7. After the hump disappears the band 2 extends up to 16 GHz, only limited by the bandwidth of the experiment. Interestingly, both power law scaling regions, for the band 1 and for the band 2, join together into a single power law decay as bias current increases. At $I_r = 13.00$ mA, the spectra exhibit a single power law spanning from 3 to 15 GHz. This merging of the power laws indicates that the dynamics are now scale-free over a larger frequency range.. Figure 3.11 and Figure 3.12 together show that the behavior of the dynamics shows a transition from an exponential to a power law decay as bias current increases. Power law behavior has only been reported to the best of our knowledge in the context of the CGLE for one dimension with fifth or seventh order nonlinearities [217], where dynamics showed self-similar intermittent bursts.

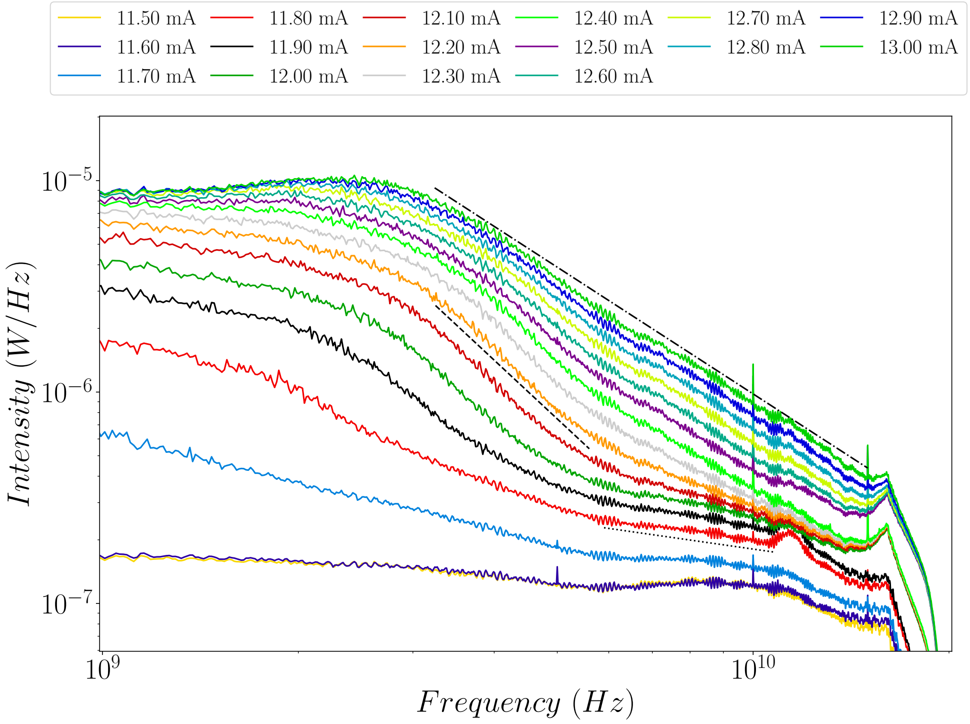

Figure 3.12: Spectra of the dynamics in double logarithmic representation for different bias currents. Dashed lines guide the eye in the range of power law decay in the band 1 range of the spectra, while the dotted line does so in the band 2. Dash-dotted line guides the eye upon the combined power law region for higher bias currents.

In Figure 3.13 we show the slopes for the spectra of the dynamics in the band 1 and and 2 ranges. The slopes were calculated by fitting a power law function as $y = \gamma x^{\beta}$ in the range of interest of individual spectra; where y are the spectra components, x are the frequency values, γ is the multiplicative factor, and β is the exponent of the power law. The exponent β corresponds to the slope of the spectra in the double logarithmic representation. In Figure 3.13 we observe that the slopes β start close to zero, and quickly separate as the bias current is increased. The slope for the band 1 lowers to a minimum close to -3 for $I_r = 12.20$ mA, and then increases to a value around -2 for $I_r = 13.00$ mA . In contrast, slopes for the band 2 become consistently stepper in the studied range until they approach the values of the slope in the band 1. Then both slopes values become more and more similar while they slightly rise in value as current increases. Such behavior for high currents in the unification of the power laws can be observed in Figure 3.12. For $I_r <$ 12.20 mA the dynamics are strongly favored by frequency components below the 6 GHz. Interestingly, the threshold currents we indicated in Section 3.4 seem to identify transitions in the slopes. The bias current with the steepest slope in the band 1 corresponds exactly to $I_{th,fb} = 12.20$ mA. And later, both power law decays start exhibiting similar slopes for currents around $I_{th,sol} = 12.87$ mA.

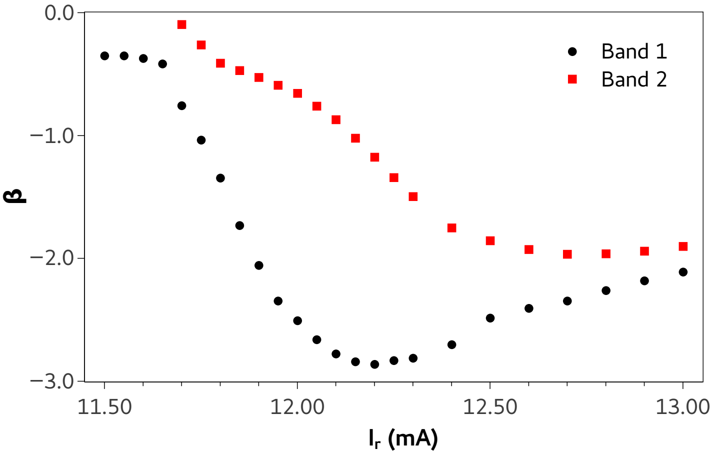

Figure 3.13: Power-law slopes of the spectra with a power law dependence in the band 1 (black circles) and the band 2 (red squares) for different bias currents.

3.8 Summary and discussion

In this chapter we studied the dynamics of a semiconductor laser with two optical delayed feedbacks. The delay lines loops had delay times of different order, where τ_2 was almost 300 times longer than τ_1. This configuration was selected to study the dynamics of the system in the framework of the findings in [187], where they theoretically studied the dynamics of the two dimensional Complex Ginzburg-Landau equation and showed that these dynamics could also be observed in a Semiconductor Laser system with two optical delays. We decided to experimentally study such delay system due to the two distinct dynamical regimes they observed. For the analysis, we used two dimensional representations of the experimental data that could be sequentially arranged to show dynamics with two dimensions in pseudo-space.

We first focused on Spiral Phase Defects, a dynamical state characterized by points in space with minimum amplitude and undefined phase that were created and annihilated in pairs due to topological constraints. After a meticulous study of the system's dynamics in the appropriate parameter space we did not observe PD. We did observe objects that shared features with PD, but not sufficiently as to refer to them as PD with complete certainty. The lack of observation of these objects could be due to several aspects. In [187] they stress on the necessary requirements of certain parameters, pump infinitesimal close to threshold and α equal to 2, to identify PD due to insufficient SNR close to threshold. Regarding the experimental realization, the accuracy and stability of the pump current in the SL may not be sufficient. Even though our SL had an $\alpha \sim 2$, the experimental α is not constant with pump current and may diverge excessively from the required one. Furthermore, experimental noise may destabilize the PD.

The second dynamical regime of interest was Defect-mediated Turbulence. This regime involved spatiotemporal chaos originating theoretically from the interplay of multiple phase defects. As bias current increased, we observed this scenario unfold by presenting the dynamical evolution of DT. The spectral study exhibited frequency components decaying exponentially in the low frequency window. Increasing bias current further showed that the dynamics of the system become faster, noticeable both in the movies and by an enhancement of the high frequency components. With increasing bias current, the spectra of the dynamics deviated from exponential and turned into a double power law, with exponents dependent on the current applied to the SL. Further increasing the current led to a single power law distribution, indicating scale-free behavior. The double power law reminds of the characteristic double power law in the study of fluid dynamics in two dimensions [213, 218]. The two exponents of the power law relate in fluid dynamics to energy and to enstrophy (associated to vorticity) transport, where energy and vorticity are transported to lower and higher spatial scales from the energy injection scale, respectively. These ideas from fluid dynamics could be significant for a deeper understanding of our power law behaviors.

These results shows experimentally the connection of delay systems with spatially extended ones. The movies illustrate that the two dimensional representation of the data is suitable due to the high temporal correlation between consecutive frames. The diverse chaotic behaviors found shows the possibility of studying spatiotemporal chaotic systems using delay systems. Such an approach provides important benefits compared to spatially extended systems, since they allow to study truly homogeneous system (where the nonlinearity is the same everywhere that depends on the SL as the only nonlinearity. This system allows to tune multiple parameters related to the dynamics. In our case, we restricted ourselves by changing only the bias current, but varying feedback strengths might also give rise to interesting dynamics. In a broader scope, the setup allows customization of the spatial dimensions, which can be done by changing the delay times and the temporal scale of the nonlinearity via the bias current. Furthermore, the present system can be extended to allow for complementary studies. Extra delay lines can be implemented to experimentally study spatiotemporal dynamics in higher dimensional pseudo-space. In addition, techniques like heterodyne detection can be used to detect the phase of the signal to retrieve the information about its dynamical evolution, and may serve to identify the defects.

Chapter 4

Time delay reservoir based on a semiconductor laser with delayed optical feedback

4.1 Introduction

In Section 1.1 we introduced semiconductor lasers, and in Section 1.2 we gazed into the rich nonlinear dynamics of these devices in the presence of optical feedback. We showed how the semiconductor lasers can exhibit dynamics with properties such as high dimensionality and bandwidth just by introducing delayed optical feedback. In Section 1.4.1 we explained the basics of reservoir computing. This machine learning technique offers excellent information processing capabilities with simply one hidden layer and by just changing the weights to the output layer. The technique relies on mapping data onto higher dimensional state spaces, redistributing the data in the new space for an easier linear separability of information with different features. This is achieved thanks to the input mask and to the nonlinear dynamics of the reservoir. As we saw in Section 1.2, a semiconductor lasers under optical feedback is a nonlinear system that can exhibit highly chaotic dynamics. Such system therefore can possess suitable characteristics to perform RC. The construction of a photonic reservoir with semiconductor lasers with optical feedback at its heart allows to employ the benefits of its highly complex and GHz-fast dynamics for information processing purposes. Previous work demonstrated that a semiconductor laser can perform reservoir computing using the concept of time delay reservoirs [130] . Successful information processing was shown with and without feedback, and under different feedback conditions [29, 165, 219].

The use of a semiconductor laser as an information processing device is a very attractive idea for several reasons. One important reason is the bandwidth of the dynamics. The dynamics of semiconductor lasers with feedback alone are of the orders of GHz [220–222]. Additionally, existing work showed how optical injection into semiconductor lasers can broaden the dynamical bandwidth to at least 80 GHz [73]. Since information processing in reservoir computing is based on the transient responses of the system, a reservoir computer with a bandwidth close to 100 GHz will provide the response of a node in the network in about few tens of picoseconds. The responses of multiple nodes are required for adequate performance. Considering the case of a typical network of several hundreds of nodes in a delay RC configuration, information would be processed in a few nanoseconds. These operations could be difficult and resources-consuming tasks for traditional computers like classification of a multidimensional input (e.g. images, audio, or multiple sensors) or forecasting in a complex deterministic environment (e.g. temperature, demand, or prices) can be performed.

An important advantage of this photonic reservoir is the possibility to implement an all-optical information processing device where information enters and exits encoded in light. Injection of information through optical means is possible thanks to the susceptibility of the semiconductor laser to injected light (Section 1.1). An optical output can be obtained since the light generated from the reservoir depends nonlinearly on what was injected. This optical response can be easily modulated by using off-the-shelf telecommunication equipment.

In addition, a remarkable characteristic of the photonic reservoir presented is its exquisite simplicity. The reservoir itself is constructed by just a semiconductor laser and a delay line. All components are off-the-shelf telecommunication components, which avoids exotic components that would increase device cost, complexity, or design effort. The simplicity and possibilities of the implementation facilitates and motivates future potential inclusion of such technology in present infrastructure, more complicated systems, and integration in dedicated chips. Semiconductor lasers with a delay feedback section have been successfully integrated on chip and exhibit chaos while occupying tiny footprints [223, 224]. The capabilities that can be provided in such small space employing simple components is proof of the extraordinary potential that semiconductor lasers have to offer.

We know already that time delay reservoirs based on a semiconductor lasers with optical feedback can successfully perform reservoir computing [29, 219]. But we lack a detailed knowledge and a deeper understanding under which conditions they can be operated well. Understanding the underlying physical reasons and dependencies of the reservoir on key parameters will shine light on the full possibilities and capabilities of these systems. This chapter is devoted to extending the understanding of a photonic reservoirs based on a semiconductor laser with delayed optical feedback and optical injection of information. We start by describing the experimental setup and the methods employed for our studies. Then we evaluate the fundamental properties of our system, together with the dependence on two important parameters (frequency detuning and feedback attenuation). We continue by evaluating the dependence on other two key parameters, injected optical power and bias current on the response laser. Afterwards we present injection with even higher detuning frequencies at side-modes of the laser inside our reservoir. Then, we push the bandwidth of our photonic reservoir by injecting information at modulation rates at the limit of our instruments. We further extend our investigations by evaluating the possibility of implementing an heterogeneous reservoir without changing a single component. At the end we provide a summary and a discussion of the results.

4.2 Experimental setup

The hardware implementation used in this chapter was based on a semiconductor laser with delayed optical feedback and modulated optical injection. This scheme showed previously excellent performance in reservoir computing techniques [29]. A scheme of the setup is depicted in Figure 4.1, and consists of off-the-shelf telecommunication components except for the laser in the feedback loop, which is lacking an optical isolator. The setup can be sub-divided into an injection, reservoir, and detection section.

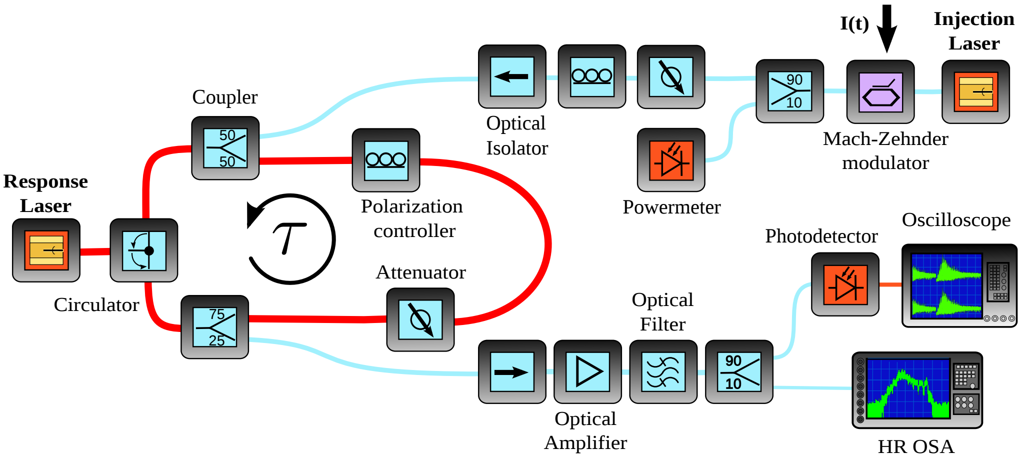

Figure 4.1: Scheme of the experimental setup. Blue lines are optical fibres. The orange line is an electrical cables. Thick red lines represent the path for optical feedback. The circular arrow represents the propagation direction of light.

The components in the top right of Figure 4.1 form the injection arm. The purpose of them is to inject information optically into the reservoir. It's main component is the injection laser, which we used to provide the light that will carry the information. This laser is a single mode Distributed Feed-Back (DFB) semiconductor laser. The laser emission exhibits a linewidth of 10 MHz (limited by the instrument resolution), with a longitudinal mode separation of 110 GHz and side mode suppression ratio of more than 50 dB. Temperature and bias current were stabilized with 0.01 K and 0.01 mA accuracy, respectively. This particular laser was chosen in combination to the Response Laser (RL) due to the possibility of emission at the same optical frequency as the RL. This could be achieved by adjusting the bias current and temperature of the injection laser. The temperature of the injection laser was varied to control its optical frequency. An Arbitrary Waveform Generator (AWG) synthesizes the electrical signal with the information to be injected with 8 bit resolution and 9.6 GHz analog bandwidth. An amplitude MZM imprints the electrical modulation carrying the information onto the constant optical intensity of the injection laser, creating the optical modulated signal for the reservoir. A polarization controller and a variable attenuator control polarization and average power of the injection keeping the peak-to-average power ratio constant. The polarization of the injected light was chosen parallel with respect to the polarization state of the SL inside the reservoir. We use an additional 50 dB optical isolator to suppress unwanted reflections into the injection section.

The signal to be injected follows the modulation scheme of the input layer described in Section 1.4.2 for a TDR. It is composed of a sequence of segments of duration equal to τ, and each segment is a mask multiplied by the value to be processed. As already described in Section 1.4.2, the mask is a sequence of values to help the reservoir explore its state phase space. The number of values that compose the mask determines the number of nodes in the network, where each virtual node is separated from its neighbors by time θ. In this chapter (except in Section 4.8) we choose for our time delay reservoir $\theta = 200$ ps. The selection of θ is based on the dynamical timescales of the nonlinearity operating inside the reservoir, in our case, a SL. θ needs to be shorter than the characteristic time scale of the dynamics, but long enough so the transient responses are measured. The time scale of the intensity dynamics of semiconductor lasers lies in the range of GHz, which motivates the choice of the specific value of θ under the nanosecond time scale [219]. The θ also determines the sampling rate necessary for the AWG, so for $\theta = 200$ ps then the sampling rate is 5 GSamples/s. In this chapter the mask used is a piecewise function of N values randomly chosen from the set $\{-1.0, -0.6, -0.2, +0.2, +0.6, +1.0\}$. Choosing a mask with six possible values offers enough variability of responses for computation [225]. This signal is then injected into the reservoir with an OC.

The reservoir is implemented by a semiconductor laser called from now on the RL, coupled to an optical fiber delay loop (highlighted in red in Figure 4.1). For the experiments in this chapter we used as RL a single mode quantum well semiconductor laser emitting at $\lambda = 1542$ nm, with a longitudinal mode separation of 145 GHz, and side mode suppression ratio of more than 40 dB. This laser presents sub-MHz linewidth and large side mode suppression ratio thanks to its Discrete Mode structure [18]. Temperature and bias current were stabilized with 0.01 K and 0.01 mA accuracy, respectively. This laser was chosen due to the possibility of electrical modulation in the GHz regime. The laser temperature is kept constant at $T_{RL} = 19.00°\text{C}$. While keeping the RL at this temperature, the injection laser emit at the same optical frequency as the RL if its temperature was stabilized at $T_{resp} = 45.550°\text{C}$. The delayed feedback loop is realized using an optical circulator, which defines a propagation direction within the feedback loop and suppresses unwanted back reflections. A crucial parameter of the reservoir is its delay time τ. The delay time of the setup needs to be a multiple of the previously defined θ value. Therefore is required that τ is a multiple of 200 ps. To fulfill this requirement, we choose the components of the reservoir so they provided an appropriate delay time with a resolution of 25 ps. The delay time then was measured to be $\tau = (66.000 \pm 0.025)$ ns, according to the method described in Section 2.2.2. This resulted in a network of $N = \frac{\tau}{\theta} = 330$ virtual nodes (Section 1.4.1). A polarization controller and a variable attenuator control the feedback conditions of the light. The feedback polarization is kept parallel relative to the polarization direction of the RL. As the polarization states of the injected and feedback light are parallel to the RL's emission, only one polarization direction is contributing to the detected signals in the experiments. The variable attenuator regulates the light intensity traveling through it. We define η as the power attenuation applied on the feedback. For minimum feedback attenuation, corresponding to $\eta = 0$ dB and to maximum feedback condition, the RL receives from the delay loop 21% of the optical output power collected from the same laser's fiber pigtail. For $\eta = 0$ dB and parallel feedback polarization, the RL's threshold current at $T_{RL} = 19.00°\text{C}$ is reduced from $I_{th} = 11.24$ mA to $I_{th,fb} = 10.55$ mA. A 75/25 OC extracts then 25% of the optical power for detection.

Detection of the generated signal by the RL is done by extracting light from the delay cavity from the 75/25 OC. The detection methods and conditions of the output signal from the reservoir are described in Section 2.1.

4.3 Methods for training and characterization of a delay laser reservoir

In this section we introduce the methods used along the chapter to study our reservoir computer. First we introduce the methods necessary to perform adequate information processing with reservoir computing. Then we proceed to the methods to study the properties and capabilities of our particular reservoir. The capabilities studied here are the consistency property (as discussed in Section 4.3.2), the memory property (as discussed in Section 4.3.3), and the performance of the reservoir computer on specific tasks defined in Section 4.3.4. This study will provide insights into the properties of the reservoir from different perspectives, and based on different principles. The relevance to study specifically these aspects is discussed in each corresponding section.

4.3.1 Determination of the output weights

In Section 1.4.1 we introduced the concept of reservoir computing. As we mentioned, the reservoir computer is formed by three distinct groups of nodes called layers. Nodes are connected to other nodes in the next layer, and the connection strength is called weight. The layers' connectivity is depicted in Section 1.4.2. We mentioned that the value of the output weights are the only ones being trained in reservoir computing. Successful computation requires considering many parameters, like the amount of nodes, the nonlinearity of the nodes, the virtual node separation θ, mask properties, etc. Finding the set of output weights that provides the lowest error at the task at hand is equally crucial. The output weights project the high dimensional responses of the reservoir, induced by the information injected, onto the final responses of the reservoir for a specific task. The output weights for a set of conditions are found through a process called training. We dedicate this section to present the learning methodology used in this chapter. First, we introduce a technique of offline learning to obtain the output weights. Second, we briefly discuss an important technical feature of the learning process regarding how many examples one needs to present to the reservoir. Last, we comment on a procedure to improve the statistical relevance of the learning applied. Many of the points discussed in this section and more information on the topic can be found in [226–228].

Offline learning

Finding the set of output weights can be done through different processes. The decision on which process to choose will depend on the conditions and features of the system. For our purposes we implement an offline learning technique. This technique falls under the category of supervised learning, where during the learning process we know beforehand what are the correct responses for a limited set of training data points, called the training data set. An offline learning technique is based on injecting the training data set into the reservoir and record the responses of the reservoir to this injection. The recorded responses of the reservoir to the training data set, together with the knowledge of what the right answers of the reservoir computer should be, allows to calculate the output weights by matrix inversion. This is performed after the reservoir has provided the nonlinear responses to all the injected information, hence the offline name.

In Section 1.4 we learned that the state of the reservoir is projected onto the output layer via the output weights as shown in Equation (1.3). For the reservoir to be successful in a task, the output weights need to be minimize the errors of the reservoir computer. Initially one doesn't know which configuration of output weights provides it. A configuration can be found if we use a data set of n inputs $x_i^{train}(n)$ with its corresponding right answers $y^{train}(n)$ to train the output weights. Index i indicates the node index and n the index of the data sequence to be processed. This data set is called the training set. The found output weights are such that $\omega_{train}^{out} = \text{argmin}_{\omega^{out}} || y_i - \omega^{out} \cdot x_i||$ with any input injected. So calculation of ω_{train}^{out} can be performed via Equation (4.1).

$$\omega_{train}^{out} = y_i^{train} \cdot \left(x_i^{train}\right)^+ \tag{4.1}$$

Superscript $+$ denotes the Moore-Penrose matrix inversion. Use of the Moore-Penrose matrix inversion avoids ill-conditioned matrices, and provides the least squares solution to a system of linear equations like ours [229]. In the case of experimental data this step is less necessary since noise in the data produces similar results through data augmentation [230]. Additionally, an extra node of constant value is added to $\mathbf{x}$ and to W_{out} to correct the constant bias of the reservoir signal.

Once the output weights are determined with the training data set and applied to the output layer, the reservoir computer can be operated to produce answers to injected data. But the trained output weights do not necessarily produce perfect answers. A reservoir computer with trained output weights can generate errors even on the training set, called training errors. It is desired that the system yields the lowest possible errors with any data set, not only with the training data set. To evaluate how the system performs in general with any data, one uses a different data set from the training data set called the testing data set. Therefore, the performance of the system can be evaluated on the testing data set using the parameters obtained from the training, and produces the test error. This error measures how well the reservoir computer performs when provided with new unseen data. The testing error is typically larger than the training error since the output weights are not adjusted to the testing data set, and ideally both errors should be identical. The difference between both errors is called the variance. Any piece of information could be used in either data set in principle. Therefore, one separates the complete data set available into the training data set and the testing data set. The fraction of data sets should be evaluated individually for different tasks and systems. In this work we separated the data set using 80% for training and 20% for testing, as this proportion proved adequate for the tasks employed in this work to reduce variance. A typical suitable compromise is to separate the data set 80% for training and 20% for testing.

Choosing the size of the data set

Ideally, testing and training errors should be identical. Using a small training data set can cause a large difference between the training and testing errors. This is due to a lack of generalization of the task by the reservoir computer, where the reservoir has not have seen enough samples to capture the real general characteristics and features of the data. So to improve on this point, learning on a larger data set can reduce the variance. To evaluate the impact of the data set size on the learning one can use a learning curve. A learning curve shows the evolution of the errors as the learning data set becomes larger. In Figure 4.2 we show the evolution of the testing and training errors for the Mackey Glass prediction task (described in Section 4.3.4) as the data set for learning grows. We can observe that for very low numbers of samples the training error is practically zero. For such small number of samples, the reservoir (almost) perfectly resolves the task when a training sample is presented. This is due to the simplicity for the higher dimensional reservoir to model a low dimensional system (due to the low number of data samples presented, the reservoir sees it as low dimensional). The test errors in this range are high, and also the variance, indicating the reservoir computer performs badly on data it has not seen and is not generalizing properly. As the number of samples increases, the training error increases and the testing error decreases. Both curves asymptotically approach as the number of samples increases, converging to the error value marked by the gray line. The converging curves indicate that the system learns to generalize the task better. Factors like the convergence rate and data availability will determine the optimal number of samples required for the training. The learning curve can also help identify training problems in the reservoir computer. For example, testing and training error may converge to a too large value. In summary, the learning curve provides helpful information on how many samples are necessary for a task, and what would the influence of using different amounts of training data.

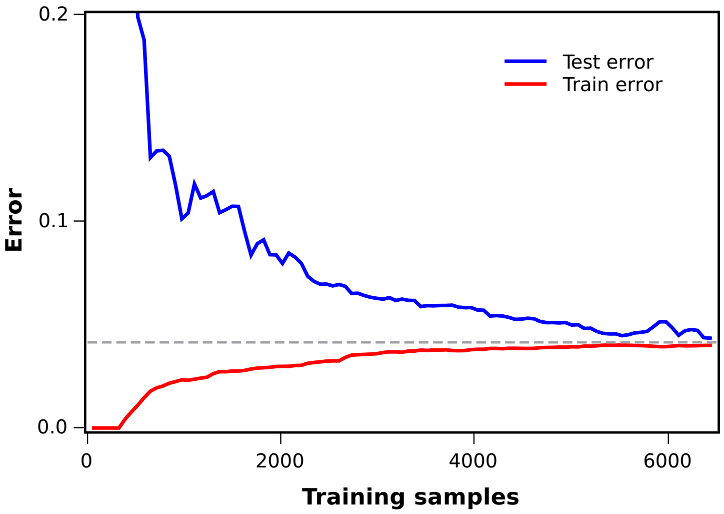

Figure 4.2: Learning curves depicting the error on a prediction task versus the amount of samples used for training and testing. Red curve indicates the error on the training data set, blue curve indicates the error on the testing data set. The dashed gray line indicates the error to which both curves converge.

Cross-validation

In the previous section we learned how to obtain output weights, and how many samples are needed to adequately train a reservoir computer. A technique widely used to obtain good statistical significance of the training with a finite data set is cross-validation. Cross-validation involves repeating the teaching process for different distributions of training data sets. The number of distributions, and therefore different groupings of the samples, is called a k-fold cross-validation. From combinatorial analysis one can see that the number of possible combinations (and folds) grows enormously with the number of samples. Typically, the test data set (assuming it has fewer samples than the training set) for a certain fold shares no samples with any other test data set of other folds. This is equivalent of saying every sample is used for testing only in one fold. To illustrate this procedure, we can imagine a data set separated in five groups named 1, 2, 3, 4, and 5. Planning to use 20% of the data set for testing is equivalent to say in this case we use one group (amounting to 20% of the data) for testing and all the remaining for training. Cross-validation can be applied here to create a 5-fold validation, as the number of folds available depends on the minimum number of samples required for adequate training. In the first run, group 5 is used on testing and groups from 1 to 4 are used for training. In the second run, group 4 is used on testing and groups from 1, 2, 3, and 5 are used for training. By sequentially repeating this process, every group is once used for testing once while all the others are used for training. The final test error, usually also called cross-validation error, is the mean value of the test errors of the individual runs. This process improves data efficiency, and provides a more complete vision of how well the reservoir computer learns as it is evaluated based on all the data available at the end. Therefore, cross-validation is beneficial. One needs to keep in mind that computation time increases as the number of folds does, therefore, a reasonable trade-off is usually made. In the present work 5-fold cross-validation was applied, and data samples were randomly associated to the different groups.

4.3.2 Consistency

Consistency is a fundamental property of dynamical systems. It relates to the similarity of the responses of a system under repetitive injection of similar, or even identical, input drives. Computational performance requires reproducible results, making consistency an essential condition for reservoir computing [126, 231]. In the framework of dynamical systems, consistency has been extensively studied along the concept of synchronization [232–238]. Many insights on the topic of consistency and synchronization can be found in Ref. [239]. The consistency properties of the system will depend on the properties of the response system under study and on the properties of the drive [79, 240]. Aspects of the nonlinear properties of the response system will strongly relate to the consistency properties. The consistency of nonlinear systems has been studied considering drives of very different natures, as for example harmonic modulation [241–244], chaotic dynamics from another nonlinear system [88, 245], delayed chaotic dynamics of the same system [89], pulses [246], or even noise [88, 247]. In the same context, consistency properties have been studied in a variety of nonlinear systems, ranging from mathematical models [232, 248], to plasma oscillators, [249], electronic circuits [236, 250], and biology [251, 252]. An extensive review can be found in [253]. Over the past years, the number of components and complexity in the systems have increased [40, 254, 255]. Without doubt, consistency is especially a topic of interest for photonic systems based on semiconductor lasers [35, 40, 79, 89, 240, 256–258]. Semiconductor lasers with optical feedback driven by external signals have shown different consistency properties depending on conditions of the laser system and the drive. This is a direct consequence of the complex phase-space of the system [198]. The importance of consistency for computational systems and the susceptibility of consistency on the parameters of the drive-response system strongly motivates our study of consistency as a fundamental property.

To obtain insight into consistency properties, we use two tools: persistence plots and consistency correlation. Each measure provides insight in a different and complementary way. Persistence plots and consistency correlation are methods based on acquiring multiple responses of the response system to injection of the same drive signal. The drive signals considered had similar amplitude and bandwidth characteristics as the input signals used for multiple other tasks and evaluations throughout the chapter.

Persistence plots are obtained by plotting the probability density of the response for every time when repeating the same drive signal often. This is an attractive method, in particular in experiments, since modern oscilloscope can provide this information directly for many repetitions. Every distribution function holds basically two pieces of information about the response at that time. The mean of the distribution function corresponds to the average value of the response. The width of the distribution relates to the consistency of the response at that precise moment, providing a temporarily local measurement of consistency. Local consistency can therefore be easily obtained from the vertical spreading of the persistence plot. A broad distribution corresponds to a large variation of responses, indicating an inconsistent response. A narrow distribution corresponds to a small variation of responses, indicating a consistent response. Consistency plots shown in this chapter are built overlapping around 500 time traces. The large number of responses overlapped for the persistence plots provides good statistics for the visualization and evaluation of consistency.

Consistency correlation is a global measure of consistency compared to the temporarily resolved information from persistence plots. We use pairs of three different responses to calculate the consistency correlation between them ($CC_{i,j}$) via Equation (4.2).

$$CC_{i,j} = \frac{< |I_i(t) - \bar{I}_i||I_j(t) - \bar{I}_j| >}{\sigma_i \, \sigma_j} \tag{4.2}$$

$$CC = \frac{1}{3}(CC_{1,2} + CC_{1,3} + CC_{2,3}) \tag{4.3}$$

In Equation (4.2) $I_i(t)$ is the intensity of the response over time, $\bar{I}_i$ is the average intensity, σ_i is the standard deviation of the response, and the subscripts i and j denote the three different responses. The value of consistency correlation is calculated by averaging $CC_{i,j}$, as indicated in Equation (4.3). To calculate the consistency correlation we use signals with at least $13 \cdot 10^6$ points. Such a large amount of points benefits the statistical significance of the consistency correlation. From the m $CC_{i,j}$, a standard deviation of the response can be calculated as the consistency correlation error and deviation from the mean.

4.3.3 Memory task

Another important property of computational and nonlinear systems is their memory. Memory is the property of a system to retain previously injected information. This property is important when tasks require past information and it is not possible to inject multiple bits of information simultaneously. Examples of tasks benefiting from memory would be those where adequate classification of an input can only been done after a certain amount of significant information has been injected. Memory in a RNN originates from the recurrent network connections, allowing information to remain in the network for a finite time [259]. Past information therefore mixes with the current input. Nevertheless, memory needs to vanish after some time to allow responses to be affected only by the most recent inputs. This property is referred to as fading memory [259]. In our photonic RNN, optical delayed feedback introduces recurrences resulting in the ring topology [29, 130, 260]. As a consequence, the optical reservoir can possess fading memory. Increasing feedback attenuation η will reduce the relative strength of recurrent connections of our RNN, affecting its available memory.

To characterize the memory properties we use a method introduced in [259]. We inject a stream of 5000 pseudo-random numbers $y(k)$ uniformly distributed between 0 and 1 into the reservoir, at a rate of one value per delay time. We train the reservoir to retrieve the number $\bar{y}_i(k)$, which was introduced i time steps before. Then we calculate the correlation m_i between the original time trace and the reconstructed one as described in Equation (4.4). This is the so called linear memory. Memory correlation values were calculated for time steps $i = 0,1,2,...,19$, where $i = 0$ corresponds to recognize the input just injected. Value i was limited to 19 because the reservoir already showed memory correlations close to zero for those time steps. This correlation value measures how well the reservoir holds injected information for a certain amount of time. By using random numbers we ensure the numbers are uncorrelated. The memory capacity of a perfectly consistent system without any external memory would be 1 (where $m_0 = 1$ and $m_k = 0$ for $k > 0$). The data set was separated into batches of 80% for training and 20% for testing. We repeat the characterization of memory correlation using three different experimental realizations under the same conditions to provide an uncertainty to the memory correlation measurement. The error of m_i (δm_i) is the standard deviation of the three measurements, indicated by the second subindex $j = 1,2,3$ in Equation (4.5). We compute the sum of memory correlations to extract the system's memory capacity Memory Capacity (MC), corresponding to an accumulated measure of memory according to Equation (4.6). The uncertainty of the MC can be calculated from the uncertainty of the previously characterized memory correlations using Equation (4.7) [261].

$$m_i = corr(\bar{y}_i(k), y(k-i)) \tag{4.4}$$

$$\delta m_i = std(m_{i,1}, m_{i,2}, m_{i,3}) \tag{4.5}$$

$$MC = \sum_{i=0}^{19} m_i \tag{4.6}$$

$$\delta MC = \sqrt{\sum_{i=0}^{19} \delta m_i^2} \tag{4.7}$$

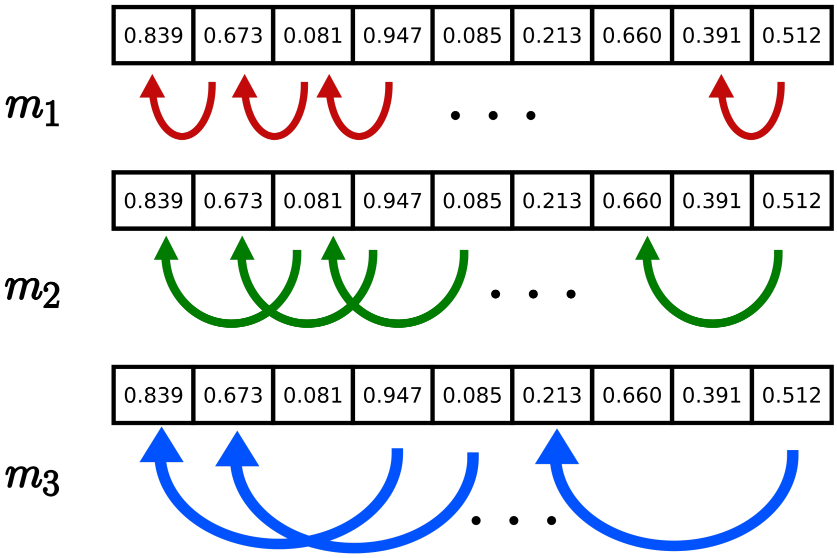

Figure 4.3: Diagram of the memory correlation concept. Different memory correlation values correspond to the extraction of the value injected a certain amount of time steps before from the response. Arrows illustrate from which value we extract which past value, and different colors indicate different number of time steps.

4.3.4 Prediction tasks

Particular tasks help to evaluate the computational capabilities of the reservoir computer. The ability of a reservoir computer to succeed on a task depends on the approximation and separation properties besides the already discussed consistency and memory properties (as we previously stated in Section 1.4.1). Instead of evaluating the approximation and separation properties individually (with methods introduced in [262], e.g.), one can directly evaluate the performance of the reservoir computer on a task. The performance on a task is not a measure of computing capability as general as a measure of the approximation and separation properties, but provides straightforward insights into the ability of the reservoir computer to process information on tasks of a certain nature. Examples of prediction tasks are forecast a portfolio's evolution in the stock market, weather forecast, navigation in a dynamical environment, or even words in a text.

Tasks can have different characteristics and goals. Time series prediction tasks (or more general nonlinear prediction tasks) belong to a class of tasks where the goal is to predict subsequent elements of a sequence. Together with classification tasks, prediction tasks are among the most common tasks in machine learning. The sequence presented to the reservoir for prediction tasks is often originating from a chaotic system. To succeed, the reservoir must reproduce the future dynamical evolution as closely as possible. This can be demanding due to the possibly complicated high dimensional structure of the chaotic attractor.

Time series prediction tasks are chosen because accurate prediction requires high consistency correlations and several memory steps. Consistency is a necessary property, and fading memory will in addition be relevant when information from the past is required to accurately infer future values. Also, high signal-to-noise ratio is beneficial for prediction tasks as noise can alter the inputs to an extent where the reservoir can not accurately predict [225, 263].

Prediction tasks involve time discretization of the evolution of the chaotic system, and feeding the reservoir one time step at a time. The prediction error is quantified by the Normalized Mean Square Error (NMSE), calculated via Equation (4.8), where $\bar{y}_k$ is the predicted time trace, y_k is the original trace, σ_y^2 is the variance of y_k, and N the length of the time trace.

$$NMSE = \frac{\sum\limits_{k=1}^{N} (\bar{y}_k - y_k)^2}{N \sigma_y^2} \tag{4.8}$$

To evaluate the ability of a system to predict future values of a chaotic time series, we use two different chaotic time series prediction tasks from machine learning as benchmark tasks. The benchmark tasks are the Santa Fe and the Mackey-Glass prediction task.

The Santa Fe prediction task involves prediction of the experimentally measured time evolution of a far infrared NH_3 (ammonia) laser exhibiting chaotic dynamics. This task was first introduced in the Complex Systems Summer School at the Santa Fe Institute [264], therefore its name. From this data set we use 4000 points, those we split them into batches of 80% for training and 20% for testing and apply 5-fold cross-validation. Figure 4.4(a) depicts a section of the data set. The time evolution of the amplitude is composed of quasi-periodic pulses of increasing amplitude. At some particular point in time, the pulse amplitude dramatically drops and then increases again. The reservoir needs to model not only the pulsating behavior, but also predict the sudden collapse of peak amplitude.

In the Mackey-Glass prediction task, the reservoir predicts future values of a time series originating from a Mackey-Glass delay equation (Equation (4.9)) with $\tau = 17$ (and usually $\alpha = 0.2$, $\beta = 10$, $\gamma = 0.1$), exhibiting rather low dimensional chaotic dynamics [265, 266]. We integrated the Mackey-Glass time series with an integration step of 0.1 (Figure 4.4(b)). The Mackey-Glass time series is then downsampled by a factor of 30 to obtain the discrete time series y_k that then was used in the prediction task. We choose the prediction horizon to be three time steps ahead. By selecting the prediction step we choose the memory requirements for the reservoir computer to solve the prediction task. A data set of 6500 values was partitioned into batches of 80% for training and 20% for testing and 5-fold cross-validation was applied. In Figure 4.4(b) we can observe a section of the data set. The evolution consists of large oscillations of varying amplitude with non-periodic features.

$$\frac{\mathrm{d}y(t)}{\mathrm{d}t} = \frac{\alpha\, y(t-\tau)}{1 + y^{\beta}(t-\tau)} - \gamma\, y(t) \tag{4.9}$$

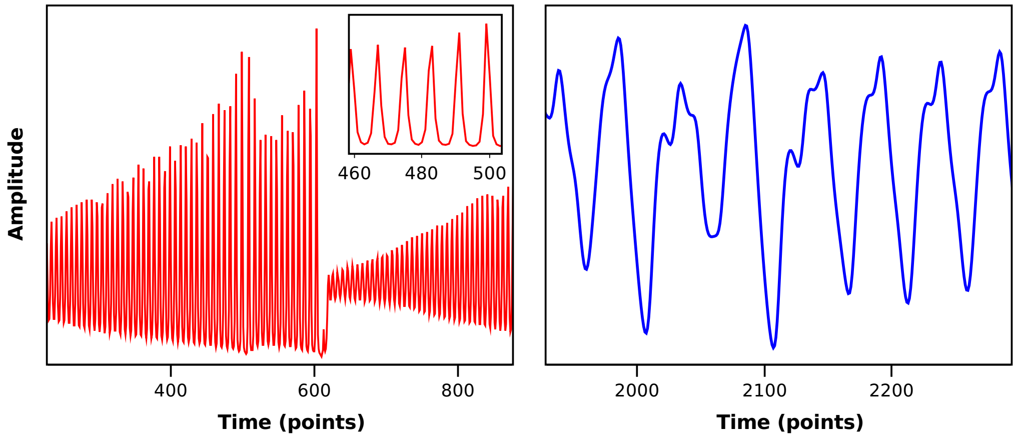

Figure 4.4: Examples of the chaotic systems employed as prediction targets. a) NH_3 laser dynamics of pulses with increasing amplitude and an amplitude collapse, with an inset to observe the individual pulses. b) Oscillations of the Mackey-Glass system.

4.4 Fundamental properties and dependence on feedback attenuation and frequency detuning

In Section 4.1 we introduced the photonic reservoir based on a semiconductor laser with delayed optical feedback and modulated optical injection. We explained its promising characteristics, and also the need and interest to study its potential further. In the following section we characterize in more detail fundamental properties of the before mentioned photonic reservoir, and investigate the parameter's influence. The considered fundamental properties are injection locking, consistency, memory properties, and performance on a prediction task. They are evaluated depending on two key parameters of the reservoir, the frequency detuning between the injection and reservoir laser and the feedback attenuation.

The frequency detuning is defined in this work as follows:

$$\Delta\nu = \nu_i - \nu_r \tag{4.10}$$

With ν_i being the optical frequency of the injection laser and (ν_r) the RL's solitary emission. We choose the spectral position of the RLs solitary emission as reference. As discussed in Section 4.2, the temperature of the injection laser was varied to control its emitted optical frequency (ν_i). While keeping the temperature and current of the RL constant, we control the frequency detuning via the temperature of the injection laser. By doing so, we keep the dynamics and properties of the reservoir unchanged while changing the frequency detuning. The frequency detuning was varied in the range of $[-60, +60]$ GHz.

The feedback attenuation relates to the amount of attenuation applied to the feedback optical power, corresponding to the ratio between the emitted power by the laser and coupled into the fiber and the optical feedback power fed back into the same device. Feedback strength is an important parameter since it is strongly related to the dynamical properties of the RL [41], and consequently to the properties of the reservoir. Therefore, feedback strength relates to the dynamics of the nodes in the time delay reservoir. The connection of feedback strength with recurrence in the network points to the idea that the feedback attenuation links to the memory properties of the reservoir. During the study in this section, other parameters were kept constant. The bias current of the RL was $I_r = 11.10$ mA. This value of current corresponds to 1% below solitary threshold of the RL. At this bias current and maximum feedback conditions, the RL exhibits chaotic dynamics. The average power injected into the delay loop was $\bar{P}_{inj} = 0.7$ mW, corresponding to 30 times the average power emitted by the RL.

4.4.1 Injection locking properties

The dynamics of a semiconductor laser, even under the presence of feedback, can be altered by optical injection of a CW or dynamical signal. In this section we focus on the influence of modulated optical injection on the reservoir system by studying highly resolved optical spectra.

In Figure 4.5(a) we depict the optical spectra of the RL with optical feedback (reservoir), without optical injection and for a bias current of $I_r = 11.10$ mA and $\eta = 0$ dB. For these conditions, the reservoir exhibits a broad spectrum characteristic of the chaotic dynamics induced by the non-attenuated delayed optical feedback. Moreover, we show the optical spectrum of the modulated signal we inject into the reservoir detuned by $\Delta\nu = -30$ GHz for comparison. The spectrum shows a central narrow peak corresponding to the injection laser emission and clear, almost symmetric side bands. These side bands are shifted by $\nu_{sb} = 5\,\text{GHz} = \theta^{-1}$ and are caused by the temporal modulation of the injection signal. The injected signal share bandwidth and modulation amplitude properties with the signals used to characterize the memory properties in the following sections.

With dynamical optical injection, the reservoir shows different optical spectra depending on the spectral detuning of the injected light. We classify the response spectra into three categories: fully locked, partially locked, and unlocked. Examples of spectra from those three categories are shown in Figure 4.5(b). Fully locked behavior corresponds to the case that all the RLs emission is concentrated within on frequency components of the injected field. In this case, injection dominates the emission behavior of the reservoir. This case corresponds to the light gray optical spectra in Figure 4.5(b). The unlocked cases correspond to the response spectra being almost unperturbed despite the optical injection. The unlocked example in the dark gray case shown in Figure 4.5(b) shows the spectrum of the RL almost unmodified by the injection along with spectrally separated components corresponding to the injection. These spectral components originate from the injected field being reflected at the RLs front facet and propagation of injection through the RL medium. Partial locking corresponds to an intermediate situation between the fully locked and unlocked situation. The optical spectrum exhibits frequency components from injection as well as from the free running delay laser dynamics. We show an example of such a spectrum in Figure 4.5(b), where one can observe frequency components from the RL under delayed optical feedback.

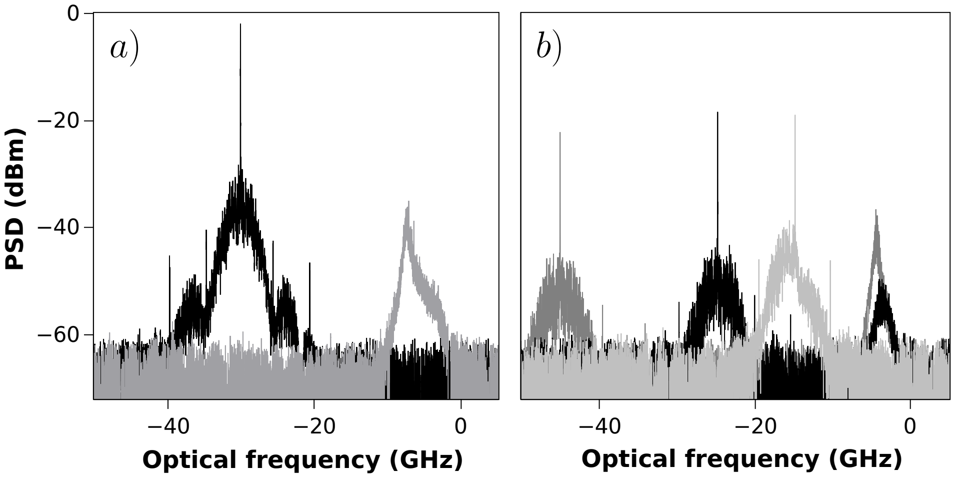

Figure 4.5: Optical spectra of optical injection, reservoir with and without optical injection. a) Optical spectra of the injected signal detuned by -30 GHz (black), and RL with $\eta = 0$ dB and no injection (gray).(b) Examples of RL spectra for different spectral detuning: full locking for $\Delta\nu = -15$ GHz (light gray), partial locking for $\Delta\nu = -25$ GHz (black), and unlocking for $\Delta\nu = -45$ GHz (dark gray).

In Figure 4.6 we specify the previously defined locking classes in the $(\Delta\nu, \eta)$ plane for $I_{bias} = 11.10$ mA and $\bar{P}_{inj} = 0.7$ mW. For $\eta > 12$ dB, the response spectra are fully locked in the range of the studied $\Delta\nu$ studied. For lower η we are able to observe all three classes. As the injection detuning is varied from $\Delta\nu = -60$ to 0 GHz, the system shows transitions from unlocked, partially locked, and finally to fully locked behavior. As injection detuning further increases from $\Delta\nu = 0$ to $+60$ GHz, the system shows transitions from fully locked, to partially locked, and then to unlocked behavior. Full locking is restricted to detunings $\Delta\nu$ between -25 and $+10$ GHz for $\eta = 0$ dB. Partial locking is observed between the full locking and the unlocking regimes on both positive and negative frequency detuning sides. We observe that the width of the full locking region depends on η. As the injection moves spectrally closer to the reservoir, the dynamical response of the reservoir will be more influenced by injection. Intermediate levels of influence can be achieved under partial locking. Upon comparing the partial locking region on the positive and negative detuning side one can find similarities as well as differences. The width of the partial locking region for both sides is different. The region of partial locking is broader for positive frequency detuning compared to negative detuning. Finally, the locking cone is not centered around $\Delta\nu = 0$ GHz, but around the maximum gain region of the RL with feedback.

The reservoir under partial locking exhibits a combination of optical frequencies from the free running delay laser dynamics and injection. Frequency components from free running dynamics will depend on the parameters of the system like the frequency detuning as feedback attenuation, as injection suppresses the frequency components closer to the injection components. In Figure 4.7, examples of optical spectra showing partial locking are depicted. In Figure 4.7(a) injection is negatively detuned and the reservoir exhibits additional spectral components on its higher frequency side. In contrasts, in Figure 4.7(b) injection is on positively detuned and the reservoir exhibits components on its lower frequency side.

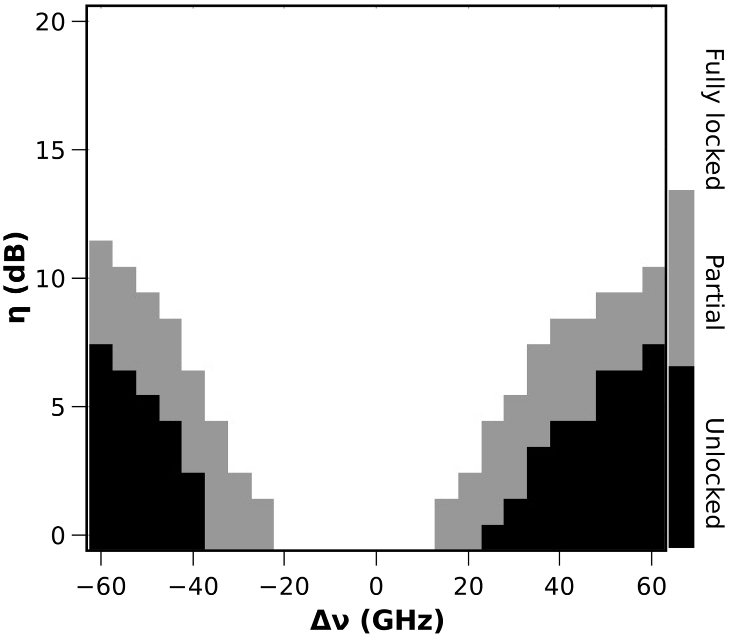

Figure 4.6: Locking categories in the $(\Delta\nu,\eta)$ plane for $I_{bias} = 11.10$ mA and $\bar{P}_{inj} = 0.7$ mW.

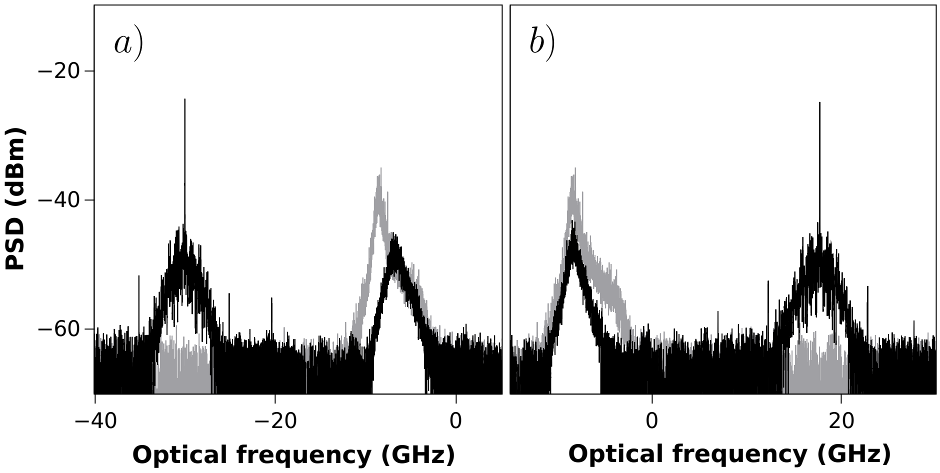

Figure 4.7: Optical spectra of the response system representing partial locking to injection with (a) $\Delta\nu = -30$ GHz (black) and (b) $\Delta\nu = +20$ GHz (black). The optical spectrum of the reservoir with no injection is shown on the background for comparison (gray).

4.4.2 Consistency properties

The next property being characterized is consistency. Basics of this property were discussed in Section 4.3.2, where also the tools used here are described in detail. In the following, the consistency of the response system is evaluated under modulated optical injection.

We first characterize the global consistency of the responses by calculating their consistency correlation for the same parameter region in which we previously evaluated injection locking properties. The results of the consistency correlation are shown in Figure 4.8. For maximum feedback, high consistency is found in a narrow range between $\Delta\nu = -20$ and $+15$ GHz, showing a consistency correlation between 0.899 and 0.948. For reference, the injected optical signal has an experimental cross-correlation of $CC = 0.994$. As feedback attenuation increases, the high consistency region broadens and reaches consistency correlation values up to $CC = 0.986$. Fixing frequency detuning, and increasing feedback attenuation therefore yields higher consistency. This underlines the destabilizing effect of feedback in the system. The consistency dependence on the parameters is found to be asymmetrical with respect to positive and negative frequency detuning. Results on the parameter dependence of consistency correlations in Figure 4.8 can be compared to the one of the locking conditions in Figure 4.6. We find that the region of high consistency coincides with the region of full locking. As the system undergoes the transition from full locking to unlocking due to parameter variation, the consistency correlation gradually reduces as soon as the system exhibits partial locking. The partial locking region shows moderate consistency correlation values, and consistency decreases further as locking is lost. Therefore, in our laser system the locking condition is closely linked to the global consistency of the responses.

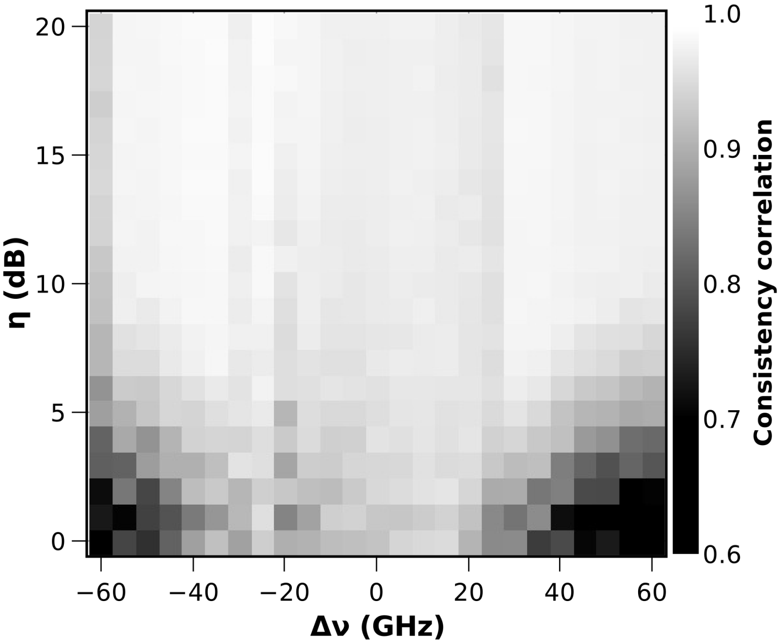

Figure 4.8: Consistency correlation dependence in the $(\Delta\nu, \eta)$ plane for $I_{bias} = 11.10$ mA and $\bar{P}_{inj} = 0.7$ mW. The highest standard deviation for the values in the figure is 0.011.

We can also characterize the local consistency of responses using the persistence plots. Persistence plots of response signals different conditions are shown in Figure 4.9. In Figure 4.9(a), the persistence plot of the injected signal is presented for comparison with the plots obtained from the RL's responses. One can observe that the injected signal is maintained homogeneous consistency over time. The other panels in Figure 4.9 are persistence plots of the response system from the same time window at different frequency detunings, while keeping $\eta = 0$ dB. At $\Delta\nu = 0$ GHz (Figure 4.9(b)) the RL shows a response with almost homogeneous local consistency over the time interval. Additionally, for these parameters we observe the presence of strong and consistent injection-induced fast frequency components in the responses. As the frequency detuning is reduced from $\Delta\nu = 0$ towards -60 GHz (Figure 4.9(c), (e), and (g)), the power variations of the responses decrease while local spreading of the persistence plots increases. These two effects combined cause a reduction of consistency correlation also observed in Figure 4.8 in the same parameter region. A more detailed analysis shows that the local consistency levels of the responses strongly depend on the frequency detuning. The time intervals for which the persistence plots show low consistency at $\Delta\nu = -20$ GHz are different from the ones at another detuning, e.g. $\Delta\nu = -35$ GHz. Similar phenomena are found for positive frequency detuning. As the frequency detuning increases, the responses lower in their power variations. Responses also exhibits regions with increasing spreading of the possible responses, but to a smaller degree compared to negative detuning. The decay of consistency as the system goes from full locking to unlocking extracted from global consistency measures can be observed also in the persistence plots. The existence of sections with different local consistency properties indicates changing local stability in phase space for different input segments. Comparing the evolution of the responses depending on frequency detuning, we also observe that for negative detuning the shape of the responses changes more than for positive detuning. All these differences in the persistence plots for varying parameters highlight the different nonlinear transformations performed by the reservoir, depending on operating conditions. Interestingly though, the responses appear quite similar is in the partial locking and unlocking state. In conclusion, local consistency in the persistence plots varies significantly in a non-trivial fashion, influenced by the present injection, the recent history of injection, and the feedback.

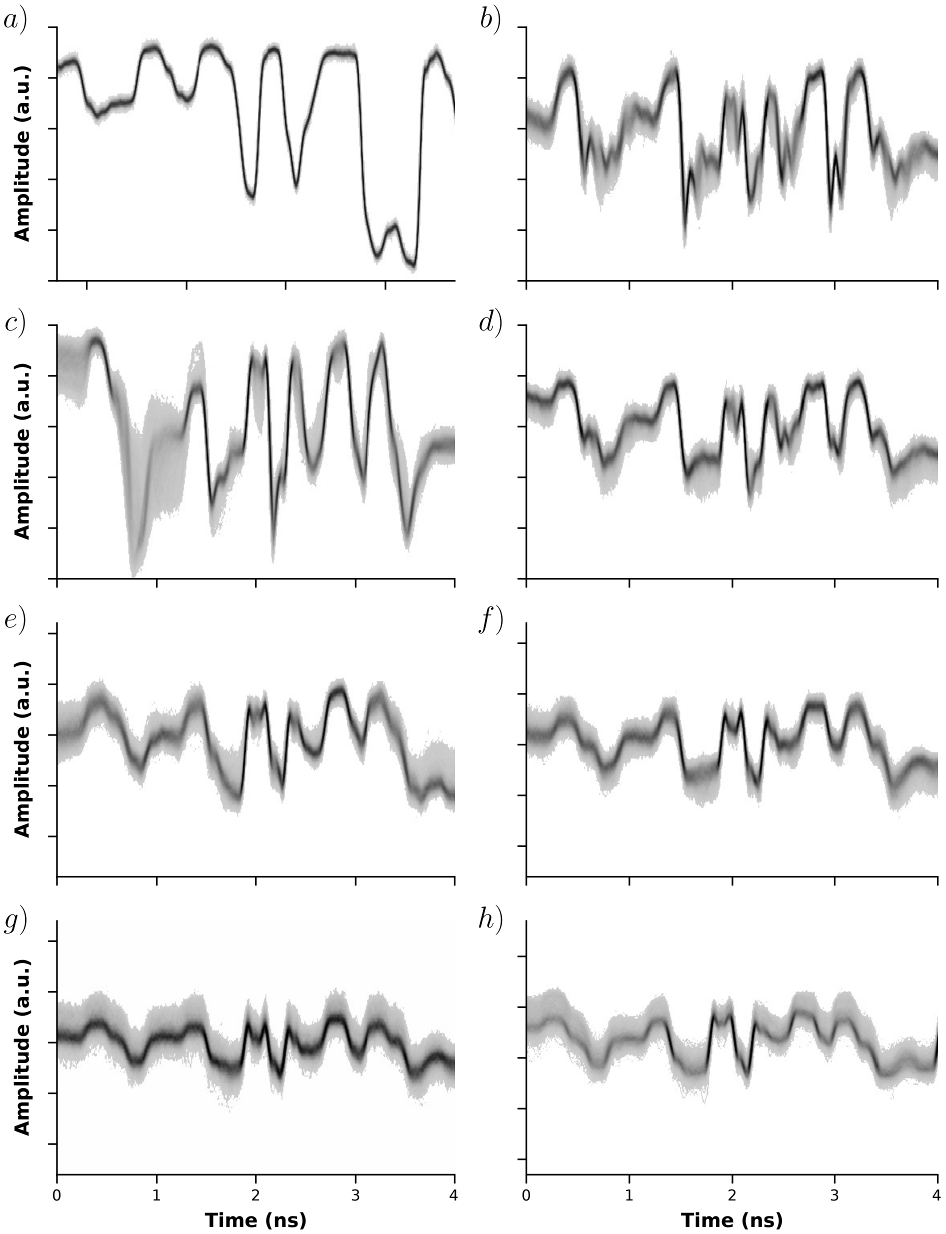

Figure 4.9: Persistence plots of the reservoir responses under modulated injection. The grayscale indicates likelihood of intensities for the response at a specific time, where black is high probability and white low probability. (a) Persistence plot of the injected signal. Persistence plots of the response system in the same time interval for $\eta = 0$ dB and $\Delta\nu$ equal to (b) 0 GHz, (c) -20 GHz, (d) $+10$ GHz, (e) -35 GHz, (f) $+20$ GHz, (g) -50 GHz, and (h) 40 GHz. Second, third, and last row are responses for parameters exhibiting full locking, partial locking, and unlocking, respectively.

4.4.3 Memory properties

Following the characterization of injection locking and consistency properties, we now characterize the memory properties of the reservoir. The method to assess the memory can be found in Section 4.3.3. To determine the memory properties we inject 5000 random numbers and apply 5-fold cross-validation (Section 4.3.1). We evaluate the memory properties of the system for the same parameter range as for the injection locking and consistency properties. First we will examine the dependence of memory correlations on $\Delta\nu$ at a fixed η. Then we will study the memory capacity dependence on both $\Delta\nu$ and η.

Figure 4.10 depicts how the memory correlation depends on the frequency detuning as we increase the memory time steps while feedback strength is at a maximum ($\eta = 0$ dB). For a frequency detuning of $\Delta\nu = -60$ GHz, memory correlation values are low as they fall below 0.2. As frequency detuning increases, memory correlation values increase as well and the memory horizon (highest time steps with a minimally relevant memory correlation value) extends further into the past. At $\Delta\nu = -35$ GHz of frequency detuning, memory correlations reach a maximum with values as high as 0.85 , and then collapse as frequency detuning crosses -30 GHz to a very short memory. This short memory remains for detunings up to $\Delta\nu = +15$ GHz. Then, memory correlation rapidly increases between $\Delta\nu = +15$ and $+20$ GHz, exhibiting correlation values as high as in the case of $\Delta\nu = -35$ GHz. Finally, memory correlation values reduce again as frequency detuning increases further. In a general perspective, the dependences of memory correlation show similar characteristics for positive and negative detuning. Both experience a sudden increase and later a decay when frequency detuning moves away from $\Delta\nu = 0$ GHz. Figure 4.10 illustrates that memory correlation values decay smoothly with increasing memory steps in the $\Delta\nu$ range of $[-60, -25]$ and $[+20, +60]$ GHz. This smooth prolonged decay of memory has previously been connected to noise in the reservoir [259]. The dependence of memory correlation with memory time steps also shows differences if the frequency detuning is positive or negative. The width of the two regions with high memory correlation values on both sides of $\Delta\nu = 0$ GHz is different, being slightly broader for positive frequencies. Upon careful observation, it can be noticed that for the cases of maximum memory correlations, $\Delta\nu = -35$ GHz and $\Delta\nu = +20$ GHz, memory correlation exhibits some has previously been. Memory correlations at $\Delta\nu = -35$ GHz show local maxima at time step $i = 3$ and $i = 9$, while in the case of $\Delta\nu = +20$ GHz the maxima are found at $i = 2$ and around $i = 7$. Our results show that memory fades and different memory lengths and profiles can be obtained by varying the frequency detuning. For frequency detuning in the region of $[-20, 15]$ GHz, we found memory correlation values decay abruptly. We observe a memory correlation close to 1 for time step $i = 1$. This shows a high memory for just the previous input. This one-step memory does not originate from the reservoir, though. After careful characterization, we can associate this memory to the AWG. Therefore, this one-step memory is not related to the reservoir dynamics.

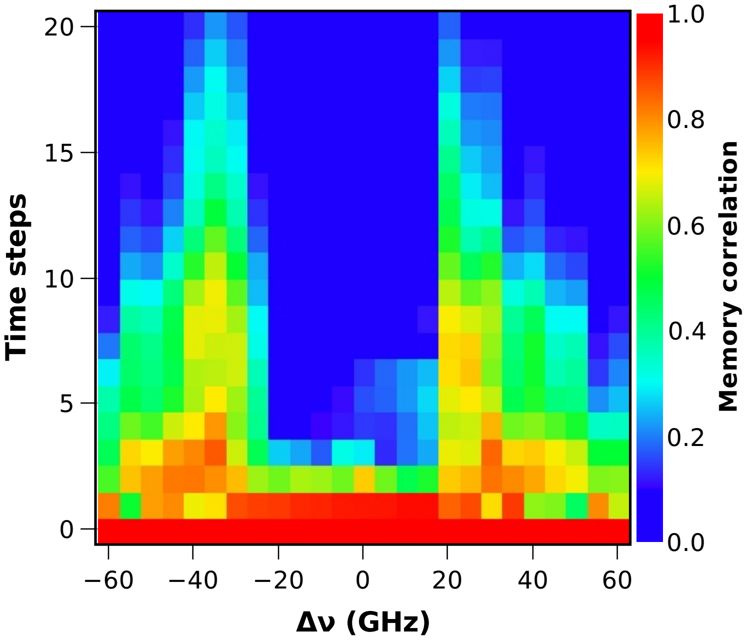

Figure 4.10: Memory correlation dependence on $\Delta\nu$ for increasing memory time steps from 0 to 19, using $\eta = 0$ dB.

After the memory correlation has been determined, it is possible to calculate the memory capacity as the sum of the memory correlation values. Having characterized the dependence of the memory correlation on the frequency detuning, we now extend the study to the dependence of the memory on feedback attenuation using the memory capacity measure (Equation (4.6)). The memory capacity for $I_r = 11.10$ mA and $\bar{P}_{inj} = 0.7$ mW is shown in Figure 4.11. The parameter range is the same as in the study of the locking and consistency properties. In the parameter space studied, the maximum MC are $MC = 11.47$ for $\Delta\nu = -35$ GHz and $\eta = 0$ dB, and $MC = 11.24$ for $\Delta\nu = +20$ GHz and $\eta = 1$ dB, respectively. The detunings correspond to the highest memory correlation cases shown in Figure 4.10. As η increases, the maximum MC for a specific η shifts to frequency detunings values further away from $\Delta\nu = 0$ GHz. In this parameter region, for $\eta > 10$ the reservoir provides only low memory. The highest uncertainty for memory capacity in Figure 4.11 is $\delta MC = 0.073$, and the highest relative uncertainty is $< 2\%$.

The results of the memory capacity in Figure 4.11 can now be compared to the previous results of injection locking properties in Figure 4.6 and of consistency properties in Figure 4.8. The region of highest memory capacity appears under partial injection locking conditions. In contrast, under full locking conditions the system exhibits low memory capacity. The level of memory capacity under full locking conditions is between $MC = 2$ and $MC = 3$. At these conditions, consistency is very high, though. At the transition from full locking to partial locking, high memory is found. After the system crosses the region of maximum memory capacity, memory capacity levels decay as $|\Delta\nu|$ increases. This occurs together with a decrease of consistency. While the system exhibits high memory capacity, consistency correlation is found to have between intermediate and high values.

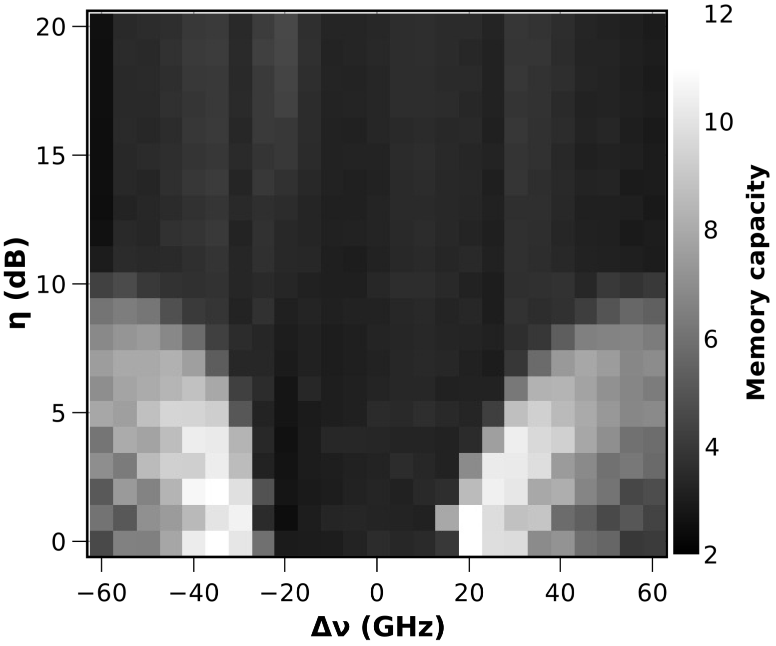

Figure 4.11: Memory capacity dependence in the $(\Delta\nu,\eta)$ plane for $I_{bias} = 11.10$ mA and $\bar{P}_{inj} = 0.7$ mW.

4.4.4 Mackey-Glass prediction performance

Now that we have characterized the fundamental the properties of the system, we evaluate its potential to perform a task sensitive to these properties. We choose here the Mackey-Glass prediction task. The basic characteristics of this task and how the performance is evaluated are described in Section 4.3.4.

In Figure 4.12 we show the results for out photonic reservoir to perform the Mackey-Glass prediction task. The performance of the reservoir is determined in the parameter space region as in the sections before. For comparison, a linear reservoir with the same number of nodes is used to do the same three steps ahead prediction on the original signal. This linear reservoir yields an $NMSE = 0.882$. The nonlinear photonic reservoir yields prediction errors as low as $NMSE = 0.048$ for $\Delta\nu = -35$ GHz and $\nu = 2$ dB. Low-error prediction is also found for positive frequency detuning, exhibiting $NMSE = 0.058$ for $\Delta\nu = +20$ GHz and $\nu = 0$ dB. In the direct vicinity of these parameters, the reservoir predicts with similar levels of performance. To understand the performance landscape, we get back to the fundamental properties. For that purpose we compare the results in Figure 4.12 with those in Figure 4.8 and Figure 4.11. One can observe that for the parameters at which the reservoir performs the task with the lowest prediction error, the reservoir exhibits a compromise of memory and consistency. Consistency or memory alone do not result in a satisfactory performance. Positions with similar prediction performance do not necessarily need to have exactly the same properties of memory and consistency. For example, for $\eta = 2$ and $\eta = 4$ dB at $\Delta\nu = -35$ GHz performance is similar, but one shows better memory and the other better consistency. At the positions in parameter space showing intermediate consistency and high memory capacity, corresponding to partial locking conditions, SNR was measured to be around 13 dB; while at positions close to $\Delta\nu = 0$ GHz exhibiting high consistency but low memory conditions, the SNR was 19 dB. For comparison, the SNR of the optically injected signal was 26 dB. The noise in the injected signal arise from the spontaneous emission of the injection laser and electrical noise in the instruments and components. Noise in the responses arises not only from the RL and the delay instabilities, but also from detection.

The relationship between properties and task performance underlines that both properties are required for prediction of nonlinear systems, and that a good compromise of them is more important than excellence in just one.

There are different ways to quantify the prediction performance. In

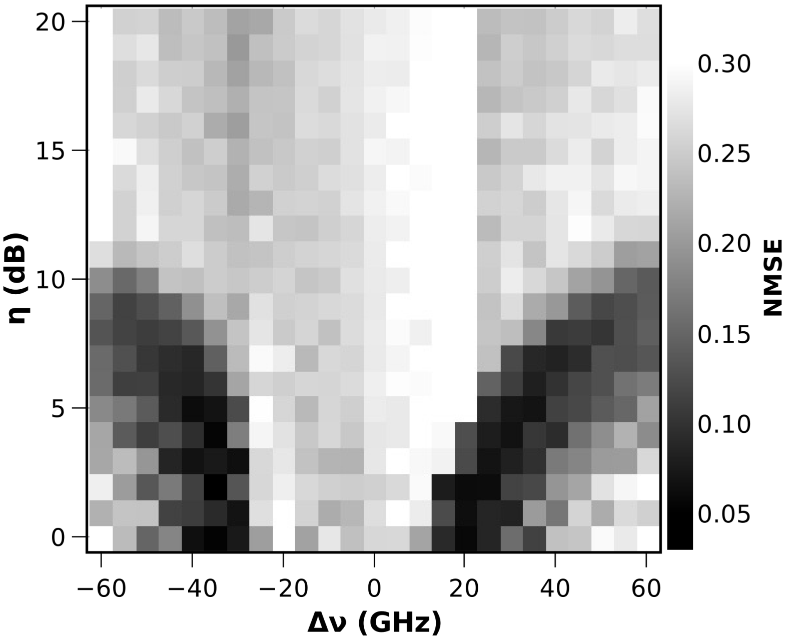

Figure 4.12: Normalized Mean Square Error (NMSE) of the Mackey-Glass prediction task. Dependence in the $(\Delta\nu, \eta)$ plane for $I_{bias} = 11.10$ mA and $\bar{P}_{inj} = 0.7$ mW.

this work we chose the NMSE as a measure of performance for the prediction tasks. The NMSE is well suited because it provides a global measure how similar the predicted values are to the real ones. Different reservoirs providing the same NMSE values for the task may generate predictions that capture different features of the targeted complex dynamical system. Furthermore, the NMSE value doesn't illustrate how the different features of the real system are learned by the reservoir. In Figure 4.13, examples of the predicted time traces for different cases are presented to illustrate how different NMSE values can relate to different reconstructed features. The prediction generated by a linear reservoir with no memory can be observed in Figure 4.13, with an associated NMSE of 0.882. The predicted values of the linear reservoir do not capture the dynamics of the Mackey-Glass system, not even the large periodic oscillations. The photonic reservoir, even at not optimized parameters, is able to capture the large amplitude oscillations of the Mackey-Glass evolution. Close to the extrema predicted time evolution shows significant deviations from the real one. Using optimized parameters the photonic reservoir provides the closest prediction to the real values. Therefore, we can see how the photonic reservoir improves its prediction by learning about general characteristics like the large amplitude oscillations and about smaller ones.

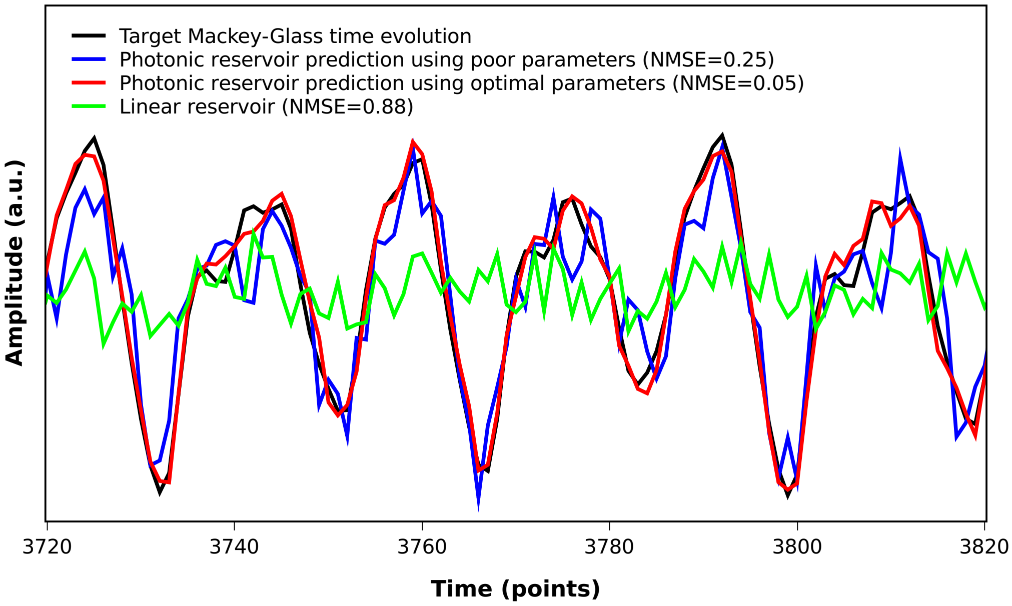

Figure 4.13: Examples of predicted time traces for different reservoirs and parameters. The time traces shown are the target Mackey-Glass values (black), the predicted evolution by the linear reservoir (green), and the predicted evolution by the photonic reservoir using non-optimized (blue) and optimized (red) parameters.

4.5 Dependence of properties and prediction error on response laser's bias and on average injected power

In the previous section we studied the impact of two key parameters, the frequency detuning and the feedback attenuation, on the fundamental properties of the reservoir and its performance in a prediction task. In this section, we characterize the impact of two other relevant parameters on the system: the bias current of the RL and the average power injected into the reservoir.

The bias current of the RL is an important parameter when studying the dynamics of a semiconductor laser with delayed feedback and/or optical injection. It determines the average power emitted by the device, with or without feedback and, moreover, to the bandwidth of the dynamics. For the solitary laser, the relaxation oscillation frequency increases as the bias current increases [7, 17]. Under sufficiently strong delayed optical feedback, the semiconductor laser exhibits an onset of instabilities as the bias current increases due to the interplay of the delayed optical feedback and the nonlinear properties of the gain medium [41, 220, 267]. These dynamical regimes comprises the Coherence Collapse and Low Frequency Fluctuations regimes. These are characterized by a reduction of coherence and fluctuations of the intensity, and exhibit a strong broadening of the laser's linewidth [221, 268].

As introduced in Section 1.4.1, reservoir computing using time delay reservoirs benefits from choosing the parameter θ comparable to the response time of the nonlinear system and a reservoir capable of exhibiting complex dynamics. Therefore, the role of the bias current is crucial for the reservoir computing properties.

The average power injected into the reservoir is an important parameter as well. How much power is injected into the semiconductor laser has proven relevant in the study of the dynamics of a semiconductor laser with and without feedback [64, 68, 75, 269, 270]. Additionally, we have previously observed that the capabilities of the reservoir depends on the locking conditions of the system for specific parameters. The injected optical power has a strong influence on these looking conditions [64, 271, 272].

For the results in this section, the feedback attenuation was kept constant at $\eta = 0$ dB. By minimizing the feedback attenuation we made sure that sufficient memory is available. The frequency detuning between the injection and the RL was chosen as $\Delta\nu = -20$ GHz. The amount of injected power was regulated with a variable attenuator of the same kind as used in the delay line to regulate the amount of optical feedback. The average injected power without attenuation was $\bar{P}_{inj} = 1.4$ mW.

Figure 4.14 depicts the results of evaluating the dependence of the reservoir properties on the amount of average injected power and the bias current. Figure 4.14(a) shows the locking conditions. All three categories (full locking, partial locking, and unlocked) are again observed again, and partial locking continues to appear between the region of full locking and unlocked behavior. For low values of I_r, a small injected power is sufficient to fully lock the system. As the bias current increases, the injection power required to lock the system increases. Figure 4.14(b) shows the consistency correlation. The responses show large correlations for high injected power, with consistency correlation values as high as $CC = 0.97$. As the bias current increases, the consistency decreases. The consistency correlation shows a similar dependence to the locking conditions. The parameter dependence of the memory capacity is shown in Figure 4.14(c). Significant memory is found again in a narrow region, with a maximum found of $MC = 9.8$ for $I_r = 11.00$ mA and attenuation of $\nu = 12$ dB ($\bar{P}_{inj} \simeq 90\,\mu$W), which is close to the MC observed previously. The region of high memory falls again within the region of partial locking conditions. Interestingly, not all regions of parameter space representing partial locking conditions offer the same memory properties. One can observe that there is an optimal value of bias current and average injected power to obtain the highest memory. For lower bias current, the maximum attainable memory reduces even if injected power is adjusted. For higher bias currents I_r, memory reduces also but at a slower rate. Under full locking conditions the system exhibits the same MC between two and four that we observed previously for full locking conditions in the $(\Delta\nu, \eta)$ parameter plane. For unlocked conditions, memory capacity values fall below two and reach almost zero, indicating a complete lack of memory. Nevertheless, in the small region close to $I_r = 11.00$ mA and attenuation around $\eta = 12$ dB we observe few points exhibiting intermediate level of memory. Finally, the performance for the Mackey-Glass prediction task is depicted in Figure 4.14(d). The region of lowest prediction error is found in the parameter region between high memory capacity and high consistency, benefiting from both properties. The lowest NMSE found is 0.064 for $I_r = 11.20$ mA and attenuation injection of $\eta = 9$ dB ($\bar{P}_{inj} = 175\mu$W). This value for I_r is right below solitary threshold. Other positions like $I_r = 10.80$ mA and attenuation on injection of 11 dB ($\bar{P}_{inj} = 110\mu$W) exhibit similar NMSE values of 0.067, proving that good performance is not constrained to a narrow parameter range. Away from this region, performance degrades as memory lowers or consistency deteriorates. We observe that optimized operation can also be obtained with low injection powers. Moreover, the injected power can be varied to access optimized properties in case that changing frequency detuning is not possible. The dependence on many parameters increases the difficulty of finding optimized operation conditions, but it also broadens the range of available options and increases the flexibility of the system.

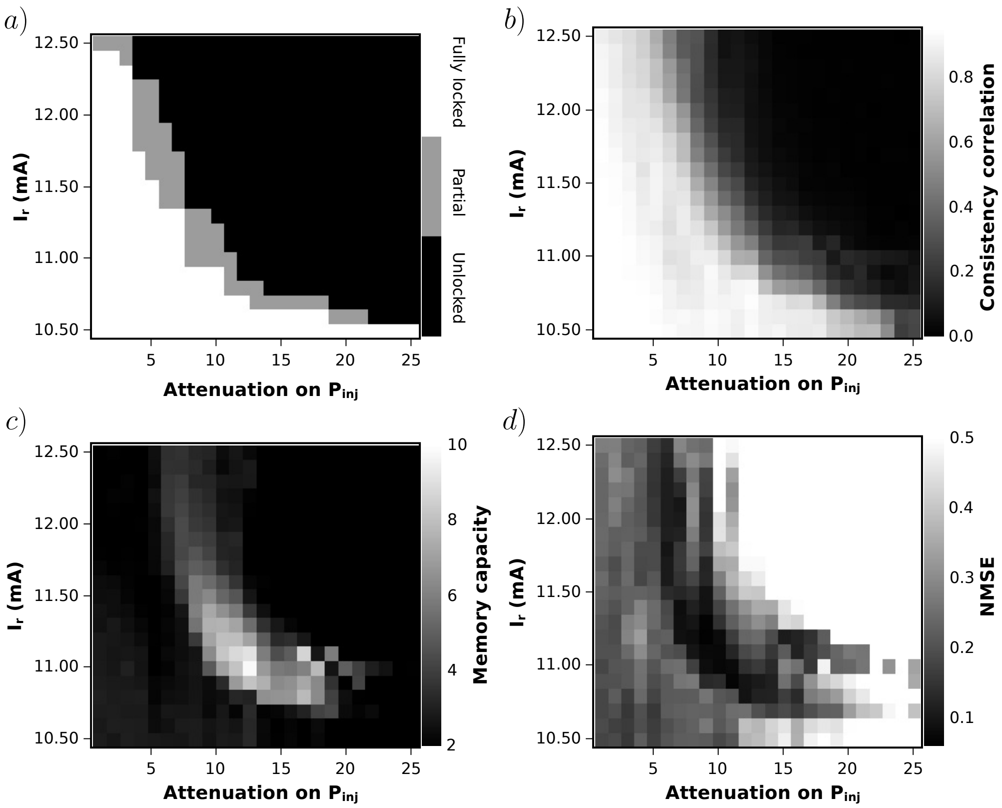

Figure 4.14: Dependence of the fundamental properties and task performance of the system on I_r and $\bar{P}_{inj}$ for $\Delta\nu = -20$ GHz and $\eta = 0dB$. (a) Injection locking conditions, (b) consistency correlation, (c) memory capacity, and (d) prediction performance.

4.5.1 Assessing optimized bias current and injection power

In the following we evaluate the impact of I_r and $\bar{P}_{inj}$, for a different detuning of $\Delta\nu = -30$ GHz. In Figure 4.15 the results of locking conditions, consistency, memory, and prediction performance are shown. We restricted our investigation to the range of injected power corresponding to an attenuation of less than 15 dB. Figure 4.15(a) shows the injection locking properties. The behavior observed here has similarities with Figure 4.14(a). However, the partial locking regions are displaced to higher values of average power injected. Therefore, the full locking region is smaller in this case compared with to the case of $\Delta\nu = -20$ GHz. As before, for unlocked conditions consistency is very low, while for full locked conditions consistency is high. In Figure 4.15(c) we can see that the region of high memory capacity is similar to the one shown in Figure 4.14(c), achieving similar values of high memory capacity. The highest memory capacity is $MC = 10.15$ for $I_r = 11.10$ mA and $\eta = 4$ dB of injection attenuation ($\bar{P}_{inj} \simeq 560\ \mu$W), 8 dB less than for $\Delta\nu = -20$ GHz. In both cases, the maximum memory capacity values are very similar and are observed for similar currents I_r. When $\Delta\nu = -30$ GHz, the required injection attenuation to obtain similar locking conditions is lower (and therefore the amount of required injected power required is higher). The results for prediction performance are shown in Figure 4.15(d). By comparing the results for $\Delta\nu = -20$ GHz and -30 GHz, we make similar observations as we did for the memory. The region in parameter space for similar performance is shifted towards lower attenuation values of the injected power, while the optimized bias current range is comparable. The lowest error attained is $NMSE = 0.064$ for $I_r = 10.90$ mA and an attenuation of $\eta = 11$ dB. The NMSE is identical to the one for $\Delta\nu = -20$ GHz. From these results we can observe that high memory and good performance in the prediction task can be obtained even at larger frequency detuning. Most strikingly, the range of bias currents of high memory capacity and low prediction errors remains the same when the frequency detuning is changed. This uncouples injection and reservoir parameter limitations, and one parameter can be compensated with the other, so that the range of possible parameters is higher.

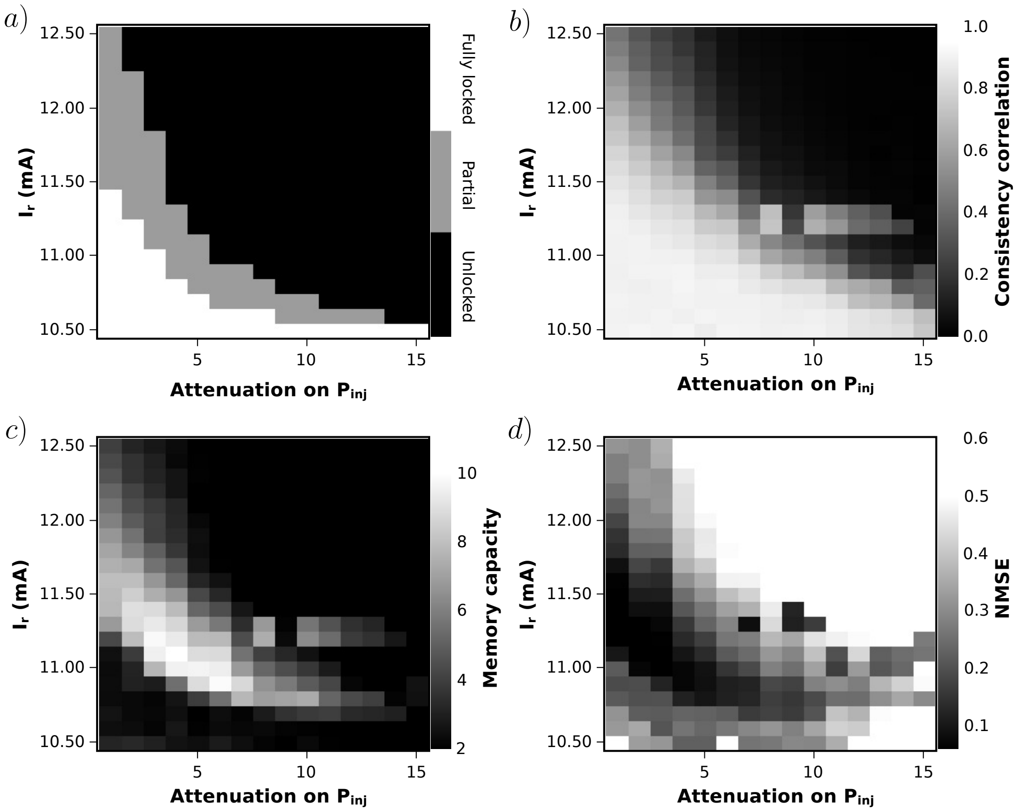

Figure 4.15: Dependence of the fundamental properties and the task performance of the system on I_r and $\bar{P}_{inj}$ for $\Delta\nu = -30$ GHz and $\eta = 0dB$. (a) Injection locking conditions, (b) consistency correlation, (c) memory capacity, and (d) prediction performance.

4.6 Properties and opportunities of side-mode injection

In the previous sections we inspected the role of frequency detuning determining the properties and performance of the system at hand. By changing the frequency detuning alone, the system exhibits different sets of properties suitable to perform specific tasks. The frequency detuning range studied so far was $[-60, +60]$ GHz. We chose this range as it covered the typical range of emission of the semiconductor laser under optical feedback. But the emission of semiconductor lasers is not restricted to that range. The combination of medium gain and resonator defines the lasing wavelength under solitary conditions. The laser resonator provides the possibility of emitting principally at evenly spaced wavelengths. Those modes are the so-called Longitudinal Modes (LMs). Among all the longitudinal modes, the mode that will emit under solitary conditions will typically be the one with the highest gain. The mode separation in our RL is 1.15 nm, which at 1.54 μm is equivalent to 148 GHz. Optical feedback and injection, however, alter the gain and losses. At frequencies at which injection is performed, losses are reduced. When full frequency locking is achieved, the mode enhanced by injection can be viewed as having less losses or higher gain than without injection. By performing optical injection at high frequency detuning, the gain difference to the main mode can be (over-)compensated and another mode can show laser emission. Locking the RL to an optical injection that is possibly detuned by hundreds of GHz from the one emitting under solitary conditions is possible. Achieving injection locking to another LM of the RL provides several interesting benefits. The possibility to lock to other LM softens the emission-wavelength restriction of the chosen semiconductor. Currently, the decision of which lasers to employ is mostly based on its possibility to emit at identical optical frequencies. This option may not always be available with the resources at hand, and may imply special requirements on the design of photonic reservoir computers like the one studied here. Side-mode injection expands the options and combinations of devices even further. Other benefits might lie in the performance properties of the system. The possibility of locking to frequencies further away from the solitary emission properties might improve the SNR or treatment of signals in the spectral domain by easily incorporating frequency filters. Another benefit would be to use the possibility of locking to other LM for Wavelength Division Multiplexing (WDM). For WDM, multiple optical carrier signals are injected into the system. By tuning parameters of the RL, selective locking to an individual carrier could be achieved even under injection of multiple optical signals. Additionally, if the spacing of the different injected signals is around the LM spacing and some degree of locking is achieved, the reservoir could perform computation employing the information from the different injected signals simultaneously. While one should be aware of possible crosstalk due the multiple injected channels being detrimental, this configuration could even benefit from providing different properties for the different signals.

In this section we study the possibility of injection locking to a neighboring LM (side-mode injection locking) and perform reservoir computing. Obtaining side-mode injection locking requires injecting at frequency detuning of at least $\Delta\nu = 150$ GHz to the free-running RL. This can be achieved by tuning the temperature and the bias current of the injection laser. To ensure similar injection conditions to before, the average injected power was adjusted with the variable optical attenuator in the injection branch. The possibility of reservoir computing at neighboring LM was studied using parameter $\eta = 0$ dB, $\bar{P}_{inj} = 0.7$ mW, and $I_r = 11.10$ mA. The properties and performance of the reservoir under side-mode injection are shown in Figure 4.16. Each point is the average of three different measurements. Each point includes error bars corresponding to the standard deviation obtained from the three measurements. The results for the previously studied range of $[-60, +60]$ GHz are shown for comparison along with the new results. In Figure 4.16(a) we can observe the locking properties and consistency correlation dependence on frequency detuning beyond the previously studied range. The vertical solid lines mark the spectral positions of the different LM. We refer to the original LM as $LM0$, to the side-mode at smaller frequencies as $LM-1$, and to the side-mode at higher frequencies as $LM+1$. The vertical dashed lines in the figure delimit the regions with different locking properties. We can observe in Figure 4.16(a) that full locking is achieved around the different LM in a range of frequencies with slightly narrower width for $LM-1$ and $LM+1$. For all the three modes, the full locking regions of $LM+1$ and $LM-1$ are displaced towards lower optical frequencies as in $LM+0$, and are surrounded by regions of partial locking. Further away from the LM, unlocking is observed in all cases. The consistency properties of the responses by locking to the different LM show similar levels and dependencies on frequency detuning than for main mode injection. In Figure 4.16(b) the memory properties of the reservoir are shown depending on the detuning. The memory capacity curves for the different LM are superimposed for comparison. Labeled as relative frequency detuning, the x-axis corresponds to the frequency detuning from the closest LM. The memory dependence on the relative frequency detuning is similar in the three cases. Under full locking the system exhibits low memory, under partial locking memory capacity is high. Finally memory lowers smoothly as the system undergoes the transition towards unlocking. The highest memory capacity is similar in all three, reaching values of $MC = 11.8$. Figure 4.16(c) show the performance of the reservoir for the Mackey-Glass prediction task. As the consistency and memory, also the performance for this task is very similar in the different cases. We observe similar minima of NMSE, with values down to $NMSE = 0.037$, and the overall dependence on frequency is similar.

The results in Figure 4.16 show that the properties of the reservoir behave similarly when injection aims at neighboring LM. The reservoir achieves similar levels of high consistency, memory, and prediction performance when optically injecting at different LM, with minimal differences. The reservoir shows successful capability to operate and offer similar performance with optical injection into neighboring LM.

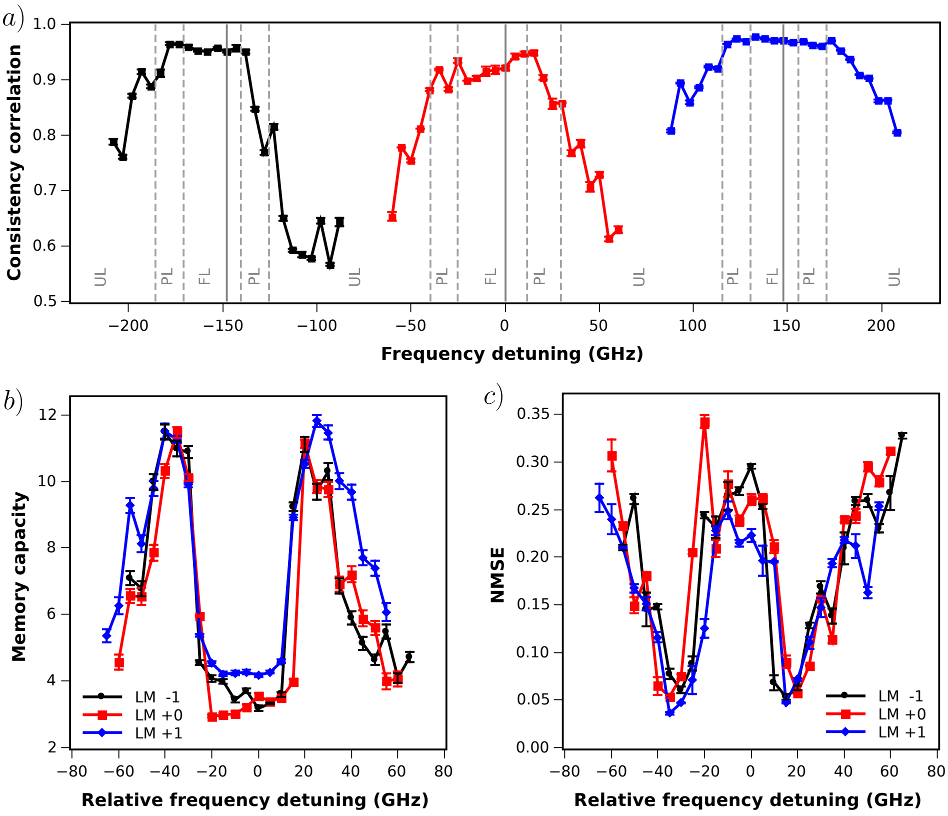

Figure 4.16: Properties of the reservoir computer depending on frequency detuning for optical signal injection around different longitudinal modes for $\eta = 0$ dB, $\bar{P}_{inj} = 0.7$ mW, and $I_r = 11.10$ mA. Each curve corresponds to injection around a different LM. (a) Consistency correlation and locking regions, delimited by dashed lines and labels FL (full locking), PL (partial locking), UL (unlocking). (b) Memory capacity results. (c) Performance on the Mackey-Glass prediction task. The lines between points are guides to the eyes.

4.7 Impact of noise

In Section 4.3.2 we stated the importance of consistency for the reservoir as a fundamental property of dynamical systems and a crucial one for computation. The different levels of consistency in previous sections have been attributed to the system's dynamics with a local sensitivity to the dynamical state. In experimental realizations, inconsistencies can also be induced by noise. In our experiment, noise arises from diverse sources, components and instruments. In the detection part the SOA, the photoreceiver, and the oscilloscope, for example, add noise to the signal extracted from the reservoir. Detection noise is typically additive noise. The injected signal has already slight differences due to the noise in the AWG, the electric amplifier, and the limited coherence of the injection laser. Noise can influence the dynamics of semiconductor lasers, and even suppress it [79, 80, 89, 243, 273, 274]. Noise in the temperature and current control of the laser adds intensity, spectral, and phase noise to the laser emission. We have seen how the responses change with parameters using persistence plots as illustrated in Figure 4.9. A drift in parameters and noise will change the responses and, therefore, result in degradation of performance in classification or prediction tasks.

Noise will set an upper bound to the achievable consistency of the responses, but also to the memory capacity and maximum performance attainable by the system. Understanding the system at hand involves understanding the limits imposed not only by the dynamics, but also by the intrinsic limitations of the components and instrumentation; and to evaluate to what degree noise will be detrimental. In reservoir computing, the reservoir's responses can have relatively small amplitudes, and noise can hide these feature. In such cases, noise will be strongly detrimental.

To observe the impact of noise, we characterize the system when recording multiple responses. For that purpose we choose $\Delta\nu = -35$ GHz, $\eta = 0$ dB, $\bar{P}_{inj} = 0.7$ mW, and $I_r = 11.10$ mA. These parameters offered the highest memory capacity and lowest error in Figure 4.11 and in Section 4.4.3, respectively. We used up to 100 responses for averaging.

In Figure 4.17 the results of averaging are shown with their corresponding standard deviations as error bars. In Figure 4.17(a) we show the impact of averaging an increasing number of time traces on the consistency and on the memory properties. The consistency correlation measurement starts at 0.94 and increases smoothly approaching 0.99 as we average from 1 response (no averaging) to 100 responses. The memory also increases as the response is averaged. In this case, memory capacity is the sum of memory correlations up to 50 time steps, and not to 20 as previously selected. This change is due to the fact that as we average responses, memory correlations increase also for larger time steps. Initial memory capacity (without averaging) is $MC = 12$, and if we limit the time steps range considered to 20 we recover the previous value of 11.4

(Figure 4.11). As more responses are used for the average, the memory capacity level increases up to 19 for 100 responses averaged. This difference corresponds to almost 60% increase of memory capacity. In Figure 4.17(b) we can observe the impact of averaging on the performance of the Mackey-Glass prediction task. For no averaging we recover the NMSE of 0.045 obtained in Figure 4.12. By averaging the response three times, the error already drops almost by a factor of five. And for averaging 100 time series, the error decreases more than one order of magnitude to $NMSE = 0.03$. This illustrates the deteriorating effect of noise in this system.

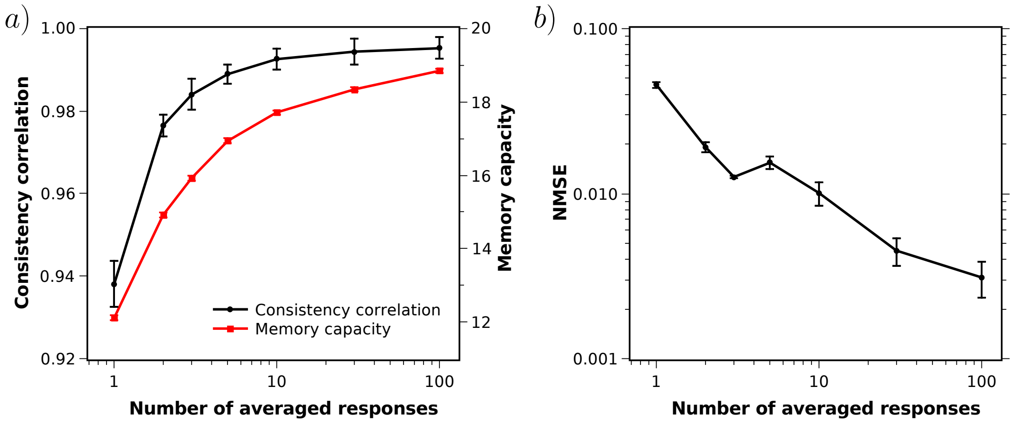

Figure 4.17: Capabilities of the reservoir computer using averaged responses for parameters $\Delta\nu = -35$ GHz, $\eta = 0$ dB, $\bar{P}_{inj} = 0.7$ mW, and $I_r = 11.10$ mA. (a) Consistency (black curve) and memory (red/gray curve) properties. (b) Semi-log plot of performance for the Mackey-Glass prediction task. The lines between points are guides for the eyes.

4.8 Performance at injection rates from 5GSa/s to 20GSa/s

In the introduction we stated a strong interest of employing semiconductor lasers as information processing devices thanks to the ultra-fast dynamics. The bandwidth of the dynamics of the semiconductor laser with feedback is of the order of GHz. This bandwidth motivated previous studies and in the present work to inject information with a mask modulated at 5 GSamples/s. Using this modulation speed results in an inter-node time interval of $\theta = 200$ ps. This time interval has proved experimentally to be adequate for the virtual nodes to exhibit nonlinear responses and provide connectivity among nodes [29]. Selecting the appropriate θ is crucial. Under optical injection the dynamical bandwidth can rise close to 100 GHz [73]. This enhancement motivates the idea that virtual nodes can provide responses on faster time scales under adequate conditions. This implies injection could be modulated at faster rates to take advantage of these even faster dynamics. Increasing the modulation rate could be useful in multiple ways. One could obtain the same number of virtual nodes in shorter time intervals, speeding up the processing time. Another option could be to increase the number of virtual nodes in a time delay reservoir while keeping the delay time, and therefore the computing time fixed.

In previous sections the modulation rate was 5 GSa/s. Now we evaluate using 10 and 20 GSa/s. Faster modulation rates are inaccessible due to technical limitations of the AWG. The use of higher modulation rates implies some differences on the conditions of the experiment that need to be kept in mind. One difference is related to the number of virtual nodes in the reservoir. We left the delay time in the experimental setup unchanged to keep the setup and conditions unchanged. This means that the number of virtual nodes in the reservoir is higher than in previous sections. Increasing the modulation rate increases the maximum number of virtual nodes by the same factor as long as the delay time is kept unchanged. For 5 GSa/s and a delay time of 66.0 ns , we had 330 virtual nodes in the reservoir. Increasing the modulation rate to 10 GSa/s and 20 GSa/s increases the number of virtual nodes to 660 and 1320, respectively. A second consideration is that sampling rate of the detection remained at 40 GSa/s. Increasing the modulation rate of the injection but keeping the sampling rate of the detection reduces the number of samples acquired for every node. The reduction of samples per node reduces the averaging effect of the detected signal, and therefore can deteriorate performance.

First, we evaluate the dependence of the performance on the frequency detuning of the injection and the feedback attenuation. Other key parameters were chosen at $\bar{P}_{inj} = 0.7$ mW and $I_r = 11.10$ mA. The range covered for frequency detuning was $\Delta\nu = [-60, +60]$ GHz, and for feedback attenuation $\eta = [0, +20]$ dB. We use all virtual nodes of the reservoir to perform the evaluation. Essentially, we replicate the conditions of the study in Section 4.4 with faster modulation rates. In Figure 4.18 the properties of the reservoir are shown when modulation rates are 10 and 20 GSa/s. In Figure 4.18(a) and (b) we depict the locking properties. The system exhibits the same kind of locking properties as observed before, i.e. full locking, partial locking, and unlocking. Remarkably, these locking regions appear for the same parameter range for the three cases of modulation rate. In Figure 4.18(c) and (d) the consistency of the responses show again similar dependencies in the $(\Delta\nu, \eta)$ plane. The consistency levels and their dependence on parameters are, moreover, very similar to the ones observed for the case of 5 GSa/s in Section 4.4. For strong feedback attenuation, responses are highly consistent for any frequency detuning. Consistency decreases smoothly for low feedback attenuation as frequency detuning moves further from $\Delta\nu = 0$ GHz. The data shows that for fast modulation, up to 20 GSa/s at least, the system is capable of responding consistently to modulated optical injection. Figure 4.18(e) and (f) shows the memory capacity of the system. Memory at 10 and 20 GSa/s appear to reach levels as high as in the case of 5 GSa/s, reaching $MC = 11.5$, at similar parameter values. High memory is found once again for partial locking and intermediate consistency conditions. For full locking conditions memory is low, as in the case of unlocking, especially when $|\Delta\nu|$ is high. In the last row of Figure 4.18 the performance of the reservoir for the Mackey-Glass prediction task is shown. The error reaches NMSE values as low as 0.047. The dependence of performance on parameters, memory, and consistency conditions is very similar to the one observed in Section 4.4. Successful prediction is observed where there are sufficiently high levels of both consistency and memory.

These results point out that for faster modulation rates the system exhibits properties and prediction performance almost identical to the once found for slower modulation rates. Furthermore, we maintain a similar parameter tolerance for optimized operation.

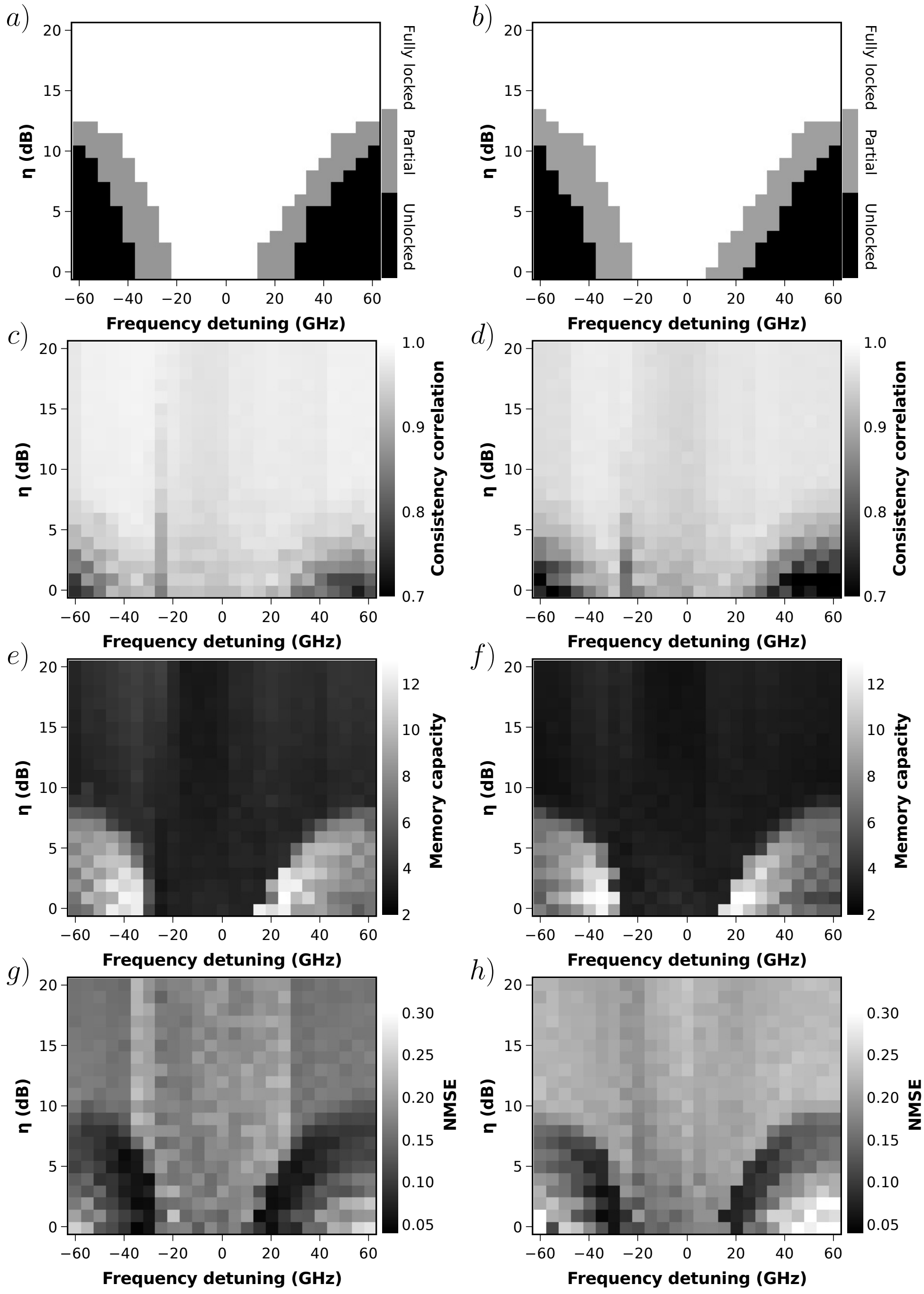

Figure 4.18: Properties and performance of the reservoir computer at faster modulation rates for $\bar{P}_{inj} = 0.7$ mW and and $I_r = 11.10$ mA. Rows are (a)(b) locking properties, (c)(d) consistency correlation, (e)(f) memory capacity, and (g)(h) prediction performance for the Mackey-Glass task for input sampling with 10 and 20 GSa/s, respectively.

Upon increasing the modulation rate, θ reduces and consequently the time intervals for the responses. The choice of the time interval θ and the dynamical bandwidth are closely connected. If θ is too small, slower dynamics will not significantly contribute to the responses. In contrast, too fast dynamics may induce transients that are damped too fast and are not captured upon detecting the response of the nodes. Therefore, computational performance can be sensitive to the interplay of the chosen interval θ and the dynamical bandwidth of the system. In semiconductor lasers, the relaxation oscillations strongly influence the overall dynamical bandwidth of the system. The frequency of the relaxation oscillations increases with the bias current on the laser. When the semiconductor laser is experiences delayed optical feedback, the bandwidth of the dynamics also increases with the bias current. Additionally, the optimal bias current for higher input modulation rates may differ from the one for slower rates. We therefore evaluate the performance of the reservoir for the Mackey-Glass task in the $\left(I_r, \bar{P}_{inj}\right)$ parameter plane. The results of this characterization are shown in Figure 4.19, and were obtained using $\Delta\nu = -20$ GHz and $\eta = 0$ dB. The obtained NMSE appears as low as 0.062 in this case for both modulation rates. The performance dependence on the bias current and average injected power is similar to the one as previously presented. Optimal performance appears in the range of bias currents between solitary and feedback threshold ($[10.50, 11.30]$ mA) and around 10 dB of attenuation on average injected power. By comparing Figure 4.19 with Figure 4.14, the region of optimal parameters is the same for the three modulation rates employed.

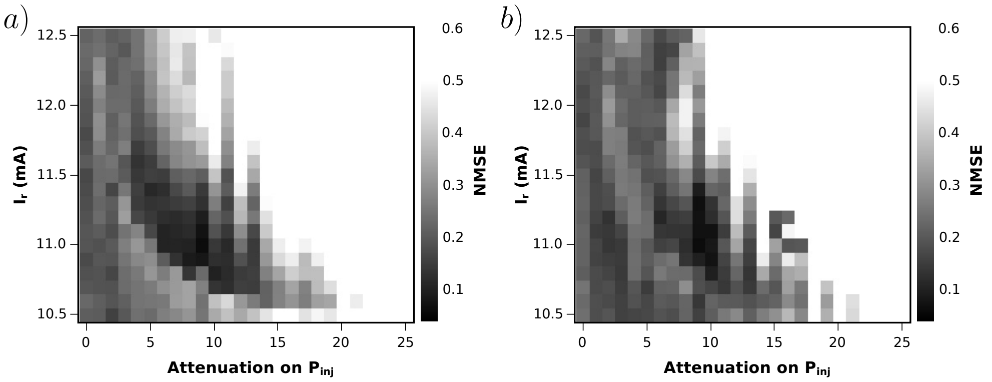

Figure 4.19: Prediction performance of the reservoir computer for higher modulation rates using $\Delta\nu = -20$ GHz and $\eta = 0$ dB. Used modulation rates were (a) 10 GSa/s and (b) 20 GSa/s.

4.9 Emulating multiple heterogeneous reservoirs

In this chapter, the reservoir employed in the experiments was so far composed of virtual nodes that all had the same properties. Such a reservoir is homogeneous for fixed parameters. But reservoirs could be constructed with nodes with different properties. In such a case, the reservoir becomes heterogeneous. A heterogeneous reservoir could benefit from the differentiation of the nodes to improve performance and robustness [275, 276]. This section aims to explore experimentally the possibility and the potential of employing heterogeneous reservoirs.

As we have seen in previous sections, the properties of nodes can be linked to the parameters of the system. By temporally modulating parameters in the experiment with a period equal to the delay time, a heterogeneous reservoir can be obtained. We choose to modulate the bias current of the RL to create our heterogeneous reservoir. This decision was motivated by several reasons. The modulation bandwidth needs to be of the order of GHz, with a period precisely set to the delay time. This can be achieved using the second channel of the AWG. Most important, the system needs to react sufficiently fast to the parameter modulation. This excludes modulation of slow parameters like device temperature. Also, the modulation amplitude needs to provide a sufficient change in parameter to access different properties. Modulating bias current complies with all the requirements, making it a suitable parameter to modulate for the heterogeneous reservoir. Modulating the average injected power could also be possible via a MZM, but it would reduce the amplitude of the modulated signal and that would decrease the SNR. A square signal with a 50% duty cycle was used for the modulation, as shown in Figure 4.20, but other duty cycles could be employed as well. The modulated current, I_{RF}, will result in two different parameters of the reservoir alternating in time, as they were independently studied in Section 4.5. The square signal creates two level of currents for the nodes, and the 50% duty cycle value separates the nodes in two equally large sets. The amplitude of the signal will determine the distance of the points visited in parameter space. We chose a modulation depth corresponding to $\sim 3\%$ of the threshold current. This allows half the reservoir to exhibit high memory and the other half to exhibit high consistency correlation for the appropriate set of remaining parameters. Experimentally, the modulation signal is injected via the RF connector on a Bias tee via which the laser drive is injected.. The laser is additionally DC biased via the DC connection on the T-bias. The DC current provides an average bias current, $\bar{I}_r$, around which the RL will be modulated. Therefore, the RL will not be actually biased at the average current $\bar{I}_r$, but alternating between $\bar{I}_r + I_{RF}$ and $\bar{I}_r - I_{RF}$.

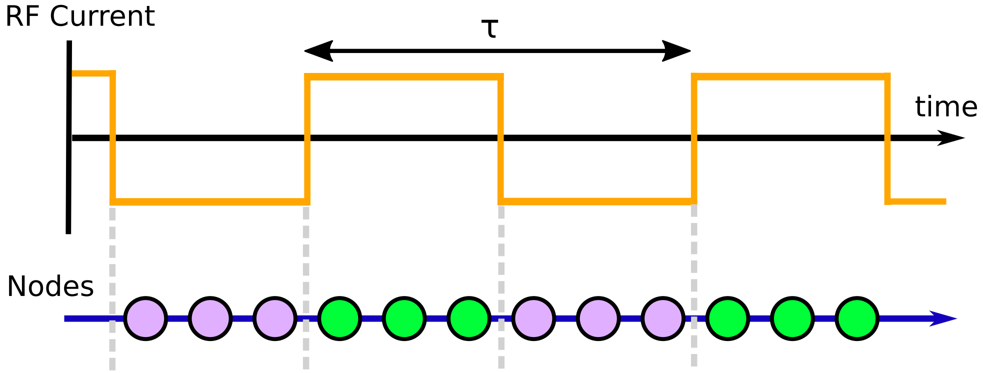

Figure 4.20: Diagram of the creation of a heterogeneous time delay reservoir by modulation of the current of the RL. The high and low levels of the I_{RF} define the two different set of nodes in the reservoir. Virtual nodes with different properties are represented in different colors.

In Figure 4.21 we show an example of the time evolution of the reservoir responses while additionally biased with the alternating current. The DC bias current $\bar{I}_r$ was chosen to be the feedback threshold $I_{th,fb}$, while $I_{RF} = \sim 3\%\, I_{th,fb}$. The temporal evolution of the reservoir response shows alternating temporal windows of width equal to half delay time caused by the modulated current. In one interval the responses exhibit larger power variations and in the other exhibits smaller power variations, caused by the RL being biased above or below $I_{th,fb}$, respectively.

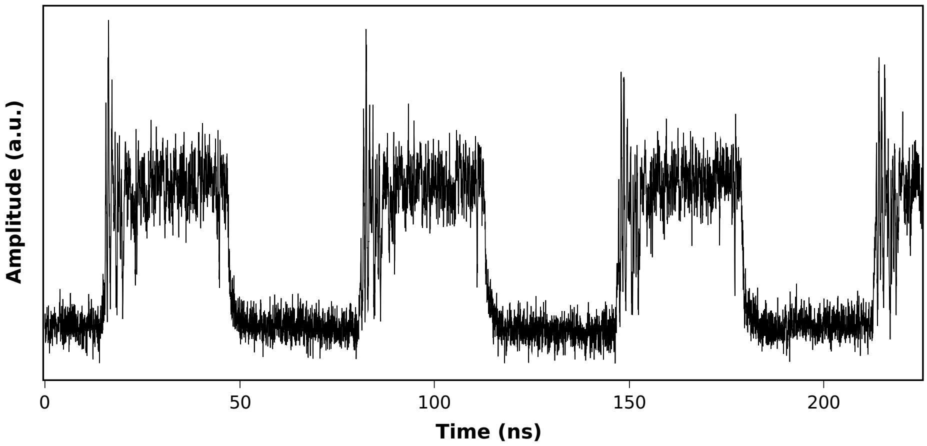

Figure 4.21: Experimental temporal evolution of the output power from the heterogeneous reservoir without optical injection. Recorded while the RL is modulated with an additional alternating $\bar{I}_r = I_{th,fb}$ and $I_{RF} = \sim 3\%\, I_{th,fb}$.

4.9.1 Memory properties

To evaluate the possibilities arising from the heterogeneous reservoir, we characterize its memory properties. In Figure 4.22, memory correlation values are shown for different values of frequency detuning and $\bar{I}_r$ of the RL. From previous results we know feedback attenuation needs to be minimum to guarantee high memory in a parameter region, so in this section we keep $\eta = 0$ dB. Additionally, we keep $\bar{P}_{inj} = 0.7$ mW. Since memory capacity showed similar levels for positive and negative detuning, we focus here just for negative detunings. The memory correlations for the heterogeneous reservoir show a similar dependence on frequency detuning as previously observed for a homogeneous reservoir for $I_r = 0.99\, I_{th}$ mA. Memory correlations are typically low for detuning close to 0 GHz, then abruptly increase for a certain detuning. Finally, they smoothly decrease as frequency detuning is chosen further away from 0 GHz. The position of abrupt memory increase depends on the bias current. From the different panels in the figure we find that memory correlation is similar to the case of the homogeneous reservoir in the studied range of average bias currents (Figure 4.14). The memory correlation vanish as average bias current increases limiting the range of bias currents exhibiting memory. Also, we can observe that the values of memory correlation attained are lower than in the case of a homogeneous reservoir. This was not expected since only half the reservoir is optimized for high memory. Nevertheless, these results show that even though the heterogeneous reservoir exhibits less memory than the homogeneous reservoir, significant memory correlations can be obtained in a considerable parameter range.

4.9.2 Prediction performance

To characterize the prediction performance, in the following we use the Santa Fe prediction task. The obtained results for the prediction error are shown in Figure 4.23. The performance of the reservoir is characterized depending on frequency detuning and average bias current of the RL. The corresponding results are depicted in Figure 4.23(a) and Figure 4.23(b) respectively. The panels show the performance of the heterogeneous reservoir and of the homogeneous reservoir for corresponding parameters. The average power injected into the reservoir was $\bar{P}_{inj} = 0.7$ mW and feedback attenuation was $\eta = 0$ dB. Figure 4.23(a) shows the error prediction depending on frequency detuning for both kinds of reservoirs, for a DC bias current of $I = 1.00\, I_{th}$. In both cases we can observe that for $\Delta\nu$ close to 0 GHz the error is larger than 0.24, which corresponds to the linear reservoir performance for this task, indicating bad performance. The low memory in this parameter range most probably causes this low performance. The error reduces reaching a minimum of $NMSE = 0.137$ when the frequency detuning is reduced to -35 GHz, to smoothly increase to $NMSE = 0.25$ as $\Delta\nu$ is reduced further. This behavior is observed both, for the homogeneous and the heterogeneous reservoir. Crucially, the minimum error attained for the heterogeneous reservoir is lower than for the homogeneous reservoir, and the frequency detuning for obtaining the minimum error is changed. Moreover, the range in which the heterogeneous reservoir outperforms the homogeneous reservoir is considerably wider. In Figure 4.23(b), the frequency detuning was set to $\Delta\nu = -35$ GHz. For DC bias current much lower

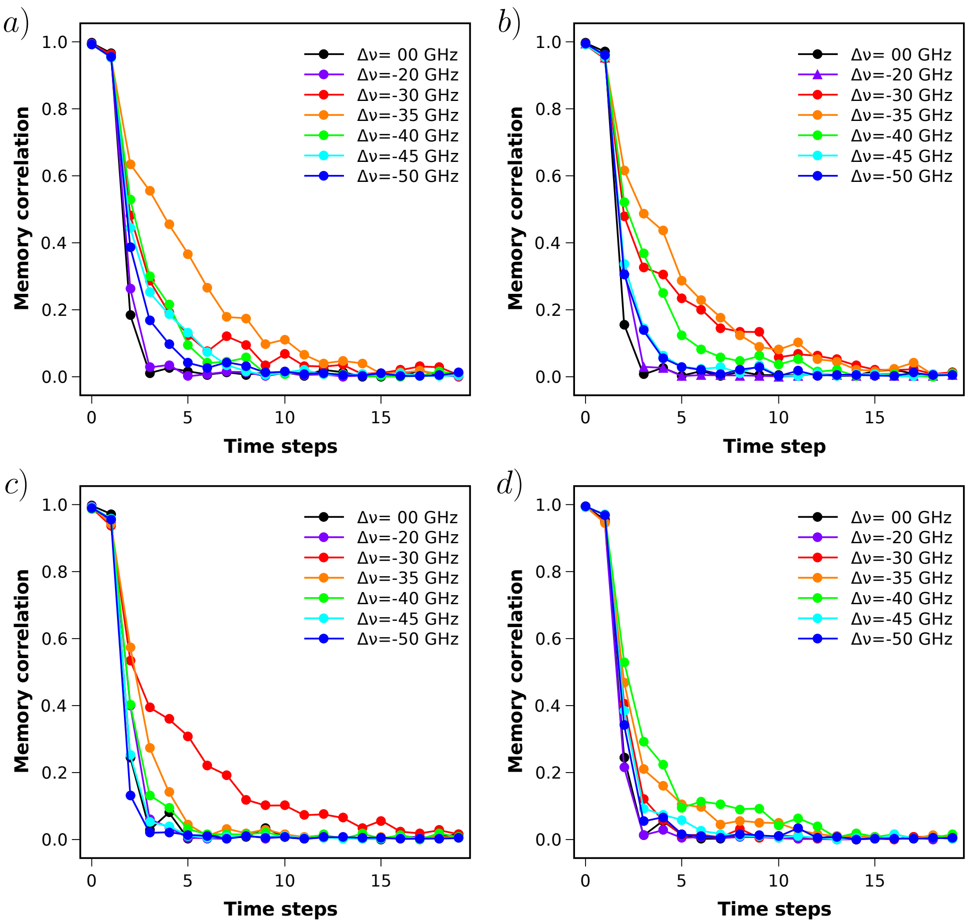

Figure 4.22: Memory correlation curves of the heterogeneous reservoir for detunings $\Delta\nu$ in the range of $[-50, 0]$ GHz for different $\bar{I}_r$. I_{RF} was kept $\sim 3\%\, I_{th,fb}$. The DC bias current was chosen as (a) $1.000\, I_{th,fb}$, (b) $1.015\, I_{th,fb}$, (c) $1.030\, I_{th,fb}$, and (d) $1.065\, I_{th,fb}$.

than threshold the obtained prediction errors are high, and as the DC bias current increases, the error exhibits a minimum at $NMSE = 0.139$. Increasing the DC bias current further, the prediction errors increase and exceed 0.24. The dependence of the prediction errors on the DC bias current is similar for the heterogeneous and the homogeneous reservoir. Therefore, from the results in Figure 4.23 one can conclude that the heterogeneous reservoir offers possible improvements compared to the homogeneous reservoir, as the heterogeneous reservoir can exhibit better performance and larger parameter tolerances.

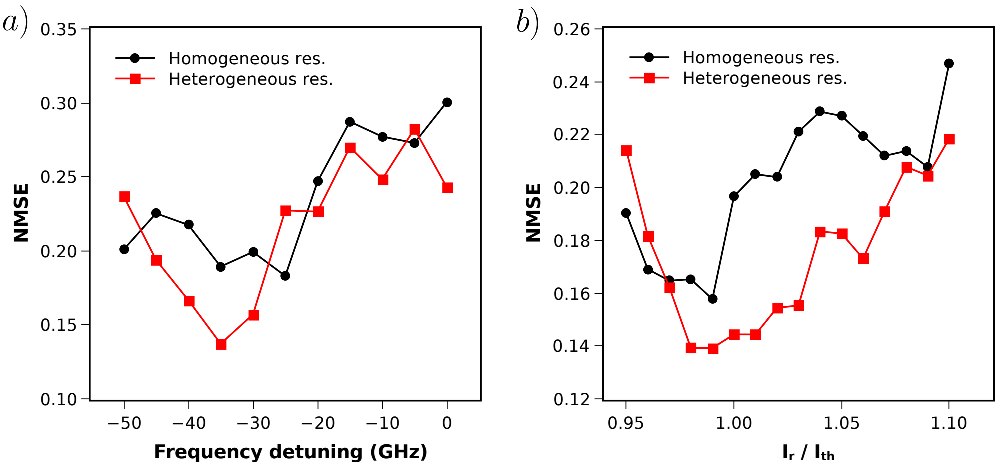

Figure 4.23: Prediction performance for the Santa Fe prediction task comparing the homogeneous and the heterogeneous reservoir. Prediction performance depending on (a) frequency detuning and on (b) $\bar{I}_r$. For panel (a) $\bar{P}_{inj} = 0.7$ mW, $\eta = 0$ dB, and $\bar{I}_r = 1.00\, I_{th}$. For panel (b) $\bar{P}_{inj} = 0.7$ mW, $\eta = 0$ dB, and $\Delta\nu = -35$ GHz.

4.10 Discussion and summary of the results

In this chapter, we presented the properties of a semiconductor laser with delayed optical feedback and optical injection as a delay-based reservoir computer. The experimental investigations focused on studying the fundamental properties of the reservoir and its computational performance. In particular, we concentrated on injection locking of the RL, consistency of the responses to modulated injection, memory properties, and the performance in chaotic signal prediction.

In Section 4.4, the fundamental properties and the performance of the system as a reservoir computer were discussed. From the optical spectra we identified three different categories: full locking, partial locking, and unlocking. The partial locking case was found for parameters between the full locking and unlocking cases, and turned out to be crucial for the system. For positive frequency detuning, partial locking occurred in a broader frequency range than for negative frequency detuning. This asymmetric dependence of locking conditions for positive or negative $\Delta\nu$ strongly resembles the asymmetry found in injection locking cones in semiconductor lasers under optical injection. The asymmetry in the locking cone originates from the gain dependence and dispersive properties on carrier density in the RL [271, 277]. We observed that the locking behavior under modulated injection shows a collection of features that are shared with the locking behavior of unidirectional coupled semiconductor lasers undergoing CW injection locking [240, 278].

After the locking properties, we characterized consistency using consistency correlation as a global, and persistence plots as a local measure. These characterizations showed that the system can provide highly consistent responses to modulated injection, proving optical injection as an efficient way to inject information into the reservoir. We found a relation between the consistency properties and the locking conditions, where the most consistent responses were observed under full locking conditions. Persistence plots showed that modulated injection can generate complex responses, that in some cases even exhibits higher frequencies components. Persistence plots also showed that the consistency of the signal can differ in different points of the response. We consider that the shape of the modulated injection and feedback affects the consistency of the responses at precise times. Understanding what conditions trigger local inconsistency could help design masks or modulation formats that could provide responses with higher consistency.

The characterization of memory properties showed that the system exhibits its largest memory capacity under partial locking conditions and strong optical feedback, with memory capacity reaching $MC = 11.5$. High memory capacity was not found when injection was strongest, but when injection and feedback balanced each other. Under partial locking, feedback can sufficiently contribute to the dynamics and impact the responses. The lower locking stability of the system under partial locking (as compared with full locking) makes its responses more susceptible to noise. Therefore, reducing the noise contributions in the responses could increase the memory of the system.

The consistency and memory properties showed a strong link to the optical spectra of the system. Based on the optical spectra alone one can infer the positions of required consistency and memory levels. This is interesting as with this knowledge, one does not always need to determine memory or consistency, but observing the changes in the optical spectra might be sufficient.

Regarding the prediction performance, we observed low error rates, reaching $NMSE = 0.048$, occurring under a combination of adequate consistency and memory properties. Interestingly, good information processing capabilities were observed for negative and positive frequency detuning (even though a semiconductor laser under CW optical injection exhibits unstable dynamics for the positive side), making both parameter regions equally suitable for operation.

In Section 4.5 we investigated the influence of the average injected power and the bias current of the RL on the properties of he system. A region of partial locking can be found by tuning either the injected power or the bias current. By repeating the experiment at a different frequency detuning we showed that the range of optimal bias currents was independent of the frequency detuning and average injected power. When either frequency detuning or average injected power changes, regions of similar performance could be reached again by tuning the other parameter. Interestingly, this shows that frequency detuning and average injected power can to a certain degree compensate for each other. Our results show that the optimized range of bias current is from $I_r = 10.80$ to 11.50 mA, corresponding to $I_r = 0.96$ and 1.02 I_{th}, respectively. It was shown that semiconductor lasers with optical feedback operated in that range of bias currents experience weak chaotic dynamics [89, 245]. In such a dynamical state, the chaotic properties of the system create the high dimensional space necessary for reservoir computing, while the repetition of the chaotic signal through consecutive delay times provides conditions to facilitate consistency and memory.

In Section 4.6 we explored the possibility of side-mode injection into the RL. We found that the longitudinal modes next to the one emitting under solitary conditions (named here $LM \pm 1$ and $LM + 0$ respectively) can be fully locked as well to the optical injected signal. Moreover, the same locking conditions and similar levels of consistency, memory, and prediction performance were found when the injection was into neighboring longitudinal modes. More specifically, by injecting into the neighbor longitudinal modes, the system showed memory capacity up to $MC = 11.8$ and prediction errors down to $NMSE = 0.037$. For these investigations the frequency detuning was changed up to ±220 GHz. This implies that it is not required to work with small detuning only. Interestingly, our findings open the door to more sophisticated setups operating simultaneously with multiple wavelengths, e. g., for WDM technology. Injection with multiple equally spaced wavelengths, but with a spacing different from the longitudinal mode spacing of the RL, could provide for a technique to select which signal to process with the reservoir (with caution of crosstalk among channels inside the reservoir). An injection wavelength spacing matching the one of the longitudinal modes of the RL could create a reservoir that processes simultaneously multiple input signals. The limits of this approach could be related to the gain medium and resonator of the semiconductor laser. We expect the gain spectrum at the position of the different longitudinal modes to determine the locking possibilities at other mode besides the one originally emitting. In the present work, the optical frequency range providing full locking was almost the same for injection at $LM + 0$ and $LM \pm 1$. This seeds the idea that injection can be possible at even further optical frequencies without even having to increase the average injected power, facilitating the process of employing multiple wavelengths for injection.

In Section 4.8, the possibility of performing information processing with faster modulation rates was studied. Results showed that the system is capable of generating useful responses and successfully perform reservoir computing at modulation rates up to at least 20 GSa/s. This demonstrates the large dynamical bandwidth of the system. Memory capacity was found to be as high as $MC = 11.5$, and prediction errors as low as $NMSE = 0.047$. The maintained performance as modulation rate was scaled up is a sign of undiscovered potential and motivates further studies on such photonic reservoirs for ultra-fast information processing applications.

Section 4.9 presented the results on employing a heterogeneous reservoir, realized simply by feeding a square signal to the RL. By doing so, the reservoir turned into an ensemble of nonlinear nodes with different properties. The heterogeneous reservoir presented lower memory than the homogeneous reservoir, but prediction performance was better for the heterogeneous reservoir due to the combination of virtual nodes with different sets of properties applying different transformations. The heterogeneous reservoir showed minimum prediction error of $NMSE = 0.137$ for the Santa Fe prediction task. Additionally, lower errors were found in a broader parameter range when using the heterogeneous reservoir, giving evidence for higher parameter tolerance. Using multiple reservoirs seems therefore promising for improved performance. It is necessary to point out that the present study using an heterogeneous reservoir explored a limited range of parameters. The results using the heterogeneous reservoir do not guarantee that the heterogeneous reservoir always performs better than the homogeneous reservoir, but they point towards an interesting direction. Additional improvement might be obtained by using even more sets of heterogeneous nodes in the same or a different configuration, as presented in [276]. The approach followed in this work proved to be promising and simple for the current experimental system, and further approaches to design heterogeneous reservoirs are possible.

In this chapter, we have studied the fundamental properties of a delayed optical feedback semiconductor laser based reservoir computer, its properties, performance, and how the system could be expanded for more complex architectures. The connection of information processing capabilities with the properties of the dynamics of the system highlights the importance to study fundamental properties as well as performance in specific tasks. Such detailed understanding of the system is necessary to gain key insights and connect the physical processes with abstract computational features. Most importantly, the obtained knowledge can become the building blocks for further research on machine learning implementations based on semiconductor lasers. The experimental implementation based on a time delay reservoir is conceptually extremely simple, efficient in its requirements for components, and provides excellent performance. Nevertheless, more complex systems and architectures are extremely interesting to investigate. In the present research we investigated one of those possibilities: the heterogeneous reservoir. Also, one could add additional optical delays to the RL, which could provide several possibilities [279]. One is to provide additional memory for specific time steps ranges. Or one could consider the longer delay as the main delay, so the shorter one would provide an extra connectivity mechanism to the virtual nodes inside the network. Another is to take advantage of the nonlinear dynamics we studied in Chapter 3 for information processing purposes. In one way or the other, it is clear that the simplicity to expand this experimental setup to more complicated configurations with potentially higher performance, just by applying simple means, highlights the singular potential and remarkable versatility of semiconductor lasers with delayed optical feedback.

Chapter 5

Towards spatially extended photonic reservoir computers

5.1 Introduction

In Section 1.4.1 we introduced RC as an unconventional information processing technique. This technique takes advantage of nonlinear dynamics to process information using a high dimensional state-space. Additionally, we discussed the importance and interest for a hardware implementation of a reservoir computer, and in particular, the interest of a photonic information processing device. We studied in Chapter 4 a reservoir computer implementation with photonic hardware. In that case we made use of the TDR concept to create a reservoir by using a single nonlinear element. This chapter takes steps towards the creation of an optical reservoir computer where the reservoir is extended in space. In this approach, the individual nodes of the reservoir are different physical elements. Spatially distributed optical neural networks are a well known idea [156, 169] . Interest in the idea grew fast due to the potential parallelism for vector matrix operations that defines the neural network evolution, as well as due to the high connectivity that could be achieved with optical system [280, 281]. Individual nodes could update their states independently, creating parallel processing channels. In electronic hardware implementations, connectivity is a recurrent problem as devices are designed on a flat subtract which creates physical connections with paths that can not cross, strongly limiting connectivity in the network. Optical based connectivity can provide higher connectivity since light beams can cross without interacting [282]. A spatially extended reservoir exhibits different benefits and challenges compared to the TDR. As challenges, one needs to create a network of nonlinear nodes to act as a reservoir, and to be able to extract the information for a final output. This network should be composed by a sufficiently large number of nodes to tackle difficult tasks, and all the nodes need to be able to potentially exhibit nonlinear dynamics. To achieve that requires control over the nodes' parameters, which can create experimental challenges for the typically large number of required elements. Benefits of a spatially extended reservoir are that the nodes respond simultaneously to the injected information, avoiding the speed penalty being a consequence of the temporal multiplexing.

In this chapter we develop an spatially extended large optical reservoir and an output layer. We present a reservoir with almost 10^3 nonlinear nodes, interconnected with neighboring nodes thanks to a single passive optical element. We incorporate learning techniques that allow the system to optimize its output weights. This study provides several steps towards a complete spatially extended photonic reservoir computer. First, we describe the experimental setup, where we detail the components we used to create the different parts of the reservoir computer. We continue by introducing the learning methodology, necessary to find optimized output weights. We proceed by evaluating the dynamics of the nodes when uncoupled and again once they are interconnected. Having observed suitable dynamics, we inject information into the system and evaluate the consistency of the responses of the reservoir before trying to process injected information. Afterwards we simulate the output layer of the photonic reservoir to support the experimental work. Finally, we use the previously obtained knowledge to experimentally demonstrate successful prediction of a chaotic timeseries and learning with low error rates.

5.2 Experimental setup

In this section we describe the experimental setup used to build an optical reservoir computer. We describe the implementation of the different parts of the reservoir computer previously described in Section 1.4.1 in separate sections. In Figure 5.1 we presented a simplified scheme of the experimental setup showing the most relevant components. These components are grouped in boxes based on their combined function. In the following sections we explain the construction of the different parts. We start by the spatially extended reservoir, composed by the nodes, the illumination, the nonlinearity, and the feedback boxes. We continue with discussing the input and the output layers. Finally, we discuss the complete experimental setup. Most of the setup is made of free space components, except for the light from the illumination laser which is partly fiber guided.

5.2.1 The spatially distributed optical reservoir

The introduction of the spatial optical reservoir is structured by the fundamental components facilitating a clear explanation. First, we describe how the nodes are defined, we continue by explaining how the nonlinearity is introduced, and we end by how coupling among nodes is achieved.

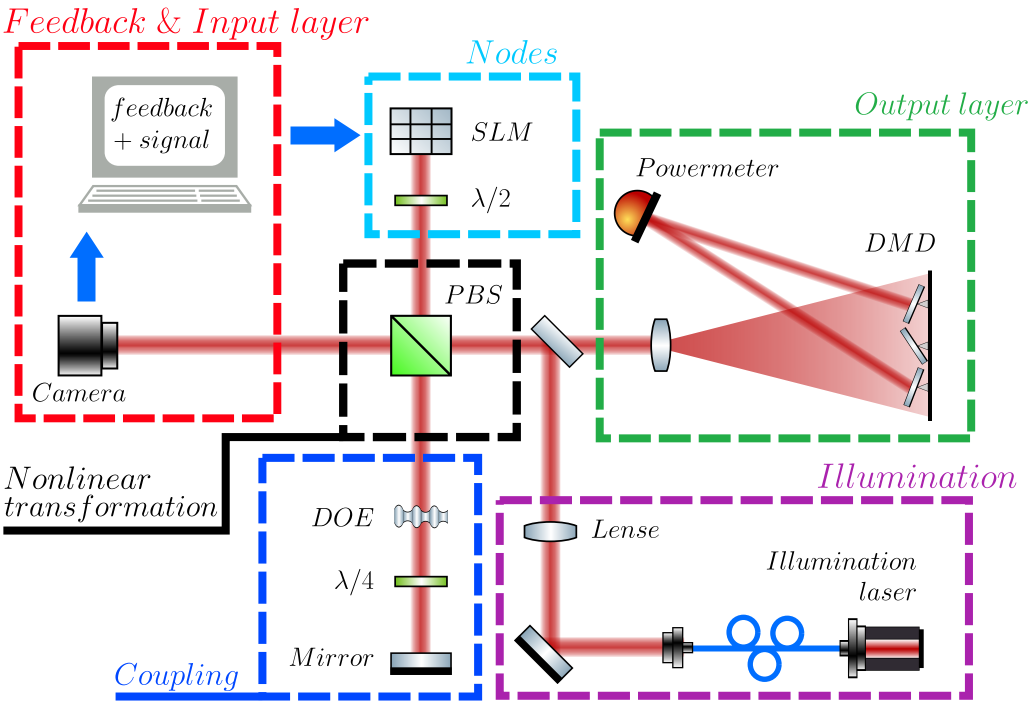

Figure 5.1: Simplified scheme of the experimental setup with grouped components. Thick red lines represent the light traveling though the components in the setup. Blue lines are optical fibers. Blue arrows represent directional communication between components. Dashed boxes indicate groups of components based on their function. Labels stand for Spatial Light Modulator (SLM), $\lambda/4$ retarder ($\lambda/4$), Polarization Beam Splitter (PBS), and Diffractive Optical Element (DOE).

Realizing the network

In a spatially extended reservoir, nodes are arranged in different positions in space. This can be achieved by using N different components for a reservoir of N nodes. This approach, can cause serious difficulties when scaled up as the amount of nodes increases. The difficulties arise since the device possibly requires individual control of every node. A reservoir may consist of 10^2 to 10^3 nodes, which means that hundreds of components would need to be operated as well as controlled, and be interconnected in a hardware implementation. We solve these problems by realizing all the nodes with a single SLM.

A SLM is a two-dimensional array of Liquid Crystal (LC) cells with the possibility the address them individually. The device used in this research is a Hamamatsu LCOS-SLM X13267-01, and it is operated with an auxiliary computer. This SLM has a highly reflective surface in the back to reflect the incoming light. We interpret individual cells of the SLM as nodes for our reservoir. Cells are squares with a lateral size of 12.5 μm, and the complete SLM surface accounts for about 75 mm^2. To create an optical reservoir, the nodes need to nonlinearly interact with light or create the light. An SLM does not create light, but the cells interact with the incident light thanks to its LC. The LC in the cells of the SLM apply a polarization specific phase shift to the incident light's electromagnetic field. The amount of phase shift on the resulting reflected light can be controlled with an offset bias voltage applied to the cell. This relation originates from the anisotropic optical properties in the LCs, which introduces birefringence in the material and therefore a refraction index that depends on the polarization of the light [283]. The offset bias across the cell determines the orientation of the LC molecules, which in turn will determine the medium indexes' of refraction (and therefore the optical path) that the light will experience. Light bounces on the highly reflective back of the cell, and double-passes the LC. The SLM can be employed as a phase modulator or a polarization modulator depending on the incident light's polarization direction with respect to the LC molecules. In the following, we use it as a polarization modulator.

Since the SLM only interacts with light, we need some other element to provide its illumination. For that purpose we use an external laser, model Thorlabs LP660-SF20. We call the light generated by this laser illumination light or simply illumination. Temperature and current conditions of the laser are set such to avoid mode-hopping behavior, ensuring single wavelength emission over time. The emitted light was in the visible red wavelength range, $\lambda \simeq 662$ nm. Since the laser is fiber pig-tailed, illumination light is guided to the setup with optical fiber. The output light is collimated using a $f_{MO1} = 20$ mm focal distance Microscope Objective (MO), model Nikon CFI Plan Achro 10X (MO1). The light is then imaged onto the SLM using another identical microscope objective. Microscope objectives were used for collimation and imaging due to their low level of optical aberrations. The illumination light is linearly polarized, and its polarization direction can be controlled with a polarization controller used in the optical fiber section. Additionally, we add a lens with focal distance $f_{il} = 200$ mm between the illumination laser and the lens to create an illumination area on the SLM, as shown in Figure 5.2. Without this lens, the light from the laser would illuminate just a point of the SLM since the tip of the fiber would be imaged as a single-point light source. We place this lens with the intention of focusing the light on the back focal-plane of the microscope objective, so that the illuminating light is collimated between MO 1 and the SLM illuminates an area of the SLM. This area includes the nodes available for the reservoir, and it is limited by the aperture of the optical components used.

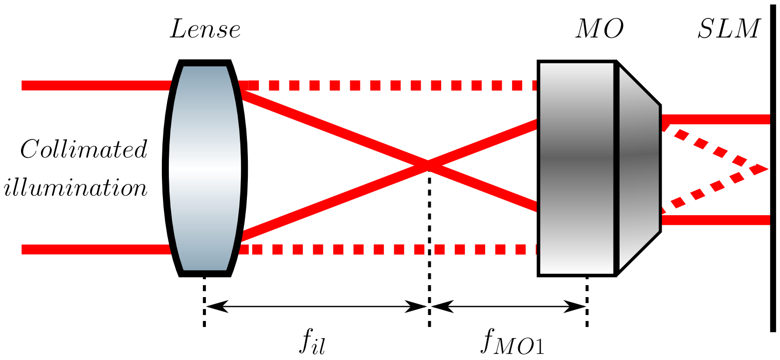

Figure 5.2: Illustration of the lens necessity for illumination of the SLM. Without the lens, light is focused on a point of the SLM. With the lens, light illuminates a wider area. Red dashed lines indicates the light beams in the absence of the lens, while the red solid lines indicates the light with the lens in place.

To observe the illuminated area on the SLM and the impact of the SLM polarization modulation on the reflected light we use a PBS as a polarization filter and a Complementary Metal-Oxide Semiconductor (CMOS) camera as illustrated in Figure 5.3. By changing the offset bias voltage of the SLM pixels, the reflected light can have different polarization directions depending on the pixel position. The offset bias of every cell can be varied from a minimum to a maximum value with 8-bit resolution, so the polarization of the light can be adjusted to polarization S, P, or a combination of both. The PBS then acts as a polarization filter by separating the light with orthogonal polarization directions, reflecting S-polarized light upwards, and while P-polarized travels to the right. This allows us to see which polarization state the light has coming from each SLM cell via the intensity distribution at the camera. To the right of the PBS we place a $\lambda/4$ retarder and a mirror with a second MO (MO2). These components are placed there for reasons explained later, as additional components are introduced here in following sections. The $\lambda/4$ retarder is placed such that the light, after being reflected by the mirror, is reflected by the PBS downwards towards the camera. MO2 is placed to image the collimated light onto the mirror. A third MO (MO3, model Nikon CFI Plan

Fluor 4X) is then used to image the light onto the CMOS camera. The camera records the spatial pattern of P-polarized light, resulting from the light reflected by the SLM and filtered by the PBS. Neutral Density (ND) filters attenuate the light to avoid saturation of the CMOS sensors in the camera. The camera provides a dimensionless value proportional to the incident light intensity with a 8-bit resolution. We covered the camera with a custom built black box to reduce environmental light on the CMOS chip. We place in front of the camera ND filters with sufficient absorbance to avoid pixel saturation on the CMOS camera while allowing for maximum dynamical range. This configuration provides the largest intensity range per node in the network while keeping the camera not saturated. Stronger illumination would saturate the camera resulting in information loss. Lower illumination would reduce the range of intensity levels for measurement from its maximum 256 levels.

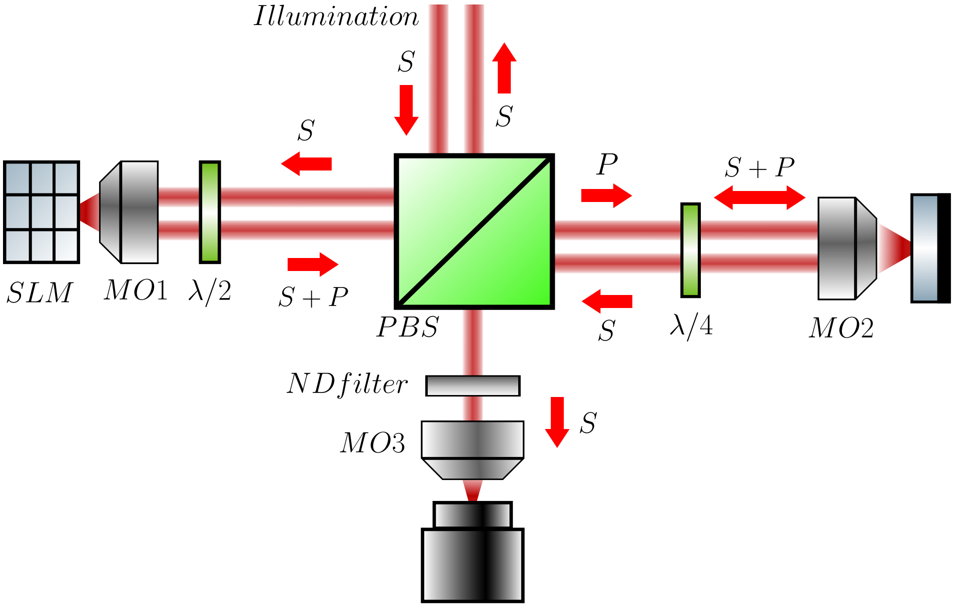

Figure 5.3: Scheme of the experimental setup used to observe the illuminated area on the SLM. Red arrows indicate the propagation direction of the light. Labels stand for Spatial Light Modulator (SLM), Microscope Objective (MO), $\lambda/4$ retarder ($\lambda/4$), Polarization Beam Splitter (PBS), and Neutral Density filter (ND).

In Figure 5.4 we show two images recorded by the camera of different SLM configurations while being illuminated. In Figure 5.4(a), the SLM is illuminated with P-polarization for a square region of pixels inside the illuminated area and with S-polarization elsewhere. The pixels of the square region are the pixels that will later become later the nodes for the reservoir. This configuration allows the reflected light to reach the camera passing through the PBS. This area is a 30×30 cells square region, so it includes 900 nodes. A square region was chosen for simplicity, and its dimension was chosen to maximize the amount of nodes. We can observe that the network area is spatially well defined, and offers high intensity contrast between areas with opposite polarized light. Vertical and horizontal black lines defining the lattice are due to a small separation between adjacent SLM cells in the device. As can be seen in this example, illumination is not completely homogeneous across the surface. In Figure 5.4(b) the SLM is inversely configured, as to obtain S-polarization for the nodes' square region and P-polarization elsewhere. The nodes appear in the "off" state in this case, and around the network area we can observe the boundaries of illumination. One can observe that the illumination has a circular profile and interference fringes due to the coherence of the light used for illumination. Given a SLM resolution of 800×600 cells, if the entire area of the SLM could be illuminated $4.8 \cdot 10^5$ nodes could be theoretically created with just one SLM.

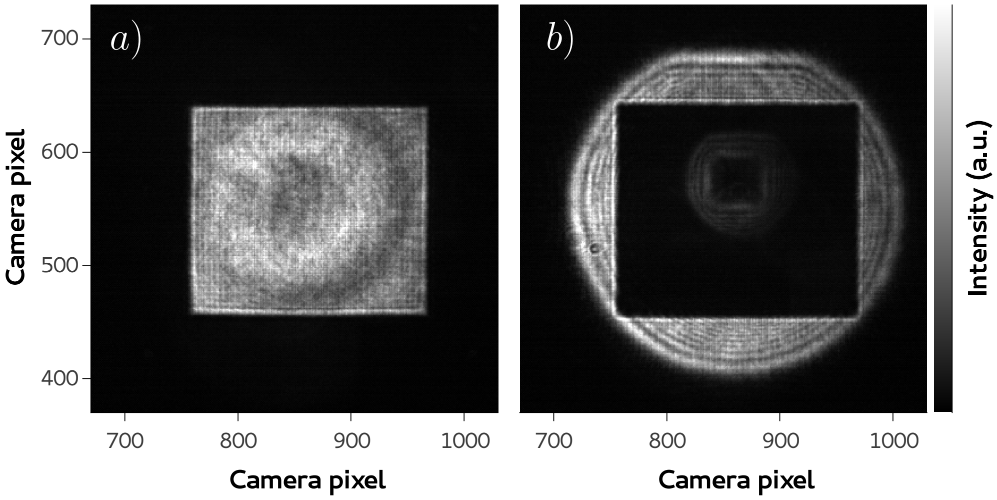

Figure 5.4: Images by the CMOS camera of the illuminated SLM with different configurations. a) SLM when the area corresponding to the network is set to provide maximum intensity towards the camera, while the rest of the SLM are set to provide minimum intensity. b) SLM configuration is opposite, so the area corresponding to the network is set to provide minimum intensity towards the camera, while the rest of the SLM are set to provide maximum intensity.

Implementing the nodes' nonlinear dynamics

The reservoir requires nodes with nonlinear responses to effectively process information. In this work we use a PBS to take advantage of the polarization modulation to implement a nonlinearity. The separation of polarization components imprints onto the intensity passing through the PBS a nonlinear transformation following a square trigonometric function as e.g. cos^2, where the phase of the cos will depend on the offset bias of the SLM cell according to Equation (5.1).

$$I_i \quad = \quad I_{i,0} \cdot cos^2\left(\frac{2\pi}{\xi} z_i + \phi\right) \tag{5.1}$$

In Equation (5.1) I_i refers to the intensity of node i after going though the PBS, and $I_{i,0}$ the intensity illuminating this same node. The associated index i for the nodes goes from 1 to 900. Inside the nonlinearity, ξ refers to the rate of polarization rotation per change of offset bias voltage on the SLM cells, and z_i is the offset bias of cell i. From Equation (5.1) we can see that the gray scale on the SLM controls the amount of intensity going though the PBS. Therefore, the polarization modulation available in the SLM combined with the filtering effect of the PBS provides the nonlinear transfer function on the light intensity for the nodes. This nonlinearity is identical to an Ikeda nonlinearity.

Using the setup in Figure 5.3 we can measure the nonlinear transformation by changing the gray scale of all the nodes and measuring the intensity recorded at the CMOS. In Figure 5.5 we show the recorded intensity for every one of the 2^8 available gray scale values. The intensity was calculated from the images as the sum of intensities from SLM positions belonging to the region hosting the network nodes. This intensity is normalized between the minimum and maximum recorded. The dependence in Figure 5.5 shows that the light intensity going through the PBS changes as the gray scale applied on the SLM increases. This dependence shows an oscillatory behavior that originates from the rotation of the polarization direction due to the SLM cells, and is indeed square trigonometric relation. We can observe that more than one period of oscillations are present, so the electric field orientation can rotate more than 2π. This transmission function is wavelength dependent since the index of refraction of the LC is also.

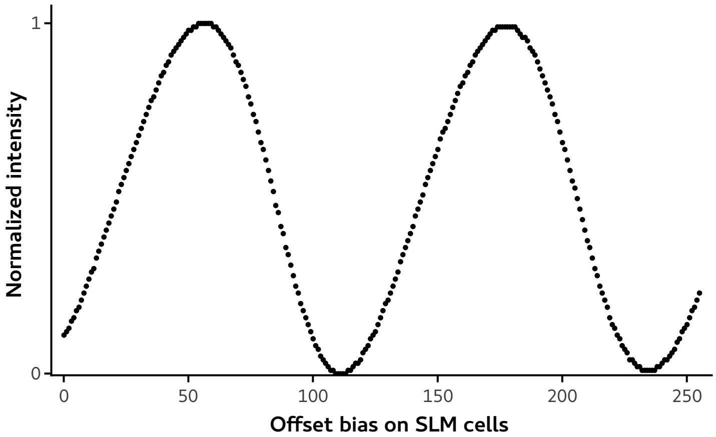

Figure 5.5: Intensity transmitted through the PBS depending on the offset bias applied to the SLM cells. Intensity is normalized between minimum and maximum power transmitted.

To implement nonlinear dynamics of the nodes, the state of the nodes need to change over time.The state of the nodes is governed by the gray scale; and the SLM can not exhibit temporal dynamics by its own. To implement temporal dynamics we measure the light intensity of every node on the CMOS camera and use this value to update the nodes to their next state. This operation is done with the computer used to control the setup (e.g. to read the camera and control the offset biases on the SLM cells), effectively turning the computer into the link that closes the feedback loop resulting in temporal dynamics. Conceptually, dynamics are implemented in the same way as in an iterative coupled map [284, 285]. In this frame, nodes update synchronously and time is discrete. To generate the dynamics, cells in the SLM are updated using Equation (5.2) as the update rule.

$$z_i(j+1) \quad = \quad \beta\, x_i(j) \, + \, \phi \tag{5.2}$$

In Equation (5.2), $x_i(j)$ is the dimensionless intensity measured by the camera for each node i at time step j, and $z_i(j+1)$ is the new offset bias of the SLM cells. The parameters in Equation (5.2) are β as the feedback strength, and ϕ as the offset bias of the cells under rest conditions (so without injection or feedback contribution). The value of these parameters determine the dynamics of the cells, so they are relevant for reservoir computing operation. Additionally, the computer needs to perform a linear mapping on the recorded network state to match the resolution of the camera to the one of the SLM. This difference of resolution originates for magnification of the image by using microscope objectives with different focal distances and the different pixel sizes of the SLM and the CMOS camera. The image on the camera is magnified by a factor f_2/f_1, where in this case f_2 is the focal distance of the MO3 and f_1 is the focal distance of MO1, which equals here to a magnification of 2.5. The pixels size for the SLM equals to 12.5 μm and for the camera equals to 5.2 μm. Therefore every pixel of the SLM is imaged on top of 36 pixels of the camera. To obtain the state of every node we average the measured intensity in the region corresponding to every node. This operation provides a x_i of suitable dimensions for the SLM. As the components in the reservoir are passive, the temporal time scale of the dynamics is governed by the time required to record an image, process it with the computer, and update the SLM cells accordingly. This process sets the update frequency to around 2 Hz.

Having described the nonlinear transformation and the implementation of the dynamics, the equation representing the intensity dynamics in our reservoir can be written as in Equation (5.3).

$$I_i(j+1) \quad = \quad I_{i,0} \cdot cos^2\left(\frac{2\pi}{\xi}\left(\alpha\,\beta \,\cdot\, I_i(j) \,+\, \phi\right)\right) \tag{5.3}$$

where $I_i(j)$ indicates the intensity of node i at time step j right after the

PBS. The measured dimensionless intensity distribution across the network, x_i in Equation (5.2), is recorded by the CMOS camera. The camera measurement can be related to intensity via $x_i = \alpha \cdot I_i$ with $\alpha = \frac{255}{I_{SAT}} \mu_{ND}$, where I is the intensity illuminating the camera pixel, μ_{ND} is the transmission factor due to the ND filters, I_{SAT} is the saturation intensity of the pixel, 255 is the gray scale 8-bit factor of the camera dynamic range, and $[\,]$ indicates rounding the number to integer.

Establishing coupling among nodes

The final ingredient for our reservoir is to introduce interaction among the nodes by some coupling mechanism. One could implement the coupling employing the computer in the setup, but we aim to do it with optical components. Coupling among nodes means that the state of the nodes affects the states of other nodes, spreading information throughout the network. For that purpose, we use the concept introduced in [153] of employing a Diffractive Optical Element (DOE). In our case we use a DOE model HOLOOR MS-443-650-Y-X. A DOE is an optical device that uses diffraction to shape and alter light beams. In our case, we use a DOE to create additional light beams, creating a 3×3 matrix as represented in Figure 5.6. The DOE creates first order diffraction beams in the vertical and in the horizontal direction of the collimated light beam at angle θ. Higher order diffraction beams can be discarded.

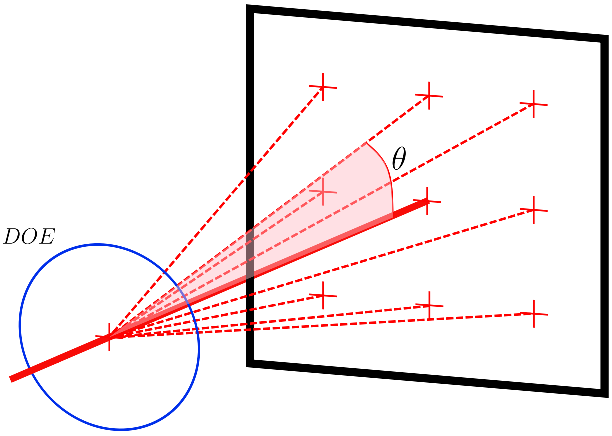

Figure 5.6: Illustration of the DOE (blue circle) splitting the light beam into diffractive orders, creating the 3×3 matrix.

The angle of these diffractive beams can be described with Equation (5.4), where m is the diffractive order, λ is the illumination wavelength, ζ is the grating period, and θ is the angle of the diffracted beam from the original.

$$m\,\lambda = \zeta sin(\theta) \tag{5.4}$$

The diffracted beams will be imaged at different positions depending on the angle between the propagation direction of the beam and the optical axis. To image the diffracted beams on top of the nodes in the network, we selected illumination wavelength, DOE grating period, and focal distance of the MO1 to match the pixels' periodicity in the SLM. This scenario is illustrated in Figure 5.7, where the diffracted beams from node B have the same angle as its neighbor, node A. So once imaged, node A and the diffracted beams from node B are imaged in the same position, effectively coupling node B to node A.

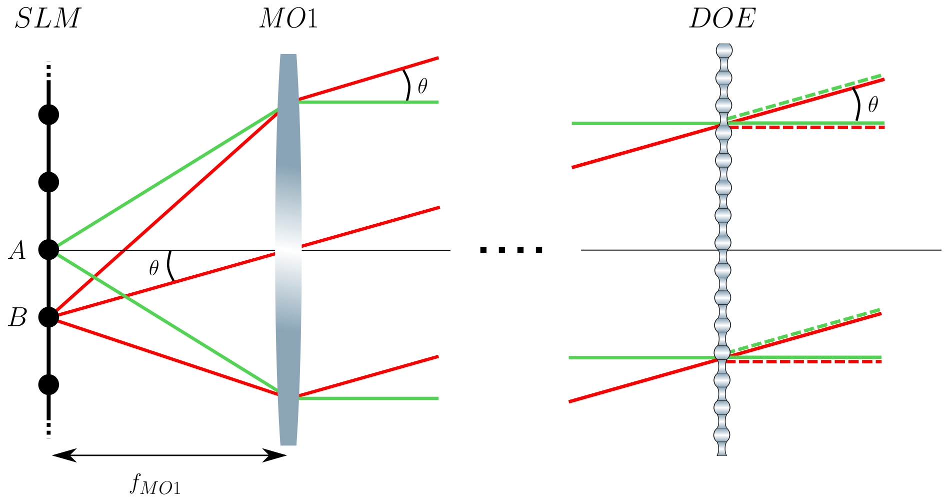

Figure 5.7: Coupling principle using a DOE. By matching the angle θ to the diffractive angle of the DOE, the diffractive modes of node B are oriented as the original beam for node A, coupling B to A. Black circles represent nodes on the SLM, solid lines the original path of the light beams, and dashed lines the path of the illustrated diffractive modes.

To increase coupling radius, we make the light from the SLM pass again the DOE, so every mode previously created experience the same diffraction. This operation extends the 3×3 matrix into a 5×5. By double passing the DOE, the coupling radius extends to one node further, increasing the number of nodes coupled. We place a mirror after the DOE to make light double pass the diffracting component, and place another microscope objective (MO2, same as MO1) in front of the mirror. Our new arrangement is depicted in Figure 5.8.

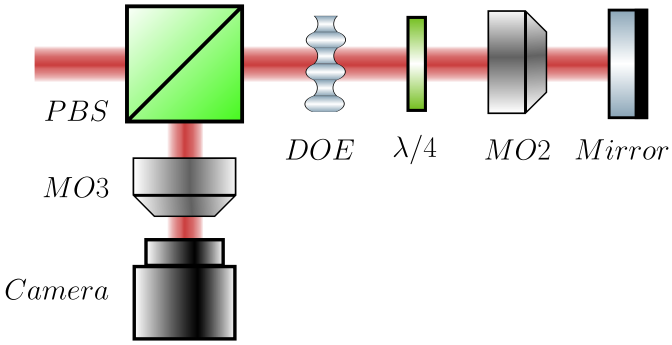

Figure 5.8: Optical setup to create the coupling mechanism. The DOE creates the diffraction beams for coupling the nodes, while the mirror provides light to double pass the DOE for extended coupling range.

To observe the impact of one node on the neighbors due to coupling, we evaluate the coupling matrix of the network. This coupling matrix indicates how strongly the state of one node affects the state of other nodes. To evaluate the coupling strength, we illuminate the SLM and record the network state at the camera when an individual node of the network is ″on″ and the rest of the network is ″off″. With the DOE in place, light from this node is sent to neighbor positions in space. This diffracted light falls on regions of the CMOS camera associated with other nodes. Light is then recorded at the camera at the positions of the one active node and neighboring nodes. The amount of light observed then at every node corresponds to the directional coupling of one node towards others. We subtract from every network state the background illumination, defined as the spatial intensity distribution measured by the camera when the whole network is inactive. Coupling strength results are shown in Figure 5.9. We depict the coupling strength of the whole network in a matrix. The node on the top left corner has index 1, and the nodes on the right have increasing indexes. The indeces of the nodes in the next line continue where the previous line ended. A diagram to represent this indexing is shown in the bottom right corner in Figure 5.9. The diagonal in the center of Figure 5.9 indicates the self coupling of the nodes. Coupling to neighboring nodes in the network are represented as additional diagonals. A broader main diagonal indicates coupling to further nodes in the horizontal direction of the network plane (e.g. left and right). Multiple diagonals indicate coupling to further nodes in the vertical dimension in the network plane. We observe in our coupling matrix four off-diagonals, exhibiting coupling up to two nodes in the up and down directions due to the higher diffraction orders from the DOE. As the intensity of light at higher orders is weaker than for lower orders, the coupling strength of off-diagonals further from the main one is lower. The coupling matrix shows coupling is available all over the network, and that all nodes couple with a similar pattern. But one can observe that the coupling strength exhibits some heterogeneity across the network, meaning that nodes couple to others differently. This heterogeneity can in fact be beneficial for reservoir computing, as the heterogeneity creates variations across the network that enrich the dynamics of the reservoir as a whole. This implementation allows nodes to connect to others in various strengths all across the network simultaneously without energy cost.

Upon including the coupling mechanism in the setup, the equation of the dynamics of the nodes can be updated with a coupling matrix $W_{i,k}^{DOE}$ to represent how the state of the nodes k couple to the state of node i. The updated equation is Equation (5.5), where now the term $I_i(n)$ is substituted by its electric field $E_k(j)$ since the resulting intensity pattern originates from weighted superposition of the electric field.

$$I_i(j+1) = \alpha\, |E_{i,0}|^2 \cdot cos^2\left(\frac{2\pi}{\xi}\left(\beta\,\alpha \cdot \left|\sum_{k=1}^{900} W_{i,k}^{DOE}\, E_k(j)\right|^2 + \phi\right)\right) \tag{5.5}$$

5.2.2 Implementation of the input layer

One needs a way to inject the information to be processed into the reservoir. Information is injected via the input layer, which in this work is implemented at the computer linking the CMOS with the SLM. This is done by modifying the update rule of the SLM in Equation (5.2) to include the contribution of the input layer. The new update rule is shown in Equation (5.6).

$$z_i(j+1) \quad = \quad \beta\, x_i(j) + \gamma\, W_{in}\, S(j) + \phi \tag{5.6}$$

The new network state $z_i(j+1)$ is calculated again considering the camera recording $x_i(j)$ with feedback strength β, the phase offset ϕ, and including

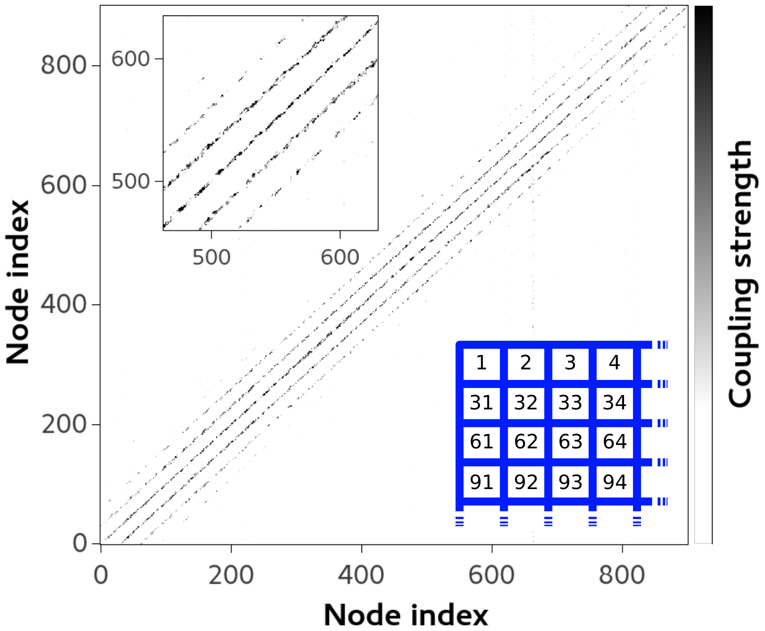

Figure 5.9: Coupling matrix of the network. The DOE connects nodes with their neighbors and next-near neighbors in both coordinates of the network. Black represents high coupling strength, while white represents absence of coupling. The top left inset zoom of the coupling matrix near the diagonal to better show the coupling strength in detail. The bottom right table depicts the indexing of the nodes in the network.

the new injection factors $\gamma W_{in} S(j)$. Injection factors are injection strength γ, the input weights W_{in}, and the injected data stream $S(j)$.

We evaluate the performance of our reservoir computer by predicting one step ahead the Mackey-Glass time series (Section 4.3.4). Therefore, the information injected $S(j)$ is a section of a Mackey-Glass time series. The input weights are a matrix with dimensions equal to the network's, so 30×30. The values of the input weights are random values uniformly distributed in the range $[0, 1]$. Even though in this work the input layer is not physically implemented, we consider a mask with features similar to the ones of a possible experimental optical input layer where information is encoded in intensity. Since the amount of intensity is always a positive value, the injected signal needs to remain positive. Therefore, we normalize the Mackey-Glass time series between zero and one. Figure 5.10 shows the mask used in this work. It is worth mentioning that this particular mask is not necessarily the best of all the possible configurations with the same properties. A search for the lowest possible error could include an exploration for a better configuration of input weights [133, 238]. Importantly, different input weights can provide different performance levels making a systematic investigation of the dependence on reservoir parameters more difficult. For this reason, we keep the input weights fixed.

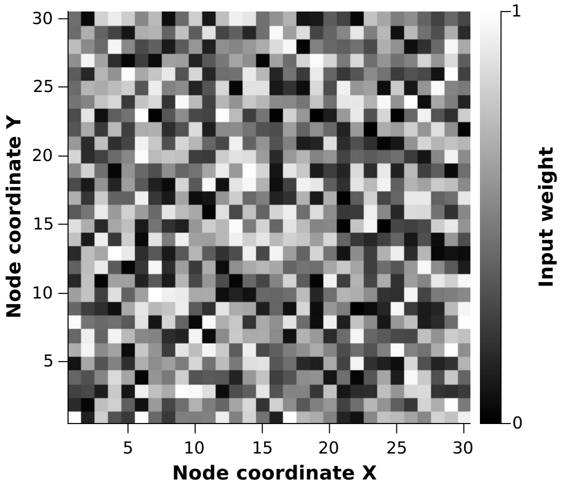

Figure 5.10: Input weights matrix used for the injection layer. The weight matrix is composed by random values between 0 and 1.

5.2.3 Implementation of the output layer

Finally, we discuss the output layer of the reservoir computer, which encodes the output of the device. In the current work this operation is attained by a two step process. One is to multiply the contribution of every node of the network by its output weight. The other is to sum all of these weighted contributions. By doing so, the output layer transforms the response of the reservoir into the final output of our reservoir computer. An experimental implementation of such output layer needs to execute these two operations. We aim to have an output layer with output weights that are easy to reconfigure. Additionally, to build a fully optical reservoir computer, the output of the reservoir computer needs to be optical. In the following we describe how we create an output layer with these capabilities.

First we need to explain how we obtain light from the reservoir for the output layer. Instead of extracting light directly from the reservoir, we use the light reflected by the PBS (light beam going upwards from the PBS in

Figure 5.3). This light is related to the one that remains in the feedback loop, and therefore holds the same information about the network state.

The complementary state is then imaged on a DMD, which will operate as an optical spatial filter to implement the output weights. This DMD is a Texas Instrument device, model DLP7000 0.7 XGA. A DMD is a two-dimensional array of individually addressable mirrors, where every mirror can serve as a pixel.The complete array has a size of 1024×768. A close-up photography of a few of these mirrors is shown in Figure 5.11(a). These mirrors are highly reflective aluminum squares, and they can be operated to tilt to $\pm 12^{\circ}$ depending on a provided binary value. In Figure 5.11(a) we can observe how some of them are tilted to opposite angles, while the rest are in an inactive ”flat” state. Each individual mirror lies on a torsional hinge and has two electrodes underneath. Below every mirror there is a dual CMOS memory with complementary memory state (if one is 0 the other is 1, and vice versa). Mirrors tilt according to the memory state when operated. We employ the two possible tilting angles of the mirrors to encode Boolean output weights values. Light illuminating the DMD will be reflected towards two paths depending on the mirrors' angle. One path sends light to continue through the output layer, therefore contributing to the final output of the reservoir computer. This case provides an output weight value of 1. The other path redirects light to the opposite direction, so this light is lost and doesn't contribute to the final output. This case provides an output weight value of 0. Such connection of the mirrors state with their output weight's values is depicted in Figure 5.11(b). As the DMD is composed by many mirrors, the mirrors associated to different nodes can provide different output weights for different nodes in the reservoir. The control of individual mirrors provides many possible configurations.

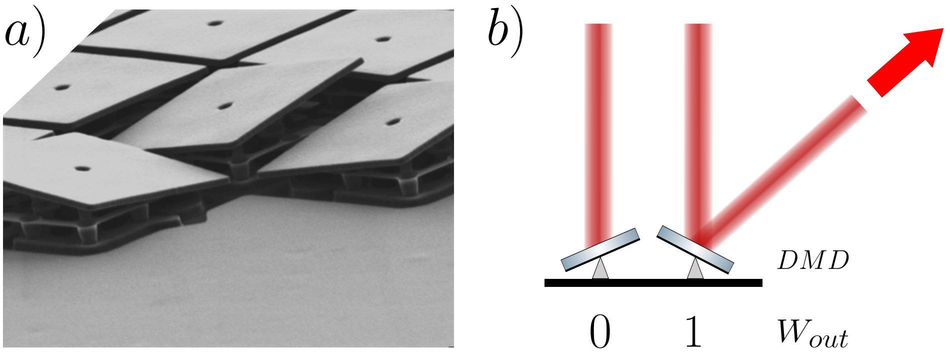

Figure 5.11: Output layer implementation with a DMD. a) Close up image of DMD mirrors showing their tilted and flat states [copyright of Texas Instruments, not necessarily the exact same device model]. b) Operation principle of the DMD for the output layer.

To ensure the mirrors act as output weights for individual nodes, the DMD mirrors plane needs to be positioned at an exact distance from a focusing lens system. To facilitate this operation, we use a lens with a focal distance of 300 mm. Using a lens with a large focal distance increases the depth of focus, and allows to manually place the DMD close to the focal plane using visual inspection of the image focus quality. Right before this lens we place a square custom-made spatial filter to reduce light coming from the SLM that does not originate from the reservoir. Additionally, we insert an extra PBS after the lens to remove any orthogonal polarization component relative to the one considered for the output layer. The image of the SLM is magnified by a factor of f_2/f_1, where f_2 is the focal distance of the lens in front of the DMD and f_1 is the focal distance of the microscope objective in front of the SLM. In this case, the magnification is $300/20 = 15$, so the image is magnified on the DMD. There are two important implications of the magnification since the area of the network state changes. As the DMD has a finite area, the magnified imaged of the SLM representing the network state state needs to remain inside the boundaries of the mirror array. Our DMD has a mirror lateral length of 13.68 μm, and an area of $14.0 \times 10.5\, mm^2$. The other implication is that the magnification associates multiple mirrors to each reservoir node. The output weight of every node consists of $(12.5 \times 15 \,/\, 13.68)^2 \approx 188$ mirrors on the DMD. The tilting of the mirrors across its diagonal requires the DMD to be installed rotated 45° to maintain the reflected light beam in the same plane as the rest of the experiment. Additionally, one needs to identify the region of the DMD illuminated by the reservoir. We did so by maximizing the reflected light from the area of the SLM used for nodes, where every node provided maximum possible intensity. In Figure 5.12(a) we show the DMD pixel array with a color code to express the mirrors' association. White indicates the mirror is not illuminated by the reservoir, and will have no effect on the output weights. We keep those mirrors tilted as $W_{out} = 0$. Colored pixels in Figure 5.12(a) indicate mirrors illuminated by the reservoir's light, where the different colors delimit regions of pixels associated to the same node. Therefore, to change the output weight of a certain node, all the mirrors identified with the same color need to be tilted. The rotation of the DMD relative to the SLM creates saw tooth shape borders between nodes on the DMD instead of straight lines, see inset of Figure 5.12(a). A photography of the actual DMD can be observed in Figure 5.12(b) with the area illuminated by the network tilted in one direction, while the rest of the mirrors are tilted with the opposite orientation.

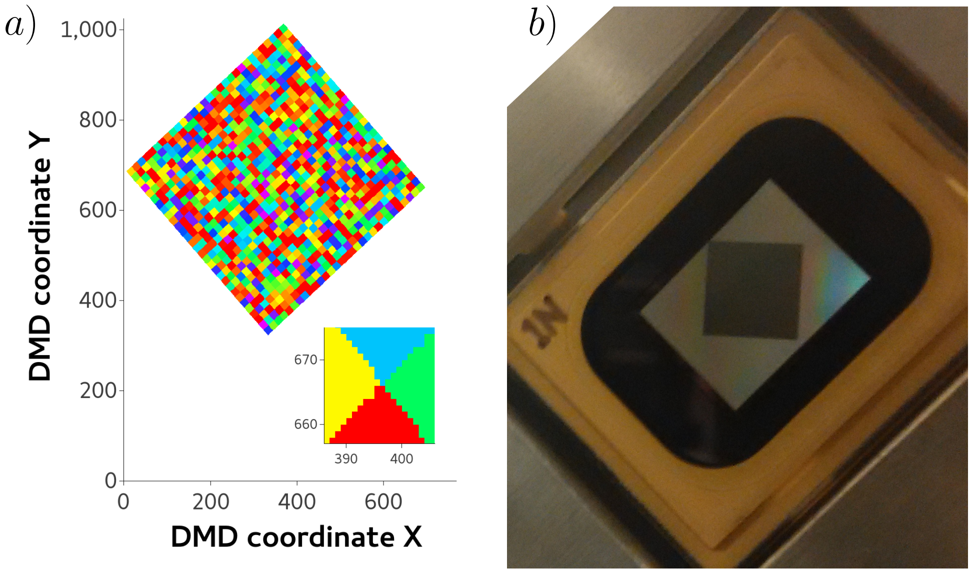

Figure 5.12: Projection of the output weights matrix on the DMD. (a) DMD array showing association of mirrors to nodes with the same color. White indicates the mirror does not contribute to the output weights, while rainbow colors indicate the mirrors operated. Individual areas of the same color delimit the mirrors that work for the same node. The network has been displaced in the y direction to provide space for the inset, while rotation is realistic. Inset shows the saw tooth pattern created between nodes. (b) Experimental DMD device with the mirrors illuminated by the network configured as weights one, and the area outside of the network configured as zeros.

To finalize the output layer, we need a way to add all the weighted contributions of the different nodes from the reservoir. This addition can be implemented using a lens to perform spatial integration. A lens focuses the light to an area smaller than the detector area, with an intensity being the accumulated intensity of all the incoming light. It is worth noting the possibility of coherence effects, as light used across the experiment comes from a coherent source. The final intensity will potentially not be the simple linear summation since coherence will cause interference. As long as the experimental setup is sufficiently stable, interference effects should remain constant and consequently only slightly affect the output. To measure the light intensity after the lens we place a photodiode at focal distance from the lens. The power at this point is the output of the reservoir computer. This power is of the order of $25\,\mu$W, and every node contributes to the final output about 30 nW, which is a small amount of power. To help detect these small quantities we cover the space between the camera and the lens with a custom black cardboard cover to reduce environmental light acting as a noise source. Additionally, the power meter averaged the measure across 10^3 individual measurements as the final power measured. This level of averaging reduced noise effects enough to observe the contribution of individual nodes.

5.2.4 Complete schematic of the experimental setup

Having explained all the components of the setup, we show a complete schematic of the electro-optical reservoir computer in Figure 5.13. The left side of Figure 5.13 shows the reservoir as previously described, with the SLM, the PBS, the DOE, and the computer connecting the camera to the SLM while also acting as input layer. The role of the computer in the setup is limited to reading out the camera and the power meter, and controlling the SLM and the DMD, and to inject information, but it is not involved in the realization of the nonlinearity in the system neither of the coupling mechanism. On the bottom right is the illumination laser and the other required components. The illumination is redirected by a mirror and a Beam Splitter (BS) to the PBS. On the right of the BS we show the output layer implementation. The dynamical evolution of the system will depend on environmental parameters as also on the state of the SLM. It was found through different experiments that the SLM takes almost two days to thermally stabilize. Prior to that moment, dynamical evolution of the reservoir under the same conditions would yield different trajectories.

5.3 Methodology to obtain optimal output weights

In the previous section we described the physical components employed to create our spatially extended reservoir computer. To properly process information for a task, the system needs to find the appropriate configuration of output weights yielding the lowest error. In Section 4.3.1 the importance of finding a sufficiently good set of output weights was already described. This section aims to describe the set of methods employed to find a suitable configuration of output weights for our particular reservoir computer.

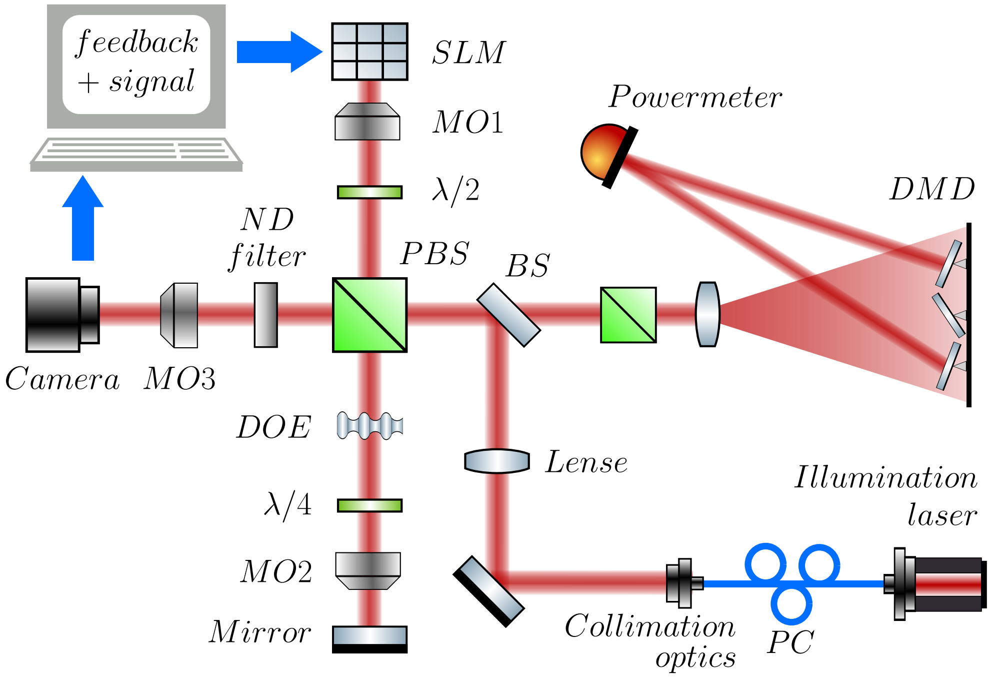

Figure 5.13: Scheme of the complete experimental setup. Red thick lines are the light traveling through the components in the setup. Blue lines are optical fibres. Blue arrows represent directional communication between components. Labels stand for Spatial Light Modulator (SLM), Microscope Objective (MO), $\lambda/4$ retarder ($\lambda/4$), Polarization Beam Splitter (PBS), Polarization Controller (PC), Beam Splitter (BS), Diffractive Optical Element (DOE), and Neutral Density filter (ND).

5.3.1 Online reinforcement learning

Different techniques can be applied for learning depending on the characteristics of the system and desired features. In this chapter we used an online learning technique. This technique differs from the previously introduced offline technique in Section 4.3.1, as in the offline technique the output weights were computed in hindsight. In the online technique, different configurations of output weights are consecutively evaluated with a training data set to find the configurations that provides lower errors. This approach offers different benefits compared to an offline technique. Online learning allows to continuously adjust the weights during potentially slightly varying environmental conditions, which can increase the robustness of the system. Performance alterations in the system may occur, caused by environmental changes or experimental drifts. Experimental drifts may affect how information is mapped and manipulated inside the reservoir computer itself. These effects would be detrimental for performance since the resulting signal from the reservoir would be one the output weights are not trained for. The possibility to readjust the output weights for the new conditions could potentially maintain similar performance. Additionally, output weights reconfiguration allows to easily change the task performed by the reservoir computer. A new task would require a different set of output weights, which can be easily implemented in the output layer to adapt the reservoir computer to the new task [286]. Furthermore, online learning needs less computation and memory than offline learning.

In this study we use a reinforcement learning based process. This process consists of multiple iteration steps, and at every step the system has a configuration of output weights and a performance measure. We exclusively used the Mackey-Glass prediction task, so the performance measure is a NMSE that is desired to be as small as possible. At every iteration we modify the best output weights configuration found. Then we inject information into the reservoir computer using this new modified output weights. From the output we compute the new NMSE associated to these new output weights, and if the new NMSE is lower than the one obtained with the previous set of optimal weights, then the new configuration replaces the previously best. If the new NMSE is higher, then we do not change the best output weights. We chose as starting point random values for our output weights matrix, and learning iterations were repeated. The success of the exploration is strongly dependent on parameters associated with this learning process.

Through the learning process, the system explores the space of output weights configurations to find regions of low errors as new configurations are evaluated. This process could be performed using different random configurations of output weights, but this is typically not the most suitable technique. Assuming that the performance landscape in the output weights space is continuous, one can change several nodes' values and evaluate what changes improve performance. Changing the value of several nodes is like evaluating the gradient in a particular direction in space, where the dimensions of the space are the output weights values. If the error is lower, the system adopts the new configuration as the optimal weights. So instead of evaluating the gradient in every possible direction, here we just evaluate it in a particular one and decide to move or not. The output weights are Boolean, so a value change from 0 to 1 or vice versa. This procedure does not ensure that the system will find the global minimum, only that it may find a local minimum. Repetition of the learning starting from different initial conditions helps to explore further the performance landscape and increases the chance of finding the global minima or a better local minimum. The error obtained with this method is a training error. To ensure a generalized learning, one needs to evaluate the system feeding unseen input information to the reservoir and check the error generated. This second error is the test error. An adequate learning procedure provides similar and low test and train errors. Deciding how many weights to change at every iteration is important for the success of learning techniques similar to gradient descent. We empirically found as a god solution to change only one output weight at every iteration.

5.3.2 Stochastic weighted node selection

We have explained how we aim to find the set of output weights that minimizes the error by switching the weight values of certain nodes. The selection of nodes can follow different approaches. One would be to do so in an ordered fashion by selecting the first, then the second, the third... until the last. In contrast, we decide to randomly select the nodes at every iteration.

We additionally include an extra step for the selection probability bias. The fundamental motivation for using selection biases is accelerating learning. By just randomly selecting the nodes, learning is less time efficient since the probability of choosing nodes that have not been previously chosen reduces as time increases. All node-weights should be efficiently explored to probe the readout weights' in the configuration space, and it should be done in a minimal time window. The implementation of the selection bias on the nodes is done in the following way. All nodes have a selection weight that starts with value 1. Every learning iteration we add to every selection weight a constant value that we choose to be $1/N$, here $N = 900$. Then we create an array of N random values between 0 and 1, and multiply this array element-wise with the weight selection of nodes array. As we only change one weight value, we select here only the highest value of the resulting list as the nodes selected to have its weight value changed for learning. We turn to 0 the selection weight of the nodes successfully chosen. Finally, we add $1/N$ to all entries of the bias matrix. Application of selection weights to the nodes pushes nodes recently evaluated to the back of the selection list. In this way, nodes that have been long time without being tested can be tested again in a (probably) quite different configuration as when they were tested previously. This procedure allows to stochastically choose the nodes to change, while at the same time favors to choose nodes that have not been selected recently.

5.3.3 Node filtering

Now we describe an additional step to optimize our learning process. We have seen how the SLM network is heterogeneously illuminated. Therefore, each node will contribute with different powers to the output of the reservoir computer. But as in any experimental realization, noise is present in our system. The impact of every node upon the outcome of the output layer should be visible in the output despite noise. If that is not the case, the contribution of the node is invisible and its output weight is therefore irrelevant. For this reason we decide to not consider nodes with power contributions below the noise level for the system's readout. The noise level is calculated as the average standard deviation of the power intensity of the DMD configured so every weight has 50% chance of having value 1. We chose to turn on only half of the output weights as it resembles a typical scenario, as one expects an intermediate amount of the output weights on the $W_{out} = 1$ state. The measured noise level averaged across ten realizations was 20.9 nW. Then we measured the power contribution of every individual node to the output of the reservoir computer. By setting all DMD mirrors to 0 besides the one to be evaluated. We also measured the background level when all nodes are off, which was subtracted from the power contribution of every node to obtain their true contributions. The resulting node filter is displayed in Figure 5.14. One can observe that all the considered nodes are in the center of the network, corresponding to the locations with a higher illumination. Nodes in the surroundings are less illuminated and contribute less, falling below the noise threshold. All nodes participate in the network dynamics still, while only the nodes considered by the filter contribute in the output layer and the learning. The considered nodes correspond to 67% of all the nodes in the network. So application of the node filter avoids testing around a third of the nodes in our experimental implementation optimizing our leaning efforts.

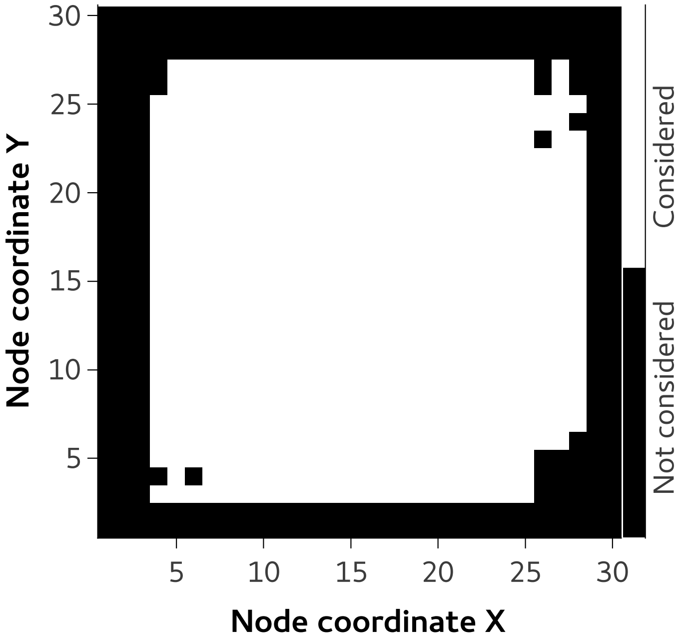

Figure 5.14: Node filter on the output weights. The filter is applied at the learning stage, where nodes not considered (in black) keep their output weights as zero, while the output weights of the considered nodes (in white) can change their output weights.

5.4 Dynamics of the reservoir

As the physical reservoir is built, one can evaluate its dynamical behavior, as its dynamics is important for information processing. For that reason in this section we explore the dynamics of some of our optical nodes, find the parameter space where these dynamics can be suitable, and evaluate how the coupling in the network affects those dynamics.

5.4.1 Dynamics of the uncoupled network

First we explore the possible dynamics of the nodes in our network while there is no coupling mechanism in action. The dynamics of the nodes unfold as the system evolves through time steps, from a starting initial condition. We choose to evaluate the dynamics as the feedback strength β is increased. Feedback strength affects the dynamics, since it regulates how much of the previous state influences the consecutive. The impact of factor α would imply changing its value from its optimal value, as it affects the amount of information captured by the camera. Parameter ϕ is set to 25.

First we look at the intensity dynamics of one individual node for different feedback strengths values. We chose node $(15,12)$ from our (30×30) array as example. In Figure 5.15 we show three distinct dynamical regimes of the node for different β values as examples of different dynamical behaviors. For $\beta = 0.5$ (Figure 5.15(a)) the system remains in a fixed point. Intensity remains mostly stable while exhibiting small variations due to noise. For $\beta = 0.9$ (Figure 5.15(b)) the system shows strong oscillatory behavior. The node state evolves jumping from a low to a high value and vice versa consecutively. Finally, for higher β (Figure 5.15(c)) we observe the node evolving with stronger intensity fluctuations than in previous cases, corresponding to possibly chaotic dynamics.

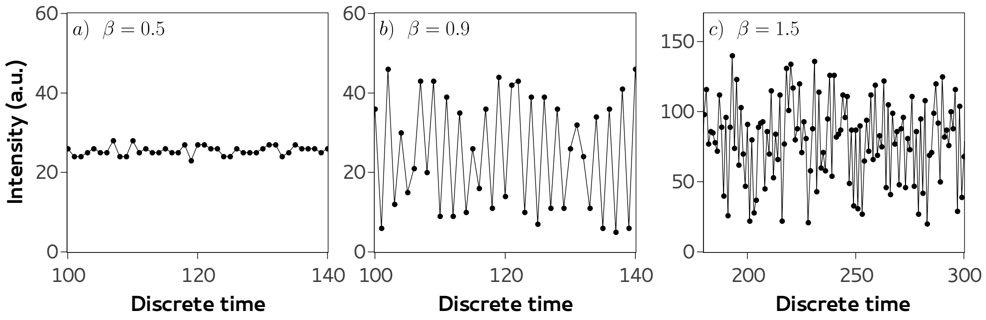

Figure 5.15: Dynamical evolution examples for a node in the network. The examples comprise (a) fixed point, (b) oscillations, and (c) complex dynamics, respectively. Lines between the points are guides to the eye.

For a more detailed study of the dynamical possibilities of the nodes, we evaluate the experimental dynamics for β in the interval $[0.0, 1.5]$ with a resolution of 0.05. For every feedback strength we record the dynamics over 2000 time steps, and create a histogram of the last 1900 intensities from the experimental dynamical evolution (the first 100 values are discarded as we considered them transients of the dynamics). As the histogram represents the distribution of intensities, it helps identify the dynamical states. We present the different histograms for every β of the node $(15,12)$ in Figure 5.16, where every column represents its corresponding histogram. Histograms are normalized so their accumulated probability are equal to one, and probabilities are given in a logarithmic gray scale to help identify regions with broader distributions. For low β

values, the node exhibits an almost constant intensity. This state is identified by the narrow histogram around a single intensity in the β range between 0.0 and 0.5. Between $\beta = 0.5$ and 0.9, the system exhibits oscillating dynamics with increasing amplitude. The bifurcation diagram shows how the histograms broadens in this range, while also two intensities are more probable than the others. This indicates the destabilization of the fixed point leading to oscillatory dynamics. At $\beta = 0.9$, the system starts to intermittently jump to higher intensities. For higher β the system ceases to show the previous kind of oscillations and starts exhibiting a broad amplitude distribution, corresponding to chaotic dynamics. The chaotic regime exhibits fluctuations in an intensity range that increases as β increases. Additionally, the histogram for such dynamics broadens so the probability of different intensities is more similar. This bifurcation diagram shows the dynamical transition of one node in the network from a fixed point to chaotic dynamics via increasing the feedback strength. Such dynamical landscape shows that a node in our experimental network can exhibit nonlinear dynamics.

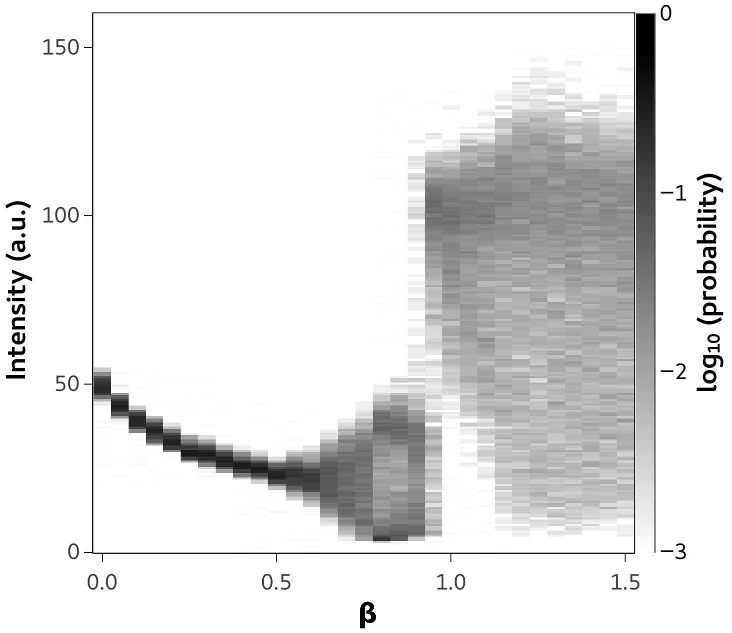

Figure 5.16: Bifurcation diagram for node (15,12) uncoupled.

The nodes in the network can experience slightly different conditions due to heterogeneities in the experimental realization. Such heterogeneities originate from the components and the SLM's inhomogeneous illumination, which has an impact on the dynamical characteristics of the nodes. In Figure 5.16 we show the bifurcation diagram of a node that represents qualitatively a typical representative. But it is important to be aware of how different the dynamics among different nodes can be. For that purpose we look here at the bifurcation diagram of other nodes. In Figure 5.17 we show the bifurcation diagrams of four different nodes. Figure 5.17(a) and (b) show the bifurcation diagrams of two nodes (11,10) and (22,16), as their bifurcation diagrams are similar to (15,12). The two nodes and (15,12) exhibit a fixed point for low feedback strengths, which develops into oscillations as β increases. For even higher β the system suddenly jumps to higher intensities and develops chaotic dynamics. These dynamics expand in intensity range until at least the limits of β studied. Qualitatively the three diagrams are similar, as the dynamics and their transitions are the same, but are not identical. For example, the specific value of β for the transitions can vary. While in Figure 5.16 and Figure 5.17(a) the transition from fixed point to oscillations is around $\beta = 0.5$, in Figure 5.17(b) the transition is closer to $\beta = 1$. The transition to chaos occurs also for higher β for node (22,16), unfolding not as sudden as for other nodes. The bifurcation diagram of node (7,2) in Figure 5.17(c) shows how the node exhibits stable dynamics over most of the range of β studied. The average intensity varies for different β, and we can observe a transition to higher intensities at $\beta = 1$, but no transition to chaotic dynamics. As a last example, node (25,13) is an example of a node that quickly transitions from a stable fixed point to chaotic dynamics, without clearly showing periodic oscillations first. So even though some nodes do not exhibit strong chaotic dynamics, the most observed behavior across the network for the nodes is to eventually exhibit chaotic dynamics as feedback strength is increased. The small variations on the experimental conditions produce notable differences on the bifurcation diagrams. But as long as they are small, the slightly different dynamical regimes can be beneficial for information processing as they enrich the high dimensional space created by the reservoir.

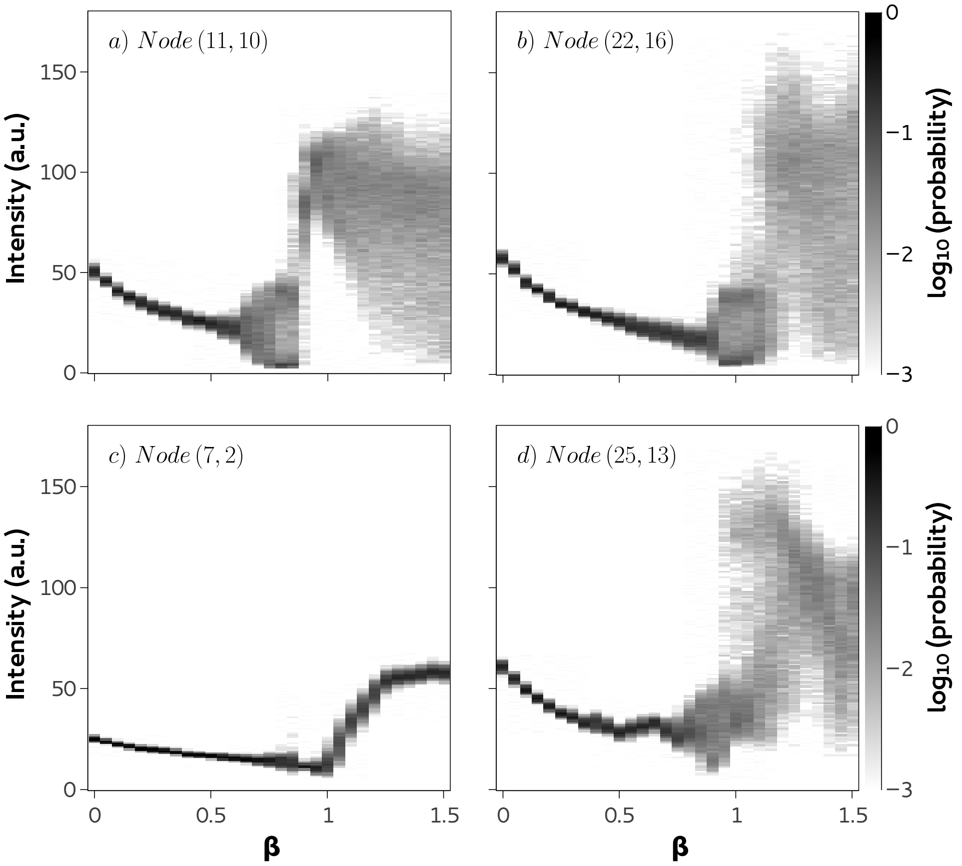

Figure 5.17: Bifurcation diagram for different uncoupled nodes across the network. The nodes represented here are (a) (11,10), (b) (22,16), (c) (7,2), (d) (25,13).

5.4.2 Dynamics of the coupled network

We have so far evaluated the dynamics of the nodes in the network while they were uncoupled. Now we place the DOE to induce the coupling mechanism among the nodes. For that purpose we use bifurcation diagrams computed in the same fashion as in Section 5.4.1. In Figure 5.18 we show the bifurcation diagram of node (15,12), the same as in Figure 5.16, but this time with coupling to neighboring nodes. We can observe that for low β the node remains in a fixed point state, as it did without the coupling, but for a wider β range indicating that in this case the coupling stabilizes the node, By comparing the bifurcation diagrams with and without coupling one can observe that with coupling the measured intensity is generally smaller. The range of stable dynamics for our node with coupling increases by a factor of about 4, from $\beta = 0.5$ to 2.0. As β increases beyond 2, the node exhibits higher intensity and for β close to 3 we observe broad chaotic dynamics. The onset of dynamics is observed for β almost 3 times higher than before, and the distribution of intensity values differs from the uncoupled cases. So we can observe that chaotic behavior is observed regardless of coupling mechanism with a sufficient β, and also that the precise characteristics of the dynamics are affected by the coupling.

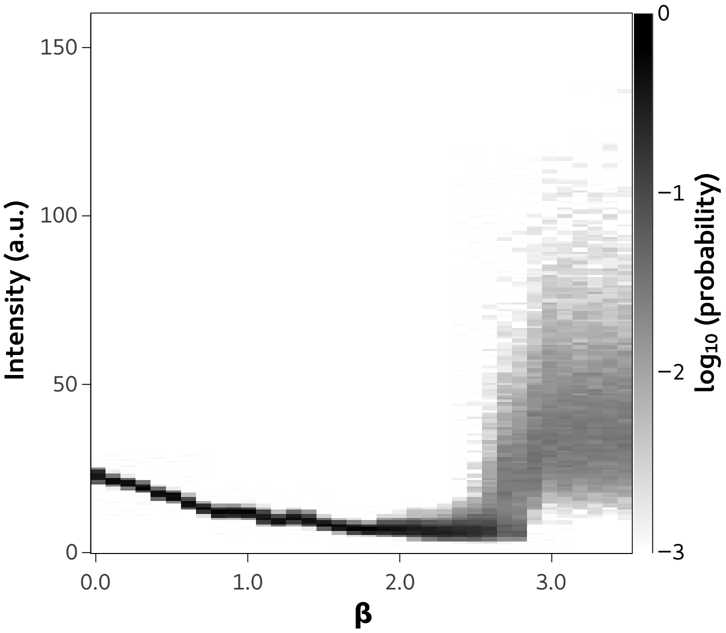

Figure 5.18: Bifurcation diagram for node (15,12) coupled.

We can also observe how the implementation of the coupling affects other nodes. In Figure 5.19 we can see such bifurcation diagrams. All the bifurcations diagrams have changed similarly as the one for the node (15,12). The nodes' dynamics have now a wider range of feedback strength showing stable dynamics until around $\beta \sim 1.5$. Some nodes exhibit around $\beta \sim 2.0$ some small amplitude oscillations, while others remain in a fixed point. For $\beta > 2.5$ the nodes exhibit chaotic dynamics, increasing the intensity and range of values. The abrupt transition to chaotic dynamics differs in degree from one node to another. While some remain at low intensities like node (7,2), others like node (25,13) exhibit chaotic dynamics with higher amplitudes. It is interesting to note that the coupling can induce chaotic dynamics in the nodes, as in the case of node (7,2). In the range studied without coupling, no clear chaotic dynamics were found for node (7,2) while other nodes showed them. With coupling, this node shows chaotic dynamics in a similar range as other nodes do. This could be an important feature of the system under conditions that restrict the dynamical possibilities, as for example limited illumination. We observe that the coupling alters significantly the dynamics of the nodes, in our case by stabilizing them.

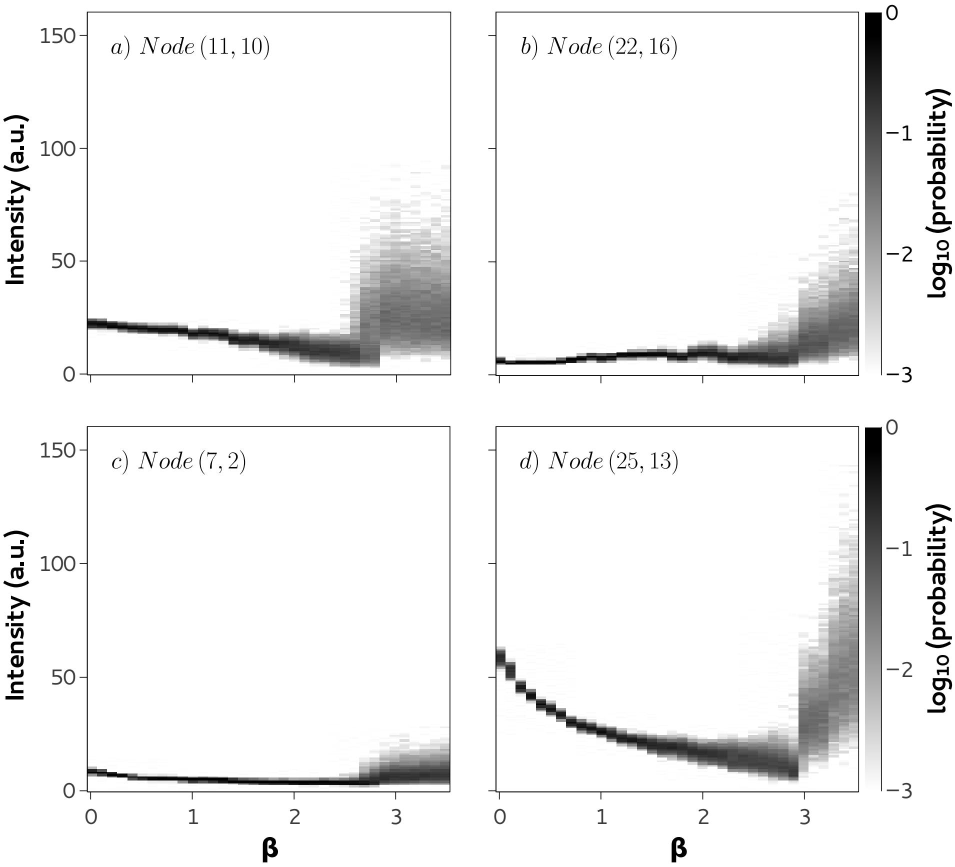

Figure 5.19: Bifurcation diagram for different coupled nodes across the network. The nodes depicted here are (a) (11,10), (b) (22,16), (c) (7,2), (d) (25,13).

To conclude this section, we observe the susceptibility of the dynamical landscape to different illumination conditions. As we previously stated, the SLM is illuminated by an external laser to provide light to the system. The amount of light employed needs to be close to the saturation intensity of the camera, but at the same time it is desired that the illumination laser emits at a wavelength as stable as possible. Once the laser parameters are fixed, the light intensity to the camera can be decreased using ND filters. The specific properties of the employed components, like the DOE or the availability of ND filters, modifies the illumination conditions in the setup. To inspect how the dynamical properties can be affected by such influence we evaluate the bifurcation diagram of node (15,12) employing different illumination conditions. In particular, we chose to operate the illumination laser at higher current and different temperature. Alongside, these new conditions required stronger ND filters. The bifurcation diagram is shown in Figure 5.20. We can observe that the diagram is qualitatively similar to Figure 5.18. Low β values results in stable states, while increasing β leads to instabilities eventually leading to chaos. The values of feedback strength where we find dynamical transitions are different. As illumination is a parameter in the node's dynamics, it is expected that a different illumination changes the boundaries of the dynamical regimes. In this case, the change of illumination increased the feedback strength for the onset of chaotic dynamics from almost $\beta = 3$ to 4. The system therefore shows flexibility, as different conditions can deliver adequate dynamical properties. Such property can be beneficial for systems undergoing fine-tuning as for adaptation to new environments.

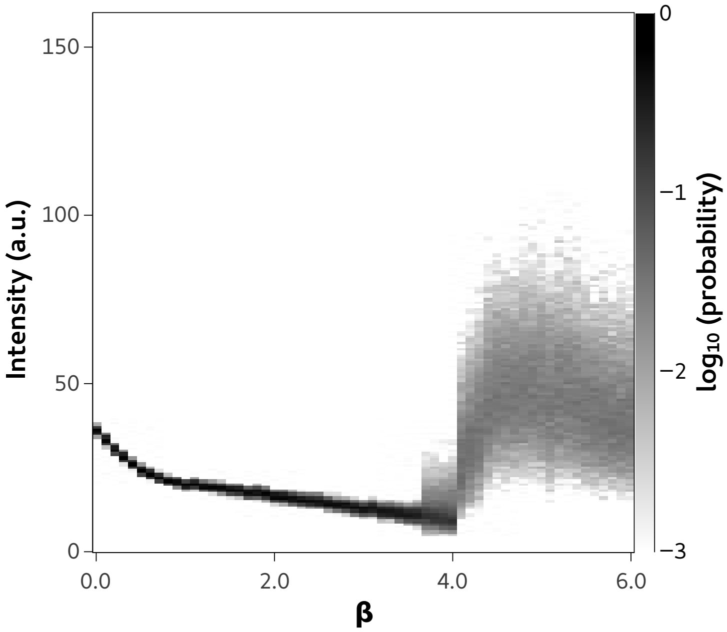

Figure 5.20: Bifurcation diagram for node (15,12) with coupling using different illumination conditions.

5.5 Consistency of the dynamics

Exhibiting nonlinear dynamics is not enough for a reservoir. The responses of the reservoir at different times under information injection, need to be as similar as possible under the same system parameters. Such system shows the property of consistency. Consistency has been previously discussed in Section 4.3.2, where we elaborated on its fundamentals and importance for computational systems. Here we evaluate consistency of the responses of the reservoir to injected information under typical operation conditions. We quantify consistency using the consistency correlation value (Equation (4.2)), in this case with just two time traces instead of three. The employed time traces are different measurements of discrete time evolution of all the nodes in the network, using identical initial conditions but different parameters. Initial conditions of the reservoir were the lowest offset bias for the nodes to exhibit minimum intensity at the camera. It is important that consistency is high for a set of parameters, but it is also important that consistency remains high over time. For that purpose we especially evaluate the consistency of the dynamics at different times by repeating the dynamical evolution using the same conditions. We record the dynamical evolution of the reservoir for the same injection for 500 discrete time steps. The injected values are consecutive points of the Mackey-Glass time series, since in this chapter we evaluate the Mackey-Glass time series prediction (Section 4.3.4). We chose 500 as it is of the order of magnitude of values that we will inject for reservoir computing. Each complete evolution takes approximately 11 minutes to complete, meaning that consistency can be evaluated around six times per hour. We evaluated consistency over a period of time of at least 15 hours.

We evaluate two different kinds of consistencies, which we call the short time consistency and the long time consistency. We define short time consistency as the consistency correlation between one time trace and the one generated immediately before. This measure of consistency indicates how much the time traces have changed in a short period of time. Long time consistency is the consistency correlation between the first time trace generated and one time trace generated a time later, both from the same session. This measure informs about how much the dynamical evolution changes in longer time windows.

Observation of the dynamical consistency delivered two fundamentally different cases depending on parameters and illumination. We depict the consistency measures dependence on time for both cases in Figure 5.21. The set of parameters for these two cases are feedback strength $\beta = 1.0$, phase shift $\phi = 25$, and injection strength $\gamma = 1.0$ and 0.5 for the high and low correlation cases, respectively. In the high correlation case we observed very high short time consistency and a high long time consistency that decays over time. This high consistency case shows that short time consistency can remain above 0.99 for long periods of time. Long time consistency in this first case decays over time, which indicates that the dynamical evolution changes by small amounts over time. Starting as high as short time consistency, long time consistency smoothly reduces to 0.975 after 15 hours. These changes are related to the accumulated differences observed in the short time consistency. These factors can lead to divergence of two chaotic dynamics, so two realizations of the experiment with identical injection and initial conditions can generate two different time traces, and limit the consistency attainable with a setup. Additionally, oscillations can be observed in the time evolution of both consistency measures. The period of such oscillations is around one hour, and the long term oscillating behavior indicates its origin is not dynamical (since the dynamical system stops and restarts multiple times in between). We speculate its origin to lie in the control module of the SLM or in changes in the room temperature via its climate control system, as temperature can affect the SLM liquid crystal cell properties. In the low correlation case we observed that both consistencies remain in a range with smaller consistency values compared with the other case. In this case we observe both consistency measures around a value of 0.85 during the whole evaluation. Short time consistency again exhibits similar values over time as compared to the previous case, indicating that dynamics differ in the same degree from the previous ones. But long time consistency also exhibits similar values, indicating that consecutive time traces differs from the previous ones as much as the last one differs from the first. So the degree of difference between dynamical evolution is time invariant in the time frames considered here.

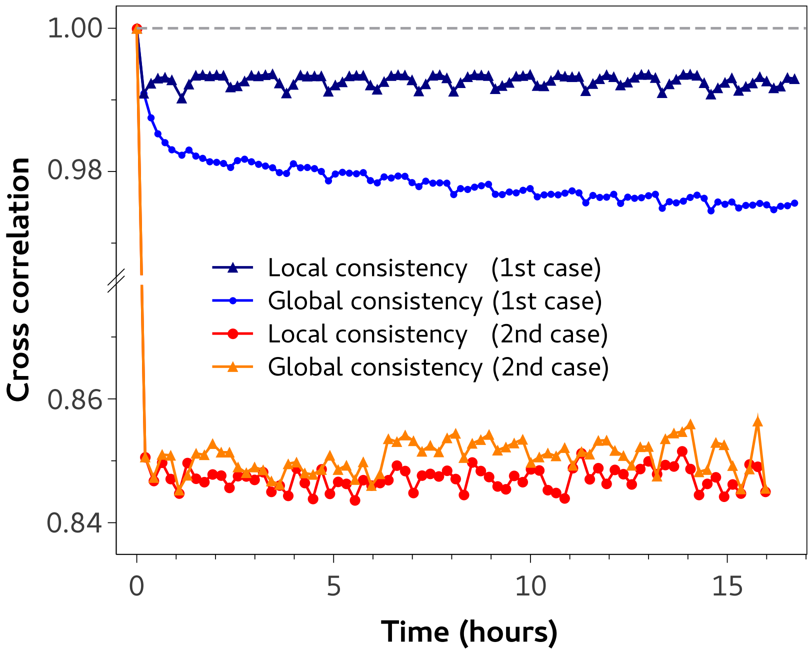

Figure 5.21: Consistency correlation over time of the dynamics of the reservoir under injection. Warm colors relate to the case of low consistencies, while cold colors relate to the case of high consistency. Circles indicate long time consistency, while triangles indicate short time consistency. The gray dashed line for consistency correlation equal to 1 indicates the maximum value for consistency. Lines between points are guide to the eye.

To observe the impact of consistency on the processing performance in our system, we use the temporal evolution considered to measure consistency in Figure 5.21, now for an information processing task. The task considered is the Mackey-Glass time series prediction task, and we use offline learning techniques to obtain and implement the readout layer weights. Details on the procedure and task can be found in Section 4.3.4. Even though here we apply offline learning, ultimately the goal in our system is to implement online learning techniques. These techniques require to consecutively recreate a dynamical evolution and evaluate how optimal a set of nodes is. Therefore, these techniques need the system to reproduce a dynamical response during all the training, and consistency is even more important then. A dynamical evolution may take several minutes, so a training involving hundreds or thousands of output weight evaluations could take days or more. During this time, the system needs to remain consistent so the learning is done on the same reservoir's response.

In Figure 5.22 we show the resulting NMSE of the test data set on the high correlation case. To assess the impact of consistency on performance, we use the first dynamical response to train the system. The training delivers an optimal set of output weights for that particular dynamical evolution. Then we use the same output weights on the other dynamical responses. Perfectly consistent responses would provide a dynamical evolution from the reservoir identical to the first one, so the output weights obtained for the first evolution would be also optimal for the second until the last evolution. When dynamical evolutions differ one from another, the output weights calculated for one may not be optimal for the other. Such situation would be visible as an increase of the error on the test data set. We compare these errors (the errors obtained using the output weights from the first evolution in all following evolutions) with the error obtained by using the optimal weights especially obtained for every individual case. These errors are shown in Figure 5.22. We can see the high correlation case shows low test errors when optimal output weights are calculated for every individual evolution (individual W_{out} in Figure 5.22). But as soon as we use the output weights calculated from the first evolution (constant W_{out}), errors progressively increase stabilizing over time around $NMSE = 0.1$. This behavior resembles the consistency dependence over time but vertically mirrored, indicating that changes in consistency directly alters performance. The error dependence also exhibits oscillations, with a period of around one hour, as we similarly observed for consistency. This is a clear observation of the impact of consistency on the performance of the system, and how degrading inconsistent behavior can be for the training.

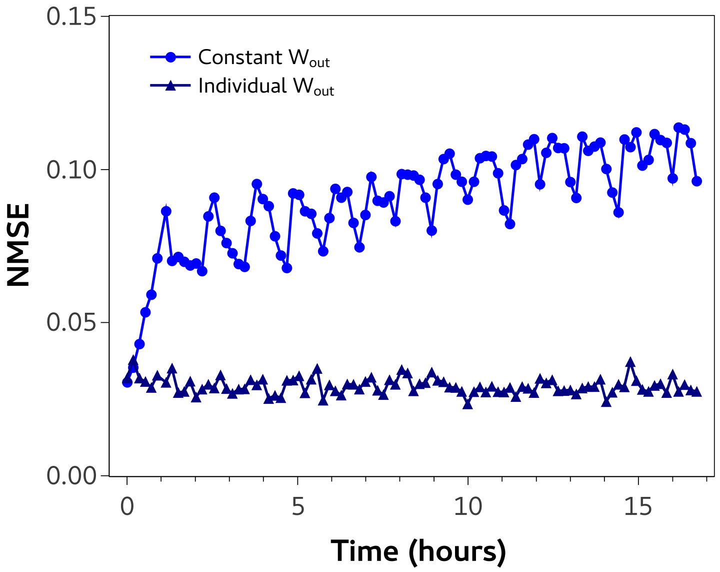

Figure 5.22: Impact of consistency on the learning. Test errors for the case of high consistency, using output weights calculated specifically for that case (triangles) or using the ones calculated from the first case (circles). Lines between points are guide to the eye.

Learning, therefore, needs to be faster than the degrading inconsistency. Any system that is not completely consistent would require some re-training after some time, but if the system forgets too fast then no optimized output weights can be obtained. Techniques previously explained in Section 5.3.2 and in Section 5.3.3 help accelerate learning to overcome inconsistency effects. The results in this section help provide a measure to determine from the beginning conditions that are promising for operation of the reservoir computer, and understand the need for fast and efficient learning techniques.

5.6 Simulated learning

With a knowledge of basic properties of the system, we focus now on making the system learn. In this section we perform simulations of the output layer and present a comparison with experimental results. Use of simulations is motivated to optimize our efforts, as they allow to evaluate the performance of the system in parameter space in less time and choose the most advantageous parameters for experimental realizations. This especially holds since there is no guarantee of a low converging error at the end of the experiment. To optimize our efforts we simulate the output layer to estimate beforehand the error for a set of parameters. In this way, we can know if a point of parameter space can provide a lower error than a linear memoryless reservoir and obtain the best learning parameters for the fastest learning.

For our simulations we need the reservoir evolution under information injection for a set of parameters. We decided to use the recorded state from the experiment as the learning is the real time-consuming part and the data makes sure all experimental effects are included. One could use this temporal evolution for information processing through an output layer. The recorded states at the camera are, however, not what arrives to the experimental output layer. One needs to transform the recorded intensity measurement as showed in Equation (5.7).

$$x_i'(j+1) \quad = \quad P_i\,(1 - f_{nl}(\ \beta\, x_i(j)\ +\ \gamma\, W_{in}\, S(j)\ +\ \phi\ )) \tag{5.7}$$

Parameter β is the feedback strength, ϕ as the offset bias of the cells under rest conditions, $x_i(j)$ is the dimensionless intensity measured by the camera for each node i at time step j, γ is the input injection strength, W_{in} are the input weights, and $S(j)$ are the injected data stream. Function f_{nl} is the nonlinear transformation the reflected light from the SLM goes through. The maximum power available for each node P_i. The next state of the SLM is calculated as in Equation (5.6), and we apply the transformation corresponding to passing through the PBS. Function f_{nl} is calculated by fitting the transmission curve in Figure 5.5 with a sin^2 function. We calculate $1 - sin^2$ to obtain the signal component that goes towards the output layer when separated by the PBS. Last, the simulated state of every node is multiplied by the maximum power available for each node P_i. Then we apply the learning rules described in Section 5.3 to find an optimal output weight set. This learning process is easily implemented via computer program. We also added white Gaussian noise in our simulations to account for inconsistencies in the network state $x_i(j)$ and in the final output $y(j)$. The network state shows a small level of inconsistency even in the best case, while the output of the output layer also presents some noise. For both cases, noise was implemented using a MATLAB function. The noise strength was set to obtain time traces with consistency correlations that equal the ones obtained experimentally.

5.6.1 Simulation versus Experiment

Here we present a comparison of the learning process from experiments with simulations of the learning on experimental reservoir dynamics recorded under identical parameter conditions. Results are shown in Figure 5.23. The experiment and simulations made use of the methodologies introduced in Section 5.3. Learning was simulated 1024 times to obtain a statistical representation of the learning evolution. Feedback strength was set to $\beta = 1.4$, injection strength to $\gamma = 0.8$, and phase shift to $\phi = 25$. These parameters showed experimental network states with consistency correlations of 0.985. We injected 150 values from the Mackey-Glass time series leaving the first 20 out to discard the transients. In Figure 5.23 we can see the experimental and the average simulated learning. The average learning evolution is placed inside a colored region delimiting the error range of one standard deviation. The train error in simulations and experiment starts high, around $NMSE = 1.2$, and coincidentally close. A broad initial error in simulations originates from the different random matrix for the output weights generated at the beginning of the learning, which identically occurs in experiments. As learning progresses, errors in both cases reduce at a similar pace, indicating that the simulations represents the experimental learning evolution at its initial stages. In the inset of Figure 5.23 we can observe the learning progression during a smaller number of iterations, where we can see the results of individual learning steps. In both, the experiment and simulation, we can see that at every learning iteration the system shows a different error. The exact error progression for both cases is different since in every learning realization the sequence of output weights to change is different. Upon every learning step, the error changes in both cases by a similar small amount compared to the absolute value. Such small change is due to changing only one output weight value at every iteration, and illustrates the small impact on the final error of changing one out of 900 nodes. Plateaus on the best error are observed where the system tried configurations of output weights that were not better than the current best. At the beginning the error by the system experiences a steeper slope, since finding a better configuration is easier. At around 300 learning iterations we observe that the two curves separate beyond one standard deviation. Experiments see its improvement pace slowed down compared to simulations. At the last stage of the learning the system has already a closer-to-optimal configuration, and finding a better one is significantly more difficult. In this last stage we observe a difference between the error obtained for the experiment and simulations.

Simulation reaches an average error slightly below the one of a linear reservoir ($NMSE = 0.17$), which is where performance converges and no further improvement is achieved by learning. In this late stage, the difference between simulations and experiment reduce through learning since the experiment keeps improving. The experiment did not reach the same low error level, but approached it in an asymptotic fashion reaching below 0.21 after 1000 learning iterations. We do not know, whether the system would reach the same error level as the simulation, but it is clear that the system is capable of learning thanks to the hardware and the implemented learning techniques. Additionally, the simulations are capable of producing similar learning evolution to experiments by using the experimental network state, providing an idea of the final error and learning rate.The discrepancy in the final error is small, and the simulation can provide a good estimation of the final error to focus our efforts in regions with low final errors. Nevertheless, the system does so far not operate better than a linear reservoir. That indicates that with the help of simulations we need to find adequate parameters where the system actually reaches lower NMSE values than the one for a linear reservoir.

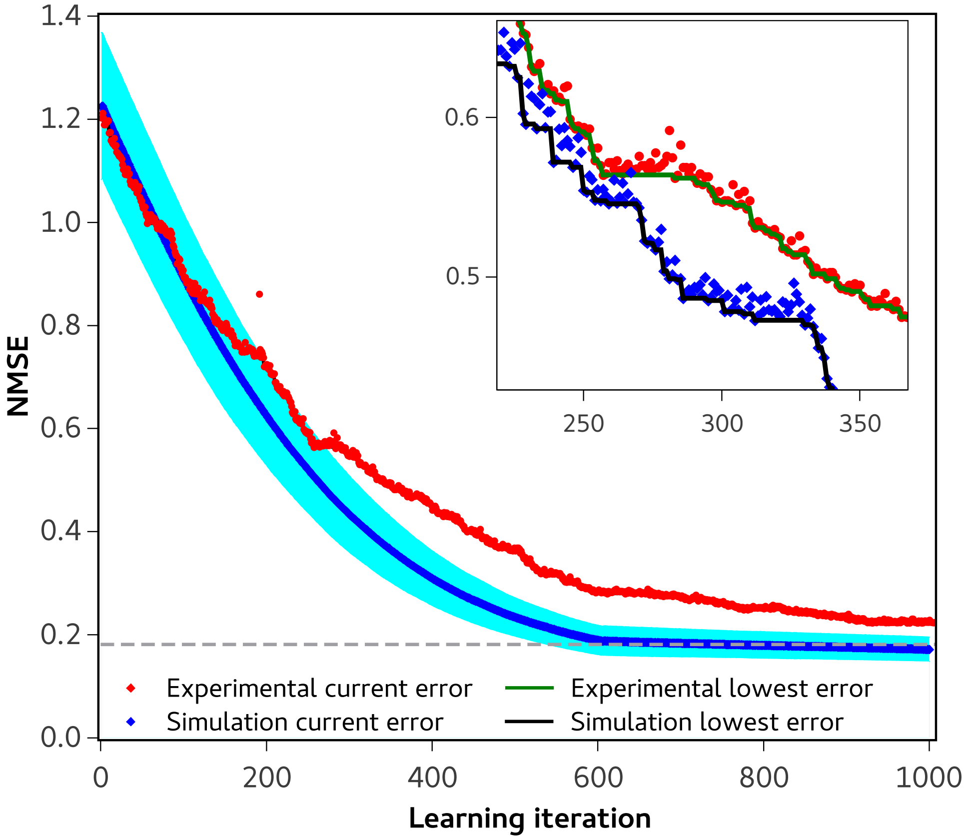

Figure 5.23: Learning evolution of an experimental case and simulations using a network state recorded from the experiment. Individual dots represent the error obtained at a certain learning iteration for the experiment (red circles), and average error from simulations (blue diamonds). The cyan area covers the vertical distance of one standard deviation of the error calculated from multiple learning simulations. The horizontal dashed gray line delimit the NMSE of a linear reservoir. The inset depicts a zoom on the curves in a smaller region and shows for simulations only one evolution as an example. Individual dots represent the error progression for the experiment (red circles), and for the one simulation (blue diamonds). Lines represent the lowest error achieved by the experiment (dark green) and the simulation (black) so far.

5.6.2 Parameter dependencies

Once we have properly simulated the output layer of our reservoir computer, we simulate the learning and the final error using just one response of the reservoir to the injected information. First we evaluate the final error in the injection gain γ and feedback gain β plane. We continue to evaluate the reservoir computing performance using the NMSE error from the Mackey Glass prediction task. Injection gain and feedback gain are each scanned in the interval $[0.1, 2.7]$. The phase shift was set to $\phi_s = 25$. The final error obtained after 2000 learning iterations is shown in Figure 5.24. We can observe that for low gains, error is high. For low γ, the impact of injection on the reservoir computer's dynamics or output is unnoticeable, and therefore information is not effectively injected. For very low β and ϕ_s, dynamics are mostly injection and no feedback is present, the reservoir mostly operates as a linear reservoir or as an extreme learning machine. One can observe for intermediate gain values a region of low error, with errors reaching below $NMSE = 0.05$. This region broadens, providing parameter tolerance. As injection or the feedback gain increase too much, the error rises. For high feedback gain, dynamics are dominated by feedback and less by injection. For high injection, the system response goes beyond the maximum value of 255 for the SLM cells, saturating the cells' state value and leading to loss of information in the process. This loss of information results in low prediction performance and errors above $NMSE = 0.2$. In summary, we observe an suitable operation region of low errors in the (β, γ) plane that we can use to address promising experiments.

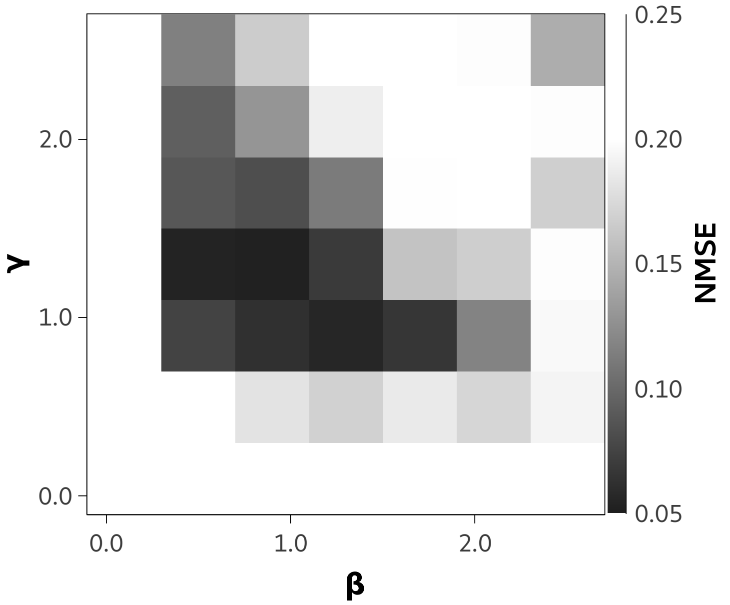

Figure 5.24: Dependence of final error on feedback and injection gains. Phase shift was set to $\phi = 25$. NMSE for the Mackey Glass prediction task obtained after 2000 learning iterations.

Knowing the β and γ values for which the system can exhibit low errors, we optimize the parameter ϕ evaluated in the range $[0, 150]$. Injection gain was set to $\gamma = 0.9$ and feedback gain to $\beta = 1.3$, so the system is operated in the range of low error as shown by Figure 5.24. Results for the NMSE are shown in Figure 5.25. The performance in this task shows low errors around ϕ_s, indicating a region of suitable ϕ values. By looking at Figure 5.5, ϕ_s makes the nodes (when without injection) rest in the linear section of the nonlinear transformation. For lower ϕ, error increases monotonically. For higher ϕ, error increases above linear reservoir performance, $NMSE = 0.17$, and remains there for higher ϕ. This loss of performance is due to a more likely saturation of the SLM cells as ϕ increases. Therefore, increasing ϕ is especially detrimental since doing so reduces the range of values for the SLM cells. We find that our experimental realization shows best performance for $\phi \approx 25$.

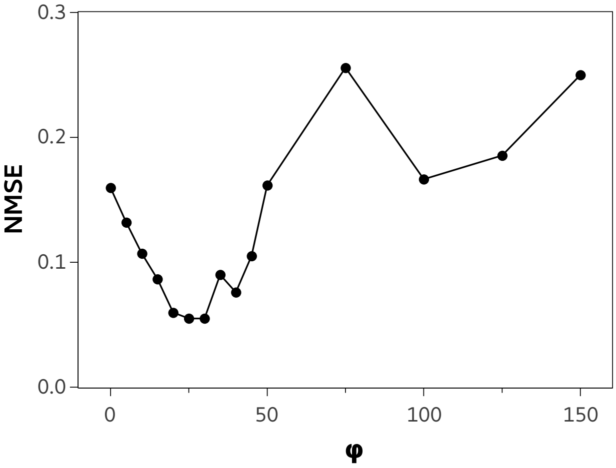

Figure 5.25: Dependence of final error on phase shift parameter. Injection gain was set to $\gamma = 0.9$ and feedback gain to $\beta = 1.3$. NMSE for the Mackey Glass prediction task obtained after 2000 learning iterations.

5.7 Experimental results using optimized parameters

We have seen that the system can successfully learn, resulting in lower errors over time. Now we know promising regions in parameter space thanks to learning simulations based on experimental reservoir dynamics. In this section we use this knowledge to experimentally operate our system with favorable parameters. Results of this section are presented in Figure 5.26. We choose the parameters in the system to target the region of low errors shown in Section 5.6.2. First, we set the task for our system to recognize the input that has been just been injected. The aim of using this task is to ensure the output layer is capable to reconstruct the information being injected and up to what level it is capable of doing so. We injected 150 consecutive points of the Mackey Glass time series, where the first 30 are considered transients of the system and therefore discarded for computation. Parameters were $\beta = 1.4$, $\gamma = 0.8$, and $\phi = \phi_s = 25$. The attained errors for this task are shown as the blue dots in Figure 5.26. One can observe that the system initially started from an error close to NMSE$= 1$, and the error progressively decreases until right under 0.03 after 2000 learning iterations. During the first 500 iterations, the error decreases substantially. Then the rate slows down and the system approaches asymptotically to the lowest error. We stopped the experiment after 2000 learning iterations, where the error amounted to $NMSE = 0.028$. We used 2000 additional points of the Mackey Glass time series to test the learning of the system on a new unseen data set. The error obtained was $NMSE = 0.040$. Next we set our system to predict the next value of our chaotic time series using the same parameter and procedure as before.. In Figure 5.26 we can see the error evolution in red. Starting high, around $NMSE = 0.6$, the difference between initial errors on both tasks originates from the initial random matrix generated for the output weights. Again we see that from the initial output weights, the system is capable of improving the configuration through learning iterations. The decreasing rate of the error is similar compared to the previous task. After 600 iterations, the system is close to its lowest error, $NMSE = 0.072$. After this point, we observe that new attempts to decrease the error result in an error slightly higher than the lowest attained, where the system remains. Simulations predict an error of $NMSE = 0.052$, which is slightly smaller than the one experimentally obtained. The system stagnated at this performance and therefore was stopped after slightly more than 1000 learning iterations. The learning was tested using 2000 unseen consecutive Mackey Glass values of the time series and the configuration of output weights that provided the lowest error, which provided a test error measure of $NMSE_{test} = 0.083$. It is worth noting that errors obtained by the system at the end of the learning were $NMSE = 0.0816$. This indicates the actual difference between the training and testing is even smaller. So indeed the system experimentally demonstrates learning and reservoir computing processing capabilities to predict chaotic evolutions.

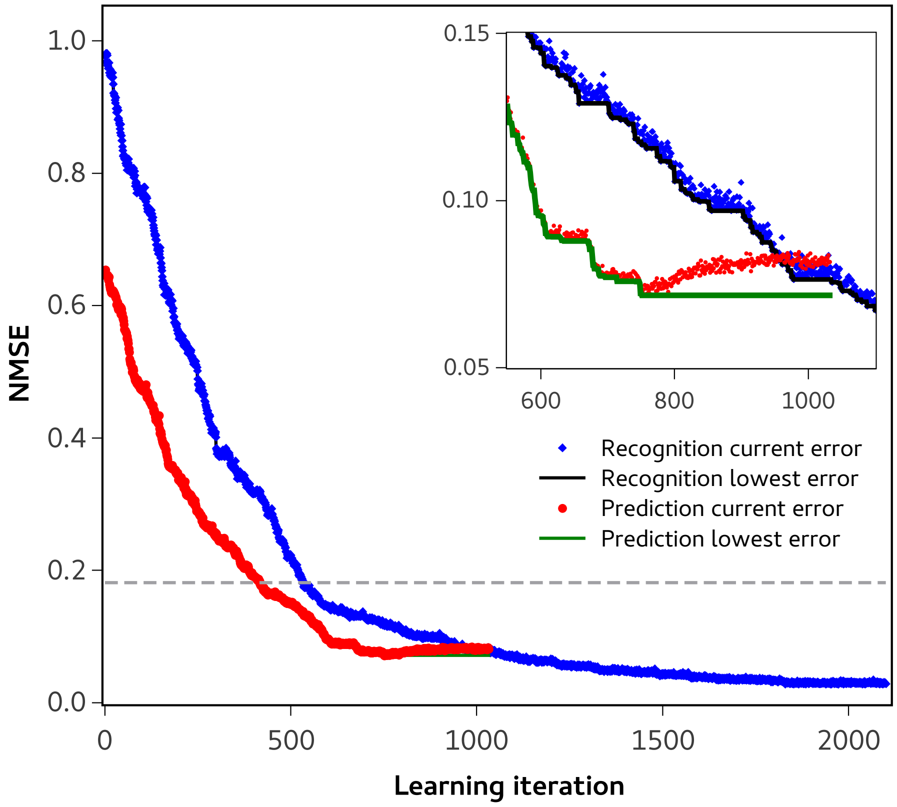

Figure 5.26: Experimental learning evolution for recognition (blue data) and prediction (red data) using optimized parameters. Green and black lines corresponds to the lowest error achieved so far for prediction and recognition, respectively. The horizontal dashed gray line delimit the NMSE of a linear reservoir on the prediction task. The inset depicts a zoom on the curves in a smaller region.

5.8 Summary and discussion

In this chapter, we demonstrated an experimental optical reservoir computer based on a spatial reservoir. The aim was to design and build several parts optically, develop learning tools, and demonstrate information processing using an optical reservoir and an optical readout layer. We realized a spatially extended optical reservoir using a SLM device to implement the individual nonlinear nodes of the reservoir. We showed how the reservoir realizes multiple independent nodes with nonlinear dynamics and how the nodes can be coupled to create a network. The input layer was realized digitally, and was designed with properties based on a possible experimental optical input layer. An experimental output layer was installed in our setup, and proved suitable even in our configuration. The study of the properties of the system demonstrated that the system can perform reservoir computing and learn to continuously adapt its own weights for the task at hand. The reservoir computer exhibited experimental errors down to $NMSE = 0.07$, with a test error of 0.08. These results demonstrates that we successfully implemented an optical recurrent neural network of hundreds of nonlinear nodes, capable of information processing using reservoir computing techniques. In the following we summarize the different points of the research in the order they were presented in the chapter, and discuss them individually.

We have created a spatial reservoir, with differentiated nodes in space based on the pixels of the SLM. Their polarization modulation properties have been employed together with a PBS to implement a nonlinear transformation. The generation of dynamics has been possible by recording the network state with a CMOS camera and using this information to update the nodes to a new state. We used a DOE to combine light from neighboring nodes, creating coupling among them. Different dynamical regimes, including chaos, were observed at different illumination conditions and different parameters. This shows the system's adaptability to different conditions, as parameters can be readjusted to recover desired dynamical properties. Since the SLM polarization rotation is wavelength dependent, the nonlinear transformation can be tuned. Nevertheless, even though a proof of concept, our experiment presents some limitations that can be addressed in future works. For example, the SLM has only 8 bit resolution. Another inconvenience is the slow update time of the reservoir, which controls the computing time of the reservoir. The presented approach works at approximately 2 Hz rate, so every input is computed in roughly 0.5 seconds. This rate is tremendously slow compared to current computing devices. Even though computing speed was not one of our goals, it is an obvious desire that future optical reservoir rely on faster mechanisms. The use of a SLM offers extension possibilities to the reservoir, like implementing a large amount of individually addressable nodes for the reservoir. In the present work we implemented 900 nodes, which is limited by the illumination conditions. By using optical components with bigger numerical aperture, larger areas of the SLM could be illuminated to increase the numbers of nodes available for the reservoir. Fortunately, the use of a DOE to implement the node's connectivities would already provide the coupling to these extra nodes. The large variety of DOE and customization possibilities could allow for many different connectivities to and within the reservoir, ranging from increasing the number of connections for every node, to extending the connection range or creating connections at multiple scales. Another improvement in the system could come from substituting the digital input layer currently in use by an optical one. Optical implementations of the input layer are desired, and would turn the presented system into an electro-optical reservoir computer where information is injected and extracted optically. Regarding the output layer, we showed how it can be implemented using a DMD and a lens. The characteristics of the DMD turn this device into a versatile component, as it allows the output weights to be individually addressed and easily reconfigured. These properties provide high capabilities for an output layer, as updated configurations of output weights can be easily applied without changing components. Furthermore, the use of a DMD offers unexplored possibilities to implement the output weights. In the present work we kept the output weights to its simplest form, as they were binary: the node contributes (1), or it does not (0). This limits computation and performance. As our output weights are Boolean, they have not negative or rational values. Implementation of such possibility would improve the performance of our reservoir computer, and can be approached in future work. Generating rational output weights in our setup can be implemented in two different ways. One way would be to use only a fraction of the mirrors associated with every node to represent output weight values. For example, when $W_i = 0.5$ only half of the mirrors for node i could be oriented towards the summation lens, when $W_i = 0.25$ a quarter of the mirrors, and so on. Another option to implement rational positive output weights is to flip the mirrors of the DMD multiple times inside every discrete time step of the reservoir computer. By having the mirror change its orientation faster than the discrete time of the reservoir, the effective value of the output weight would be the fraction of time the mirror has been oriented towards the lens. This is experimentally possible by using special libraries for fast operation, which can turn the mirrors of the DMD at 32 MHz [287]. Both approaches to extend the output weight's possible values could be applied simultaneously. Under this approach, nonetheless, one would need lower noise impact on the overall system. In our realization, observing the changes in the output due to changing one output weight value needed the sensor to average 1000 measurements. Using rational output weights would probably require even more averaging. This averaging already slowed down significantly the system overall, so a system employing higher resolution weights will strongly benefit from using power sensors with higher power resolution, especially if they are faster.

We also introduced learning techniques to find optimized output weights. We relied on a simple reinforcement learning based technique, where we tried different configurations of output weights, evaluated their performances, and updated the optimal configuration accordingly to the new performance compared to the previous one. We observed that the attained learning speed was sufficient for the system to efficiently learn. If this wasn't the case, or just faster learning were required, implementation of more sophisticated learning techniques could be implemented as the system offers the flexibility to implement other techniques. We complemented the research by simulating the output layer and the learning evolution of the system while using experimentally obtained reservoir data in order to infer the final error in the reservoir's parameter space. These simulations provided a map for the parameter space indicating where the reservoir computer could exhibit low prediction errors. Simulation of the reservoir, and later of the entire reservoir computer, may help identify better operation conditions and evaluate different learning algorithms, accelerating further the process.

To conclude, the different components performed successfully their roles in the optical reservoir computer, and successful nonlinear prediction was experimentally obtained. The system described here performed as intended in its simplest configuration, and allows for multiple improvements that could expand its capabilities. Many of the described solutions can also be implemented in future works, with identical or similar components, extending the reach of the present research.

Chapter 6

Final Summary and Outlook

6.1 Summary

Delay systems exhibit a broad range of complex dynamics, and photonic systems have proved to be excellent testbeds to observe such dynamics. In this thesis we have experimentally explored the dynamics of optical delay systems with dual delays of very different amount, and exploited the nonlinear dynamics of optical delay systems for information processing.

In Chapter 3 we studied the dynamics of a semiconductor laser under the influence of two optical delayed feedbacks. The delays were chosen at different scales, where the second delay time is orders of magnitude larger than the first delay time. We studied the dynamics by using a 2D pseudo-space representation of the evolution of the intensity emitted by the semiconductor laser, which allowed to differentiate dynamical regimes and identify key features. We focused on two dynamical regimes, one characterized by Spiral Phase Defectss and another by Defect-mediated Turbulence. In our experiments we did not observe PD, and we discussed how this could be due to the very restricted conditions needed to observe them. DT was observed in a broad parameter range, which allowed for a more detailed analysis. The system exhibited spatio-temporal chaos over a large parameter range, and consecutive representations allowed to see how the dynamical structures evolved over long periods of time. We also studied the DT dynamics using intensity distributions and spectral analysis. The spectral analysis showed the spectral components of the dynamics exhibit an exponential decay for low bias currents of the semiconductor laser. As bias current of the semiconductor laser was increased, the spectral components exhibited a double power law that merged into a single power law for higher bias currents. This research showed how the semiconductor laser can exhibit new dynamical regimes by simply adding an extra delay to the system. Furthermore, the research showed the connection between delay systems and spatially extended systems, and that homogeneous spatial systems could be studied in the future thanks to delay systems with multiple delays.

In Chapter 4 we studied the use of a semiconductor laser under delayed optical feedback and optical injection as a delay-based reservoir computer. We chose this system as it already demonstrated successful reservoir computer operation and the ultra-fast complex dynamics that it can exhibit makes it very promising for reservoir computing. We focused on the fundamental properties of this photonic system and on further capabilities. We investigated the properties of injection locking, consistency, and memory, and evaluated the performance of the system on a prediction task. Memory and consistency properties were understood from a dynamical point of view and linked to the injection locking properties. Good prediction was observed where the system exhibited a balance between consistency and memory properties, indicating that both of them are necessary for success on a prediction task. These results were consistently obtained as we evaluated the impact of other critical parameters in the photonic system. The parameter evaluation also showed an acceptable parameter tolerance for optimized operation. Subsequently, we extended the capabilities of the system. We demonstrated that this photonic reservoir computer is capable of processing information at 20 GSa/s, in our case limited by the instrumentation, with similar performance compared to slower speeds. Maintained performance at faster modulation indicates that information processing devices based on semiconductor lasers might operate at even higher speeds. Fundamental properties were also evaluated in a much wider optical frequency span, showing that suitable properties and good prediction performance can be observed when the injection is hundreds of GHz detuned from the solitary emission of the semiconductor laser inside the reservoir. This opens the door to injection at multiple wavelengths, where the reservoir acts on a single or multiple injected channels simultaneously. Last, we demonstrated how one can create a delay-based reservoir with nodes with different sets of properties, i.e. heterogeneous reservoirs. In this case, we accomplished it by additionally modulating the injection current of the semiconductor laser using a square waveform. The resulting reservoir exhibited an improved prediction performance and parameter tolerance compared to the same reservoir without the bias current modulation.

In Chapter 5 we discussed the design and implementation of an spatially extended Recurrent Neural Network consisting of hundreds of coupled nonlinear nodes, implemented an output layer, and demonstrated successful operation in a prediction task. The reservoir was realized with a Spatial Light Modulator, where pixels corresponded to individual nodes, and coupling was achieved with a DOE. The nonlinear properties were implemented by using a PBS together with the polarization modulation available with the SLM. Dynamics were realized by measuring the state of the nodes and feeding it back electronically to the SLM. The nodes in the reservoir exhibited nonlinear dynamics, and high connectivity was achieved connecting nodes beyond nearest neighbors. The input layer was implemented digitally in this study. The output layer was implemented with a DMD and a lens, where the use of a DMD allowed the output weights to be reconfigured simultaneously. We introduced a set of learning rules based on reinforcement learning, which controlled the state of the DMD and therefore the output weights in the reservoir computer. We simulated the learning to aid our experimental efforts and chose optimal parameters for the system. Despite limitations like the Boolean output weights, our system succeeded to learn and to achieve very low errors in a prediction task. This work demonstrates that large reservoirs are possible without using hundreds of individual components for every node, and a strong connectivity and parallel output layer can be devised with off-the-shelf components.

6.2 Outlook

We have obtained many interesting results through our study of delayed optical systems. But while we were doing so, we unveiled new questions that are so far left unanswered.

In future studies of the dynamics of a semiconductor laser under the influence of two optical delayed feedbacks, special efforts could be made to observe the PD. This could be addressed by choosing components and instruments with the intention to increase the probability of observing the PD. Deeper evaluations of the impact of different feedback strengths and distributions across the delays could be addressed, since in our case we were restricted to the maximum attained feedback and identical feedback strengths. Increasing the ratio of delay times (together with the memory depth of the oscilloscope) would provide 2D representations with higher vertical resolution. This would provide better resolved dynamics. One could also further analyze the dynamics with techniques borrowed from other fields like fluid dynamics, where spatio-temporal chaos have been studied for long time. And eventually, addition of extra longer delays would allow to study spatial systems in three and higher dimensions with a purely temporal system, where the nonlinearity could be provided by the semiconductor laser or any other photonic device of choice.

Regarding the use of a semiconductor laser under delayed optical feedback and optical injection as a delay-based reservoir computer, we mentioned several interesting directions of future research. We discussed the possibility of implementing this system in WDM setups thanks to locking properties of the reservoir to injections hundreds of GHz away from solitary emission. It would be very interesting to study the behavior and performance of the reservoir with data from real optical communications systems. Another idea we presented was the use of heterogeneous reservoirs. This idea deserves deeper study, as even though our investigation was in a limited parameter range, it provided promising results. Reservoirs with more node diversity could be used, and different approaches to implement them could be explored. One extension of high interest to this system is the realization of an optical output layer. In the current work this element was realized digitally and offline. An experimental optical realization of the output layer would allow the system to become a fully optical information processing device, where the input as well as the output would be optical. This would be a final step toward real-time information processing, making the system even more attractive for real-life applications.

Our implementation of a spatially extended reservoir offers exciting work for future research. One opportunity is to extend or change the connectivity of the network with other DOEs. The most interesting directions would involve for example controlling the DMD in the output layer to implement rational values for the output weights. This would avoid a strong limitation in the performance of the reservoir, without having to change a single element in the experimental setup. Implementation of an optical input layer would also be highly interesting. This could be implemented by spatially spreading the injected information with a consistent and complex distribution. This input layer could also be designed to inject more than one value simultaneously to provide for multiple inputs.

Albeit the research carried out in this thesis exhibits many interesting avenues for future work, highly attractive research can originate from combining the knowledge from different chapters. The number of delays in our delay-based reservoir in Chapter 4 could be increased to create a reservoir like the one in Chapter 3 but including optical injection. With this expansion, the system would employ the rich landscape of complex spatio-temporal dynamics we witnessed for information processing purposes. Additionally, the network of virtual nodes in such system could have a different structure, in this case a waterfall network where every node is under its own feedback (similar the one proposed in [160] but including the feedback). The number of nodes and the connectivity could increase significantly. A promising line of research would be to replace the spatially extended reservoir in Chapter 5 by a network of autonomous photonic devices with nonlinear behavior. And one could use semiconductor lasers with delayed optical feedback and optical injection for that purpose. Since injection would be optical, every node in the reservoir would be like the whole reservoir in Chapter 4. The nodes would then exhibit similar complex dynamics to the ones we used, which demonstrated suitable for information processing. The spatially extended reservoir would also then operate at GHz speed, compared to the current Hz speeds, immensely boosting computing volume. Furthermore, one could even imagine extending the number of delays for each node in such spatially extended reservoir in an effort to combine all the work along all this thesis.

To conclude, we have investigated the delay dynamics of photonic systems with one or multiple delays, and have used the delay dynamics of optical systems for information processing using neural networks techniques. We focused on the complex dynamics of these configurations and took advantage of them to demonstrate functionality and flexibility. The possibilities for improvement and new research are various, particularly due to the interdisciplinary nature of this work.. We wish for these ideas to see the light, not only because of the scientific interest in them, but also for the promising benefits that they might provide to a broader field of sciences.

List of Figures

1.1 Schematic of an experimental setup in delayed feedback experiments using optical fiber components. 20
1.2 P-I curve and example of power time series for the SL for solitary and with optical feedback 22
1.3 Power spectra of the SL with different feedback conditions . 23
1.4 Optical spectra of the SL with different feedback conditions 24
1.5 Example of an ANN 27
1.6 Example of a RNN 30
1.7 Illustration of the TDR 33
1.8 Illustration of the masking process 34

2.1 Detection section of the setup 41
2.2 Illustration of the pulse propagation method for time delay measurement 43

3.1 Scheme of the experimental setup with the two delay lines . 51
3.2 P-I curves of the SL for the three different feedback conditions 52
3.3 Experimental dynamics in the PD parameter range 55
3.4 Close up on a PD candidate. 55
3.5 Single frame of the 2D representation of the turbulent spatiotemporal dynamics of the delay system for $I_r = 11.75$ mA. 57
3.6 Zoom into the turbulent spatiotemporal dynamics for $I_r = 11.75$ mA. 57
3.7 Single frames of the 2D representations of the turbulent spatiotemporal dynamics of the delay system for $I_r = 12.00$, 12.40 and 13.00 mA. 59
3.8 Zoom into the turbulent spatiotemporal dynamics for $I_r = 12.00$, 12.40 and 13.00 mA. 60
3.9 Histogram of the intensity values for $I_r = 11.75$ mA 61
3.10 Histogram of the intensity values for different bias currents 62

3.11 Spectra of the dynamics in semilogarithmic axis for different bias currents 64
3.12 Spectra of the dynamics in double logarithmic representation for different bias currents 66
3.13 Power-law slopes of the spectra with a power law dependence in the GHz and the supra-GHz range for different bias currents. 67

4.1 Scheme of the experimental setup 74
4.2 Learning curves depicting the error performing a Mackey-Glass prediction task versus the amount of samples used for training and testing 80
4.3 Diagram of the memory correlation concept 85
4.4 Examples of the chaotic systems employed as prediction targets 87
4.5 Optical spectra of optical injection, reservoir with and without optical injection 90
4.6 Locking cases in the $(\Delta\nu, \eta)$ plane for $I_{bias} = 11.10$ mA and $\bar{P}_{inj} = 0.7$ mW 91
4.7 Optical spectra of the response system representing partial locking for positive and negative frequency detuning 92
4.8 Consistency correlation dependence in the $(\Delta\nu, \eta)$ plane . . . 93
4.9 Persistence plots of the reservoir responses under modulated injection 95
4.10 Memory correlation dependence on $\Delta\nu$ for increasing memory time steps 97
4.11 Memory capacity in the $(\Delta\nu, \eta)$ plane 98
4.12 Normalized Mean Square Error (NMSE) of the Mackey-Glass prediction task. 100
4.13 Examples of predicted time traces for different reservoirs and parameters 101
4.14 Dependence of the fundamental properties and task performance of the system on I_r and $\bar{P}_{inj}$ for $\Delta\nu = -20$ GHz . . 104
4.15 Dependence of the fundamental properties and the task performance of the system on I_r and $\bar{P}_{inj}$ for $\Delta\nu = -30$ GHz 106
4.16 Properties of the reservoir computer depending on frequency detuning for optical signal injection around different longitudinal modes 109
4.17 Performance of the reservoir computer using averaged responses 111

4.18 Properties and performance of the reservoir computer at faster modulation rates . . . 114
4.19 Prediction performance of the reservoir computer for higher modulation rates . . . 116
4.20 Diagram of the creation of a heterogeneous time delay reservoir by modulation of the current of the RL . . . 117
4.21 Experimental temporal evolution of the output power from the heterogeneous reservoir without optical injection . . . 118
4.22 Memory correlation curves of the heterogeneous reservoir . 120
4.23 Prediction performance for the Santa Fe prediction task comparing the homogeneous and the heterogeneous reservoir . . . 121

5.1 Simplified scheme of the experimental setup with grouped components . . . 130
5.2 Illustration of illumination of the SLM . . . 132
5.3 Scheme of the experimental setup used to observe the illuminated area on the SLM . . . 133
5.4 Images by the CMOS camera of the illuminated SLM with different configurations . . . 135
5.5 Intensity transmitted through the PBS. . . . 136
5.6 Illustration of the DOE splitting the light beam into diffractive orders . . . 138
5.7 Coupling principle using a DOE . . . 139
5.8 Optical setup to create the coupling mechanism . . . 140
5.9 Coupling matrix of the network . . . 142
5.10 Input weights matrix used for the injection layer . . . 143
5.11 Output layer implementation with a DMD . . . 145
5.12 Projection of the output weights matrix on the DMD . . . 147
5.13 Scheme of the complete experimental setup . . . 149
5.14 Node filter on the output weights . . . 153
5.15 Dynamical evolution examples for a node in the network . . 154
5.16 Bifurcation diagram for node (15,12) uncoupled . . . 155
5.17 Bifurcation diagram for different uncoupled nodes across the network . . . 157
5.18 Bifurcation diagram for node (15,12) coupled . . . 158
5.19 Bifurcation diagram for different coupled nodes across the network . . . 159
5.20 Bifurcation diagram for node (15,12) with coupling using different illumination conditions . . . 161

5.21 Consistency correlation over time of the dynamics of the reservoir under injection 163
5.22 Impact of consistency on the learning 165
5.23 Learning evolution of an experimental case and simulations using a network state recorded from the experiment . 169
5.24 Dependence of final error on feedback and injection gain . . 171
5.25 Dependence of final error on phase shift parameter 172
5.26 Experimental learning evolution for recognition (blue data) and prediction (red data) using optimized parameters . . . 174

Abbreviations

ACF Autocorrelation Function (pp. 42, 43)

ANN Artificial Neural Network (pp. 26–29, 34, 35, 185)

AWG Arbitrary Waveform Generator (pp. 75, 97, 110, 112, 116)

BS Beam Splitter (pp. 148, 149)

CGLE Complex Ginzburg-Landau equation (pp. 46, 47, 54, 56, 61, 62, 65, 67)

CMOS Complementary Metal-Oxide Semiconductor (pp. 132, 133, 135–138, 140, 141, 144, 175, 187)

DBR Distributed Bragg Reflector (p. 18)

DFB Distributed Feedback (p. 18)

DMD Digital Micro-mirror Display (pp. 4, 6, 7, 144–148, 152, 176, 181–183, 187)

DOE Diffractive Optical Element (pp. 4, 5, 7, 130, 138–142, 148, 149, 157, 160, 175, 181, 183, 187)

DT Defect-mediated Turbulence (pp. 3, 5, 6, 47, 56, 68, 180)

ESA Electrical Spectrum Analizer (pp. 21, 41)

ESN Echo State Network (p. 30)

FNN Feed-forward Neural Network (pp. 27, 29, 30)

IBM International Business Machines (pp. 16, 28)

LASER Light Amplification by Stimulated Emission of Radiation (p. 16)

LC Liquid Crystal (pp. 130, 131, 136)

LiDAR Light Detection and Ranging (p. 17)

LKE Lang Kobayashi equations (pp. 47, 61)

LM Longitudinal Mode (pp. 107–109)

MC Memory Capacity (pp. 84, 97, 98, 103)

MO Microscope Objective (pp. 131–133, 137, 139, 140, 149)

MZM Mach Zehnder Modulator (pp. 43, 75, 117)

ND Neutral Density (pp. 133, 138, 149, 160)

NMSE Normalized Mean Square Error (pp. 86, 100, 103, 105, 108, 111, 113, 115, 150, 164, 168–172, 174, 186)

OC Optical Coupler (pp. 49–51, 75, 76)

OSA Optical Spectrum Analyzer (pp. 41, 42)

OTF Optical Tunable Filter (p. 41)

PBS Polarization Beam Splitter (pp. 4, 5, 7, 130, 132–136, 138, 143, 145, 148, 149, 166, 175, 181, 187)

PD Spiral Phase Defects (pp. 3, 5, 6, 47, 51, 53–56, 68, 180, 182, 185)

PMOF Polarization Maintained Optical Feedback (p. 50)

RC Reservoir Computing (pp. 26, 30–32, 35, 72, 128)

RL Response Laser. The response laser is the reservoir's laser, under optical injection and feedback. (pp. 75, 76, 88–91, 93, 99, 101, 102, 107, 116–119, 121–125, 187)

RNN Recurrent Neural Network (pp. 29–31, 181, 185)

RO Relaxation Oscillations (pp. 18, 22)

SL Semiconductor Laser (pp. 16–26, 35, 36, 40–43, 46, 47, 49–53, 56, 58, 64, 67–69, 75, 185)

SLM Spatial Light Modulator (pp. 4, 5, 7, 130–137, 139–141, 145, 146, 148, 149, 152, 155, 159, 162, 163, 166, 170, 171, 174, 175, 181, 187)

SNR Signal-to-Noise ratio (pp. 41, 50, 68, 99, 107, 117)

SOA Semiconductor Optical Amplifier (pp. 35, 41, 110)

TDR Time Delay Reservoir (pp. 31–36, 75, 128, 185)

WDM Wavelength Division Multiplexing (pp. 107, 123, 182)

Bibliography

[1] B. E. A. Saleh and M. C. Teich. *Fundamentals of Photonics*. Wiley Series in Pure and Applied Optics. New York, USA: John Wiley & Sons, Inc., 1991. DOI: 10.1002/0471213748 (cit. on pp. 16, 21).

[2] W. W. Chow and S. W. Koch. *Semiconductor-Laser Fundamentals*. Berlin, Heidelberg: Springer Berlin Heidelberg, 1999. DOI: 10.1007/978-3-662-03880-2 (cit. on pp. 16, 17).

[3] N. G. Basov, O. N. Krokhin, and P. Y. M. "Production of negative-temperature states in p–n junctions of degenerate semiconductors". *Journal of Experimental and Theoretical Physics* 13.2 (1961), pp. 1320–1321 (cit. on p. 16).

[4] R. N. Hall, G. E. Fenner, J. D. Kingsley, T. J. Soltys, and R. O. Carlson. "Coherent Light Emission From GaAs Junctions". *Physical Review Letters* 9.9 (1962), pp. 366–368. DOI: 10.1103/PhysRevLett.9.366 (cit. on p. 16).

[5] M. I. Nathan, W. P. Dumke, G. Burns, F. H. Dill, and G. Lasher. "Stimulated emission of radiation from GaAs p-n junctions". *Applied Physics Letters* 1.3 (1962), pp. 62–64. DOI: 10.1063/1.1777371 (cit. on p. 16).

[6] T. M. Quist, R. H. Rediker, R. J. Keyes, W. E. Krag, B. Lax, A. L. McWhorter, and H. J. Zeigler. "Semiconductor maser of GaAs". *Applied Physics Letters* 1.4 (1962), pp. 91–92. DOI: 10.1063/1.1753710 (cit. on p. 16).

[7] O. Svelto and D. C. Hanna. *Principles of Lasers*. 4th ed. 1998, p. 628 (cit. on pp. 16, 17, 102).

[8] A. Donges and R. Noll. *Laser Measurement Technology*. Vol. 188. Springer Series in Optical Sciences. Berlin, Heidelberg: Springer Berlin Heidelberg, 2015, p. 422. DOI: 10.1007/978-3-662-43634-9 (cit. on p. 16).

[9] Y. Deng and D. Chu. “Coherence properties of different light sources and their effect on the image sharpness and speckle of holographic displays”. *Scientific Reports* 7.1 (2017), pp. 1–12. DOI: `10.1038/s41598-017-06215-x` (cit. on p. 16).

[10] J. R. Whinnery, J. H. Ausubel, and H. D. Langford. *Lasers: invention to application*. Washington, D.C.: National Academies Press, 1987. DOI: `10.17226/1003` (cit. on p. 16).

[11] J. Duarte. *Tunable Laser Applications*. CRC Press, 2016, p. 444 (cit. on p. 16).

[12] B. P. Abbott et al. “Observation of Gravitational Waves from a Binary Black Hole Merger”. *Physical Review Letters* 116.6 (2016), p. 061102. DOI: `10.1103/PhysRevLett.116.061102`. arXiv: `1602.03837` (cit. on p. 17).

[13] Z. Shirakashi, T. Goto, H. Takagi, Y. Nakamura, P. B. Lim, H. Uchida, and M. Inoue. “Reconstruction of non-error magnetic hologram data by magnetic assist recording”. *Scientific Reports* 7.1 (2017), pp. 1–8. DOI: `10.1038/s41598-017-12442-z` (cit. on p. 17).

[14] P. J. Winzer, D. T. Neilson, and A. R. Chraplyvy. “Fiber-optic transmission and networking: the previous 20 and the next 20 years.” *Optics Express* 26.18 (2018), p. 24190. DOI: `10.1097/01.wnf.0000185825.34819.ba` (cit. on p. 17).

[15] J. Ohtsubo. *Semiconductor Lasers*. Vol. 111. Springer Series in Optical Sciences. Berlin, Heidelberg: Springer Berlin Heidelberg, 2013, p. 579. DOI: `10.1007/978-3-642-30147-6` (cit. on pp. 17–19, 23, 25).

[16] C. Henry. “Theory of the linewidth of semiconductor lasers”. *IEEE Journal of Quantum Electronics* 18.2 (1982), pp. 259–264. DOI: `10.1109/JQE.1982.1071522` (cit. on p. 17).

[17] T. Erneux and P. Glorieux. *Laser Dynamics*. 2010, p. 361. DOI: `10.1017/CBO9780511776908` (cit. on pp. 18, 23, 102).

[18] B. Kelly, R. Phelan, D. Jones, C. Herbert, J. O’Carroll, M. Rensing, J. Wendelboe, C. Watts, A. Kaszubowska-Anandarajah, P. Perry, C. Guignard, L. Barry, and J. O’Gorman. “Discrete mode laser diodes with very narrow linewidth emission”. *Electronics Letters* 43.23 (2007), p. 1282. DOI: `10.1049/el:20072311`. arXiv: `0504102 [arXiv:physics]` (cit. on pp. 18, 76).

[19] K. Lüdge. *Nonlinear Laser Dynamics: From Quantum Dots to Cryptography*. Ed. by K. Lüdge. Weinheim, Germany: Wiley-VCH Verlag GmbH & Co. KGaA, 2011. DOI: `10.1002/9783527639823` (cit. on p. 19).

[20] T. H. Maiman, R. H. Hoskins, I. J. D'Haenens, C. K. Asawa, and V. Evtuhov. "Stimulated optical emission in fluorescent solids. II. Spectroscopy and stimulated emission in ruby". *Physical Review* 123.4 (1961), pp. 1151–1157. DOI: `10.1103/PhysRev.123.1151`. arXiv: `arXiv:1011.1669v3` (cit. on p. 19).

[21] P. King and G. Steward. "Metrology with an optical maser". *New Scientist* 17 (1963), pp. 180–182 (cit. on p. 19).

[22] I. Fischer, T. Heil, and W. Elsäßer. "Emission dynamics of semiconductor lasers subject to delayed optical feedback: An experimentalist's perspective". *AIP Conference Proceedings* 548.1 (2000), pp. 218–237. DOI: `10.1063/1.1337766` (cit. on pp. 19, 21, 51).

[23] C. Masoller. "Effect of the external cavity length in the dynamics of a semiconductor laser with optical feedback". *Optics Communications* 128.July (1996), pp. 363–376 (cit. on p. 19).

[24] J. P. Toomey, D. M. Kane, C. McMahon, A. Argyris, and D. Syvridis. "Integrated semiconductor laser with optical feedback: transition from short to long cavity regime". *Optics Express* 23.14 (2015), p. 18754. DOI: `10.1364/OE.23.018754` (cit. on p. 19).

[25] O. Ushakov, S Bauer, O Brox, H.-J. Wünsche, and F Henneberger. "Self-organization in semiconductor lasers with ultrashort optical feedback." *Physical review letters* 92.4 (2004), p. 043902. DOI: `10.1103/PhysRevLett.92.043902` (cit. on p. 19).

[26] N. Oliver, M. C. Soriano, D. W. Sukow, and I. Fischer. "Dynamics of a semiconductor laser with polarization-rotated feedback and its utilization for random bit generation". *Optics Letters* 36.23 (2011), pp. 4632–4634. DOI: `10.1364/OL.36.004632` (cit. on p. 19).

[27] Y. Akizawa, T. Yamazaki, A. Uchida, T. Harayama, S. Sunada, K. Arai, K. Yoshimura, and P. Davis. "Fast random number generation with bandwidth-enhanced chaotic semiconductor lasers at 8 × 50 Gb/s". *IEEE Photonics Technology Letters* 24.12 (2012), pp. 1042–1044. DOI: `10.1109/LPT.2012.2193388` (cit. on pp. 19, 26).

[28] N. Oliver, M. C. Soriano, D. W. Sukow, and I. Fischer. “Fast Random Bit Generation Using a Chaotic Laser: Approaching the Information Theoretic Limit”. *IEEE Journal of Quantum Electronics* 49.11 (2013), pp. 910–918. DOI: `10.1109/JQE.2013.2280917` (cit. on p. 19).

[29] D. Brunner, M. C. Soriano, C. R. Mirasso, and I. Fischer. “Parallel photonic information processing at gigabyte per second data rates using transient states.” *Nature communications* 4 (2013), p. 1364. DOI: `10.1038/ncomms2368` (cit. on pp. 19, 35, 72–74, 83, 112).

[30] C. Lu, J. Wang, and K. Deng. “Imaging and profiling surface microstructures with noninterferometric confocal laser feedback”. *Applied Physics Letters* 66.16 (1995), pp. 2022–2024. DOI: `10.1063/1.113679` (cit. on p. 19).

[31] F. Y. Lin and J. M. Liu. “Chaotic lidar”. *IEEE Journal on Selected Topics in Quantum Electronics* 10.5 (2004), pp. 991–997. DOI: `10.1109/JSTQE.2004.835296` (cit. on pp. 19, 46).

[32] G. Giuliani, M. Norgia, S. Donati, and T. Bosch. “Laser diode self-mixing technique for sensing applications”. *Journal of Optics A: Pure and Applied Optics* 4.6 (2002). DOI: `10.1088/1464-4258/4/6/371` (cit. on p. 19).

[33] T. Suzuki, T. Endo, T. Iwana, and O. Sasaki. “A tunable external cavity laser diode possessing a stable wavelength”. *Optical Review* 14.1 (2007), pp. 23–28. DOI: `10.1007/s10043-007-0023-3` (cit. on p. 19).

[34] A. Argyris, D. Syvridis, L. Larger, V. Annovazzi-Lodi, P. Colet, I. Fischer, J. García-Ojalvo, C. R. Mirasso, L. Pesquera, and K. A. Shore. “Chaos-based communications at high bit rates using commercial fibre-optic links.” *Nature* 438.7066 (2005), pp. 343–346. DOI: `10.1038/nature04275` (cit. on p. 19).

[35] H. G. Winful and L. Rahman. “Synchronized chaos and spatiotemporal chaos in arrays of coupled lasers”. *Physical Review Letters* 65.13 (1990), pp. 1575–1578. DOI: `10.1103/PhysRevLett.65.1575` (cit. on pp. 19, 82).

[36] K. Hicke, O. D’Huys, V. Flunkert, E. Schöll, J. Danckaert, and I. Fischer. “Mismatch and synchronization: Influence of asymmetries in systems of two delay-coupled lasers”. *Physical Review E - Statistical, Nonlinear, and Soft Matter Physics* 83.5 (2011), pp. 1–11. DOI: `10.1103/PhysRevE.83.056211` (cit. on p. 19).

[37] S. Ohara, A. Karsaklian, D. Bosco, K. Ugajin, A. Uchida, T. Harayama, and M. Inubushi. "Dynamics-dependent synchronization in coupled semiconductor lasers on a chip". 032216 (2017), pp. 1–9. DOI: `10.1103/PhysRevE.96.032216` (cit. on p. 19).

[38] M. Nixon, M. Friedman, E. Ronen, A. A. Friesem, N. Davidson, and I. Kanter. "Synchronized cluster formation in coupled laser networks". *Physical Review Letters* 106.22 (2011), pp. 1–4. DOI: `10.1103/PhysRevLett.106.223901` (cit. on p. 19).

[39] S. Heiligenthal, T. Jüngling, O. D'Huys, D. A. Arroyo-Almanza, M. C. Soriano, I. Fischer, I. Kanter, and W. Kinzel. "Strong and weak chaos in networks of semiconductor lasers with time-delayed couplings". *Physical Review E - Statistical, Nonlinear, and Soft Matter Physics* 88.1 (2013), p. 012902. DOI: `10.1103/PhysRevE.88.012902` (cit. on p. 19).

[40] A. Argyris, M. Bourmpos, and D. Syvridis. "Experimental synchrony of semiconductor lasers in coupled networks". *Optics Express* 24.5 (2016), p. 5600. DOI: `10.1364/OE.24.005600` (cit. on pp. 19, 82).

[41] R. Tkach and A. Chraplyvy. "Regimes of feedback effects in 1.5 um distributed feedback lasers". *Journal of Lightwave Technology* LT-4.11 (1986), pp. 1655–1661. DOI: `10.1109/JLT.1986.1074666` (cit. on pp. 20, 88, 102).

[42] K. Petermann. "External Optical Feedback Phenomena in Semiconductor Lasers". *IEEE Journal on Selected Topics in Quantum Electronics* 1.2 (1995), pp. 480–489. DOI: `10.1109/2944.401232` (cit. on p. 20).

[43] C. Risch, C. Voumard, F. Reinhart, and R. Salathe. "External-cavity-induced nonlinearities in the light versus current characteristic of (Ga,Al)As continuous-wave diode lasers". *IEEE Journal of Quantum Electronics* 13.8 (1977), pp. 692–696. DOI: `10.1109/JQE.1977.1069418` (cit. on pp. 21, 52, 53).

[44] M.-W. Pan, B.-P. Shi, and G. R. Gray. "Semiconductor laser dynamics subject to strong optical feedback". *Optics Letters* 22.3 (1997), p. 166. DOI: `10.1364/OL.22.000166` (cit. on p. 21).

[45] M. van Exter, W. Hamel, J. Woerdman, and B. Zeijlmans. "Spectral signature of relaxation oscillations in semiconductor lasers". *IEEE Journal of Quantum Electronics* 28.6 (1992), pp. 1470–1478. DOI: `10.1109/3.135299`. arXiv: `arXiv:1011.1669v3` (cit. on p. 22).

[46] R. Lang and K. Kobayashi. "External optical feedback effects on semiconductor injection laser properties". *IEEE Journal of Quantum Electronics* 16.3 (1980), pp. 347–355. DOI: `10.1109/JQE.1980.1070479` (cit. on p. 22).

[47] Fischer, G. H. Van Tartwijk, Levine, W. Elsaßer, Gobel, and Lenstra. "Fast pulsing and chaotic itinerancy with a drift in the coherence collapse of semiconductor lasers." *Physical review letters* 76.2 (1996), pp. 220–223. DOI: `10.1103/PhysRevLett.76.220` (cit. on p. 22).

[48] T Heil, I. Fischer, and W. Elsaßer. "Coexistence of low-frequency fluctuations and stable emission on a single high-gain mode in semiconductor lasers with external optical feedback". *Physical Review A - Atomic, Molecular, and Optical Physics* 58.4 (1998), R2672–R2675. DOI: `10.1103/PhysRevA.58.R2672` (cit. on p. 22).

[49] V. Rottschäfer and B. Krauskopf. "The ECM backbone of the Lang-Kobayashi equations: a geometric picture". *International Journal of Bifurcation and Chaos* 17.05 (2007), pp. 1575–1588. DOI: `10.1142/S0218127407017914` (cit. on p. 22).

[50] W. H. Steier and H. L. Stover. "Locking of Laser Oscillators by Light Injection". *IEEE Journal of Quantum Electronics* 2.4 (1966), pp. 111–112. DOI: `10.1109/JQE.1966.1073970` (cit. on p. 24).

[51] S. Kobayashi and T. Kimura. "Coherence of injection phase-locked AlGaAs semiconductor laser". *Electronics Letters* 16.17 (1980), p. 668. DOI: `10.1049/el:19800474` (cit. on p. 24).

[52] L. E. Erickson and A. Szabo. "Spectral narrowing of dye laser output by injection of monochromatic radiation into the laser cavity". *Applied Physics Letters* 18.10 (1971), pp. 433–435. DOI: `10.1063/1.1653482` (cit. on p. 24).

[53] P. Gallion, H. Nakajima, G. Debarge, and C. Chabran. "Contribution of spontaneous emission to the linewidth of an injection-locked semiconductor laser". *Electronics Letters* 21.14 (1985), p. 626. DOI: `10.1049/el:19850443` (cit. on p. 24).

[54] G. M. Stéphan. "Spectral properties of an injected laser". *Physical Review A - Atomic, Molecular, and Optical Physics* 58.3 (1998), pp. 2467–2471. DOI: `10.1103/PhysRevA.58.2467` (cit. on p. 24).

[55] A. E. Siegman. *Lasers*. University Science Books, 1986, p. 1286 (cit. on p. 25).

[56] N. Schunk and K. Petermann. "Noise Analysis of Injection-Locked Semiconductor Injection Lasers". *IEEE Journal of Quantum Electronics* 22.5 (1986), pp. 642–650. DOI: `10.1109/JQE.1986.1073018` (cit. on p. 25).

[57] A. Furusawa. "Amplitude squeezing of a semiconductor laser with light injection". *Optics Letters* 21.24 (1996), p. 2014. DOI: `10.1364/OL.21.002014` (cit. on p. 25).

[58] M. Bondiou, R. Gabet, G. M. Stéphan, and P. Besnard. "Linewidth of an optically injected semiconductor laser". *Journal of Optics B: Quantum and Semiclassical Optics* 2.1 (2000), pp. 41–46. DOI: `10.1088/1464-4266/2/1/307` (cit. on p. 25).

[59] C. E. Tanner and C. Wieman. "Precision measurement of the Stark shift in the 6S1/2 to 6P3/2 cesium transition using a frequency-stabilized laser diode". *Physical Review A* 38.1 (1988), pp. 162–165. DOI: `10.1103/PhysRevA.38.162` (cit. on p. 25).

[60] K. Komori, Y. Takasu, M. Kumakura, Y. Takahashi, and T. Yabuzaki. "Injection-Locking of Blue Laser Diodes and Its Application to the Laser Cooling of Neutral Ytterbium Atoms". *Japanese Journal of Applied Physics* 42.Part 1, No. 8 (2003), pp. 5059–5062. DOI: `10.1143/JJAP.42.5059` (cit. on p. 25).

[61] T. Hosoya, M. Miranda, R. Inoue, and M. Kozuma. "Injection locking of a high power ultraviolet laser diode for laser cooling of ytterbium atoms". *Review of Scientific Instruments* 86.7 (2015), p. 073110. DOI: `10.1063/1.4927132`. arXiv: `1412.0794` (cit. on p. 25).

[62] Z. Hadzibabic, C. A. Stan, K. Dieckmann, S. Gupta, M. W. Zwierlein, A. Görlitz, and W. Ketterle. "Two-Species Mixture of Quantum Degenerate Bose and Fermi Gases". *Physical Review Letters* 88.16 (2002), p. 4. DOI: `10.1103/PhysRevLett.88.160401`. arXiv: `0112425 [cond-mat]` (cit. on p. 25).

[63] J. Sacher, D. Baums, P. Panknin, W. Elsaßer, and E. O. Göbel. "Intensity instabilities of semiconductor lasers under current modulation, external light injection, and delayed feedback". *Physical Review A - Atomic, Molecular, and Optical Physics* 45.3 (1992), pp. 1893–1905. DOI: `10.1103/PhysRevA.45.1893` (cit. on p. 25).

[64] E. K. Lee, H. S. Pang, J. D. Park, and H. Lee. "Bistability and chaos in an injection-locked semiconductor laser". *Physical Review A - Atomic, Molecular, and Optical Physics* 47.1 (1993), pp. 736–739. DOI: `10.1103/PhysRevA.47.736` (cit. on pp. 25, 102).

[65] V. Annovazzi-Lodi, S. Donati, and M. Manna. "Chaos and locking in a semiconductor laser due to external injection". *IEEE Journal of Quantum Electronics* 30.7 (1994), pp. 1537–1541. DOI: `10.1109/3.299485` (cit. on p. 25).

[66] J.-M. L. J.-M. Liu and T. Simpson. "Four-wave mixing and optical modulation in a semiconductor laser". *IEEE Journal of Quantum Electronics* 30.4 (1994), pp. 957–965. DOI: `10.1109/3.291366` (cit. on p. 25).

[67] S. Eriksson and A. M. Lindberg. "Periodic oscillation within the chaotic region in a semiconductor laser subjected to external optical injection." *Optics letters* 26.3 (2001), pp. 142–4. DOI: `63029[pii]` (cit. on p. 25).

[68] S. Wieczorek, B. Krauskopf, T. B. Simpson, and D. Lenstra. "The dynamical complexity of optically injected semiconductor lasers". *Physics Reports* 416.1-2 (2005), pp. 1–128. DOI: `10.1016/j.physrep.2005.06.003` (cit. on pp. 25, 102).

[69] K. Schires, A. Hurtado, I. D. Henning, and M. J. Adams. "Comprehensive experimental analysis of nonlinear dynamics in an optically-injected semiconductor laser". *AIP Advances* 1.3 (2011). DOI: `10.1063/1.3625868` (cit. on p. 25).

[70] J. Nishizawa and K. Ishida. "Injection-induced modulation of laser light by the interaction of laser diodes". *IEEE Journal of Quantum Electronics* 11.7 (1975), pp. 515–519. DOI: `10.1109/JQE.1975.1068656` (cit. on p. 25).

[71] R. Lang and K. Kobayashi. "Suppression of the Relaxation Oscillation in the Modulated Output of Semiconductor Lasers". *IEEE Journal of Quantum Electronics* 12.3 (1976), pp. 194–199. DOI: `10.1109/JQE.1976.1069116` (cit. on p. 25).

[72] T. B. Simpson, J. Liu, and A. Gavrielides. "Bandwidth enhancement and broadband noise reduction in injection-locked semiconductor lasers". *IEEE Photonics Technology Letters* 7.7 (1995), pp. 709–711. DOI: `10.1109/68.393181` (cit. on p. 25).

[73] E. K. Lau, X. Zhao, H.-K. Sung, D. Parekh, C. Chang-Hasnain, and M. C. Wu. “Strong optical injection-locked semiconductor lasers demonstrating > 100-GHz resonance frequencies and 80-GHz intrinsic bandwidths”. *Optics Express* 16.9 (2008), p. 6609. DOI: `10.1364/OE.16.006609` (cit. on pp. 25, 72, 112).

[74] T. B. Simpson, J. M. Liu, K. F. Huang, and K Tai. “Nonlinear dynamics induced by external optical injection in semiconductor lasers”. *Quantum and Semiclassical Optics: Journal of the European Optical Society Part B* 9.5 (1997), pp. 765–784. DOI: `10.1088/1355-5111/9/5/009` (cit. on p. 25).

[75] F. Mogensen, H. Olesen, and G. Jacobsen. “Locking conditions and stability properties for a semiconductor laser with external light injection”. *IEEE Journal of Quantum Electronics* 21.7 (1985), pp. 784–793. DOI: `10.1109/JQE.1985.1072760` (cit. on pp. 25, 102).

[76] G. H. Van Tartwijk and G. P. Agrawal. “Laser instabilities: A modern perspective”. *Progress in Quantum Electronics* 22.2 (1998), pp. 43–122. DOI: `10.1016/S0079-6727(98)00008-1` (cit. on p. 25).

[77] Y Takiguchi, K Ohyagi, and J. Ohtsubo. “Bandwidth-enhanced chaos synchronization in strongly injection-locked semiconductor lasers with optical feedback.” *Optics Letters* 28.5 (2003), pp. 319–321. DOI: `10.1364/OL.28.000319` (cit. on p. 26).

[78] H. Someya, I. Oowada, H. Okumura, T. Kida, and A. Uchida. “Synchronization of bandwidth-enhanced chaos in semiconductor lasers with optical feedback and injection”. *Optics Express* 17.22 (2009), p. 19536. DOI: `10.1364/OE.17.019536` (cit. on p. 26).

[79] K. Kanno and A. Uchida. “Consistency and complexity in coupled semiconductor lasers with time-delayed optical feedback”. *Physical Review E - Statistical, Nonlinear, and Soft Matter Physics* 86.6 (2012), p. 066202. DOI: `10.1103/PhysRevE.86.066202` (cit. on pp. 26, 81, 82, 110).

[80] H. Aida, M. Arahata, H. Okumura, H. Koizumi, A. Uchida, K. Yoshimura, J. Muramatsu, and P. Davis. “Experiment on synchronization of semiconductor lasers by common injection of constant-amplitude random-phase light”. *Optics Express* 20.11 (2012), p. 11813. DOI: `10.1364/OE.20.011813` (cit. on pp. 26, 110).

[81] P. Colet and R. Roy. “Digital communication with synchronized chaotic lasers”. *Optics Letters* 19.24 (1994), pp. 2056–2058. DOI: `10.1364/OL.19.002056` (cit. on p. 26).

[82] S Tang and J. M. Liu. "Message encoding-decoding at 2.5 Gbits/s through synchronization of chaotic pulsing semiconductor lasers". *Optics Letters* 26.23 (2001), pp. 1843–1845. DOI: 10.1364/OL.26.001843 (cit. on p. 26).

[83] K. Hirano, T. Yamazaki, S. Morikatsu, H. Okumura, H. Aida, A. Uchida, S. Yoshimori, K. Yoshimura, T. Harayama, and P. Davis. "Fast random bit generation with bandwidth-enhanced chaos in semiconductor lasers". *Optics Express* 18.6 (2010), p. 5512. DOI: 10.1364/OE.18.005512. arXiv: 0401040 [nlin] (cit. on p. 26).

[84] T. B. Simpson, J. M. Liu, M. Almulla, N. G. Usechak, and V. Kovanis. "Linewidth sharpening via polarization-rotated feedback in optically injected semiconductor laser oscillators". *IEEE Journal on Selected Topics in Quantum Electronics* 19.4 (2013). DOI: 10.1109/JSTQE.2012.2237016 (cit. on p. 26).

[85] B. Garbin, J. Javaloyes, G. Tissoni, and S. Barland. "Topological solitons as addressable phase bits in a driven laser". *Nature Communications* 6 (2015), pp. 1–7. DOI: 10.1038/ncomms6915. arXiv: 1409.6350 (cit. on p. 26).

[86] P. Li, Y. Guo, Y. Guo, Y. Fan, X. Guo, X. Liu, K. Li, K. A. Shore, Y. Wang, and A. Wang. "Ultrafast Fully Photonic Random Bit Generator". *Journal of Lightwave Technology* 36.12 (2018), pp. 2531–2540. DOI: 10.1109/JLT.2018.2817512 (cit. on p. 26).

[87] J. Nakayama, K. Kanno, and A. Uchida. "Laser dynamical reservoir computing with consistency: an approach of a chaos mask signal". *Optics Express* 24.8 (2016), p. 8679. DOI: 10.1364/OE.24.008679 (cit. on pp. 26, 34).

[88] A. Uchida, R. McAllister, and R. Roy. "Consistency of nonlinear system response to complex drive signals". *Physical Review Letters* 93.24 (2004), pp. 1–4. DOI: 10.1103/PhysRevLett.93.244102 (cit. on pp. 26, 82).

[89] N. Oliver, T. Jüngling, and I. Fischer. "Consistency Properties of a Chaotic Semiconductor Laser Driven by Optical Feedback". *Physical Review Letters* 114.12 (2015), p. 123902. DOI: 10.1103/PhysRevLett.114.123902 (cit. on pp. 26, 82, 110, 123).

[90] J. G. White, E. Southgate, J. N. Thomson, and S. Brenner. "The Structure of the Nervous System of the Nematode Caenorhabditis elegans". *Philosophical Transactions of the Royal Society B: Biological*

Sciences 314.1165 (1986), pp. 1–340. DOI: 10.1098/rstb.1986.0056 (cit. on p. 26).

[91] L. R. Varshney, B. L. Chen, E. Paniagua, D. H. Hall, and D. B. Chklovskii. “Structural Properties of the Caenorhabditis elegans Neuronal Network”. *PLoS Computational Biology* 7.2 (2011). Ed. by O. Sporns, e1001066. DOI: 10.1371/journal.pcbi.1001066. arXiv: arXiv:0907.2373v4 (cit. on p. 26).

[92] S. Herculano-Houzel. “The human brain in numbers: a linearly scaled-up primate brain”. *Frontiers in Human Neuroscience* 3.November (2009), pp. 1–11. DOI: 10.3389/neuro.09.031.2009 (cit. on p. 26).

[93] D. A. Drachman. “Do we have brain to spare?” *Neurology* 64.12 (2005), pp. 2004–2005. DOI: 10.1212/01.WNL.0000166914.38327.BB. arXiv: arXiv:1011.1669v3 (cit. on p. 26).

[94] D. K. Cullen, M. E. Gilroy, H. R. Irons, and M. C. Laplaca. “Synapse-to-neuron ratio is inversely related to neuronal density in mature neuronal cultures”. *Brain Research* 1359 (2010), pp. 44–55. DOI: 10.1016/j.brainres.2010.08.058. arXiv: NIHMS150003 (cit. on p. 26).

[95] M. Jordan. *Serial order: A parallel distributed processing approach*. Tech. rep. 1986, p. 40 (cit. on pp. 26, 29).

[96] W. S. McCulloch and W. Pitts. “A logical calculus of the ideas immanent in nervous activity”. *The Bulletin of Mathematical Biophysics* 5.4 (1943), pp. 115–133. DOI: 10.1007/BF02478259. arXiv: arXiv:1011.1669v3 (cit. on p. 26).

[97] E. M. Izhikevich. “Which model to use for cortical spiking neurons?” *IEEE Transactions on Neural Networks* 15.5 (2004), pp. 1063–1070. DOI: 10.1109/TNN.2004.832719 (cit. on p. 27).

[98] R. FitzHugh. “Mathematical models of threshold phenomena in the nerve membrane”. *The Bulletin of Mathematical Biophysics* 17.4 (1955), pp. 257–278. DOI: 10.1007/BF02477753 (cit. on p. 28).

[99] W. Gerstner. “Chapter 12 A framework for spiking neuron models: The spike response model”. 2001, pp. 469–516. DOI: 10.1016/S1383-8121(01)80015-4 (cit. on p. 28).

[100] W. Gerstner and W. M. Kistler. *Spiking Neuron Models*. Cambridge: Cambridge University Press, 2002. DOI: 10.1017/CBO9780511815706 (cit. on p. 28).

[101] W. Maass. "Noisy spiking neurons with temporal coding have more computational power than sigmoidal neurons". *Advances in Neural Information Processing Systems* 9 (1997), pp. 211–217. DOI: `10.1.1.49.2055` (cit. on p. 28).

[102] D. Crevier. *AI: the tumultuous history of the search for artificial intelligence*. New York, New York, USA: Basic Books, 1993, p. 386 (cit. on p. 28).

[103] B. Widrow. *An Adaptive 'Adaline' Neuron Using Chemical 'Memistors'*. 1960 (cit. on p. 28).

[104] A. G. Ivakhnenko and V. G. Lapa. *Cybernetics and forecasting techniques*. American Elsevier Pub. Co, 1967, p. 168 (cit. on p. 28).

[105] M. Minsky and S. A. Papert. *Perceptrons An Introduction to Computational Geometry*. Cambridge, MA: MIT Press, 1969, p. 258 (cit. on p. 29).

[106] P. J. Werbos. *Beyond Regression: New Tools for Prediction and Analysis in the Behavioral Sciences*. Harvard University, 1975, p. 906 (cit. on p. 29).

[107] Z. C. Lipton, J. Berkowitz, and C. Elkan. "A Critical Review of Recurrent Neural Networks for Sequence Learning" (2015), pp. 1–38. DOI: `10.1145/2647868.2654889`. arXiv: `1506.00019` (cit. on p. 29).

[108] J. J. Hopfield. "Neural networks and physical systems with emergent collective computational abilities." *Proceedings of the National Academy of Sciences* 79.8 (1982), pp. 2554–2558. DOI: `10.1073/pnas.79.8.2554`. arXiv: `arXiv:1411.3159v1` (cit. on p. 29).

[109] W. A. Little. "The existence of persistent states in the brain". *Mathematical Biosciences* 19.1-2 (1974), pp. 101–120. DOI: `10.1016/0025-5564(74)90031-5`. arXiv: `arXiv:1011.1669v3` (cit. on p. 29).

[110] J. L. Elman. "Finding structure in time". *Cognitive Science* 14.2 (1990), pp. 179–211. DOI: `10.1016/0364-0213(90)90002-E` (cit. on p. 29).

[111] J. Kilian and H. T. Siegelmann. "The Dynamic Universality of Sigmoidal Neural Networks". *Information and Computation* 128.1 (1996), pp. 48–56. DOI: `10.1006/inco.1996.0062` (cit. on p. 29).

[112] A. Graves, A.-r. Mohamed, and G. Hinton. "Speech Recognition With Deep Recurrent Neural Networks". *Icassp* 3 (2013), pp. 6645–6649. DOI: `10.1109/ICASSP.2013.6638947`. arXiv: `arXiv:1303.5778v1` (cit. on p. 29).

[113] J. Bradbury and R. Socher. "MetaMind Neural Machine Translation System for WMT 2016". *WMT* 2 (2016), pp. 264–267 (cit. on p. 29).

[114] A. Karpathy and L. Fei-Fei. "Deep Visual-Semantic Alignments for Generating Image Descriptions". *IEEE Transactions on Pattern Analysis and Machine Intelligence* 39.4 (2017), pp. 664–676. DOI: `10.1109/TPAMI.2016.2598339`. arXiv: `1412.2306` (cit. on p. 29).

[115] S. C. Prasad and P. Prasad. "Deep Recurrent Neural Networks for Time Series Prediction". *ArXiv* 95070.July (2014), pp. 1–54. arXiv: `1407.5949` (cit. on p. 29).

[116] Z. Che, S. Purushotham, K. Cho, D. Sontag, and Y. Liu. "Recurrent Neural Networks for Multivariate Time Series with Missing Values". *Scientific Reports* 8.1 (2018), pp. 1–12. DOI: `10.1038/s41598-018-24271-9`. arXiv: `1606.01865` (cit. on p. 29).

[117] S. S. Haykin. *Neural networks : a comprehensive foundation*. 3rd. Harlow: Prentice Hall, 2008, p. 937 (cit. on p. 30).

[118] H. Jaeger. "A tutorial on training recurrent neural networks , covering BPPT , RTRL , EKF and the " echo state network " approach". *GMD Report* 159 (2002), pp. 1–46 (cit. on p. 30).

[119] H. Jaeger. "The " echo state " approach to analysing and training recurrent neural networks – with an Erratum note 1". *GMD Report* 148 (2010), pp. 1–47. DOI: `citeulike-article-id:9635932` (cit. on p. 30).

[120] W. Maass, T. Natschläger, H. Markram, T Natschlager, and H. Markram. "Real-time computing without stable states: a new framework for neural computation based on perturbations". *Neural computation* 14.11 (2002), pp. 2531–2560. DOI: `10.1162/089976602760407955` (cit. on pp. 30, 31).

[121] J. Steil. "Backpropagation-decorrelation: online recurrent learning with O(N) complexity". *2004 IEEE International Joint Conference on Neural Networks (IEEE Cat. No.04CH37541)*. Vol. 2. IEEE, pp. 843–848. DOI: `10.1109/IJCNN.2004.1380039` (cit. on p. 30).

[122] D. Verstraeten, B. Schrauwen, and D. Stroobandt. "Reservoir Computing with Stochastic Bitstream Neurons". *Proceedings of the 16th Annual ProRISC Workshop* (2005), pp. 454–459 (cit. on p. 30).

[123] D. Verstraeten, B. Schrauwen, M. D'Haene, and D. Stroobandt. "An experimental unification of reservoir computing methods". *Neural Networks* 20.3 (2007), pp. 391–403. DOI: `10.1016/j.neunet.2007.04.003` (cit. on pp. 30, 31).

[124] T. Cover. "Geometrical and statistical properties of systems of linear inequalities with applications in pattern recognition". *IEEE Transactions on Electronic Computers* (1965), pp. 326–334. DOI: `10.1109/PGEC.1965.264137`. arXiv: `1503.0680` (cit. on p. 30).

[125] B. Schrauwen, D. Verstraeten, and J. Van Campenhout. "An overview of reservoir computing: theory, applications and implementations". *Proceedings of the 15th European Symposium on Artificial Neural Networks* April (2007), pp. 471–82. DOI: `1854/11063` (cit. on p. 31).

[126] M. C. Soriano, D. Brunner, M. Escalona-Morán, C. R. Mirasso, and I. Fischer. "Minimal approach to neuro-inspired information processing". *Frontiers in Computational Neuroscience* 9.June (2015), pp. 1–11. DOI: `10.3389/fncom.2015.00068` (cit. on pp. 31, 81).

[127] A. Rodan and P. Tino. "Minimum complexity echo state network". *IEEE Transactions on Neural Networks* 22.1 (2011), pp. 131–144. DOI: `10.1109/TNN.2010.2089641` (cit. on p. 31).

[128] A. Rodan and P. Tiňo. "Simple Deterministically Constructed Cycle Reservoirs with Regular Jumps". *Neural Computation* 24.7 (2012), pp. 1822–1852. DOI: `10.1162/NECO_a_00297` (cit. on p. 31).

[129] D. Brunner, B. Penkovsky, B. A. Marquez, M. Jacquot, I. Fischer, and L. Larger. "Tutorial: Photonic Neural Networks in Delay Systems". *Journal of Applied Physics* accepted f (2018). DOI: `10.1063/1.5042342` (cit. on pp. 31, 32).

[130] L. Appeltant, M. C. Soriano, G. Van der Sande, J. Danckaert, S. Massar, J. Dambre, B. Schrauwen, C. R. Mirasso, I. Fischer, and G. V. D. Sande. "Information processing using a single dynamical node as complex system - Supplementary information". *Nature communications* 2 (2011), p. 468. DOI: `10.1038/ncomms1476` (cit. on pp. 31, 72, 83).

[131] M. Le Berre, E. Ressayre, A Tallet, H. M. Gibbs, D. L. Kaplan, and M. H. Rose. "Conjecture on the dimensions of chaotic attractors of delayed-feedback dynamical systems". *Physical Review A - Atomic, Molecular, and Optical Physics* 35.9 (1987), pp. 4020–4022. DOI: `10.1103/PhysRevA.35.4020` (cit. on p. 32).

[132] F. Duport, B. Schneider, A. Smerieri, M. Haelterman, and S. Massar. "All-optical reservoir computing". *Optics Express* 20.20 (2012), p. 22783. DOI: `10.1364/OE.20.022783` (cit. on pp. 32, 35).

[133] L. Appeltant, G. Van der Sande, J. Danckaert, and I. Fischer. "Constructing optimized binary masks for reservoir computing with delay systems." *Scientific reports* 4 (2014), p. 3629. DOI: `10.1038/srep03629` (cit. on pp. 34, 143).

[134] V. Mnih, K. Kavukcuoglu, D. Silver, A. Graves, I. Antonoglou, D. Wierstra, and M. Riedmiller. "Playing Atari with Deep Reinforcement Learning" (2013), pp. 1–9. DOI: `10.1038/nature14236`. arXiv: `1312.5602` (cit. on p. 34).

[135] D. Silver, J. Schrittwieser, K. Simonyan, I. Antonoglou, A. Huang, A. Guez, T. Hubert, L. Baker, M. Lai, A. Bolton, Y. Chen, T. Lillicrap, F. Hui, L. Sifre, G. van den Driessche, T. Graepel, and D. Hassabis. "Mastering the game of Go without human knowledge". *Nature* 550.7676 (2017), pp. 354–359. DOI: `10.1038/nature24270` (cit. on p. 34).

[136] X. Song, H. Fang, X. Jiao, and Y. Wang. "Autonomous mobile robot navigation using machine learning". *2012 IEEE 6th International Conference on Information and Automation for Sustainability* (2012), pp. 135–140. DOI: `10.1109/ICIAFS.2012.6419894` (cit. on p. 34).

[137] L. Ran, Y. Zhang, Q. Zhang, and T. Yang. "Convolutional neural network-based robot navigation using uncalibrated spherical images". *Sensors (Switzerland)* 17.6 (2017), pp. 1–18. DOI: `10.3390/s17061341` (cit. on p. 34).

[138] G. Sepulveda, J. C. Niebles, and A. Soto. "A Deep Learning Based Behavioral Approach to Indoor Autonomous Navigation". Dl (2018). arXiv: `1803.04119` (cit. on p. 34).

[139] S. Menon, S. Fok, A. Neckar, O. Khatib, and K. Boahen. "Controlling Articulated Robots in Task-Space with Spiking Silicon Neurons". *5th IEEE RAS/EMBS International Conference on Biomedical Robotics and Biomechatronics* (2014), pp. 181–186. DOI: `10.1109/BIOROB.2014.6913773` (cit. on p. 34).

[140] S. Min, B. Lee, and S. Yoon. "Deep learning in bioinformatics". *Briefings in bioinformatics* 18.5 (2017), pp. 851–869. DOI: `10.1093/bib/bbw068`. arXiv: `1603.06430` (cit. on p. 34).

[141] M. He, J. Liao, L. Yuan, and P. V. Sander. "Neural Color Transfer between Images *" (2017). arXiv: `1710.00756` (cit. on p. 34).

[142] I. Wallach, M. Dzamba, and A. Heifets. "AtomNet: A Deep Convolutional Neural Network for Bioactivity Prediction in Structure-based Drug Discovery" (2015), pp. 1–11. DOI: `10.1007/s10618-010-0175-9`. arXiv: `1510.02855` (cit. on p. 34).

[143] C. Mead and M. Ismail. *Analog VLSI Implementation of Neural Systems*. Ed. by C. Mead and M. Ismail. Vol. 80. The Kluwer International Series in Engineering and Computer Science. Boston, MA: Springer US, 1989, p. 249. DOI: `10.1007/978-1-4613-1639-8` (cit. on p. 35).

[144] J. V. Arthur and K. Boahen. "Recurrently connected silicon neurons with active dendrites for one-shot learning". *IEEE International Conference on Neural Networks - Conference Proceedings* 3 (2004), pp. 1699–1704. DOI: `10.1109/IJCNN.2004.1380858` (cit. on p. 35).

[145] S. Choudhary, S. Sloan, S. Fok, A. Neckar, E. Trautmann, P. Gao, T. Stewart, C. Eliasmith, and K. Boahen. "Silicon Neurons That Compute". *Lecture Notes in Computer Science (including subseries Lecture Notes in Artificial Intelligence and Lecture Notes in Bioinformatics)*. Vol. 7552 LNCS. PART 1. 2012, pp. 121–128. DOI: `10.1007/978-3-642-33269-2_16` (cit. on p. 35).

[146] P. a. Merolla, J. V. Arthur, R. Alvarez-Icaza, A. S. Cassidy, J. Sawada, F. Akopyan, B. L. Jackson, N. Imam, C. Guo, Y. Nakamura, B. Brezzo, I. Vo, S. K. Esser, R. Appuswamy, B. Taba, A. Amir, M. D. Flickner, W. P. Risk, R. Manohar, and D. S. Modha. "A million spiking-neuron integrated circuit with a scalable communication network and interface". *Science* 345.6197 (2014), pp. 668–673. DOI: `10.1126/science.1254642` (cit. on p. 35).

[147] R. A. Nawrocki, R. M. Voyles, and S. E. Shaheen. "A Mini Review of Neuromorphic Architectures and Implementations". *IEEE Transactions on Electron Devices* 63.10 (2016), pp. 3819–3829. DOI: `10.1109/TED.2016.2598413` (cit. on p. 35).

[148] J. Torrejon, M. Riou, F. A. Araujo, S. Tsunegi, G. Khalsa, D. Querlioz, P. Bortolotti, V. Cros, K. Yakushiji, A. Fukushima, H. Kubota, S. Yuasa, M. D. Stiles, and J. Grollier. "Neuromorphic computing with nanoscale spintronic oscillators". *Nature* 547.7664 (2017), pp. 428–431. DOI: `10.1038/nature23011`. arXiv: `1701.07715` (cit. on p. 35).

[149] K. Caluwaerts, M. D'Haene, D Verstraeten, and B Schrauwen. "Locomotion Without a Brain: Physical Reservoir Computing in Tensegrity Structures". *Artificial Life* 19.1 (2012), pp. 35–66. DOI: `10.1162/ARTL_a_00080` (cit. on p. 35).

[150] C. Fernando and S. Sojakka. "Pattern Recognition in a Bucket". *Advances in Artificial Life* (2003), pp. 588–597. DOI: `10.1007/978-3-540-39432-7_63` (cit. on p. 35).

[151] P. Aaser, M. Knudsen, O. H. Ramstad, R. van de Wijdeven, S. Nichele, I. Sandvig, G. Tufte, U. Stefan Bauer, Ø. Halaas, S. Hendseth, A. Sandvig, and V. Valderhaug. "Towards making a cyborg: A closed-loop reservoir-neuro system". *Proceedings of the 14th European Conference on Artificial Life ECAL 2017*. Cambridge, MA: MIT Press, 2017, pp. 430–437. DOI: `10.7551/ecal_a_072` (cit. on p. 35).

[152] K. Vandoorne, P. Mechet, T. Van Vaerenbergh, M. A. A. Fiers, G. Morthier, D. Verstraeten, B. Schrauwen, J. Dambre, and P. Bienstman. "Experimental demonstration of reservoir computing on a silicon photonics chip." *Nature communications* 5 (2014), p. 3541. DOI: `10.1038/ncomms4541` (cit. on p. 35).

[153] D. Brunner and I. Fischer. "Reconfigurable semiconductor laser networks based on diffractive coupling". *Optics letters* 40.16 (2015), pp. 1–5. DOI: `10.1364/OL.40.003854` (cit. on pp. 35, 138).

[154] A. N. Tait, T. F. de Lima, M. A. Nahmias, B. J. Shastri, and P. R. Prucnal. "Multi-channel control for microring weight banks". *Optics Express* 24.8 (2016), p. 8895. DOI: `10.1364/OE.24.008895` (cit. on p. 35).

[155] M. A. Nahmias, A. N. Tait, L. Tolias, M. P. Chang, T. Ferreira de Lima, B. J. Shastri, and P. R. Prucnal. "An integrated analog O/E/O link for multi-channel laser neurons". *Applied Physics Letters* 108.15 (2016), p. 151106. DOI: `10.1063/1.4945368` (cit. on p. 35).

[156] D. Psaltis and N Farhat. "Optical information processing based on an associative-memory model of neural nets with thresholding and feedback." *Optics letters* 10.2 (1985), pp. 98–100. DOI: `10.1364/OL.10.000098` (cit. on pp. 35, 128).

[157] K. Alexander, T. Van Vaerenbergh, M. A. A. Fiers, P. Mechet, J. Dambre, and P. Bienstman. "Excitability in optically injected microdisk lasers with phase controlled excitatory and inhibitory response". *Optics Express* 21.22 (2013), pp. 26182–26191. DOI: `10.1364/OE.21.026182` (cit. on p. 35).

[158] B. J. Shastri, M. A. Nahmias, A. N. Tait, A. W. Rodriguez, B. Wu, and P. R. Prucnal. "Spike processing with a graphene excitable laser". *Scientific Reports* 6.August 2015 (2016), p. 19126. DOI: `10.1038/srep19126` (cit. on p. 35).

[159] M. A. Nahmias, B. J. Shastri, A. N. Tait, and P. R. Prucnal. "A leaky integrate-and-fire laser neuron for ultrafast cognitive computing". *IEEE Journal on Selected Topics in Quantum Electronics* 19.5 (2013). DOI: `10.1109/JSTQE.2013.2257700` (cit. on p. 35).

[160] K. Vandoorne, W. Dierckx, B. Schrauwen, D. Verstraeten, R. Baets, P. Bienstman, and J. Van Campenhout. "Toward optical signal processing using Photonic Reservoir Computing". *Optics Express* 16.15 (2008), p. 11182. DOI: `10.1364/OE.16.011182` (cit. on pp. 35, 183).

[161] A. Akrout, P. Antonik, M. Haelterman, and S. Massar. "Towards autonomous photonic reservoir computer based on frequency parallelism of neurons". Ed. by B. Jalali, D. R. Solli, S. K. Turitsyn, G. Steinmeyer, and N. G. R. Broderick. Vol. 10089. 2017, 100890S. DOI: `10.1117/12.2250865` (cit. on p. 35).

[162] Q. Vinckier, F. Duport, A. Smerieri, K. Vandoorne, P. Bienstman, M. Haelterman, and S. Massar. "High performance photonic reservoir computer based on a coherently driven passive cavity". *Optica* 2.5 (2015), pp. 438–446. DOI: `10.1364/OPTICA.2.000438`. arXiv: `1501.03024` (cit. on p. 35).

[163] F. Laporte, A. Katumba, J. Dambre, and P. Bienstman. "Numerical demonstration of neuromorphic computing with photonic crystal cavities". *Optics Express* 26.7 (2018), p. 7955. DOI: `10.1364/OE.26.007955` (cit. on p. 35).

[164] F. Denis-le Coarer, M. Sciamanna, A. Katumba, M. Freiberger, J. Dambre, P. Bienstman, and D. Rontani. *All-optical reservoir computing on a photonic chip using silicon-based ring resonators*. 2018. DOI: 10.1109/JSTQE.2018.2836985 (cit. on p. 35).

[165] D. Brunner, M. C. Soriano, and I. Fischer. "High-speed optical vector and matrix operations using a semiconductor laser". *IEEE Photonics Technology Letters* 25.17 (2013), pp. 1680–1683. DOI: 10.1109/LPT.2013.2273373 (cit. on pp. 35, 72).

[166] L. Larger, M. C. Soriano, D. Brunner, L. Appeltant, J. M. Gutierrez, L. Pesquera, C. R. Mirasso, and I. Fischer. "Photonic information processing beyond Turing: an optoelectronic implementation of reservoir computing". *Optics Express* 20.3 (2012), pp. 3241–3249. DOI: 10.1364/OE.20.003241. arXiv: 9605103 [cs] (cit. on p. 35).

[167] L. Larger, A. Baylón-Fuentes, R. Martinenghi, V. S. Udaltsov, Y. K. Chembo, and M. Jacquot. "High-Speed Photonic Reservoir Computing Using a Time-Delay-Based Architecture: Million Words per Second Classification". *Physical Review X* 7.1 (2017), p. 011015. DOI: 10.1103/PhysRevX.7.011015 (cit. on p. 35).

[168] D. Psaltis, D Brady, and K Wagner. "Adaptive optical networks using photorefractive crystals." *Applied optics* 27.9 (1988), pp. 1752–1759. DOI: 10.1364/AO.27.001752 (cit. on p. 35).

[169] C. Denz. *Optical Neural Networks*. Ed. by T. Tschudi. Wiesbaden: Vieweg+Teubner Verlag, 1998. DOI: 10.1007/978-3-663-12272-2 (cit. on pp. 35, 128).

[170] F. Horst, S. Abel, R. Dangel, Y. Baumgartner, J. Fompeyrine, and B. J. Offrein. "Optical Signal Processing for Neural Networks". *Advanced Photonics 2018 (BGPP, IPR, NP, NOMA, Sensors, Networks, SPPCom, SOF)*. Washington, D.C.: OSA, 2018, SpW4G.4. DOI: 10.1364/SPPCOM.2018.SpW4G.4 (cit. on p. 35).

[171] F. T. Arecchi, G. Giacomelli, A. Lapucci, and R. Meucci. "Two-dimensional representation of a delayed dynamical system". *Physical Review A - Atomic, Molecular, and Optical Physics* 45.7 (1992), R4225–R4228. DOI: 10.1103/PhysRevA.45.R4225 (cit. on pp. 36, 48, 56).

[172] G. Giacomelli, R. Meucci, A. Politi, and F. T. Arecchi. "Defects and Spacelike Properties of Delayed Dynamical Systems". *Physical Review Letters* 73.8 (1994), pp. 1099–1102. DOI: 10.1103/PhysRevLett.73.1099 (cit. on pp. 36, 56).

[173] R. Hegger, M. Bünner, and H. Kantz. "Identifying and modeling delay feedback systems". *Physical Review Letters* 81.2 (1998), pp. 3–6. DOI: 10.1103/PhysRevLett.81.558. arXiv: 9907019 [chao-dyn] (cit. on p. 42).

[174] B. P. Bezruchko, A. S. Karavaev, V. I. Ponomarenko, and M. D. Prokhorov. "Reconstruction of time-delay systems from chaotic time series." *Physical Review E - Statistical, Nonlinear, and Soft Matter Physics* 64.5 Pt 2 (2001), p. 056216. DOI: 10.1103/PhysRevE.64.056216 (cit. on p. 42).

[175] M. Siefert. "Practical criterion for delay estimation using random perturbations". *Physical Review E* 76.2 (2007), p. 026215. DOI: 10.1103/PhysRevE.76.026215 (cit. on p. 42).

[176] D. Rontani, A. Locquet, M. Sciamanna, D. S. Citrin, and S. Ortin. "Time-delay identification in a chaotic semiconductor laser with optical feedback: A dynamical point of view". *IEEE Journal of Quantum Electronics* 45.7 (2009), pp. 879–891. DOI: 10.1109/JQE.2009.2013116 (cit. on pp. 42, 43).

[177] X. Porte, O. D'Huys, T. Jüngling, D. Brunner, M. C. Soriano, and I. Fischer. "Autocorrelation properties of chaotic delay dynamical systems: A study on semiconductor lasers". *Physical Review E - Statistical, Nonlinear, and Soft Matter Physics* 90.5 (2014), pp. 1–10. DOI: 10.1103/PhysRevE.90.052911 (cit. on p. 43).

[178] D. R. Tobergte and S. Curtis. *Applied Aspects of Optical Communication and LIDAR*. Vol. 53. 9. 2013, pp. 1689–1699. DOI: 10.1017/CBO9781107415324.004. arXiv: arXiv:1011.1669v3 (cit. on p. 46).

[179] B. W. Schilling, D. N. Barr, G. C. Templeton, L. J. Mizerka, and C. W. Trussell. "Multiple-return laser radar for three-dimensional imaging through obscurations." *Applied Optics* 41.15 (2002), pp. 2791–9. DOI: 10.1364/AO.41.002791 (cit. on p. 46).

[180] C. L. Smith. *Advanced Process Control*. Hoboken, NJ, USA: John Wiley & Sons, Inc., 2010, p. 368. DOI: 10.1002/9780470612903 (cit. on p. 46).

[181] X. Rodet. "Models of Musical Instruments from Chua ' s Circuit with Time Delav". *IEEE Transactions on Circuits and Systems* 40.10 (1993), pp. 696–701 (cit. on p. 46).

[182] P. Hagmann, M. Kurant, X. Gigandet, P. Thiran, V. J. Wedeen, R. Meuli, and J. P. Thiran. "Mapping human whole-brain structural networks with diffusion MRI". *PLoS ONE* 2.7 (2007). DOI: 10.1371/journal.pone.0000597 (cit. on p. 46).

[183] R. Szalai and G. Orosz. "Decomposing the dynamics of heterogeneous delayed networks with applications to connected vehicle systems". *Physical Review E - Statistical, Nonlinear, and Soft Matter Physics* 88.4 (2013), pp. 1–5. DOI: 10.1103/PhysRevE.88.040902. arXiv: 1305.6771 (cit. on p. 46).

[184] K. Josić, J. M. López, W. Ott, L. J. Shiau, and M. R. Bennett. "Stochastic delay accelerates signaling in gene networks". *PLoS Computational Biology* 7.11 (2011). DOI: 10.1371/journal.pcbi.1002264 (cit. on p. 46).

[185] J. Martínez-Llinàs, X. Porte, M. C. Soriano, P. Colet, and I. Fischer. "Dynamical properties induced by state-dependent delays in photonic systems". *Nature Communications* 6.May (2015), p. 7425. DOI: 10.1038/ncomms8425 (cit. on p. 46).

[186] D. Wang, L. Wang, T. Zhao, H. Gao, Y. Wang, X. Chen, and A. Wang. "Time delay signature elimination of chaos in a semiconductor laser by dispersive feedback from a chirped FBG". *Optics Express* 25.10 (2017), p. 10911. DOI: 10.1364/OE.25.010911 (cit. on p. 46).

[187] S. Yanchuk and G. Giacomelli. "Pattern Formation in Systems with Multiple Delayed Feedbacks". *Physical Review Letters* 112.17 (2014), p. 174103. DOI: 10.1103/PhysRevLett.112.174103. arXiv: arXiv:1403.3585v1 (cit. on pp. 46–49, 51, 54, 56, 57, 60–62, 67, 68).

[188] Y. Kuramoto. *Chemical Oscillations, Waves, and Turbulence*. Vol. 19. Springer Series in Synergetics. Berlin, Heidelberg: Springer Berlin Heidelberg, 1984. DOI: 10.1007/978-3-642-69689-3 (cit. on p. 47).

[189] A. C. Newell, T Passot, and J. Lega. "Order Parameter Equations for Patterns". *Annual Review of Fluid Mechanics* 25.1 (1993), pp. 399–453. DOI: 10.1146/annurev.fl.25.010193.002151 (cit. on p. 47).

[190] T. Bohr, M. H. Jensen, G. Paladin, and A. Vulpiani. *Dynamical Systems Approach to Turbulence*. Cambridge: Cambridge University Press, 1998. DOI: 10.1017/CBO9780511599972 (cit. on p. 47).

[191] L. M. Pismen. *Vortices in Nonlinear Fields*. Oxford University Press, 1999, p. 306 (cit. on p. 47).

[192] M. Cross and H. Greenside. *Pattern Formation and Dynamics in Nonequilibrium Systems*. Cambridge: Cambridge University Press, 2009, p. 535. DOI: `10.1017/CBO9780511627200` (cit. on p. 47).

[193] J. Farmer, E. Ott, and J. A. Yorke. "The dimension of chaotic attractors". *Physica D: Nonlinear Phenomena* 7.1-3 (1983), pp. 153–180. DOI: `10.1016/0167-2789(83)90125-2` (cit. on p. 47).

[194] G. Giacomelli, F. Marino, M. A. Zaks, and S. Yanchuk. "Coarsening in a bistable system with long-delayed feedback". *EPL (Europhysics Letters)* 99.5 (2012). DOI: `10.1209/0295-5075/99/58005` (cit. on p. 47).

[195] T. Erneux. *Applied Delay Differential Equations*. Vol. 3. 2009, p. 241. DOI: `10.1007/978-0-387-74372-1` (cit. on p. 47).

[196] K. Ikeda, H. Daido, and O. Akimoto. "Optical Turbulence: Chaotic Behavior of Transmitted Light from a Ring Cavity". *Physical Review Letters* 45.9 (1980), pp. 709–712. DOI: `10.1103/PhysRevLett.45.709` (cit. on pp. 47, 56, 62).

[197] G. Giacomelli and A. Politi. "Relationship between delayed and spatially extended dynamical systems". *Physical Review Letters* 76.15 (1996), pp. 2686–2689. DOI: `10.1103/PhysRevLett.76.2686` (cit. on p. 47).

[198] M. C. Soriano, J. García-Ojalvo, C. R. Mirasso, and I. Fischer. "Complex photonics: Dynamics and applications of delay-coupled semiconductors lasers". *Reviews of Modern Physics* 85.1 (2013), pp. 421–470. DOI: `10.1103/RevModPhys.85.421` (cit. on pp. 47, 82).

[199] I. Henning and J. Collins. "Measurements of the semiconductor laser linewidth broadening factor". *Electronics Letters* 19.22 (1983), pp. 927–929. DOI: `10.1049/el:19830633` (cit. on p. 49).

[200] G. Toulouse and M. Kléman. "Principles of a classification of defects in ordered media". *Journal de Physique Lettres* 37.6 (1976), pp. 149–151. DOI: `10.1051/jphyslet:01976003706014900` (cit. on p. 53).

[201] N. D. Mermin. "The topological theory of defects in ordered media". *Reviews of Modern Physics* 51.3 (1979), pp. 591–648. DOI: `10.1103/RevModPhys.51.591` (cit. on p. 53).

[202] P. S. Hagan. "Spiral Waves in Reaction-Diffusion Equations". *SIAM Journal on Applied Mathematics* 42.4 (1982), pp. 762–786. DOI: `10.1137/0142054` (cit. on pp. 54, 62).

[203] P. Coullet, L. Gil, and J. Lega. "Defect-mediated turbulence". *Physical Review Letters* 62.14 (1989), pp. 1619–1622. DOI: 10.1103/PhysRevLett.62.1619 (cit. on pp. 54, 56–58).

[204] Y. Kuramoto and T. Tsuzuki. "Persistent Propagation of Concentration Waves in Dissipative Media Far from Thermal Equilibrium". *Progress of Theoretical Physics* 55.2 (1976), pp. 356–369. DOI: 10.1143/PTP.55.356 (cit. on p. 56).

[205] P. L. Ramazza, S. Residori, E Pamapaloni, and A. Larichev. "Transition to space-time chaos in a nonlinear optical system with two-dimensional feedback". *Physical Review A - Atomic, Molecular, and Optical Physics* 54.1 (1996), p. 982. DOI: 10.1103/PhysRevA.53.400 (cit. on p. 56).

[206] I. S. Aranson, L. Kramer, and A. Weber. "Formation of asymmetric states of spiral waves in oscillatory media". *Physical Review E* 48.1 (1993), R9–R12. DOI: 10.1103/PhysRevE.48.R9 (cit. on p. 56).

[207] W. V. Saarloos. "The Complex Ginzburg-Landau equation for beginners". *Spatio-temporal Patterns in Nonequilibrium Complex Systems* (1994), pp. 1–11 (cit. on p. 56).

[208] H. Chaté and P. Manneville. "Phase diagram of the two-dimensional complex Ginzburg-Landau equation". *Physica A: Statistical Mechanics and its Applications* 224.1 (1996), pp. 348–368. DOI: 10.1016/0378-4371(95)00361-4. arXiv: 1608.07519 (cit. on pp. 56, 57).

[209] H. Chaté and P. Manneville. "Phase Diagram of the Two-Dimensional Complex Ginzburg-Landau Equation". 1 (2016), pp. 1–16. DOI: 10.1016/0378-4371(95)00361-4. arXiv: 1608.07519 (cit. on p. 56).

[210] E. G. Turitsyna, G. Falkovich, V. K. Mezentsev, and S. K. Turitsyn. "Optical turbulence and spectral condensate in long-fiber lasers". *Physical Review A* 80.3 (2009), p. 031804. DOI: 10.1103/PhysRevA.80.031804 (cit. on p. 56).

[211] E. G. Turitsyna, S. V. Smirnov, S. Sugavanam, N. Tarasov, X. Shu, S. A. Babin, E. V. Podivilov, D. V. Churkin, G. Falkovich, and S. K. Turitsyn. "The laminar–turbulent transition in a fibre laser". *Nature Photonics* 7.10 (2013), pp. 783–786. DOI: 10.1038/nphoton.2013.246 (cit. on p. 56).

[212] L. Carpi and C. Masoller. "Persistence and stochastic periodicity in the intensity dynamics of a fiber laser during the transition to optical turbulence". *Physical Review A* 97.2 (2018), p. 023842. DOI: `10.1103/PhysRevA.97.023842` (cit. on p. 56).

[213] G. Boffetta and R. E. Ecke. "Two-Dimensional Turbulence". *Annual Review of Fluid Mechanics* 44.1 (2012), pp. 427–451. DOI: `10.1146/annurev-fluid-120710-101240` (cit. on pp. 62, 68).

[214] B. Shraiman, a. Pumir, W. van Saarloos, P. Hohenberg, H. Chaté, and M. Holen. "Spatiotemporal chaos in the one-dimensional complex Ginzburg-Landau equation". *Physica D: Nonlinear Phenomena* 57.3-4 (1992), pp. 241–248. DOI: `10.1016/0167-2789(92)90001-4` (cit. on p. 62).

[215] R. Montagne and L. G. Brunnet. "Dynamic spectral analysis of phase turbulence". *Physica A: Statistical Mechanics and its Applications* 319 (2003), pp. 295–304. DOI: `10.1016/S0378-4371(02)01388-2` (cit. on p. 62).

[216] T. Yamada and Y. Kuramoto. "A Reduced Model Showing Chemical Turbulence". *Progress of Theoretical Physics* 56.2 (1976), pp. 681–683. DOI: `10.1143/PTP.56.681` (cit. on p. 65).

[217] C. D. Levermore and D. R. Stark. "Inertial ranges for turbulent solutions of complex Ginzburg-Landau equations". *Physics Letters, Section A: General, Atomic and Solid State Physics* 234.4 (1997), pp. 269–280. DOI: `10.1016/S0375-9601(97)00589-6` (cit. on p. 65).

[218] R. H. Kraichnan. "Inertial-range transfer in two-and three-dimensional turbulence". *Journal of Fluid Mechanics* 47.3 (1971), pp. 525–535. DOI: `10.1017/S0022112071001216` (cit. on p. 68).

[219] K. Hicke, M. Escalona-Morán, D. Brunner, M. C. Soriano, I. Fischer, C. R. Mirasso, M Escalona, D. Brunner, M. C. Soriano, I. Fischer, C. R. Mirasso, M. Escalona-Moran, D. Brunner, M. C. Soriano, I. Fischer, and C. R. Mirasso. "Information Processing Using Transient Dynamics of Semiconductor Lasers Subject to Delayed Feedback". *IEEE Journal of Selected Topics in Quantum Electronics* 19.4 (2013), pp. 1501610–1501610. DOI: `10.1109/JSTQE.2013.2241738` (cit. on pp. 72, 73, 75).

[220] R. F. Broom. "Self modulation at gigahertz frequencies of a diode laser coupled to an external cavity". *Electronics Letters* 5.23 (1969), p. 571. DOI: `10.1049/el:19690430` (cit. on pp. 72, 102).

[221] D. Lenstra, B. H. Verbeek, and A. J. den Boef. “Coherence Collapse in Single-Mode Semiconductor Lasers Due to Optical Feedback”. *IEEE Journal of Quantum Electronics* 21.6 (1985), pp. 674–679. DOI: `10.1109/JQE.1985.1072725` (cit. on pp. 72, 102).

[222] A. Wang, Y. Wang, and H. He. “Enhancing the bandwidth of the optical chaotic signal generated by a semiconductor laser with optical feedback”. *IEEE Photonics Technology Letters* 20.19 (2008), pp. 1633–1635. DOI: `10.1109/LPT.2008.2002739` (cit. on p. 72).

[223] A. Argyris, M. Hamacher, K. E. Chlouverakis, A. Bogris, and D. Syvridis. “Photonic integrated device for chaos applications in communications”. *Physical Review Letters* 100.19 (2008), pp. 1–4. DOI: `10.1103/PhysRevLett.100.194101` (cit. on p. 73).

[224] S. Sunada, T. Harayama, K. Arai, K. Yoshimura, P. Davis, K. Tsuzuki, and A. Uchida. “Chaos laser chips with delayed optical feedback using a passive ring waveguide.” *Optics express* 19.7 (2011), pp. 5713–24. DOI: `10.1364/OE.19.005713` (cit. on p. 73).

[225] M. C. Soriano, S. Ortín, D. Brunner, L. Larger, C. R. Mirasso, I. Fischer, and L. Pesquera. “Optoelectronic reservoir computing: tackling noise-induced performance degradation.” *Optics express* 21.1 (2013), pp. 12–20. DOI: `10.1364/OE.21.000012` (cit. on pp. 75, 86).

[226] F. Pedregosa, G. Varoquaux, A. Gramfort, V. Michel, B. Thirion, O. Grisel, M. Blondel, P. Prettenhofer, R. Weiss, V. Dubourg, J. Vanderplas, A. Passos, D. Cournapeau, M. Brucher, M. Perrot, and É. Duchesnay. “Scikit-learn: Machine Learning in Python”. *Journal of Machine Learning Research* 12 (2012), pp. 2825–2830. DOI: `10.1007/s13398-014-0173-7.2`. arXiv: `1201.0490` (cit. on p. 77).

[227] T. Hastie, R. Tibshirani, and J. Friedman. “The Elements of Statistical Learning”. *The Mathematical Intelligencer* 27.2 (2001), pp. 83–85. DOI: `10.1198/jasa.2004.s339`. arXiv: `1010.3003` (cit. on p. 77).

[228] C. M. Bishop. *Pattern Recognition and Machine Learning*. Vol. 4. 4. 2006, p. 738. DOI: `10.1117/1.2819119`. arXiv: `0-387-31073-8` (cit. on p. 77).

[229] R. Penrose and J. A. Todd. “A generalized inverse for matrices”. *Mathematical Proceedings of the Cambridge Philosophical Society* 51.03 (1955), p. 406. DOI: `10.1017/S0305004100030401` (cit. on p. 78).

[230] R. O. Duda, P. E. Hart, and D. G. Stork. *Pattern Classification*. 2001. DOI: `10.1007/BF01237942`. arXiv: `0-387-31073-8` (cit. on p. 78).

[231] N. D. Haynes, M. C. Soriano, D. P. Rosin, I. Fischer, and D. J. Gauthier. “Reservoir computing with a single time-delay autonomous Boolean node”. *Physical Review E - Statistical, Nonlinear, and Soft Matter Physics* 91.2 (2015), p. 5. DOI: 10.1103/PhysRevE.91.020801. arXiv: 1411.1398 (cit. on p. 81).

[232] L. M. Pecora and T. L. Carroll. “Synchronization in chaotic systems”. *Physical Review Letters* 64.8 (1990), pp. 821–824. DOI: 10.1103/PhysRevLett.64.821. arXiv: arXiv:1504.04577v2 (cit. on pp. 81, 82).

[233] L. M. Pecora and T. L. Carroll. “Driving systems with chaotic signals”. *Physical Review A - Atomic, Molecular, and Optical Physics* 44.4 (1991), pp. 2374–2383. DOI: 10.1103/PhysRevA.44.2374 (cit. on p. 81).

[234] R. He and P. G. Vaidya. “Analysis and synthesis of synchronous periodic and chaotic systems”. *Physical Review A* 46.12 (1992), pp. 7387–7392. DOI: 10.1103/PhysRevA.46.7387 (cit. on p. 81).

[235] A. S. Pikovsky, M. G. Rosenblum, G. V. Osipov, and J. Kurths. “Phase synchronization of chaotic oscillators by external driving”. *Physica D: Nonlinear Phenomena* 104.3-4 (1997), pp. 219–238. DOI: 10.1016/S0167-2789(96)00301-6 (cit. on p. 81).

[236] T. Jüngling, H. Benner, H. Shirahama, and K. Fukushima. “Complete chaotic synchronization and exclusion of mutual Pyragas control in two delay-coupled Rössler-type oscillators”. *Physical Review E - Statistical, Nonlinear, and Soft Matter Physics* 84.5 (2011), p. 10. DOI: 10.1103/PhysRevE.84.056208. arXiv: 1106.4420 (cit. on pp. 81, 82).

[237] G. Van der Sande, M. C. Soriano, I. Fischer, and C. R. Mirasso. “Dynamics, correlation scaling, and synchronization behavior in rings of delay-coupled oscillators.” *Physical Review E - Statistical, Nonlinear, and Soft Matter Physics* 77.5 Pt 2 (2008), p. 055202. DOI: 10.1103/PhysRevE.77.055202 (cit. on p. 81).

[238] M. C. Soriano, G. Van der Sande, I. Fischer, and C. R. Mirasso. “Synchronization in Simple Network Motifs with Negligible Correlation and Mutual Information Measures”. *Physical Review Letters* 108.13 (2012), p. 134101. DOI: 10.1103/PhysRevLett.108.134101 (cit. on pp. 81, 143).

[239] A. S. Pikovsky, M. G. Rosenblum, and J. Kurths. *Synchronization: A Universal Concept in Nonlinear Sciences*. Vol. 56. 1. Cambridge University Press, 2003, pp. 47–47 (cit. on p. 81).

[240] K. Kanno, A. Uchida, and M. Bunsen. “Complexity and bandwidth enhancement in unidirectionally coupled semiconductor lasers with time-delayed optical feedback”. *Physical Review E - Statistical, Nonlinear, and Soft Matter Physics* 93.3 (2016), p. 032206. DOI: `10.1103/PhysRevE.93.032206` (cit. on pp. 81, 82, 122).

[241] Y. Liu, N. Kikuchi, and J. Ohtsubo. “Controlling dynamical behavior of a semiconductor laser with external optical feedback”. *Physical Review E - Statistical, Nonlinear, and Soft Matter Physics* 51.4 (1995), R2697–R2700. DOI: `10.1103/PhysRevE.51.R2697` (cit. on p. 82).

[242] D. W. Sukow and D. J. Gauthier. “Entraining power-dropout events in an external-cavity semiconductor laser using weak modulation of the injection current”. *IEEE Journal of Quantum Electronics* 36.2 (2000), pp. 175–183. DOI: `10.1109/3.823463` (cit. on p. 82).

[243] J. M. Buldú, J. García-Ojalvo, C. R. Mirasso, and M. C. Torrent. “Stochastic entrainment of optical power dropouts”. *Physical Review E - Statistical, Nonlinear, and Soft Matter Physics* 66.2 (2002), pp. 1–5. DOI: `10.1103/PhysRevE.66.021106` (cit. on pp. 82, 110).

[244] N. Oliver, L. Larger, and I. Fischer. “Consistency in experiments on multistable driven delay systems”. *Chaos* 103115.26 (2016). DOI: `10.1063/1.4966021` (cit. on p. 82).

[245] S. Heiligenthal, T. Dahms, S. Yanchuk, T. Jüngling, V. Flunkert, I. Kanter, E. Schöll, and W. Kinzel. “Strong and Weak Chaos in Nonlinear Networks with Time-Delayed Couplings”. *Physical Review Letters* 107.23 (2011), p. 234102. DOI: `10.1103/PhysRevLett.107.234102` (cit. on pp. 82, 123).

[246] N. Oliver. “Complex Dynamics of Photonic Delay Systems: a story about consistency and unpredictability”. PhD thesis. Universitat de les Illes Balears, 2015, p. 152 (cit. on p. 82).

[247] R. Toral, C. R. Mirasso, E. Hernández-García, and O. Piro. “Analytical and Numerical Studies of Noise-induced Synchronization of Chaotic Systems”. 665 (2001), p. 10. DOI: `10.1063/1.1386397`. arXiv: `0104044 [nlin]` (cit. on p. 82).

[248] G. Giacomelli, S. Barland, M. Giudici, and A. Politi. “Characterizing the response of chaotic systems”. *Physical Review Letters* 104.19 (2010), pp. 1–4. DOI: `10.1103/PhysRevLett.104.194101` (cit. on p. 82).

[249] T Fukuyama, M Okugawa, T Fukuyama, and M Okugawa. “Dynamic characterization of coupled nonlinear oscillators caused by the instability of ionization waves Dynamic characterization of coupled nonlinear oscillators caused by the instability of ionization waves”. 032302 (2017). DOI: `10.1063/1.4977804` (cit. on p. 82).

[250] T. Jüngling and I. Fischer. “Synchronization of Heterogeneous Oscillators by Noninvasive Time-Delayed Cross Coupling”. 194101.November (2015), pp. 1–5. DOI: `10.1103/PhysRevLett.115.194101` (cit. on p. 82).

[251] V. S. Anishchenko, A. G. Balanov, N. B. Janson, N. B. Igoshevo, and G. V. Bordyugov. “Entrainment between heart rate and weak noninvasive forcing”. *International Journal of Bifurcation and Chaos* 10.10 (2000), pp. 2339–2348. DOI: `10.1142/S0218127400001468` (cit. on p. 82).

[252] X.-J. Wang. “Neurophysiological and computational principles of cortical rhythms in cognition.” *Physiological Reviews* 90.3 (2010), pp. 1195–268. DOI: `10.1152/physrev.00035.2008`. arXiv: `NIHMS150003` (cit. on p. 82).

[253] E. Schöll and H. G. Schuster. *Handbook of Chaos Control*. Ed. by E. Schll and H. G. Schuster. Weinheim, Germany: Wiley-VCH Verlag GmbH & Co. KGaA, 2007, p. 897. DOI: `10.1002/9783527622313` (cit. on p. 82).

[254] O. D’Huys, S. Zeeb, T. Jüngling, S. Heiligenthal, S. Yanchuk, and W. Kinzel. “Synchronisation and scaling properties of chaotic networks with multiple delays”. *EPL (Europhysics Letters)* 103.1 (2013), p. 10013. DOI: `10.1209/0295-5075/103/10013`. arXiv: `1302.7277` (cit. on p. 82).

[255] F. Montani, O. A. Rosso, F. S. Matias, S. L. Bressler, and C. R. Mirasso. “A symbolic information approach to determine anticipated and delayed synchronization in neuronal circuit models”. *Philosophical Transactions of the Royal Society A: Mathematical, Physical and Engineering Sciences* 373.2056 (2015), p. 20150110. DOI: `10.1098/rsta.2015.0110` (cit. on p. 82).

[256] S. Sivaprakasam and K. A. Shore. “Demonstration of optical synchronization of chaotic external-cavity laser diodes.” *Optics Letters* 24.7 (1999), pp. 466–8. DOI: `10.1364/OL.24.000466` (cit. on p. 82).

[257] A. Uchida, R. McAllister, R. Meucci, and R. Roy. “Generalized synchronization of chaos in identical systems with hidden degrees of freedom.” *Physical Review Letters* 91.17 (2003), p. 174101. DOI: `10.1103/PhysRevLett.91.174101` (cit. on p. 82).

[258] Y. Hong, M. W. Lee, P. S. Spencer, and K. A. Shore. “Synchronization of chaos in unidirectionally coupled vertical-cavity surface-emitting semiconductor lasers”. *Optics Letters* 29.11 (2004), p. 1215. DOI: `10.1364/OL.29.001215` (cit. on p. 82).

[259] H. Jaeger. “Short term memory in echo state networks”. *GMD Report* 152 (2002), p. 60 (cit. on pp. 83, 84, 96).

[260] L. Larger, B. Penkovsky, and Y. Maistrenko. “Laser chimeras as a paradigm for multistable patterns in complex systems”. *Nature Communications* 6 (2015), p. 7752. DOI: `10.1038/ncomms8752` (cit. on p. 83).

[261] J. Taylor. *Introduction to Error Analysis. The study of uncertainties in physical measurements*. 2nd. Sausalito, California: University Science Books, 1997, p. 349 (cit. on p. 84).

[262] R. Legenstein and W. Maass. “Edge of chaos and prediction of computational performance for neural circuit models”. *Neural Networks* 20.3 (2007), pp. 323–334. DOI: `10.1016/j.neunet.2007.04.017` (cit. on p. 85).

[263] J. Dambre, D. Verstraeten, B. Schrauwen, and S. Massar. “Information processing capacity of dynamical systems.” *Scientific Reports* 2 (2012), p. 514. DOI: `10.1038/srep00514` (cit. on p. 86).

[264] N. A. Gershenfeld, A. S. Weigend, N. A. Gershenfeld, and A. S. Weigend. “The future of time series”. *Time Series Prediction: Forecasting the Future and Understanding the Past* (1993), pp. 1–70 (cit. on p. 86).

[265] H. Jaeger and H. Haas. “Harnessing Nonlinearity: Predicting Chaotic Systems and Saving Energy in Wireless Communication”. *Science* 304.5667 (2004), pp. 78–80. DOI: `10.1126/science.1091277` (cit. on p. 87).

[266] M. C. Mackey and L. Glass. *Oscillation and chaos in physiological control systems*. 1977. DOI: `10.1126/science.267326` (cit. on p. 87).

[267] R. Broom, E. Mohn, C. Risch, and R. Salathe. “Microwave self-modulation of a diode laser coupled to an external cavity”. *IEEE Journal of Quantum Electronics* 6.6 (1970), pp. 328–334. DOI: `10.1109/JQE.1970.1076461` (cit. on p. 102).

[268] C. Risch and C. Voumard. “Self-pulsation in the output intensity and spectrum of GaAs-AlGaAs cw diode lasers coupled to a frequency-selective external optical cavity”. *Journal of Applied Physics* 48.5 (1977), p. 2083. DOI: `10.1063/1.323922` (cit. on p. 102).

[269] V. Kovanis, A. Gavrielides, T. B. Simpson, and J. M. Liu. “Instabilities and chaos in optically injected semiconductor lasers”. *Applied Physics Letters* 67.19 (1995), pp. 2780–2782. DOI: `10.1063/1.114591` (cit. on p. 102).

[270] S. Eriksson and Å. M. Lindberg. “Observations on the dynamics of semiconductor lasers subjected to external optical injection”. *Journal of Optics B: Quantum and Semiclassical Optics* 4.2 (2002), pp. 149–154. DOI: `10.1088/1464-4266/4/2/311` (cit. on p. 102).

[271] R. Lang. “Injection locking properties of a semiconductor laser”. *IEEE Journal of Quantum Electronics* 18.6 (1982), pp. 976–983. DOI: `10.1109/JQE.1982.1071632` (cit. on pp. 102, 122).

[272] G. H. Van Tartwijk and D. Lenstra. “Semiconductor lasers with optical injection and feedback”. *Quantum and Semiclassical Optics: Journal of the European Optical Society Part B* 7.2 (1995), pp. 87–143. DOI: `10.1088/1355-5111/7/2/003` (cit. on p. 102).

[273] V. Flunkert, O. D’Huys, J. Danckaert, I. Fischer, and E. Schöll. “Bubbling in delay-coupled lasers”. *Physical Review E - Statistical, Nonlinear, and Soft Matter Physics* 79.6 (2009), pp. 1–4. DOI: `10.1103/PhysRevE.79.065201`. arXiv: `0901.4282` (cit. on p. 110).

[274] D. A. Arroyo-Almanza, A. N. Pisarchik, I. Fischer, C. R. Mirasso, and M. C. Soriano. “Spectral properties and synchronization scenarios of two mutually delay-coupled semiconductor lasers”. *Optics Communications* 301-302 (2013), pp. 67–73. DOI: `10.1016/j.optcom.2013.03.040` (cit. on p. 110).

[275] L. Grigoryeva, J. Henriques, L. Larger, and J.-P. Ortega. “Optimal nonlinear information processing capacity in delay-based reservoir computers”. *Scientific Reports* 5.1 (2015), p. 12858. DOI: `10.1038/srep12858`. arXiv: `1411.2515` (cit. on p. 116).

[276] S. Ortín and L. Pesquera. "Reservoir Computing with an Ensemble of Time-Delay Reservoirs". *Cognitive Computation* 9.3 (2017), pp. 327–336. DOI: `10.1007/s12559-017-9463-7` (cit. on pp. 116, 124).

[277] K. Kobayashi, H. Nishimoto, and R. Lang. "Experimental observation of asymmetric detuning characteristics in semiconductor laser injection locking". *Electronics Letters* 18.2 (1982), p. 54. DOI: `10.1049/el:19820038` (cit. on p. 122).

[278] Y.-H. Liao and F. Y. Lin. "Dynamical characteristics and their applications of semiconductor lasers subject to both optical injection and optical feedback." *Optics Express* 21.20 (2013), pp. 23568–78. DOI: `10.1364/OE.21.023568` (cit. on p. 122).

[279] R. Martinenghi, S. Rybalko, M. Jacquot, Y. K. Chembo, and L. Larger. "Photonic Nonlinear Transient Computing with Multiple-Delay Wavelength Dynamics". *Physical Review Letters* 108.24 (2012), p. 244101. DOI: `10.1103/PhysRevLett.108.244101` (cit. on p. 125).

[280] K. Wagner and D. Psaltis. "Multilayer optical learning networks". *Applied Optics* 26.23 (1987), p. 5061. DOI: `10.1364/AO.26.005061` (cit. on p. 128).

[281] M. S. Cohen. "Design of a new medium for volume holographic information processing". *Applied Optics* 25.14 (1986), p. 2288. DOI: `10.1364/AO.25.002288` (cit. on p. 128).

[282] Y. S. Abu-Mostafa and D. Psaltis. "Optical Neural Computers". *Scientific American* 256.3 (1987), pp. 88–95. DOI: `10.1038/scientificamerican0387-88` (cit. on p. 128).

[283] B. E. A. Saleh and M. C. Teich. *Fundamentals of Photonics*. New York, New York, USA: John Wiley & Sons, 2007, p. 1200 (cit. on p. 131).

[284] S. H. Strogatz. *Nonlinear Dynamics And Chaos*. 1994 (cit. on p. 137).

[285] E. Ott. *Chaos in Dynamical Systems*. 2002. DOI: `10.1017/CBO9780511803260`. arXiv: `arXiv:1011.1669v3` (cit. on p. 137).

[286] P. Antonik, A. Smerieri, F. Duport, M. Haelterman, and S. Massar. "FPGA Implementation of reservoir computing with online learning". *Belgian-Dutch Conference on Machine Learning* (2015) (cit. on p. 150).

[287] T. Instrument. *DLP7000 DLP ® 0 . 7 XGA 2x LVDS A DMD*. Tech. rep. (cit. on p. 176).